INSTITUTO POTOSINO DE INVESTIGACIÓN CIENTÍFICA Y TECNOLÓGICA, A.C.

POSGRADO EN GEOCIENCIAS APLICADAS

Origin, stratigraphy and evolution of the Oligocene rhyolitic volcanism in the central and southern Mesa Central of Mexico (Villa García, Zacatecas and La Herradura, San Luis Potosí), by means of geochemistry, petrology and geochronology.

Tesis que presenta

Pascal Sieck

Para obtener el grado de

Doctor(a) en Geociencias Aplicadas

Director (Codirectores) de la Tesis:

Dr. Pablo Dávila-Harris

Dr. Rubén López-Doncel

San Luis Potosí, S.L.P., Septiembre de 2019

IPICYT

Constancia de aprobación de la tesis

La tesis ***"Origin, stratigraphy and evolution of the Oligocene rhyolitic volcanism in the central and southern Mesa Central of Mexico (Villa García, Zacatecas and La Herradura, San Luis Potosí), by means of geochemistry, petrology and geochronology"*** presentada para obtener el Grado de Doctor en Geociencias Aplicadas, fue elaborada por **Pascal Sieck** y aprobada el diecinueve de septiembre del dos mil diecinueve por los suscritos, designados por el Colegio de Profesores de la División de Geociencias Aplicadas del Instituto Potosino de Investigación Científica y Tecnológica, A.C.

Dr. Pablo Dávila Harris
Codirector de la tesis

Dr. Rubén López Doncel
Codirector de la tesis

Dr. Aaron James Martin
Miembro del Comité Tutoral

Dr. Alfredo Aguillón Robles
Miembro del Comité Tutoral

Créditos Institucionales

Esta tesis fue elaborada en el Laboratorio de Petrografia de la División Geociencias Aplicadas del Instituto Potosino de Investigación Científica y Tecnológica, A.C., bajo la dirección del Dr. Pablo Dávilla-Harris.

Durante la realización del trabajo el autor recibió una beca académica del Consejo Nacional de Ciencia y Tecnología (590738) y del Instituto Potosino de Investigación Científica y Tecnológica, A. C.

IPICYT

Instituto Potosino de Investigación Científica y Tecnológica, A.C.

Acta de Examen de Grado

El Secretario Académico del Instituto Potosino de Investigación Científica y Tecnológica, A.C., certifica que en el Acta 012 del Libro Primero de Actas de Exámenes de Grado del Programa de Doctorado en Geociencias Aplicadas está asentado lo siguiente:

En la ciudad de San Luis Potosí a los 19 días del mes de septiembre del año 2019, se reunió a las 11:30 horas en las instalaciones del Instituto Potosino de Investigación Científica y Tecnológica, A.C., el Jurado integrado por:

Dr. Aaron James Martin _	**Presidente**	**IPICYT**
Dr. Alfredo Aguillón Robles	**Secretario**	**UASLP**
Dr. Pablo Dávila Harris	**Sinodal**	**IPICYT**
Dr. Rubén López Doncel	**Sinodal externo**	**UASLP**

a fin de efectuar el examen, que para obtener el Grado de:

DOCTOR EN GEOCIENCIAS APLICADAS

sustentó el C.

Pascal Sieck

sobre la Tesis intitulada:

Origin, stratigraphy and evolution of the Oligocene rhyolitic volcanism in the central and southern Mesa Central of Mexico (Villa García, Zacatecas and La Herradura, San Luis Potosí), by means of geochemistry, petrology and geochronology

que se desarrolló bajo la dirección de

Dr. Pablo Dávila Harris
Dr. Rubén López Doncel (UASLP)

El Jurado, después de deliberar, determinó

APROBARLO

Dándose por terminado el acto a las 13:00 horas, procediendo a la firma del Acta los integrantes del Jurado. Dando fe el Secretario Académico del Instituto.

A petición del interesado y para los fines que al mismo convengan, se extiende el presente documento en la ciudad de San Luis Potosí, S.L.P., México, a los 19 días del mes de septiembre de 2019.

Dr. Marcial Bonilla Marín
Secretario Académico

Mtra. Ivonne Lizette Cuevas Vélez
Jefa del Departamento del Posgrado

INSTITUTO POTOSINO DE INVESTIGACIÓN CIENTÍFICA Y TECNOLÓGICA, A.C.
IPICYT
SECRETARIA ACADEMICA

Acknowledgements

I thank Dr. Pablo Dávila Harris and Dr. Rubén López-Doncel for the takeover of the supervision of my thesis and the associated detailed support, assistance and discussion of the critical issues. Furthermore, I like to thank them for their help in finding the topic of the thesis, the financial support for the field work, the laboratory work, and the analysis.

Many thanks to Dr. Alfredo Aguillón-Robles and Dr. Aaron Martin for their comments and tips during the last four years. In addition, I would like to thank Dr. Alfredo Aguillón-Robles, Erasmo Mata Martínez, Miguel Ángel Cortina Rangel from the UASLP and María Mercedes Zavala Arriaga from IPICYT for assistance with sample preparation and the analysis. At the same time, I would like to thank Dr. Klaus Wemmer for the implementation of the K-Ar dates. Many thanks to Carlos Ortega Obregon from the UNAM in Juriquilla for the U-Pb age data and Dra. Noemi Salazar Hermenegildo from the UNAM in Morelia for the help with the EPMA. In addition, I would like to thank Ana Iris Peña Maldonado and Beatriz Adriana Rivera Escoto from the LINAN in the IPICYT for the SEM and XRF analysis.

I thank the financial support of the National Council of Science and Technology, Mexico (CONACYT) through Ph.D. scholarship number 590738.

I would like to sincerely thank my wife Marcela for her helpful tips, the great motivation and the support during the writing of this work and the bearing of my temporarily bad temper. Thanks to you the time in Mexico was and is a wonderful and unforgettable experience.

Zum Schluss, aber nicht zuletzt, noch ein riesiges Dankeschön an meine Familie, ohne eure Unterstützung wäre die Durchführung dieser Arbeit gar nicht erst möglich gewesen.

Content

List of figures

List of tables

Abstract

The Mesa Central province forms part of the southern Sierra Madre Occidental silicic large igneous province. Oligocene felsic volcanism is common in the center and southern portion of the Mesa Central physiographic province. Generally, rhyolitic dome complexes and ignimbrites occur aligned with regional fault systems, mostly associated with the southern Basin and Range extension, and thus suggesting that faults controlled the felsic magmas that formed these domes, lava flows, and ignimbrites, however not all have been studied in detail. The present work presents data on the volcanic stratigraphy, geochemistry, geochronology, and petrology of the Oligocene felsic volcanism in this area. In the La Herradura area the garnet-bearing rhyolite and a rhyolitic ignimbrite forms together with an andesite a typical K-rich sub-alkaline intra-plate tectonic setting bimodal series. Electron microprobe analysis indicates that the garnet is homogeneous and primarily almandine with subordinately pyrope, grossular, spessartine, and andradite. Garnet chemistry as well as the chemistry of the host rhyolite implies the crystallization as a primary phase from a lower crustal peraluminous magma. The absence of crustal xenoliths, the idiomorphic shape and the garnet chemistry as well as the geochemistry of the host rhyolite in combination with geothermobarometric analysis and U-Pb zircon single grain age determination on zircon inclusion in garnet (31.70 ± 0.21 Ma and 32.22 ± 0.67 Ma) and zircons derived from whole rock samples (31.52 ± 0.48 Ma and 31.32 ± 0.97) confirms the crystallization of garnet as a primary phase from a lower crustal peraluminous magma. The appearance of primary magmatic almandine-rich garnets is confirmed by rhyolite-MELTS simulations on the crystallization. Trace element analyses on the rhyolitic ignimbrite and the garnet-bearing rhyolite suggest that the petrogenesis of these acidic rocks involved partial melting of the lower crust and fractional crystallization. The andesitic lava flow is metaluminous and its trace element patterns suggest that the parental magma was derived from upper mantle partial melting and that it was stored at the mantle-crust boundary.

The Oligocene Villa Garcia Ignimbrite complex in the southern portion of the Mesa Central is built up by a composite volcanic stratigraphy. A rhyolitic lava flow initiates the volcanic activity and two voluminous rhyolitic ignimbrites form, together with an andesitic lava flow the top of the stratigraphy. Both ignimbrites the older Villa Garcia ignimbrite (31.59 ± 0.14 Ma and 31.15 ± 0.12 Ma) and the younger Loreto Ignimbrite (28.97 ± 0.11 Ma and 28.66 ± 0.07 Ma) are densely welded

and show lava-like to rheomorphic structures. Geochemical features show that the rhyolitic magmas are derived in an intra-plate setting from a process including partial melting of the lower crust and fractional crystallization during ascent, in case of the ignimbrites also during magma storage and in a shallow magma chamber. The andesitic lava flow is metaluminous, contains olivine and pyroxene, and its trace element patterns suggest that the parental magma was derived from upper mantle partial melting. I propose that the southern Basin and Range extension event favored the direct ascent of these magmas from the source through the brittle, where slight interaction with the country rock took place, to the surface.

Key words:

Oligocene, Mexico, Mesa Central, Sierra Madre Occidental, Rhyolitic volcanism, Garnet-bearing rhyolite, Rheomorphic ignimbrite, Bimodal volcanism

Resumen

La provincia de la Mesa Central se localiza en la porción meridional de Provincia Silícica de la Sierra Madre Occidental. El volcanismo félsico oligocénico es común en la parte centro-sur de la Provincia Fisiográfica de la Mesa Central. Generalmente, afloran complejos volcánicos asociados a estructuras dómicas e ignimbritas de composición riolítica principalmente, que se encuentran extravasados en el sistema de fallas regionales con orientación NW-SE, considerados como una extensión del "*Basin and Range*", a lo que se ha considerado que las fallas y fisuras han controlado el emplazamiento del magmatismo félsico que generaron derrames de lavas e ignimbritas originando estructuras dómicas; y que en su mayoría no han sido estudiados a detalle. El presente trabajo, muestra datos sobre la estratigrafía volcánica, geoquímica, geocronología y petrología de volcanismo félsico emplazado durante el Oligoceno en el área de La Herradura; en donde se describe una asociación de lavas riolitas con granate e ignimbritas riolíticas asociadas a lavas andesíticas enriquecidas en K, subalcalinas asociadas a un ambiente tectónico intraplaca, generando una serie de volcanismo bimodal. Análisis de microsonda electrónica, indican que el granate es homogéneo con composición de almandino con subordinados de piropo, grosularita, espersartita y andradita. La química mineral y la geoquímica de la lava, sugiere que el granate está asociada a una fase primaria de cristalización de un magma con carácter peraluminoso originado en la base de la corteza. La ausencia de xenolitos corticales, los granates idiomórficos, su química mineral y la geoquímica de la roca entera del magma riolítico combinado con análisis geotermobarómetricos y edad isotópica U-Pb en circón como inclusión en el cristal de granate (31.70 ± 0.21 y 32.22 ± 0.67 Ma) y circones asociados con la cristalización del magma (31.52 ± 0.48 y 31.32 ± 0.97 Ma), confirman que la cristalización del granate se asocia a la fase primaria de cristalización de un magma peraluminoso en la base dela corteza. La cristalización de granate magmático primario con composición almandino, se confirma con simulaciones de cristalización realizadas con el programa rhyolite-MELTS. El análisis de elementos traza en las ignimbritas y lavas riolíticas con granate, sugieren que la petrogénesis de este magmatismo félsico está asociado a la fusión parcial de la base de la corteza y a cristalización fraccionado de los magmas. Los derrames de lavas de composición andesítica muestran un carácter metaluminoso y sus patrones de elementos traza sugieren que el magma original está derivado de la fusión parcial del manto superior y generó una cámara magmática en la frontera manto-corteza.

El complejo ignimbrítico de Villa García del Oligoceno, se ubica en la porción sur de la Mesa Central y está constituido por una secuencia volcánica estratigráfica compuesta. La actividad volcánica se inició con lavas riolíticas, seguido por dos derrames ignimbríticos voluminosos, asociados con derrames de lavas de composición andesíticos hacia la cima de la secuencia estratigráfica. Ambas ignimbritas, la ignimbrita Villa García es la más antigua (con una edad Ar-Ar de 31.59 ± 0.14 y 31.15 ± 0.12 Ma) y la más joven la ignimbrita Loreto (28.97 ± 0.11 y 28.66 ± 0.07 Ma), están densamente soldada rheomórfica. Sus rasgos geoquímicos, muestran que los magmas riolíticos son derivados en un ambiente tectono-magmático de tipo intraplaca que incluyen procesos de fusión parcial de la base de la corteza y procesos de cristalización fraccionada generados en el ascenso del magma, el origen de las ignimbritas está asociada a una cámara magmática de poca profundidad. Los derrames de lava de composición andesítica con carácter metaluminoso contiene minerales de olivino y piroxeno y conjugados con sus patrones de elementos traza sugieren que el magma original fue originado en el manto superior por fusión parcial. Se propone, que la porción SE del "*Basin and Range*" el evento de extensión favoreció el ascenso de estos magmas desde su fuente a través de la corteza frágil, en donde hubo interacción con la roca encajonante hacia la superficie.

Palabras clave:

Oligoceno, México, Mesa Central, Sierra Madre Occidental, vulcanismo riolitico, riolita con granate, ignimbrita reomórfica, volcanismo bimodal

1. Introduction

1.1. The Sierra Madre Occidental: A Silicic Large Ingenious Province

Silicic Large Igneous Provinces (SLIP) like the Sierra Madre Occidental (SMO, Figure 1a and 1b) and its southeastern portion, the Mesa Central (MC) are rare and important in the geological history because of their extent (> 0.1 Mkm^2) large amount of primary volcanic and volcanoclastic rocks (> 0.25 Mkm^3), and possibility to induce environmental change (Bryan, 2007; Cather et al., 2009; Jicha et al., 2009; Bryan and Ferrari, 2013; Murray et al., 2013). SLIPs have a lifespan from approximately 50 Ma, whereas more than 75 % of the total magmatic volume is emplaced during a short time range between one and five Ma (Bryan, 2007; Bryan and Ernst, 2008; Murray et al., 2013). Furthermore, SLIPs are volumetrically dominated by volcanic rocks of dacitic to rhyolitic composition (> 80 vol.%), but compositions can range from basalt to high-silica rhyolite (Bryan, 2007; Bryan and Ernst, 2008; Murray et al., 2013). Prior studies imply that SLIPs might be initiated as pre-rifting magmatic events and might be characteristic of continental regions undergoing extensive lithospheric extension such as the Basin and Range extension in the SMO (Bryan et al., 2002; Bryan, 2007; Best et al., 2013; Bryan and Ferrari, 2013; Murray et al., 2013). Consequently, as the extension of the crust is proposed as a main factor that favors the formation of large silicic magma volumes, it is important to define the timing extensional deformation in relation to magmatism as a significant assumption toward understanding silicic large igneous province processes as well as very large magnitude explosive silicic eruptions (Hildreth, 1981; Wark, 1991; Brooks Hanson and Glazner, 1995; Aguirre-Díaz and Labarthe-Hernández, 2003; Costa et al., 2011; Murray et al., 2013).

The Sierra Madre Occidental (SMO) is the largest continuous ignimbrite province in the world (Swanson and McDowell, 1984; Aguirre-Díaz and Labarthe-Hernández, 2003; Aguirre-Díaz et al., 2008) and the largest silicic igneous province in North America (McDowell and Keizer, 1977; McDowell and Clabaugh, 1979; Ward, 1995; Aguirre-Díaz et al., 2008; Bryan and Ferrari, 2013). It extends from the Basin and Range Province of the western United States in the north to its intersection with the Trans-Mexican volcanic belt in the south over more than 1200 km (Swanson and McDowell, 1984; Aguirre-Díaz and Labarthe-Hernández, 2003; Aguirre-Díaz et al., 2008). The SMO is elevated plateau region that is up to 3 km high and covers ~ 400,000 km^2 with conservative average ignimbrite thickness of 1 km (McDowell and Keizer, 1977; McDowell and

Clabaugh, 1979; Ferrari et al., 2002; Aguirre-Díaz and Labarthe-Hernández, 2003; Ferrari et al., 2007; Bryan and Ferrari, 2013).

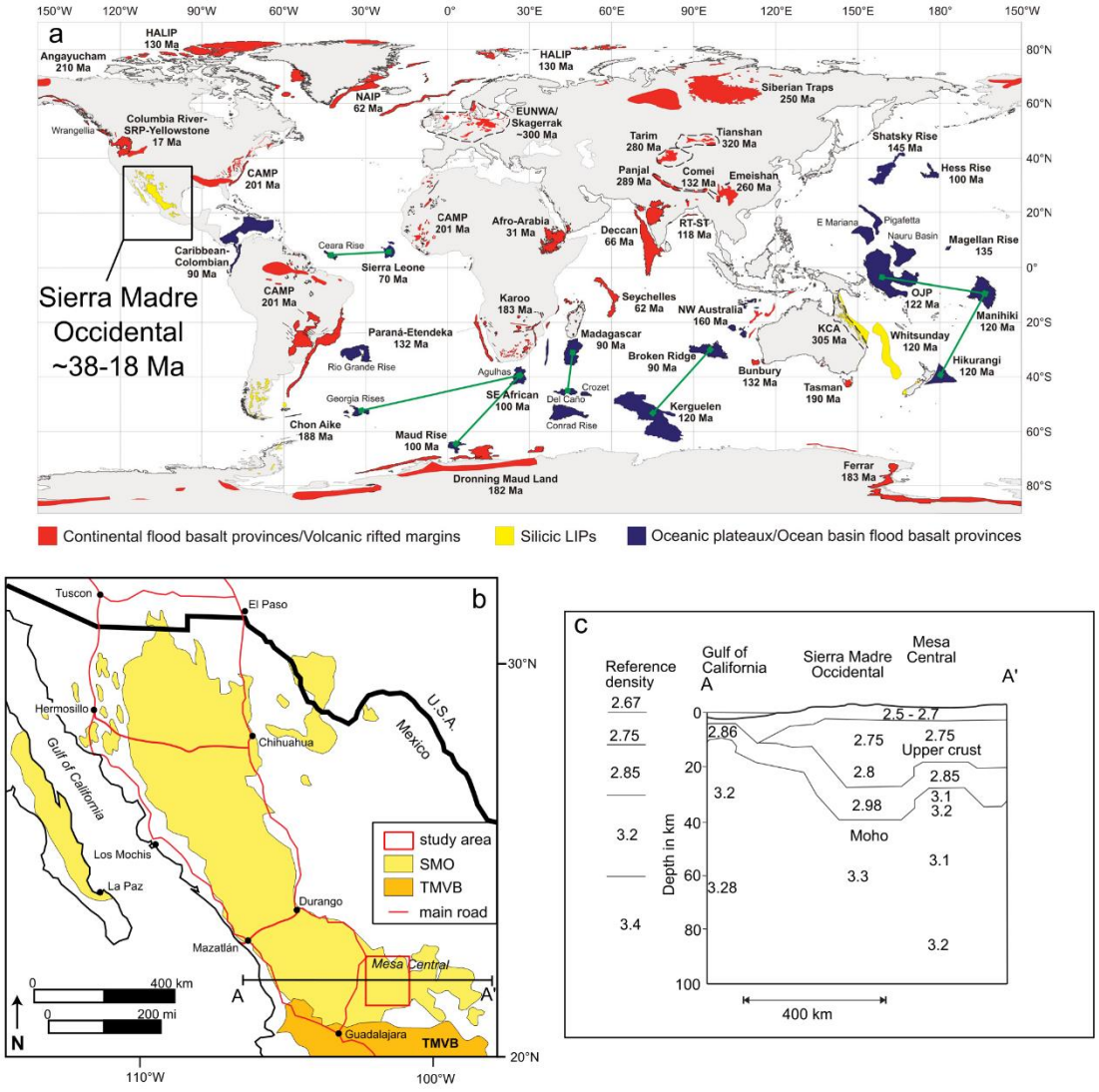

Figure 1: a) Global distribution of large igneous provinces (LIPs). CAMP: Central Atlantic magmatic province; EUNWA: European, northwest Africa; HALIP: High Arctic large igneous province; NAIP: North Atlantic igneous province; OJP: Ontong Java Plateau; RT-ST: Rajmahal Traps–Sylhet Traps; SRP: Snake River Plain; KCA: Kennedy-Connors-Auburn. Figure taken from Bryan and Ferrari (2013). b) Generalized map of the extend of the Sierra Madre Occidental and its southeastern portion, the Mesa Central. Figure changed after Murray et al. (2013). c) Crustal structure and thickness of the Sierra Madre Occidental and its southeastern portion the Mesa Central, the location of section is shown b). Figure modified after Nieto-Samaniego et al. (2007).

The crustal thickness of the SMO (Figure 1c) is with up to 55 km one of the largest in Mexico, whereas the crustal thickness to the Gulf of Mexico is reduced to ~ 22 km (Nieto-Samaniego et al., 2007). The crustal thickness of the southeastern portion of the SMO, the MC is interpreted to be 30 – 32 km (Nieto-Samaniego et al., 2007) but still under discussion. Due to its elevated core, the ignimbrites are lying horizontal in the center part of the SMO and they are tilted and faulted

along the flanks of the SMO (Bryan and Ferrari, 2013). The volcanism appearing in the SMO silicic large igneous province is simultaneous to the extensive mid-Cenozoic ignimbrite flare-up occurring in most parts of the southwestern North American Cordillera from the Middle Eocene to Late Miocene (Coney, 1978; Armstrong and Ward, 1991; Wark, 1991; Ferrari et al., 2002; Lipman, 2007; Cather et al., 2009; Best et al., 2013). The volcanism associated to the SMO silicic large igneous province spreads until its southeastern portion the MC, to parts of the southern Basin and Range in eastern Chihuahua and Durango (Gunderson et al., 1986; Aguirre-Díaz and McDowell, 1991, 1993; Nieto-Samaniego et al., 2007; Murray et al., 2013) and to the Mexican state of Baja California Sur (Umhoefer et al., 2001; Ferrari et al., 2002; Ferrari et al., 2018). Previous works showed that most the volume (~400,000 km³) of rhyolitic ignimbrites and rhyolites were erupted between 38 Ma and 18 Ma with two main peaks at ca. 34–28 Ma and ca. 24–18 Ma (Ferrari et al., 2002; 2007; Nieto-Samaniego et al., 2007; Bryan and Ferrari, 2013). In addition, previous works showed that the emplacement of the thick ignimbrite packages was very rapid (McDowell and Keizer, 1977; Ferrari et al., 2002; Swanson et al., 2006; McDowell and McIntosh, 2012) with fast magma generation of the silicic magma and fast ascent and eruption of the rhyolitic ignimbrites (Bryan et al., 2008). During the Oligocene volcanic pulse (ignimbrite flare up, 34–28 Ma) at least a volume of 300,000 km³ (75 % of the total volume of volcanic rocks) was erupted, whereas the other 25 % of the erupted volume is associated to the Miocene pulse (Bryan and Ferrari, 2013; Ferrari et al., 2018). Most of the erupted volume (85 – 90 %) is represented by rhyolitic ignimbrites and the remaining by rhyolitic lavas, domes as well as basaltic and andesitic lavas (Bryan and Ferrari, 2013; Ferrari et al., 2018). The early Miocene volcanic pulse is compared to the underlaying the Oligocene volcanic pulse more widespread to the western part of the SMO (Baja California; e.g., Umhoefer et al., 2001; Ferrari et al., 2002; Ferrari et al., 2018). Current works have proved the presence of early Miocene bimodal volcanic and exhumed intrusive rocks offshore, confirming the pre-rift connection between the Mexican mainland and Baja California (Bryan and Ferrari, 2013; Bryan et al., 2014). The distribution and the intense of the early Miocene pulse differs strongly from the northern to the southern portion of the SMO (Bryan and Ferrari, 2013). In the northern part of the SMO the early Miocene volcanism was mainly mafic and less abundant (McDowell et al., 1997). In the southwestern portion of the SMO the Ignimbrites associated to the early Miocene pulse are similar to the Oligocene peak (McDowell and Keizer, 1977; Ferrari et al., 2002; Bryan and Ferrari, 2013). In the MC the Miocene volcanic activity is

mainly associated to the formation of mafic alkaline volcanism (Tristán-González et al., 2009 a; Aguillón-Robles et al., 2014). The Miocene volcanic activity is the last phase of rhyolitic volcanism associated to the SMO silicic large igneous province (Ferrari et al., 2018). The following Pliocene volcanism is mainly alkaline and mafic to intermediate (Aranda-Gómez et al., 2005; Ferrari et al., 2018)

1.2. The Mesa Central of Mexico, the southeastern portion of the Sierra Madre Occidental silicic large province.

The southeastern portion of the SMO is built up by the Mesa Central, an elevated plateau region with more than half of its total area is found above 2000 m (Nieto-Samaniego et al., 2007). It can be distinguished into two regions, a southern and a northern part, mainly differing in their elevation. The boundary that separates the southern from the northern portion of the MC is marked by a ~ 1600 km long and NW-striking lineament, the San Luis – Tepehuanes fault system (Alaniz-Álvarez et al., 2001; Nieto-Samaniego et al., 2007). The MC is covered by Oligocene and Miocene volcanic rocks, associated to the Ignimbrite Flare-up (Aguirre-Díaz and McDowell, 1991; Ferrari et al., 2002; Aguirre-Díaz et al., 2008; Bryan and Ferrari, 2013).

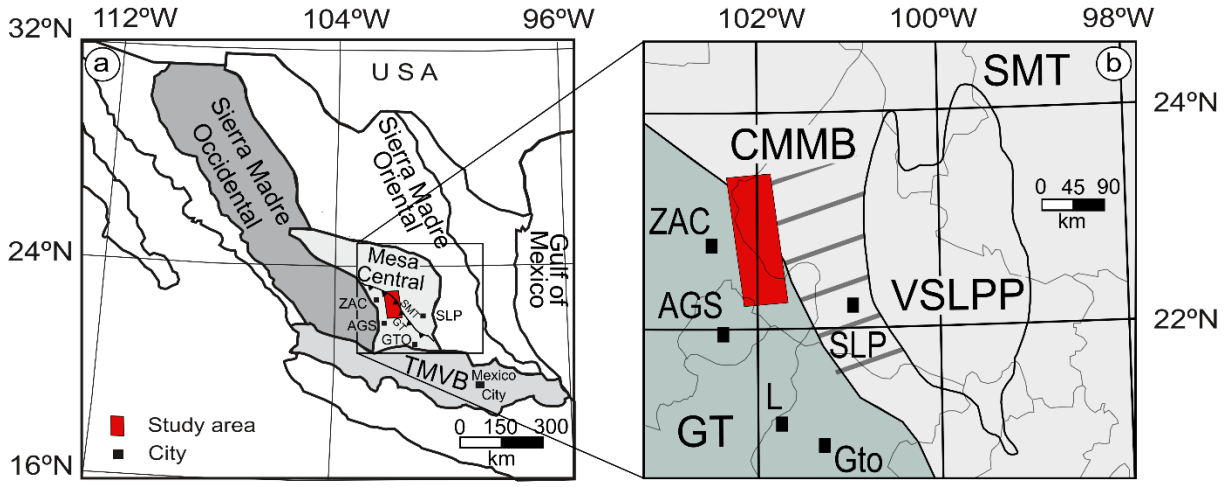

Figure 2: Location of the study area. a) Spatial relationship with the main geological provinces of northern Mexico. b) Location of volcano-tectonic features of San Luis Potosí and Zacatecas, the Guerrero Terrane (GT) and Sierra Madre Terranes (SMT). The SMT are subdivided in the Central Mexico Mesozoic Basin (CMMB) and the Valles-San Luis Potosí Platform (VSLPP). a) and b) modified after Mortensen et al. (2008) and Aguillón-Robles et al. (2014). ZAC: Zacatecas city; AGS: Aguascalientes city; GTO: Guanajuato city; SLP: San Luis Potosí city; L: Leon; TMVB: Trans Mexican Volcanic Belt. Figure taken and changed from Sieck et al., 2019.

However, in the Mesa Central, especially in the study area (Figure 2) 80 vol.% of middle Oligocene felsic magmatism (34 Ma – 28 Ma) is represented by lava domes and only 20 vol.% by ignimbrites (Aguillón-Robles et al., 2009). The Oligocene rhyolitic volcanism is cotemporaneous to the first peak of the ignimbrite flare up in the SMO silicic large province and are between 32 and 29 Ma (Nieto-Samaniego et al., 1996; Nieto-Samaniego et al., 2007; Aguillón-Robles et al., 2009; Tristán-González et al., 2009 a; Ferrari et al., 2018) and is more present in the southern and western portion, with mainly felsic compositional variations (Labarthe-Hernández et al., 1982; Nieto-Samaniego et al., 1996; Nieto-Samaniego et al., 2007; Aguillón-Robles et al., 2009; 2009 b; Tristán-González et al., 2009 a). The lower part of the Oligocene volcanic rocks are lava flows and domes and subordinated some pyroclastic rocks, like ignimbrites (Labarthe-Hernández et al., 1982; Nieto-Samaniego et al., 2007; Tristán-González et al., 2009 a; Ferrari et al., 2018). The domes and lava flows form up to 400 m thick complexes and are more abundant in the southern and central portion of the MC (Nieto-Samaniego et al., 2007; Aguillón-Robles et al., 2009). In the central part of the Mesa Central some of the rhyolitic lava flows and domes form together with mafic volcanic rocks typical bimodal volcanic suits (Tristán-González, 1986; Aguirre-Díaz et al., 2008; Tristán-González et al., 2008; Rodríguez-Ríos and Torres-Aguilera, 2009; Tristán-González et al., 2009 a; Aguillón-Robles et al., 2014; Sieck et al., 2019). The upper part of the Oligocene volcanic sequence is built up by mainly explosive volcanic rocks that form a cover of mainly ignimbrites and minor other pyroclastic rocks on top of the rhyolitic lava flows and domes (Torres-Hernández et al., 2006; Nieto-Samaniego et al., 2007; Tristán-González et al., 2009 a). Labarthe-Hernández et al. (1982) defined the lithostratigraphic units of the widely distributed ignimbrites in the southern and center part of the MC. The origin of the ignimbrites is still not clear due to the absence of caldera and caldera-like structures in the MC. A possible explanation was established by Aguirre-Díaz and Labarthe-Hernández (2003), they proposed that the ignimbrites are originated by graben calderas that form along graben in the MC and they support their theory on the presence of large pyroclastic dykes (e.g. Torres-Hernández et al., 2006).

The second volcanic peak of the ignimbrite flare up in the SMO silicic large province is also present in the Mesa Central and associated to mainly mafic alkaline basalts and andesites, related to an intense phase of the Basin and Range extension (Tristán-González et al., 2009 b; Aguillón-Robles et al., 2014). The following Pliocene and Quaternary volcanism in the MC are mainly

associated to cinder cones and maars of alkaline mafic to intermediate compositions (Labarthe-Hernández et al., 1982; Aranda-Gómez et al., 2005; Nieto-Samaniego et al., 2007).

1.3. Generation of rhyolitic magmas in the Sierra Madre Occidental silicic large province and its southeastern portion the Mesa Central

Silicic magmatism in the Sierra Madre Occidental and the Mesa Central was first associated to the formation of intrusive rocks, with age ranges between 45 – 35 Ma of mainly granodioritic compositions and in lesser extend granitic, tonalitic and dioritic compositions (Ferrari et al., 2018). The exposure of the intrusive rocks is widespread throughout the SMO and the MC and the youngest intrusive rocks are contemporaneous with the first ignimbrite flare up of the SMO silicic large igneous provinces (Ferrari et al., 2018). The plutonic rocks show enrichment in large ionic lithophile elements with regard to highfield-strength elements (HFSE) that are typical for subduction related rocks (Kelley and Cottrell, 2009; Waters and Lange, 2016). Additionally, the intrusive rocks are characterized by high contents of Sr, Ba, Ni as well as light rare earth elements. The tectonic conditions that yielded in the formation of the high Ba-Sr plutonic rocks is still discussed, but the characteristic compositions are related to the partial melting of a thickened continental crust or metasomatized mantle sources in an extensional or a flat-slab regime (Pinto-Linares et al., 2008; Mascuñano et al., 2013). Ferrari et al. (2018) interpreted the high Ba and Sr volcanic rocks as a first phase of a low volume partial melting of a subduction modified lithospheric mantle following the end of the Laramide Orogeny.

The first phase of the ignimbrite flare-up (38 -28 Ma) is, as described above, mainly represented by felsic ignimbrites, lava flows and domes. The felsic volcanism continued in lower volume until approximately 18 Ma in the southern portion of the SMO and the MC (Ferrari et al., 2002; 2007; Nieto-Samaniego et al., 2007; Bryan and Ferrari, 2013). During 38 – 18 Ma the rhyolitic volcanism, with composite ranges to dacite and rhyolite, is mainly high-K calc-alkaline to shoshonitic and metaluminous and peraluminous compositions are equally represented (Orozco-Esquivel et al., 2002; Ferrari et al., 2007). Many of the rhyolitic volcanic rocks emplaced during the first phase of the ignimbrite flare up as well as the second phase have a ferroan (calc-alkaline) character (Orozco-Esquivel et al., 2002; Ferrari et al., 2007). The ferroan character of the rhyolitic volcanic rocks is associated to the formation and evolving of magmas under reduced conditions, which leads to the enrichment of iron (Frost and Frost, 2008). In lesser extent, the rhyolitic rocks

show a magnesian (shoshonitic) composition, these rocks are linked to a magma formation and/or evolution under more oxidizing compositions, which might be resulted in a high fO_2 derived from slab-derived components to a mantle source in subduction zones (Kelley and Cottrell, 2009; Waters and Lange, 2016). In addition, many of the rhyolitic rocks have compositions associated to intraplate settings (e.g. Nieto-Samaniego et al., 2007; Aguillón-Robles et al., 2009; Ferrari et al., 2018) and within the first phase of the ignimbrite flare up of the ferroan rhyolitic rocks, a suite of high-silica and topaz-bearing rhyolites (e.g. Christiansen et al., 1986) was emplaced during 32 – 30 Ma in the northern portion of the SMO and between 31 – 28 Ma in the southern part of the SMO and in the MC (e.g. Leroy et al., 2002; Nieto-Samaniego et al., 2007; Rodríguez-Ríos et al., 2007).

The northern SMO is dominated by metaluminous to weakly peraluminous high-silica rhyolites, which contain modal ferroaugite and that were emplaced as mainly ignimbrites and subordinated lavas and domes in bimodal suits together with basaltic rocks (Cameron et al., 1980; Gunderson et al., 1986; Magonthier, 1988; McDowell, 2007). In contrast, in the southern part of the SMO and in the MC the high-silica rhyolitic rocks are mainly peraluminous, fluorine-rich, topaz- and ferroaugite-bearing that were emplaced as lava domes and lavas in bimodal volcanic suits together with basalts and andesites, associated to extensional faults (e.g., Orozco-Esquivel et al., 2002; Aguillón-Robles et al., 2009; Tristán-González et al., 2009 a). The formation and emplacement of the ferroaugite-bearing high-silica rhyolitic volcanism during the Oligocene is principally relevant because these rocks are originated to magmas with low oxygen fugacity and associated to an intraplate extensional setting (e.g., Carmichael, 1991; Waters and Lange, 2016). In the MC temporal and spatial overlap of the Basin and Range extension and the high-silica rhyolitic volcanism was reported by many authors (e.g. Aguillón-Robles et al., 2009; Tristán-González et al., 2009 b).

Besides the above described differences in the mineralogy of the high-silica rhyolites in the northern portion and in the southern portion of the SMO and the MC the volcanism displays similarities in the behavior of trace elements, most of the rocks show a general enrichment in lithophile elements like U, Rb, Nb, Hf, and Th and a depletion in elements like Sr, Eu, and Ba, which are feldspar-compatible elements, as well as flat rare earth element patterns (e.g. Orozco-Esquivel et al., 2002; Ferrari et al., 2007; Aguillón-Robles et al., 2009). The geochemical features are related to the melting of the lower crust and/or the fractional crystallization of upper mantle-

derived magmas (e.g., Cameron et al., 1980; Christiansen et al., 1986; Magonthier, 1988; Orozco-Esquivel et al., 2002). The ferroaugite and fluorine-rich rhyolitic volcanism was generated and emplaced in a short time during the first flare-up implying a transient event of crustal extension under high strain rate (Orozco-Esquivel et al., 2002; Aguillón-Robles et al., 2009), which favored the ascent of mantle-derived basaltic melts that acted as the heat source for crustal melting or as parent magmas (e.g. Rodríguez-Ríos and Torres-Aguilera, 2009).

After the ignimbrite flare-ups the rhyolitic volcanism decreased remarkably between 20 and 18 Ma across the SMO and its southeastern portion the MC (Orozco-Esquivel et al., 2002; Nieto-Samaniego et al., 2007; Tristán-González et al., 2009 a). In the northern part of the SMO silicic volcanism reappear between 14 and 10 Ma with the emplacement of ferroaugite-bearing (ferroan) high-silica rhyolites close to the paleotrench (Vidal-Solano et al., 2007). Studies throughout the Gulf of California suggest that this rhyolitic volcanism is the final burst of extension, which completed the rupture of the before thinned crust of western Mexico and initiating the transtensional opening of the Gulf of California (Ferrari et al., 2013; Bryan et al., 2014; Duque-Trujillo et al., 2015).

1.4. Aim and objectives

Silicic large igneous provinces are rare and important in the earth history (SMO, Figure 1a and b, e.g. Bryan, 2007; Bryan and Ferrari, 2013) and they are able to induce an environmental changes (Bryan, 2007; Cather et al., 2009; Jicha et al., 2009; Bryan and Ferrari, 2013; Murray et al., 2013). Therefore, a better understanding of the origin of this voluminous felsic volcanism during the Oligocene is important in order to forecast the formation of silicic large igneous provinces like the SMO and its southeastern portion the MC. The present work combines geochemical data with well constrained geological, stratigraphically and geochronological data in order to understand the origin of this voluminous felsic volcanism during the Oligocene. New radiometric ages as well as EPMA are included in this study, which were needed to resolve some specific time constraints. All these combined data allow a better understanding about how the magmatic processes in the southern and central part of the Mesa Central changed with time and allow better constrains on the evolution of the tectono-magmatic processes involved in the generation and evolution of these rhyolitic magmas. This work presents first and new major and trace geochemical information and radiometric ages that were necessary to resolve some specific time constraints tie to this

geological–stratigraphic and geochronological control. Therefore, two volcanic complexes are described and interpreted regarding their geological, geochemical, and geochronological evolution. First the garnet-bearing rhyolites of La Herradura associated to bimodal volcanism and second Villa Garcia Ignimbrite complex, in the center of the MC, which represent the general nature of the felsic effusive Oligocene volcanism in the southern Mesa Central, and that particularly occurs in a zone of major extension and minimum crustal thickness with respect other areas of the Sierra Madre Occidental. The work is based on geological maps that most of which are the products of regional geologic maps drawn up in the past years (Labarthe-Hernández et al., 1982, 1989; Labarthe-Hernández and Jiménez-López, 1991, 1992; Labarthe-Hernández and Tristán-González, 1988; Tristán-González, 1986), as well as new and more detailed geological mapping and the present available literature.

2. Geological and tectonic setting

2.1. Geological setting

The study area is located in the MC (Figure 3), more precisely at the boundary of the Guerrero Terrane and the Sierra Madre terranes (Campa and Coney, 1983). The oldest rocks of the Guerrero Terrane are upper Triassic to early Jurassic accretionary subduction-related complex including quartz-rich turbidites. The turbidites contain zircons similar in provenance and compositions to those from Triassic Potosí fan rocks, but compared to the latter they are strongly deformed and metamorphosed (Centeno-García and Silva-Romo, 1997; Centeno-García et al., 2008; 2011; Centeno-García, 2017). The latter contains blocks of chert, limestones and MORB-type pillow basalts (Centeno-García et al., 1993; 2008; Martini et al., 2010; Centeno-García, 2017). The subduction complexes are overlain by Middle Jurassic evolved volcanic arc rocks, which are in turn unconformably overlain by Early and Late Cretaceous subaerial and marine arc-related volcano-sedimentary assemblages affected by greenschist facies metamorphism (Ranson et al., 1982; Freydier et al., 1996; Centeno-García and Silva-Romo, 1997; Centeno-García et al., 2008). The Sierra Madre terranes include the Valles-San Luis Potosí Platform (VSLPP) and the Central Mexico Mesozoic Basin (CMMB). The VSLPP consist of a Paleozoic and Precambrian basement, unconformably overlain by Jurassic clastic sediments (Barboza-Gudiño et al., 2008). A Cretaceous marine sequence of evaporites and shallow water limestones, recording a maximum transgression during the Albian-Cenomanian, overlies Precambrian and Jurassic rocks (Carrillo-Bravo, 1982). The CMMB is constituted by a marine Mesozoic sedimentary sequence more than 5 km thick, ranging in age from late Triassic to late Cretaceous (Carrillo-Bravo, 1982). The oldest rocks in the CMMB are Triassic low-grade metamorphic marine sedimentary rocks (Barboza-Gudiño et al., 1998; Hoppe et al., 2002), that are unconformably overlain by Lower to Middle Jurassic continental arc deposits of the Nazas Formation or “Nazas Arc” (Pantoja-Alor, 1972; López-Infanzón, 1986; Barboza-Gudiño et al., 1999; Bartolini et al., 1999; Bartolini et al., 2003; Barboza-Gudiño et al., 2008). Marine sedimentation throughout the Mesa Central is recorded from the Oxfordian to the end of Cretaceous. Contemporaneously, more than 4 km thick, shallow marine carbonate sequences and clastic sediments accumulated in the VSLPP and CMMB, covering a large portion of the central-eastern Mesa Central between the Late Triassic to Late Cretaceous

(Carrillo-Bravo, 1982). Additionally, debris flow and turbiditic deposits are recorded between the western margin of the VSLPP and the transition zone towards the CMMB (López-Doncel, 2003).

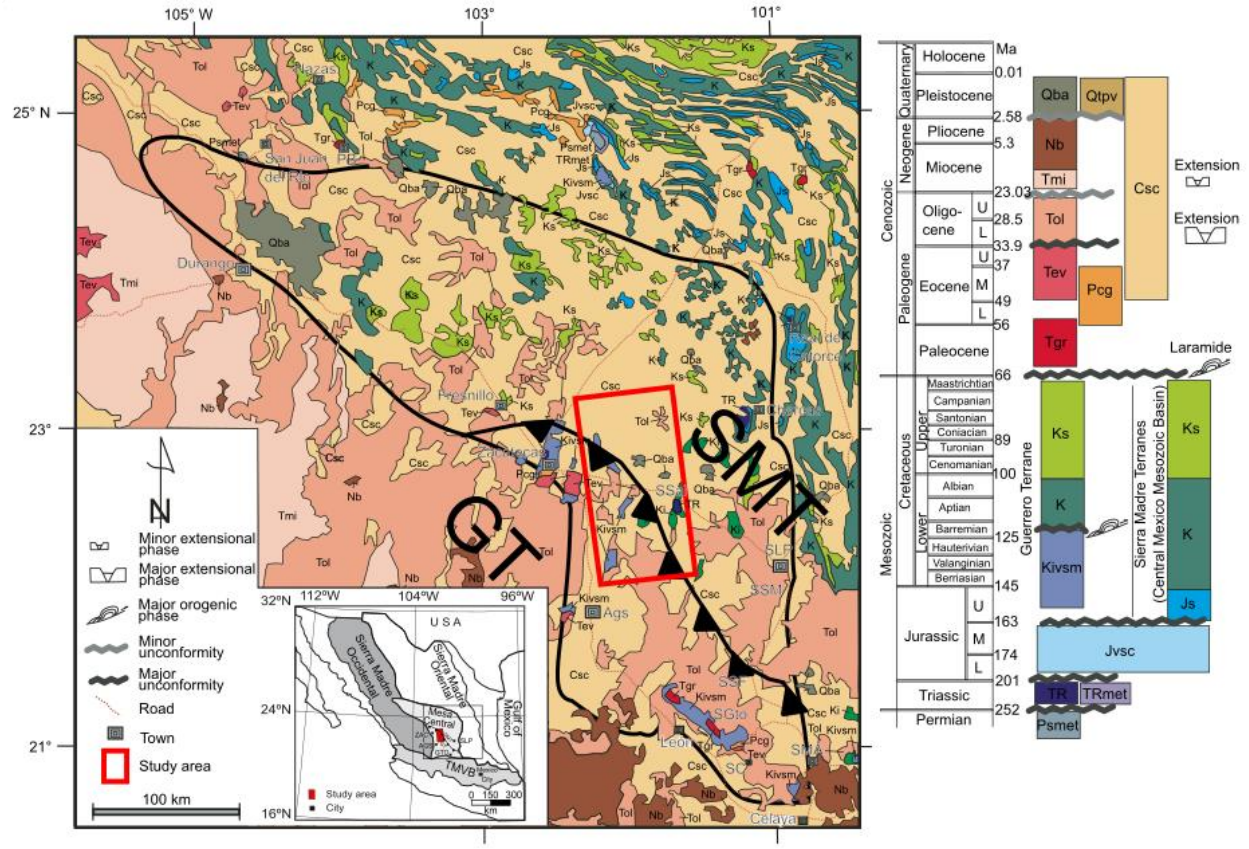

Figure 3: Geological map of the Mesa Central of Mexico. Modified after Nieto-Samaniego et al. (2007). GT: Guerrero Terrane; SMT: Sierra Madre Terranes; Ags: Aguascalientes; PB: Peñón Blanco; SGTO: Sierra de Guanajuato; SLP: San Luis Potosí; SMA: San Miguel de Allende; SSM: Sierra de San Miguelito; SSF: Sierra de San Felipe; SSal: Sierra de Salinas; SC: La Sauceda; Qba: Quaternary basalt; Qtpv: Quaternary-Pliocene volcanic rock; Nb: Neogene basalt; Tmi: Miocene ignimbrite; Csc: Cenozoic continental strata; Tol: Oligocene rhyolitic rocks; Tev: Eocene volcanic rocks; Pcg: Paleogene continental conglomerate; Tgr: Tertiary granite; Ks: Upper Cretaceous marine strata; K: Lower Cretaceous marine strata; Kivsm: Upper Jurassic-Lower Cretaceous volcanosedimentary marine strata; Js: Upper Jurassic marine strata; Jvsc: Middle Jurassic volcanosedimentary continental strata; TR: Triassic marine strata; Trmet: Triassic metamorphic rocks; Psmet: Paleozoic metamorphic rocks.

All these Mesozoic sequences were strongly deformed during the Laramide Orogeny, close to the Cretaceous-Paleogene boundary (Guzman and de Cserna, 1963; Eguiluz De Antuñano et al., 2000; Tristán-González et al., 2009 b). A Paleocene-Eocene sedimentary sequence consisting mostly of red beds and continental clastic deposits, including intercalations of andesitic lavas (Aranda-Gómez and McDowell, 1998; Tristán-González et al., 2009 a), overlies unconformably the Mesozoic rocks. This Paleocene-Middle Eocene sequence is successively overlain by Oligocene volcanic rocks that include two groups of different origins (Orozco-Esquivel et al., 2002; Nieto-Samaniego et al., 2007).

The lower group consists of mainly rhyolitic volcanic rocks, ranging in composition to latite and dacite (Labarthe-Hernández et al., 1982; Nieto-Samaniego et al., 2007; Tristán-González et al., 2009 a). This group consists mainly of effusive rocks, like lava flows and domes, with some pyroclastic rocks (Labarthe-Hernández et al., 1982; Nieto-Samaniego et al., 2007; Aguillón-Robles et al., 2009; Tristán-González et al., 2009 a). These Lava flows and domes form large volcanic complexes, mainly aligned in NNW-SSE direction that is stated to be the direction of the Basin and Range extension (Tristán-González et al., 2008; Aguillón-Robles et al., 2009; Rodríguez-Ríos and Torres-Aguilera, 2009; Aguillón-Robles et al., 2014). In some parts of the MC, the rhyolitic volcanic rocks form together with basaltic to andesitic volcanic rocks bimodal suits, ranging in age in the Mesa Central between 32 and 28 Ma (Tristán-González, 1986; Aguirre-Díaz and Labarthe-Hernández, 2003; Torres-Hernández et al., 2006; Tristán-González et al., 2008; Rodríguez-Ríos and Torres-Aguilera, 2009; Tristán-González et al., 2009 b; Aguillón-Robles et al., 2014; Sieck et al., 2019). In the center part of the Mesa Central the earliest rhyolites associated to bimodal volcanism contain primary magmatic almandine garnets (Sieck et al., 2019). The geochemistry of rhyolitic magmas of the lower group implies an origin of partial melting of the lower parts of the continental crust in an intra-plate setting, whereas the mafic magmas, associated to the bimodal volcanism are derived from partial melting of the upper mantle in the transition from a subduction to an intraplate setting in a continental extension regime (Tristán-González, 1986; Aguirre-Díaz and Labarthe-Hernández, 2003; Torres-Hernández et al., 2006; Tristán-González et al., 2008; Rodríguez-Ríos and Torres-Aguilera, 2009; Tristán-González et al., 2009 b; Aguillón-Robles et al., 2014; Sieck et al., 2019).

The upper group of the Oligocene volcanic rocks consists of mainly ignimbrites and other pyroclastic rocks of rhyolitic composition. These Ignimbrites and pyroclastic rocks cover the rhyolitic lavas and domes and are widespread in the Mesa Central, but their thickness rarely reaches 250 m (McDowell and Clabaugh, 1979; Aguirre-Díaz and Labarthe-Hernández, 2003; Nieto-Samaniego et al., 2007; Aguirre-Díaz et al., 2008). The ages of the upper group range between 29 and 25 Ma (Nieto-Samaniego et al., 1996; Nieto-Samaniego et al., 2007; Tristán-González et al., 2009 a). In the central and southern portion of the Mesa Central there is a noticeable absence of calderas and caldera-like structures (Nieto-Samaniego et al., 2007), Aguirre-Díaz and Labarthe-Hernández (2003) proposed that the ignimbrites are formed due to fissure-fed eruption and they support their theory on the presence of large pyroclastic dykes. The upper group

was originated by a process of disequilibrium and crustal extension resulting in partial melting in the crust, with small contamination of mantle-derived magmas (Orozco-Esquivel et al., 2002; Nieto-Samaniego et al., 2007). Many of these Oligocene volcanic rocks of the lower and upper group are interlayered with sedimentary rocks (Nieto-Samaniego et al., 2007; Tristán-González et al., 2009 a).

The Oligocene volcanic and sedimentary rocks are unconformably overlain by an early Miocene basaltic intra-plate volcanism, which is related to a major phase of the Basin and Range extension (Aguirre-Díaz and McDowell, 1991; Nieto-Samaniego et al., 2007; Tristán-González et al., 2009 b). The Miocene volcanic rocks are widespread in the Mesa Central and extend until the northern portion of the Trans-Mexican Volcanic Belt (Nieto-Samaniego et al., 2007).

The volcanic evolution in the Mesa Central culminates with a Pliocene – Quaternary intraplate, mantle-derived volcanism (Aranda-Gómez et al., 2005). In the center part of the Mesa Central, in the Mexican state of San Luis Potosí, the Pliocene – Quaternary volcanism exists as lavas or cinder cones and as maars (Labarthe-Hernández et al., 1982; Aranda-Gómez et al., 2005). In the western parts of the Mesa Central, e.g. in the Mexican state of Durango the Pliocene – Quaternary volcanism covers an area of ~ 2000 km^2 with more than 100 Quaternary cinder cones and maars (Swanson, 1989; Aranda-Gómez et al., 2005; Nieto-Samaniego et al., 2007). This volcanism contains many crustal material, such as granulite, amphibolite xenoliths, and upper mantle xenoliths, such as lherzolite, dunnite and peridotite (Swanson, 1989; Schaaf et al., 1994). The Pliocene – Quaternary volcanic rocks are interlayered with continental sedimentary rocks (Nieto-Samaniego et al., 2007). All over the Mesa Central occur continental river basins, containing fluvial and lacustrine Quaternary rocks (Nieto-Samaniego et al., 2007).

2.2. Tectonic setting

The Mesa Central is bounded by several major fault systems (Figure 4) that are associated to the Basin and Range extension event (Nieto-Samaniego et al., 2007; Tristán-González et al., 2009 b; Tristán-González et al., 2009 a). The southernmost boundary of the MC is formed by the El Bajío major normal fault system (Nieto-Samaniego et al., 2007). The eastern part of this fault system ranges from Celaya to Irapuato, in the Mexican state of Guanajuato, where the faults strike NW-SE and ENE to NE (Trujillo-Candelaria, 1985). The western part of the El Bajío major normal fault system is observed in the southwestern portion of the Sierra de Guanajuato, from Irapuato to

Leon, in the Mexican state of Guanajuato, where movements of 850 m were measured in Oligocene volcanic rocks (Quintero-Legorreta, 1992; Nieto-Samaniego et al., 2007). The eastern boundary of the Mesa Central is formed up by the N-S directed normal fault system, the Taxco–San Miguel de Allende Fault System. The normal fault system extends from San Miguel de Allende in the Mexican state of Guanajuato to the Sierra de Catorce in the northern part of the Mexican state of San Luis Potosí (Alaniz-Álvarez et al., 2002; Alaniz-Álvarez and Nieto-Samaniego, 2005; Nieto-Samaniego et al., 2007). Furthermore, the normal fault system is consistent with the paleographic boundary of the CMMB to the west, and the VSLPP to the east (Barboza-Gudiño et al., 2004). The Taxco–San Miguel de Allende fault system has been described east of the Sierra de Catorce (Barboza-Gudiño et al., 2004), the Villa de Arista graben, north of the city of San Luis Potosí and the city of San Luis Potosí (Tristán-González, 1986), and in San Miguel de Allende in the Mexican state of Guanajuato and in the Mexican state of Queretaro as group of parallel normal faults (Alaniz-Álvarez et al., 2001; Nieto-Samaniego et al., 2007). The southern portion of the Mesa Central is limited to the western Sierra Madre Occidental by the Aguascalientes Graben, a N-S trending half-graben with a 150 km long major fault. The displacement of the main fault is ca 900 m (Nieto-Samaniego et al., 2007). The Aguascalientes Graben is limited to the north by the San Luis–Tepehuanes Fault System, a NW-SE–striking major lineament that limits the MC to the southwest. It extends from San Luis de La Paz in the Mexican state of Guanajuato to Tepehuanes in the Mexican state of Durango. The eastern part of the lineament from about 50 km west of Salinas de Hidalgo in the Mexican state of San Luis Potosí, where the fault system limits the Aguascalientes graben, to San Luis de La Paz separates the southern and northern portion of the MC. In this area various NW-SE striking normal faults with Oligocene age have been studied by several authors (Labarthe-Hernández and Tristán-González, 1980; Labarthe-Hernández and Jiménez-López, 1992; 1993; 1994; Nieto-Samaniego et al., 1997; Xu et al., 2004). In the Mexican state of Zacatecas two fault systems are identified, belonging to the San Luis–Tepehuanes Fault System, an older, late Eocene NW-SE trending fault system that is cross-cut by a younger, early Oligocene N-S fault system (e.g. Ponce S and Clark, 1988). The San Luis–Tepehuanes Fault System in the area between Fresnillo and Sombrete, in the Mexican state of Zacatecas is represented by NW-SE trending fault system, of Oligocene age with mineralization and displacements of about 1000 m (de Cserna, 1976; Albinson F, 1988). The northwestern part of the

San Luis–Tepehuanes Fault System is built up by the Tepehuanes graben in the Mexican state of Durango, consisting of a NW-SE trending fault system (Nieto-Samaniego et al., 2007).

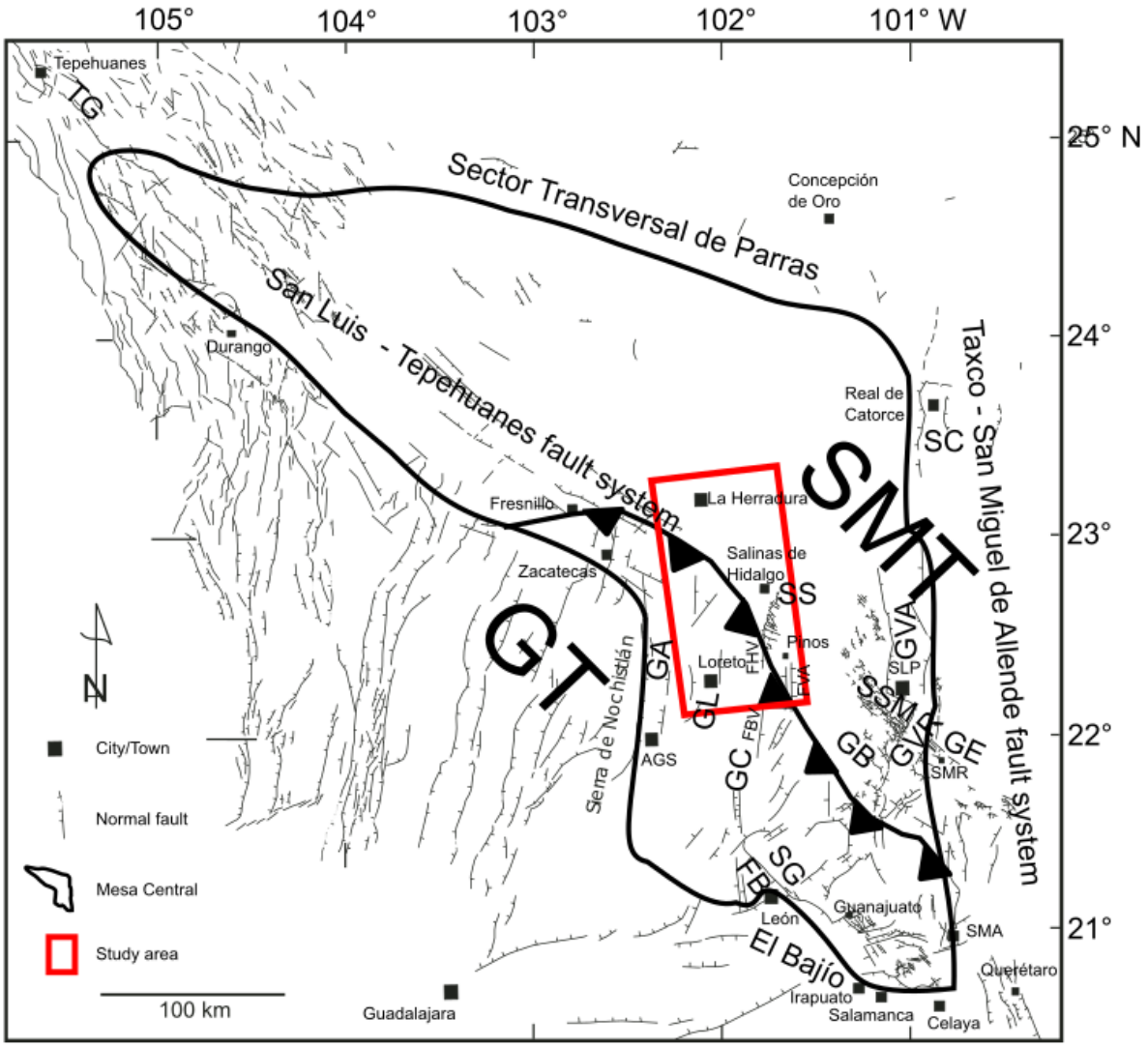

Figure 4: Major structures of the Mesa Central. GT: Guerrero Terrane; SMT Sierra Madre Terranes; TG: Tepehuanes graben; GA: Aguascalientes graben; GL: Loreto graben; FVH: Villa Hidalgo fault; FBV: Buena Vista fault; FVA: Villa de Arriaga fault; GC: El Cuarenta graben; FB: El Bajío fault; GB: Bledos graben; GVR: Villa de Reyes graben; GVA: Villa de Arista graben; GE: Enramadas graben; SSM: Sierra de San Miguelito; SG: Sierra de Guanajuato; SC: Sierra de Catorce; SS: Sierra de Salinas; AGS: Aguascalientes; SLP: San Luis Potosí; SMR: Santa María del Río; SMA: San Miguel de Allende. Figure modified after Nieto-Samaniego et al. (2007).

The Oligocene rhyolitic lavas and ignimbrites in the Mesa Central were emplaced on top of a continental crust with a thickness of about 30-33 km (Fix, 1975; Smith and Jones, 1979; Rivera and Ponce, 1986). Compared to the Mesa Central the crustal thickness of the Sierra Madre Occidental is between ca. 37 and 40 (Nieto-Samaniego et al., 1999; Nieto-Samaniego et al., 2007).

In the seismic models interpreted by Fix (1975) a zone of about 20 % partial melting occurs under the thinned continental crust of the Mesa Central. The presence of partial melted xenolithic mantle rocks in Quaternary volcanic confirm the presence of a partially melted mantle zone beneath the continental crust of the Mesa Central (Schaaf et al., 1994; Aranda-Gómez et al., 2005). The lower continental crust of the MC is built up Precambrian metamorphosed crystalline rocks, followed by first, strongly deformed and slightly metamorphosed Mesozoic rocks of the Sierra Madre terranes in the eastern part and the Guerrero terranes in the western part of the MC, second, a Lower to Upper Cretaceous sedimentary succession, and third, the mid-Tertiary volcanic succession of the SMO (Burt and Sheridan, 1987; Ruiz et al., 1988; Henry and Aranda-Gómez, 1992; Centeno-García and Silva-Romo, 1997; Dickinson and Lawton, 2001; Nieto-Samaniego et al., 2007). During late Cretaceous time the Guerrero terranes were accreted over the Sierra Madre terrane (Centeno-García and Silva-Romo, 1997; Centeno-Garcia et al., 2011; Centeno-García, 2017). Many authors proposed a correlation of the accretion of the Guerrero composite terranes and the regional shortening of the SMO Fold and Thrust Belt (Campa and Coney, 1983; Salinas-Prieto et al., 2000; Keppie, 2004; Talavera-Mendoza et al., 2007; Fitz-Diaz et al., 2011; Centeno-García, 2017). The accretion of the Guerrero composite terranes as well as the Laramide Orogeny are both initiated in the SMO and they intersect in time and their structures (Fitz-Diaz et al., 2011). During the accretion of the Guerrero terranes and the Laramide Orogeny, at Late Cretaceous to Early Paleocene, the older rocks were affected by shortening, faulting, and deformation due to compression in northeastern direction (Tardy et al., 1975; de Cserna, 1976; Padilla and Sánchez, 1985; Tristán-González et al., 2008). Cuéllar-Cárdenas et al. (2012) showed, based on Ar-Ar dating that the deformation front moved from W-E. During Late Paleocene to Early Eocene the Mesa Central was affected by episodic right-lateral transtension and during Eocene to Miocene by episodic extension (Tristán-González et al., 2009 a; Tristán-González et al., 2009 b). The episodic extension event is related to the Basin and Range regional extension event and resulted in the formation of several sets of normal faults with a NW-SE main orientation (Stewart, 1978; Henry and Aranda-Gómez, 1992; Tristán-González et al., 2009 a; Tristán-González et al., 2009 b). Early Oligocene felsic volcanism, mainly evolved explosive ignimbrite-forming eruptions and effusive rhyolitic lava domes and flows, occurred contemporaneous with an intense episode of the Basin and Range extension (Labarthe-Hernández et al., 1982; Tristán-González, 1986; Aguirre-Díaz and Labarthe-Hernández, 2003; Torres-Hernández et al., 2006; Tristán-González et al., 2008; Tristán-

González et al., 2009 a; Tristán-González et al., 2009 b). The maximum extension of the Basin and Range extension event took place during about 28–26 Ma, resulting in the formation series of horsts, grabens and half-grabens, such as the Aguascalientes and the Villa de Reyes Graben that are associated to the large eruptions of ignimbrite-forming pyroclastic flows and subordinated mafic volcanism in the SMO and its southeastern portion the MC (Labarthe-Hernández et al., 1982; Tristán-González, 1986; Henry and Aranda-Gómez, 1992; Nieto-Samaniego et al., 1999; Aranda-Gómez et al., 2000; Nieto-Samaniego et al., 2007; Tristán-González et al., 2009 b; Tristán-González et al., 2009 a). Episodic extension proceeded until Miocene, perhaps until Quaternary (Tristán-González et al., 2009 a; Tristán-González et al., 2009 b).

3. Analytical Methods

3.1. Petrography and whole-rock geochemistry

3.1.1. Sample preparation

Sample preparation was done at the Applied Geosciences Department, IPICYT (Instituto Potosino de Investigación Científica y Tecnológica). For the geochemical analysis fresh, non-devitrified samples were used. Samples were crushed in a jaw crusher and afterwards milled in an agate planetary mono mill. Petrographic and whole-rock geochemical analyses were performed on 15 samples of La Herradura, 34 samples of volcanic and volcanoclastic rocks from Villa Garcia. Loss of ignition (LOI) values were determined in the Geochemical Laboratory at the Geology Institute of the UASLP (Universidad Autónoma de San Luis Potosí). Therefore, 2 g of each sample was heated up to 1000°C for 6 h and afterwards cooled down in an exiccator. Next, the samples were weighed again to calculate the LOI. For the petrographic analysis the samples were cut into small cubes and polished in 4 steps until they are optically flat. The polished cubes are mounted on a glass slide and polished until a final thickness of ca. 30 µm is reached.

3.1.2. X-ray fluorescence analysis

Determination of major element concentrations of both, La Herradura and Villa Garcia samples were carried out by X-ray fluorescence analysis. The X-ray fluorescence analysis (XRF) essentially serves the rapid and quantitative determination of major and minor elements. The samples are irradiated with high-energy, primary X-ray radiation, as a result, an electron near the nucleus of the atom is transferred from its ground state to an energetically higher state, leaving the region close to the nucleus. The vacancy near the nucleus is occupied by another electron with a higher energy level (atomic shell) that emits a fluorescence radiation in the X-ray spectra when it is moving to the vacancy. The emitted radiation is specific for every element and the atomic shell from where the vacancy is occupied. For the detection of the emitted fluorescence radiation a wavelength or energy dispersive spectrometer is used. The intensity of the measured spectra depends strongly on the concentrations of the elements in the sample and for the determination of the concentration from the intensity spectrum certificated standards with known concentrations are used. The samples have to be homogenous, since the X-ray radiation reaches a maximum depth of

1000 µm into it. A detailed description of the X-ray fluorescence analysis can be found in Beckhoff et al. (2006).

Major element analysis of the La Herradura samples were carried out by X-ray fluorescence, with a PANalytical AXIOS Advanced sequential X-ray spectrometer at the Geoscience Centre (GZG) of the University of Göttingen. Crushed and dried samples were mixed with a mixture of lithium tetraborate, lithium metaborate, and LiF (Fluxana FX-X65) and melted down to glass tablets. For the dilution 3900 mg of this flux and 1750 mg of the sample are weighed in platinum-gold crucibles and fused for 15 min at 1100°C. All elements are analyzed using the SSTmAX-4-kW rhodium target X-ray tube for sample excitation. The Axios spectrometer is equipped with the SuperQ 4 software for data processing. For the analyses of major elements, the laboratory gives analytical precision better than 0.5-2% and detection limits of < 3 ppm.

The major element analysis of the Villa Garcia samples was done in the IPICYT using a wavelength dispersive X-ray fluorescence (WDXRF) spectrometer Rigaku ZSX Primus II model (rhodium X-ray tube; 4 kW maximum power). For the analysis 3.5 g of the dried samples were mixed with 3.0 g pure N, N′-ethylene bis(stearamide) beads, <840 µm as wax (Sigma-Aldrich). For the preparation of the pressed powder pellets 310 MPa press was used. Similar, 6.5 g pure N, N′-ethylene bis(stearamide) beads, <840 µm as wax (Sigma-Aldrich) was pressed and used as a blank for the measurement. The details of the methods can be found in Verma et al. (2018).

3.1.3. Inducted Coupled Plasma- Quadrupole Mass Spectrometer

The analyses of trace elements of the samples of La Herradura and Villa Garcia were obtained at the Geochemical Laboratory at the Geology Institute of the UASLP with a Thermo Scientific Serie X2, Inducted Coupled Plasma- Quadrupole Mass Spectrometer (ICP-QMS). For the analysis 100 mg of the powered sample was digested with ultrex degree acids of HNO_3, HF and HCl. For the measurement, the dissolved samples are uniformly absorbed by a peristaltic pump and transferred through a nebulizer into the plasma torch. The plasma torch that ionize the samples is generated by high-frequency electric field that is induced in ionized argon and due to the high temperature of about 5000 K, even elements that are difficult to thermally ionize can be completely ionized.

The plasma torch consists of three concentric quartz glass tubes. The outer tube is flown through by the plasma and is used for cooling, the middle tube is flown through by the auxiliary gas, which determines the position of the plasma relative to the sample injector, and the innermost tube is used

to transport the sample. The generated ions are accelerated in the direction of the mass spectrometer by a potential difference of 3-20 kV. The samples first pass through the two pinhole apertures, the sampler cone and the skimmer cone. Between these two there is an expansion chamber in which a low vacuum is generated with a mechanical vacuum pump. Behind the skimmer cone follows the focusing system in medium vacuum and the quadrupole mass analyzer in high vacuum. The ion beam is focused by the ion optics and directed into the quadrupole. The quadrupole consists of four cylindrical electrodes arranged parallel to one another. The respective opposite pairs of electrodes are the same polarity and are simultaneously connected to a high-frequency voltage and DC voltage. The magnetic field strength, induced by the quadrupole acts perpendicular to the ion current, thereby the ions are deflected according to their mass to charge ratio (m / z), lighter ions are deflected more strongly than heavier ones and the number of individual ions is detected at a mass detector. The mass fraction is between less than one percent for light elements and one percent for heavy elements and is corrected by an internal standard. The detection limit of the trace element analysis in the Geochemical Laboratory at the Geology Institute of the UASLP is reported with < 0.02 ppm. The details of the analytical method is reported by Almaguer-Rodríguez (2010).

All analyses, major and trace elements, were validated by repeated independent sample preparation, blanks and analyses of minimum three different international reference standards.

3.2. Mineral chemistry

3.2.1. Sample preparation

Thin sections were prepared in Applied Geosciences Department, IPICYT and in the Instituto de Geologia (UASLP) (see 3.1.1. Sample preparation) and in addition they were polished in two steps (3 and 1 μm) and vaporized with carbon for the analysis. The samples were analyzed in the Unidad Michoacán of the Instituto de Geofísica of the UNAM (Universidad Nacional Autónoma de México).

3.2.2. Electron Probe Micro Analyzer

Similar to the X-ray fluorescence analysis, the electron probe micro analyzer (EPMA) uses the artificial excitation of electrons for the chemical analysis of a sample. Therefore, thermally generated electrons are accelerated in a high-voltage field and bundled into a beam. When the

electron beam hits a solid phase, a multiplicity of interactions occurs, e.g. they are slowed down through inelastic interactions with outer atomic electrons of the sample, whereas elastic deflections by atomic nuclei determine their spatial distribution. In some cases, the electrons leaving the sample again, they have been deflected by angles of more than 90°. The secondary electrons removed from the samples and the backscattered electrons are applied for the creation of images. Furthermore, the interactions with the electron beam and the atomic nuclei leads to emission of a continuous X-ray spectrum. The emitted X-rays are not just specific for each element they are also specific for the electron transfer from the outer to inner shells. The analysis of the specific X-ray radiation can be done in two ways, wavelength dispersive spectroscopy (WDS) and energy dispersive spectroscopy (EDS). The WDS is performed with crystal spectrometers, resulting in a low detection limit (> 30 ppm). The EDS uses a cooled semiconductor detector, which has the disadvantage of significantly lower detection limits compared to the WDS. With the EDS, the main components can be analyzed simultaneously within a few seconds, compared to the wavelengths of all components measured in succession in the WDS. Furthermore, in the case of the electron beam microprobe, it is possible to determine the distribution of the chemical elements over a certain area, this being done by measuring many neighboring points, with distances of less than 1 µm. The comparison with international and internal standards and the inclusion of possible errors provides the composition of the sample. A detailed description of the EPMA can be found in Reed (2005).

Major elements in plagioclase, clinopyroxene, orthopyroxene, hornblende, and garnet were analyzed using a JEOL JXA-8600 Electron Microprobe (EPMA). Analyses were made using 15 keV accelerating voltage and 10 nA beam current. The beam (spot resolution 1 µm) was focused to analyze plagioclase, pyroxenes, garnets, and ilmenite but was defocused to 10 µm to analyze amphiboles, in order to avoid water loss and sodium migration. Measurements allow a spot resolution of 1–10 µm and a detection limit of < 30 ppm. All elements with an atomic number $Z \geq 5$ can be measured.

3.3. Geochronology

3.3.1. U-Pb zircon LA-ICP-MS age determinations

U-Pb zircon ages were obtained for six samples of La Herradura rocks, four whole rock samples and two samples of zircon inclusions in garnet, at the Laboratorio de Estudios Isotópicos, Centro

de Geociencias, UNAM. Therefore, all 6 samples were crushed, using a jaw crusher and sieved and, afterwards, the mineral fractions that are < 180 µm of 4 samples were separated by wet concentration with a Wilfley table from the resulting heavy mineral separates the magnetic minerals were separated with a hand magnet. From two samples the mineral fraction between 1 and 2 mm was used to separate garnets using a binocular. The garnets were crushed in an agate mortar and next, the magnetizable minerals of all six samples were separated using a Frantz Magnetic Barrier Laboratory Separator Model LB-1 in four passes under an applied amperage of 0.3 A, 0.6 A, 0.9 A, and 1.2 A. Thereafter, a density separation with LST, a heavy liquid containing lithium heteropolytungstates in the form of extremely soluble, colorless hydrated crystals, was carried out on the non-magnetizable fraction. From the resulting heavy mineral fraction, the idiomorphic and inclusion-free zircons were manually separated using a binocular.

Uranium has three naturally occurring isotopes and each is radioactive, however, for the U-Pb age determination of zircons only ^{238}U and ^{235}U are important. Zircon ($ZrSiO_4$) can substitute in small amounts U for Zr, in contrast, Pb cannot be substituted in the crystal lattice. All Pb in a zircon crystal is the product of radioactive decay of U and remains in the zircon crystal up to the closure temperature of more than 800 °C (Pristiner Zircon; Mezger and Krogstad, 1997). Both isotopes, ^{238}U and ^{235}U decay over a series of nuclides of different half-life times to ^{206}Pb and ^{207}Pb. The radioactive decay is summarized in the following formulas:

$$^{235}U \rightarrow 7\,He + 4\,\beta^- + {}^{207}Pb + 45\,MeV$$

$$^{238}U \rightarrow 8\,He + 4\,\beta^- + {}^{208}Pb + 47\,MeV$$

By analyzing the concentrations of the different uranium and lead isotopes the age t of the zircon can be calculated by the equations:

$$t_{235} = \frac{1}{\lambda_{235}} \times \left(\frac{^{207}Pb}{^{235}U} + 1 \right)$$

$$t_{238} = \frac{1}{\lambda_{238}} \times \left(\frac{^{206}Pb}{^{238}U} + 1 \right)$$

with the decay constants λ for the isotopes ^{235}U ($\lambda_{235} = 9.84850 \times 10^{-10}$) and ^{238}U ($\lambda_{238} = 1.55125 \times 10^{-10}$).

The results of both U-Pb systems should be identical in an undisturbed system since both uranium isotopes were incorporated into the crystal system at the same time. Both calculated ages are usually shown in a ^{206}Pb/^{238}U versus ^{207}Pb/^{235}U concordia diagram after Wetherill (1956). Detailed

information about the U-Pb system and Concordia diagrams are given in Faure and Mensing (2005).

U–Pb zircon ages were defined by laser ablation inductively coupled plasma mass spectrometry (LA–ICPMS). Therefore, a quadrupole ICPMS (Thermo Xii Series) was coupled to a resolution M050 excimer laser ablation workstation, using a 23-µm spot for the analysis. The laboratory and the laser ablation system are described by Solari et al. (2010). Detailed description of the methods and evaluation of the measurements can be found in Ortega-Obregón et al. (2014) and Solari et al. (2015). Measurements were verified by using the Plešovice zircon (Sláma et al., 2008) as a bracketing standard for isotope ratios and standard glass NIST 610 to recalculate elemental concentrations.

Iolite software (Paton et al., 2010) was used for the U-Pb isotopic data reduction, age calculations and error propagations. The $^{207}Pb/^{206}Pb$ age calculations, the data visualization and common Pb correction were carried out with the VisualAge data reduction scheme for Iolite (Petrus and Kamber, 2012). The calculation of concordia ages and concordia plots were performed with the Isoplot 3.0 macro for Excel (Ludwig, 2003).

3.3.2. K-Ar whole rock age determinations

K-Ar whole rock ages were measured in 3 samples from La Herradura volcanic rocks in the Geoscience Center of the University of Göttingen. Whole rock samples were prepared in two different ways for argon and potassium analysis. While the material for the determination of potassium was ground down to < 20 micrometers, a much coarser grain size was used for the determination of argon, in order to avoid excessive argon loss due to comminution.

K has three natural isotopes, but for the K-Ar age determination just the radioactive ^{40}K isotope and the decay to ^{40}Ar is of importance. The main part of the ^{40}Ar is formed by electron capture, an electron can penetrate into the nucleus and turns a proton into a neutron. In this process either an excited state ^{40}Ar is created that reaches the fundamental state (11% of all ^{40}K decays) by emission of γ radiation or an ^{40}Ar is formed directly in the fundamental state (0.16% of all ^{40}K decays). In 0.001% of all ^{40}K decays, ^{40}K decays to ^{40}Ar by β^+ decay. For the determination of the K-Ar ages the dual decay process of ^{40}K must be considered. Therefore, the total decay constant λ_{tot} and respective decay constants for the decays from ^{40}K to ^{40}Ar (λ_E) and ^{40}K to ^{40}Ca (λ_{β^-}) must be known. The K-Ar age calculations are The age calculations are based on the constants

recommended by the IUGS quoted in (Steiger and Jäger, 1977). By analyzing the concentrations of the concentration of the ^{40}K and the concentration of $^{40}Ar^*$ that is generated by the radioactive decay of ^{40}K the age *t* can be calculated by the equation:

$$t = \frac{1}{\lambda_{tot}} \times \ln\left(\frac{^{40}Ar*}{^{40}K} \times \frac{\lambda_{tot}}{\lambda_E} + 1\right)$$

In order for the calculated *t* to be interpreted as a geological age, it must be ensured that the mineral or rock is a closed system and that the ratio of ^{40}K and $^{40}Ar^*$ is the product of the radioactive decay of ^{40}K. This implies that no inherited $^{40}Ar^*$ isotopes are incorporated during crystallization and it must be ensured that no parent or daughter isotope was at any time added or removed by any process to the mineral or rock. Due to their low closure temperature (300 ± 50 ° C; Purdy and Jäger, 1976), the K-Ar age can be interpreted as an eruption age of the volcanic rocks.

The argon isotopic composition was measured in a Pyrex glass extraction and purification line coupled to a Thermo Scientific ARGUS VI™ noble gas mass spectrometer operating in static mode. The amount of radiogenic ^{40}Ar was determined by isotope dilution method using a highly enriched ^{38}Ar spike from Schumacher, Bern (Schumacher, 1975). The spike is calibrated against the biotite standard HD-B1 (Fuhrmann et al., 1987). Potassium was determined in duplicate by flame photometry using a BWB-XP flame photometer™. The samples were dissolved in a mixture of HF and HNO_3 according to the technique of Heinrichs and Herrmann (2013). The analytical error for the K-Ar age calculations is given on a 95% confidence level (2σ). Details concerning argon and potassium analyses in Göttingen laboratory are given in Wemmer (1991).

3.3.3. Ar-Ar sanidine age determinations

Sample preparation was done at the Applied Geosciences Department, IPICYT (Instituto Potosino de Investigación Científica y Tecnológica). For the sample preparation fresh, non-devitrified samples were used. Therefore, four samples of the Villa Garcia Ignimbrite and Loreto Ignimbrite were crushed in a jaw crusher and afterwards the samples were sieved. Idiomorphic and inclusion free Sanidine crystals were separated under a binocular from the mineral fraction > 1mm by hand-picking.

The Ar-Ar dating method is basically founded on the K-Ar method (see 3.3.2. K-Ar whole rock age determinations), but compared to the K-Ar dating the age can be determined in a single experiment. Therefore, the samples are irradiated in a nuclear reactor with fast neutrons. This turns

a fraction of ^{39}K into ^{39}Ar, by adding a neutron to the ^{39}K nucleus, resulting in the release of a proton and energy. ^{39}Ar is not a naturally occurring argon isotope and the mass is directly proportional to the amount of ^{39}K in the sample and likewise to the amount of ^{40}K, because the natural abundances of the potassium isotopes are known. It has to be noted that the amount of ^{39}Ar produced during irradiation not just depends on the amount of ^{39}K in the sample, it also depends on the intensity and the duration of irradiation. Because the neutron irradiation parameters vary for each irradiation a reference material (standard/monitor mineral) has to be irradiated as well.

The measurement of the amounts of ^{40}Ar* and ^{39}Ar in two steps, first the extraction and second the purification of argon. The extraction of the gaseous argon isotopes does not have to be done in one step, but could be done in several steps of increasing temperature. From the argon isotopes extracted and analyzed during every heating step an age is calculated. The step-heating method gives information about the thermal history of the sample, like partially opened systems. The Ar-Ar ages are calculated after the formula:

$$t_u = \frac{1}{\lambda_{tot}} \ln\left\{J \times \left(\frac{^{40}Ar^*}{^{39}Ar}\right)_u + 1\right\}$$

Where t_u is age of the sample, λ_{tot} is total decay constant of K, $^{40}Ar^*$ is the mass of ^{40}Ar generated by the radioactive decay of ^{40}K, ^{39}Ar is the mass of ^{39}Ar generated by the irradiation in a nuclear reactor with fast neutrons, and u denotes unknown sample. The factor J is an irradiation parameter that combines all of the constant factors and can be simplified determined by:

$$J = \frac{e^{\lambda ts} - 1}{\left(^{40}Ar^*/^{39}Ar\right)_s} = \frac{e^{\lambda tu} - 1}{\left(^{40}Ar^*/^{39}Ar\right)_u}$$

Where s denotes standard and with λ_{ts} and λ_{tu} as decay constants of the standard and the sample. Substitution of the parameter J leads to a simplified formula for the calculation of the Ar-Ar age of the sample:

$$t_u = \frac{1}{\lambda_{tot}} \ln\left\{\frac{\left(^{40}Ar^*/^{39}Ar\right)_u}{\left(^{40}Ar^*/^{39}Ar\right)_s} \times \left(e^{\lambda ts} - 1\right) + 1\right\}$$

The Sanidine crystal samples were irradiated in the U-enriched research reactor of McMaster University in Hamilton, Ontario, Canada in package JUR03 at position 8C. In order to block thermal neutrons during irradiation, samples and neutron flux monitors were covered with a Cd liner. The Fish Canyon Tuff sanidine standard FCT-2 (28.198 ± 0.044 Ma; Kuiper et al., 2008) was used as fluence monitor. Irradiated Sanidine samples were analyzed at Laboratorio

Interinstitucional de Geocronología de Argón (LIGAr), Centro de Geociencias, UNAM-Campus Juriquilla, Mexico. They were analyzed by an Isotopx NGX multicollector noble gas mass spectrometer, using a 20 W Coherent Innova 200-20 Ar-ion laser for gas extraction, and an automated gas clean-up line with one cold finger and two SAES GP-50 getters. Ion beams of argon isotopes were simultaneously measured in four Faraday collectors with 1012 Ω amplifiers (m/z 36 to 39), and one collector with 1011 Ω amplifier (m/z 40). Each run consisted in 20 cycles of 10 s, with integration time of 1 s, preceded by 30 baseline measurements with integration time of 1s. Repeated air measurements interspersed with sample unknowns were used to correct for mass discrimination and atmospheric Ar contamination, using a $^{40}Ar/^{36}Ar$ ratio of 295.5 for atmospheric Ar. Prior to every step and air measurement a blank measurement was carried out. Data reduction was carried out using the software NGX-Red 1.0® and AgeCalc 1.0® developed at CICESE (Centro de Investigación Científica y de Educación Superior de Ensenada). Argon isotopic data were corrected during the blank subtraction for mass discrimination, as well as calcium, potassium, and chlorine neutron induced interference reactions. The following parameters were used for the correction of the neutron induced interference reaction: $(^{39}Ar/^{37}Ar)_{Ca} = 6.50 \times 10^{-4}$; $(^{36}Ar/^{37}Ar)_{Ca}$ = 2.55 x 10-4; $(^{40}Ar/^{39}Ar)_{K} = 0$. Mass 36 was also corrected for chlorine-derived ^{36}Ar [$^{35}Cl(n, \gamma)$ $^{36}Cl \rightarrow {}^{36}Ar + \beta^-$ with $t_{1/2} = 3.01 \times 10^5$ a]. Isotope concentrations of ^{37}Ar and ^{39}Ar were corrected for radioactive decay. For all calculations the decay constants of Steiger and Jäger (1977) were used and straight-line calculations were performed with the equations presented in York et al. (2004). The results are given with 2σ errors and the errors in the integrated, plateau and isochron ages include the uncertainty in the J parameter. The integrated ages were calculated adding the fractions of the step-heating experiments. The plateau age was calculated as the weighted mean of at least three consecutive fractions representing 50% or more of released ^{39}Ar that are in agreement within 1σ error, excluding the uncertainty in J.

3.4. Geothermobarometry

3.4.1 Basics and sample preparation

Geothermobarometry is the preferred analytical tool used for studies on the pressure and temperature of mineral formation. Pressure temperature (*P-T*) estimates obtained through thermobarometry offers major constrains to the interpretation of structural and magmatic evolution of the crystallization of magmatic minerals, especially in understanding of crystallization

processes in magma chambers and/or during ascent of magmas. Geothermobarometry not only gives information about formation pressure and temperature of minerals it also delivers together with analytical results such as geochemistry and age data, a robust constrain on interpretation of the development of magmas and magmatic processes.

Most commonly used thermobarometric methods to determine the P-T conditions of minerals and magmatic processes range from the classical thermobarometry to phase equilibria modelling. Primarily these methods are based on the assumption of thermodynamic equilibrium and partitioning of elements between minerals. Equilibrium between minerals at different P-T are totally governed by their thermodynamic properties and are reflected in their chemical composition, which are then used with either a pressure sensitive net transfer reactions or temperature sensitive exchange reactions to calculate the P-T estimates. Due to the technical improvement, the conventional geothermobarometers as well as the phase equilibria models are more precise, which delivers more accurate results for the P-T constraints.

Sample preparation was done at the Applied Geosciences Department, IPICYT (Instituto Potosino de Investigación Científica y Tecnológica). Analysis were carried out using an EPMA (see 3.2. Mineral chemistry) and laser Raman spectroscopy. For the laser Raman spectroscopy sample preparation fresh, non-devitrified samples were used. Therefore, two samples of the garnet-bearing La Herradura Rhyolite were crushed in a jaw crusher and afterwards the samples were sieved. Idiomorphic garnets were separated from the mineral fraction > 1mm by hand-picking, using a binocular

3.4.2. Apatite in garnet barometry

The growth of minerals, for example in magma chambers can result in the intergrowth or encapsulation of minerals in crystals. The molar volume of the encapsulated mineral and the host at the time of encapsulation corresponds to same P-T conditions of the entrapment (Ashley et al., 2017). Apatite in garnet barometry primarily depends on thermoelastic properties of the host (garnet) and the inclusion (apatite), which takes into account the elastic difference between the host and the trapped inclusion at elevated P-T and at earth's surface (Rosenfeld and Chase, 1961; Ashley et al., 2015; 2017). This method investigates physical characteristics of an inclusion-host pair to gain insight into entrapment conditions when those minerals grew together. Garnet is a uncommon mineral in rhyolitic volcanic rocks, in which inclusions of quartz, micas, feldspar, and

accessory minerals are reported (Harangi et al., 2001; Mirnejad et al., 2008; Sieck et al., 2019). These inclusions in garnets are often used for various purposes, such as the garnet-ilmenite cation exchange thermometer (Pownceby et al., 1987, 1991) or for barometry from pressurized quartz inclusions (Rosenfeld and Chase, 1961; Enami et al., 2007; Ashley et al., 2014). Garnet as an isotropic host mineral, with its high bulk modulus makes it an applicable mineral for geothermobarometry. The high bulk modulus of garnet allows for stress retention within the inclusion, resulting in the preservation of the formation pressure during uprise of magmas or exhumation (Ashley et al., 2014; 2016; 2017). Garnet and apatite make a good host-inclusion pair for barometric analysis because of their physical characteristics; apatite is soft and compressible whereas garnet is isotropic and incompressible (Ashley et al., 2017). Due to its compressibility, the pressure at which apatite inclusion was entrapped within garnet is partially retained in the inclusion (P_{incl}) and is always higher than the external pressure (atmospheric pressure) applied at earth's surface. Using the elastic theory for host and inclusion pair, this residual pressure can be used to estimate the entrapment P-T conditions during garnet growth (Rosenfeld and Chase, 1961; Enami et al., 2007; Ashley et al., 2014; Kohn, 2014; 2016; 2017).

Apatite in garnet barometry using laser Raman spectroscopy was established to estimate the formation pressure of apatite during the entrapment of apatite using the frequency shift of Raman spectrum from the apatite inclusions in garnet (Ashley et al., 2017). Apatite inclusions were measured in the Instituto Potosino de Investigación Cientifica y Tecnológica using a Renishaw Invia Raman microscope equipped with 633 nm Nd Laser, CCD detector and confocal microscope with 1800 mm/lines. For all analysis an 100x confocal objective with a pinhole diameter of 25 µm was used, giving a spatial resolution of 1 um and a spectral resolution of ~ <0.1 cm-1. The room temperature was kept at 21 ± 1 °C. Raman spectra were collected using 6 accumulations of 10 seconds each. For inclusions with low counts the accumulations were doubled. The frequency of Raman bands was calibrated with the 520 cm^{-1} band on a Si wafer, set to 520.7 cm-1 using the auto calibration of the instrument. As external standard Durango apatite (Young et al., 1969) was used, whereas apatite from the thin sections was utilized as internal standard. Both, Durango apatite and Matrix apatite were measured multiple times during the sessions. The formation pressure was calculated using the calculation:

$$P\ (bar) = a * (\Delta\nu_{964} - c * T^2 - d * T - e)^2 + b * (\Delta\nu_{964} - c * T^2 - d * T - e)$$

from Ashley et al. (2017). Where P is the entrapment pressure in bar, T is the entrapment temperature in °C, $\Delta\nu_{964}$ the shift of the Raman band at ca. 964 cm^{-1} from the exposed apatites from the surface of the garnet to the fully in garnet encapsulated aptite, and $a, b, c, d,$ and e are regression coefficients equal to 7.35 ± 1.88, 2265 ± 59, –0.0000134 ± 0.0000011, –0.0070 ± 0.00018, and 0.287 ± 0.029.

For further explanations see Ashley et al. (2017) and the references within.

3.4.3. Garnet-ilmenite cation exchange thermometer

Formation temperature was defined by using the garnet-ilmenite cation exchange thermometer (Pownceby et al., 1987). The garnet-ilmenite thermometer uses Fe-Mn portioning between garnet and ilmenite and has a marked temperature sensitivity and the chemical and structural simplicity of the garnet and ilmenite is an advantage compared to other geothermometers (Pownceby et al., 1987). Garnet and ilmenite are appropriate pair for the geothermometry because the two minerals are associated to a wide range of igneous and metamorphic rocks in the crust aa well as in the upper mantle and due to the simplicity of the system (Pownceby et al., 1987; 1991).

Only ilmenite inclusions in garnet were used for the garnet-ilmenite thermometer. Compositions of garnet and ilmenite were defined using the electron microprobe at the UNAM Campus in Morelia (see 3.2. Mineral chemistry). Therefore, transects from the garnet through the ilmenite inclusions within were measured. The temperature was calculated after the equation:

$$T(K) = \frac{14{,}642 - 2{,}200\left(2X_{Mn}^{ilm} - 1\right) + 539\left(X_{Mn}^{grt} - X_{Fe}^{grt}\right) + 12{,}083X_{Mg}^{grt}}{RlnK_D + 7.67X_{Mg}^{grt} + 4.203}$$

from Martin et al. (2010), including the experimental calibration for the binary system by Pownceby et al. (1991), the formulation modification by (Ganguly et al., 1996 a), as well as a correction for Mg in garnet using the garnet solution model of (Ganguly et al., 1996 b). In the formula X_{Mn} as mole fraction of Mn, defined as $X_{Mn} = Mn/(Fe^{2+} + Mg + Ca + Mn)$, X_{Fe}, defined as $X_{Fe} = Fe^{2+}/(Fe^{2+} + Mg + Ca + Mn)$ and X_{Mg}, defined as $X_{Mg} = Mg/(Fe^{2+} + Mg + Ca + Mn)$, ilm is ilmenite, grt is garnet, R is the gas constant in joules per mole per Kelvin, and K_D is the equilibrium Fe–Mn distribution coefficient between garnet and ilmenite, defined as $K_D = (Fe/Mn)^{ilm}/(Fe/Mn)^{grt}$.

For further explanations see cited references above and the references within.

3.4.4. Two-feldspar geothermometer

A first formulation of the two-feldspar thermometer was published by Barth (1934) who first suggested that the relative solution of albite into plagioclase and alkali feldspar could be formulated as an analytic geothermometer. Since the first published formulations of the two-feldspar thermometer several revisions were published (Stormer, 1975; Powell and Powell, 1977; Whitney and Stormer, 1977; Fuhrman and Lindsley, 1988; Elkins and Grove, 1990; Benisek et al., 2004). Formation temperature was defined by using the two-feldspar thermometer after Putirka (2008) that used 41 experimental data for the revision of the two-feldspar thermometer. For the analysis only plagioclase inclusions in alkali feldspars and intergrowth grains were used for the two-feldspar thermometer. Compositions of plagioclase and alkali feldspar were defined using the electron microprobe at the UNAM Campus in Morelia (see 3.2. Mineral chemistry). Therefore, transects from the alkali feldspars through the plagioclase inclusions within and in case of intergrowth from alkali feldspar to plagioclase were measured. The temperature was calculated after the equation 27 b in Putirka (2008):

$$T(°C) = \frac{-442 - 3.72P(kbar)}{-0.11 + 0.1ln\left(\frac{X_{Ab}^{afs}}{X_{Ab}^{pl}}\right) - 3.27\left(X_{An}^{afs}\right) + 0.098ln\left(X_{An}^{afs}\right) + 0.52\left(X_{An}^{plag}X_{Ab}^{plag}\right)}$$

In the formula $P(kbar)$ is the pressure in kbar. X_{Ab}^{afs} is the mole fraction of albite in alkali feldspar, X_{An}^{afs} is the mole fraction of anorthite in alkali feldspar, and X_{Ab}^{plag} and X_{An}^{plag} analogous the mole fractions of albite and anorthite in plagioclase. Since the formula requires the formation pressure $P(kbar)$ for the calculation of the formation temperature it needs to be calculated from a geobarometer or it has to be assumed.

3.4.5. Uncertainties

Two types of uncertainties are considered for the thermobarometric calculations, first, analytical uncertainties and errors associated with the measurement and second, error related with calculation of residual pressure, formation pressure, and formation temperature from the Raman measurements and EPMA. Furthermore, a type of uncertainties in thermobarometric calculations are the absolute errors that are the value that the calculated temperatures and pressures differs from the pressure or temperature and the actual formation conditions. The absolute error includes information such as uncertainty about which compositions in heterogeneous minerals represent

desired equilibrium conditions (Kohn and Spear, 1991). The absolute error is typically minimum between ±75– 100 °C and ±1–3 kbar (Hodges and McKenna, 1987; Kohn and Spear, 1991).
The second type of error is the uncertainty of one thermobarometric calculation or model relative to another. In general, the absolute error is bigger as the relative error. The relative error can be minimized by comparing estimates using the same thermometer or barometer.
The variation in the analysed standards was collected throughout the day and it was used for the calculation of the uncertainties for each standard. The uncertainties of the standards were added and propagated to the sample analysis to estimate the analytical uncertainties of each measurement. That is the most conservative approach for the estimation of the uncertainties related to the analytical instruments and measurements, including the instrumental drift, variation in laser power and the variation in room temperature during the day.
For all measurements the analytical errors on the analytical instruments and the errors on the formation pressures and temperatures were manually calculated by linearly propagating the uncertainties in measurements associated with the analysis.

3.5. Modeling of the crystallization of the rhyolitic magmas using rhyolite-MELTS

In order to obtain information on the crystallization of the rhyolitic magmas in the Mesa Central, geochemical crystallization models, using rhyolite-Melts (Gualda et al., 2012; Ghiorso and Gualda, 2015) were carried out. The aim in using the rhyolite-MELTS simulations is not to model in detail the crystallization of volcanic rocks in the study area, but rather to obtain important information on over which crystallization can take place and which minerals can crystallize from the magmas that originated the volcanic rocks in the study area. Rhyolite-MELTS is a modified calibration of the original thermodynamic modeling MELTS software (Ghiorso and Sack, 1995; Asimow and Ghiorso, 1998). It was designed to model the relation between phases (mineral, rock and liquid) during melting and crystallization and it is used for the modeling of magmatic process such as equilibrium crystallization, partial melting, fractional crystallization, and assimilation over a temperature and pressure range of 500-2000 °C and 0-2 GPa (Ghiorso and Sack, 1995; Asimow and Ghiorso, 1998). The MELTS software uses the thermodynamic principals such as variations in temperature, pressure, and volume in a system to forecast the chemical variations in the magmatic system and it can predict which minerals will crystallize from the evolving magma, the proportions of the minerals, and the composition of the mineral at each stage of temperature-

pressure composition (Ghiorso and Sack, 1995; Asimow and Ghiorso, 1998). Furthermore, MELTS can predict the change in composition of the residual magma for magmatic processes such as melting or fractional crystallization (Ghiorso and Sack, 1995; Asimow and Ghiorso, 1998). MELTS is based on experimental results as well as calculations, results should not be considered as an explicit representation of the evolution of magmas but more as predictive models (Ghiorso and Sack, 1995; Asimow and Ghiorso, 1998).

The models are based on thermodynamics, that minimizes the Gibbs free energy (G), Enthalpy (H), entropy (S), pressure, and temperature. The program calculates the minimum Gibbs free energy for every given set of pressure, temperature and composition (Ghiorso and Sack, 1995; Asimow and Ghiorso, 1998).

MELTS was applied to understand the evolution and behavior of relatively dry mafic and intermediate magmas (Ghiorso, 1997; Gaetani et al., 1998). Due to the lack of suitable thermodynamics models of hydrous mafic silicates the use of MELTS for wet intermediate magma compositions was limited (Ghiorso and Sack, 1995; Asimow and Ghiorso, 1998; Gualda et al., 2012). A modified calibration of MELTS, rhyolite-MELTS, was introduced by Gualda et al. (2012) to optimize the simulation for fluid-bearing silicic systems. The advance of rhyolite-MELTS compared to the original MELTS software is the prediction of the quartz-feldspar saturation surface in temperature, pressure, and composition (Gualda et al., 2012). Furthermore, it is more efficient in calculating the feldspar and pyroxene phase saturation, and implements the rhombohedral oxide solution model of Ghiorso and Evans (2008).

4. Almandine garnet-bearing rhyolites associated to bimodal volcanism in the Mesa Central of Mexico: Geochemical, petrological and geochronological evolution.

4.1. General information

The chapter 4. Almandine garnet-bearing rhyolites associated to bimodal volcanism in the Mesa Central of Mexico: Geochemical, petrological and geochronological evolution is mainly based on the publication Almandine garnet-bearing rhyolites associated to bimodal volcanism in the Mesa Central of Mexico: Geochemical, petrological and geochronological evolution by Sieck et al. (2019) published in Journal of South American Earth Science, Volume 92, June 2019, pages 310 – 318. The publication is available under: https://doi.org/10.1016/j.jsames.2019.03.018. See also Appendix A

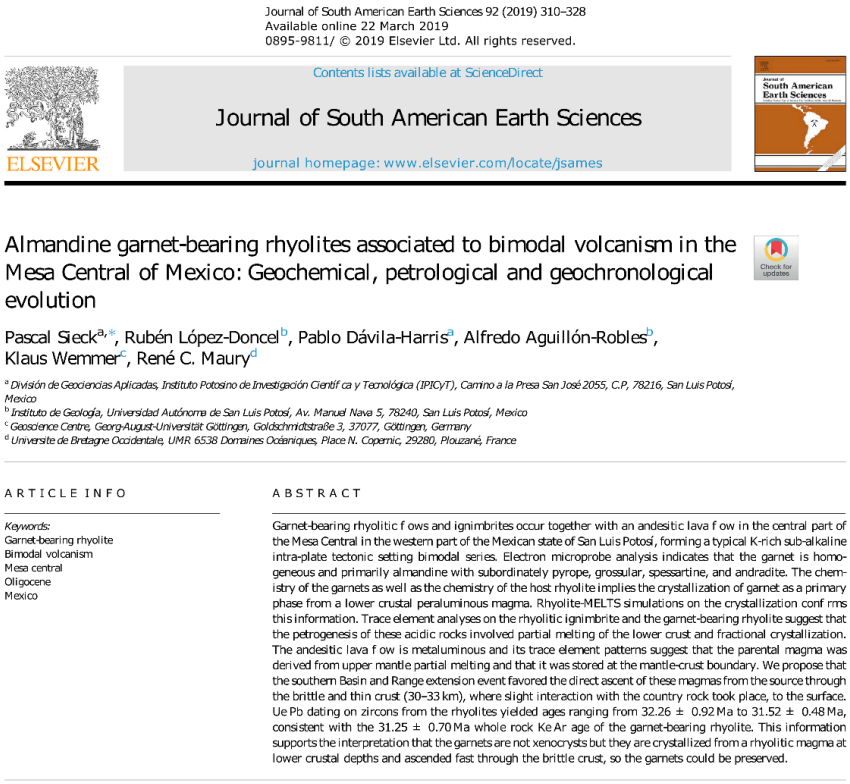

Journal of South American Earth Sciences 92 (2019) 310–328
Available online 22 March 2019
0895-9811/

Contents lists available at ScienceDirect

Journal of South American Earth Sciences

journal homepage: www.elsevier.com/locate/jsames

Almandine garnet-bearing rhyolites associated to bimodal volcanism in the Mesa Central of Mexico: Geochemical, petrological and geochronological evolution

Pascal Sieck[a,*], Rubén López-Doncel[b], Pablo Dávila-Harris[a], Alfredo Aguillón-Robles[b], Klaus Wemmer[c], René C. Maury[d]

[a] División de Geociencias Aplicadas, Instituto Potosino de Investigación Científica y Tecnológica (IPICyT), Camino a la Presa San José 2055, C.P. 78216, San Luis Potosí, Mexico
[b] Instituto de Geología, Universidad Autónoma de San Luis Potosí, Av. Manuel Nava 5, 78240, San Luis Potosí, Mexico
[c] Geoscience Centre, Georg-August-Universität Göttingen, Goldschmidtstraße 3, 37077, Göttingen, Germany
[d] Universite de Bretagne Occidentale, UMR 6538 Domaines Océaniques, Place N. Copernic, 29280, Plouzané, France

ARTICLE INFO

Keywords:
Garnet-bearing rhyolite
Bimodal volcanism
Mesa central
Oligocene
Mexico

ABSTRACT

Garnet-bearing rhyolitic flows and ignimbrites occur together with an andesitic lava flow in the central part of the Mesa Central in the western part of the Mexican state of San Luis Potosí, forming a typical K-rich sub-alkaline intra-plate tectonic setting bimodal series. Electron microprobe analysis indicates that the garnet is homogeneous and primarily almandine with subordinately pyrope, grossular, spessartine, and andradite. The chemistry of the garnets as well as the chemistry of the host rhyolite implies the crystallization of garnet as a primary phase from a lower crustal peraluminous magma. Rhyolite-MELTS simulations on the crystallization conditions this information. Trace element analyses on the rhyolitic ignimbrite and the garnet-bearing rhyolite suggest that the petrogenesis of these acidic rocks involved partial melting of the lower crust and fractional crystallization. The andesitic lava flow is metaluminous and its trace element patterns suggest that the parental magma was derived from upper mantle partial melting and that it was stored at the mantle-crust boundary. We propose that the southern Basin and Range extension event favored the direct ascent of these magmas from the source through the brittle and thin crust (30–33 km), where slight interaction with the country rock took place, to the surface. U–Pb dating on zircons from the rhyolites yielded ages ranging from 32.26 ± 0.92 Ma to 31.52 ± 0.48 Ma, consistent with the 31.25 ± 0.70 Ma whole rock K–Ar age of the garnet-bearing rhyolite. This information supports the interpretation that the garnets are not xenocrysts but they are crystallized from a rhyolitic magma at lower crustal depths and ascended fast through the brittle crust, so the garnets could be preserved.

In addition, the chapter 4 includes new and unpublished data on the origin of the almandine garnets from the La Herradura area, as well as a more detailed description of the volcanic units of the La Herradura area.

4.2. Introduction

Almandine garnet-bearing rhyolitic rocks are uncommon in the geologic record (Harangi et al., 2001) and are not described in the Sierra Madre Occidental (SMO) and its southeastern part the Mesa Central (MC). Garnets often occur in high-grade metamorphic terranes, but are uncommon in volcanic rocks where their formation can result from three kind of processes. They can either be a residual phase derived from partially melted metamorphic rocks (Hensen and Green, 1973), a phase crystallized from a contaminated melt during or following assimilation of country rocks (Lantai, 1991; Stevens et al., 2007), or a primary phase crystallized from an apparently uncontaminated host magma (Fitton, 1972; Harangi et al., 2001; René and Stelling, 2007). Garnet compositional data might help to understand the petrogenetic processes from origin to eruption, or emplacement of garnet-bearing magmas. Previous research show that almandine-rich garnet could crystallize from Al-rich silicic magmas as a liquidus or near liquidus phase at high pressures of 7-18 kbar and temperatures of ~850 – 1050°C (Green and Ringwood, 1968, 1972; Wood, 1974; Harangi et al., 2001).

Bimodal volcanism is widespread in earth history and have been reported in intra-continental extension settings (Tristán-González et al., 2008; Rodríguez-Ríos and Torres-Aguilera, 2009; Tristán-González et al., 2009 a; Aguillón-Robles et al., 2014; Guo et al., 2016), active continental margins (Espinoza et al., 2008), and oceanic settings including island arcs (Shukuno et al., 2006), and back arc basin/rift systems (Hochstaedter et al., 1990).

Bimodal volcanism has been documented in the southern and central part of the Mesa Central, especially in the San Luis Potosí Volcanic Field, where ignimbrites of rhyolitic composition (e.g., the Panalillo Ignimbrite, 26.8 ± 1.3 Ma) are associated with basalts (e.g. the La Placa Basalt, 27.2 ± 0.6 Ma). Both rock types have very similar Oligocene ages and display geochemical characteristics typical for bimodal volcanism (Tristán-González et al., 2008; Rodríguez-Ríos and Torres-Aguilera, 2009; Tristán-González et al., 2009 a; Aguillón-Robles et al., 2014).

Previous studies on bimodal volcanism in the southern and central Mesa Central show that partial melting and fractional crystallization are the two main magmatic processes involved (Aguillón-Robles et al., 2009; Aguillón-Robles et al., 2014). Rhyolitic domes located near the study area are thought to be derived from partial melting, generated by metasomatized lithospheric fluids and crustal extension, of the base of the continental crust and then to have experienced fractional crystallization during magma ascent (Aguillón-Robles et al., 2009). Associated basaltic to

andesitic magmas are most likely derived from partial melting, generated in a post-subduction setting, of the upper mantle (Tristán-González et al., 2009 b; Aguillón-Robles et al., 2014).

The study area is located near La Herradura, in the Mexican state of San Luis Potosí, 150 km northeast of the city of San Luis Potosí (Figure 5). One of the main characteristics of the volcanic rocks of La Herradura area is the presence of hypidiomorphic to idiomorphic garnet crystals. Garnet-bearing rhyolites, named the La Herradura rhyolite, is underlain by light pink to gray, porphyritic, rhyolitic ignimbrite (El Sombrero Ignimbrite), and are spatially and temporally associated with andesitic lava flows (Zaragoza Andesite).

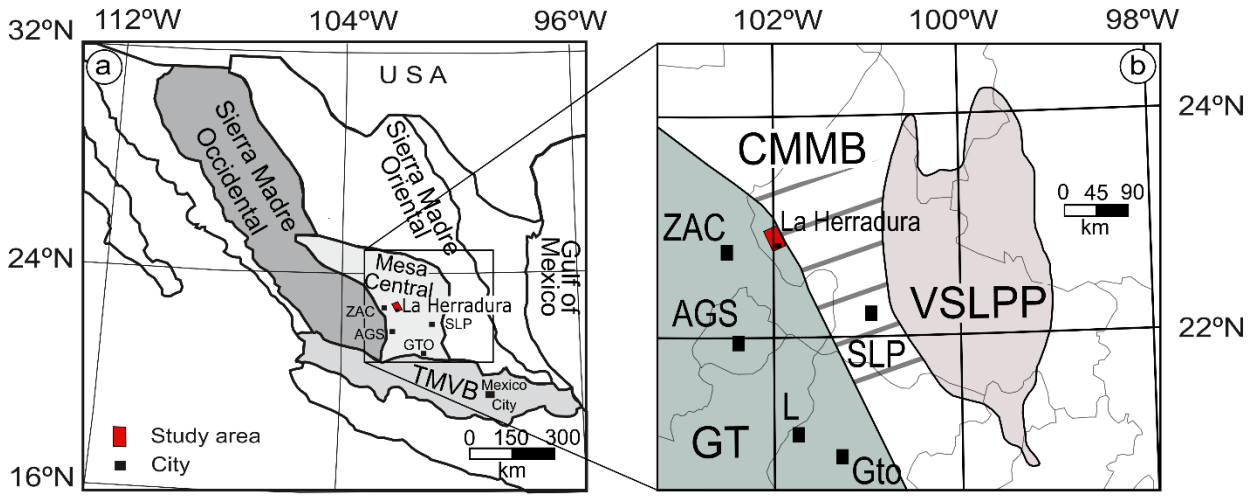

Figure 5: Location of the La Herradura area. a) Spatial relationship with the main geological provinces of northern Mexico. b) Location of volcano-tectonic features of San Luis Potosí and Zacatecas. a) and b) modified after Mortensen et al. (2008) and Aguillón-Robles et al. (2014). ZAC: Zacatecas city; AGS: Aguascalientes city; GTO: Guanajuato city; SLP: San Luis Potosí city; L: Leon; TMVB: Trans Mexican Volcanic Belt; GT: Guerrero Terrane; CMMB: Central Mexico Mesozoic Basin; VSLPP: Valles-San Luis Potosí Platform.

The general rareness of almandine garnet-bearing rocks and further experimental results indicating a high-pressure origin proposing that their formation and eruption is favored by special geodynamic conditions (Green, 1977, 1992; Harangi et al., 2001). Hence, the garnet-bearing volcanic rocks and their bimodal suit can provide information regarding the geodynamics of the magma genesis in the central part of the Mesa Central. Furthermore, the study of the garnets and their host volcanic rocks will improve our information about the formation of garnet-bearing magmas.

The aim of this work is to investigate the origins of garnet-bearing lavas based on the study of their geological, petrological, geochemical and age features. The interpretation of these dataset provides

new information on the origin of garnet-bearing rhyolites using the case study of La Herradura and their associated bimodal suite.

4.3. Geological Setting

In the study area, the oldest rocks exposed consist of a lower Cretaceous marine sequence including limestones, clay-rich limestones, and shales, unconformably overlain by the rhyolitic El Sombrero Ignimbrite (Figure 6). The garnet-bearing La Herradura rhyolite covers the 85 m thick El Sombrero Ignimbrite (Figure 7 a and b). Labarthe-Hernández and Jiménez-López (1991) reported a K-Ar whole rock age of 30.2 ± 1.5 Ma for the garnet-bearing La Herradura rhyolite and proposed that the NW-SE trending ridges and plateaus are the result of fissure-fed volcanism. The andesitic lava, of the Oligocene Zaragoza Andesite overlies the La Herradura rhyolite.

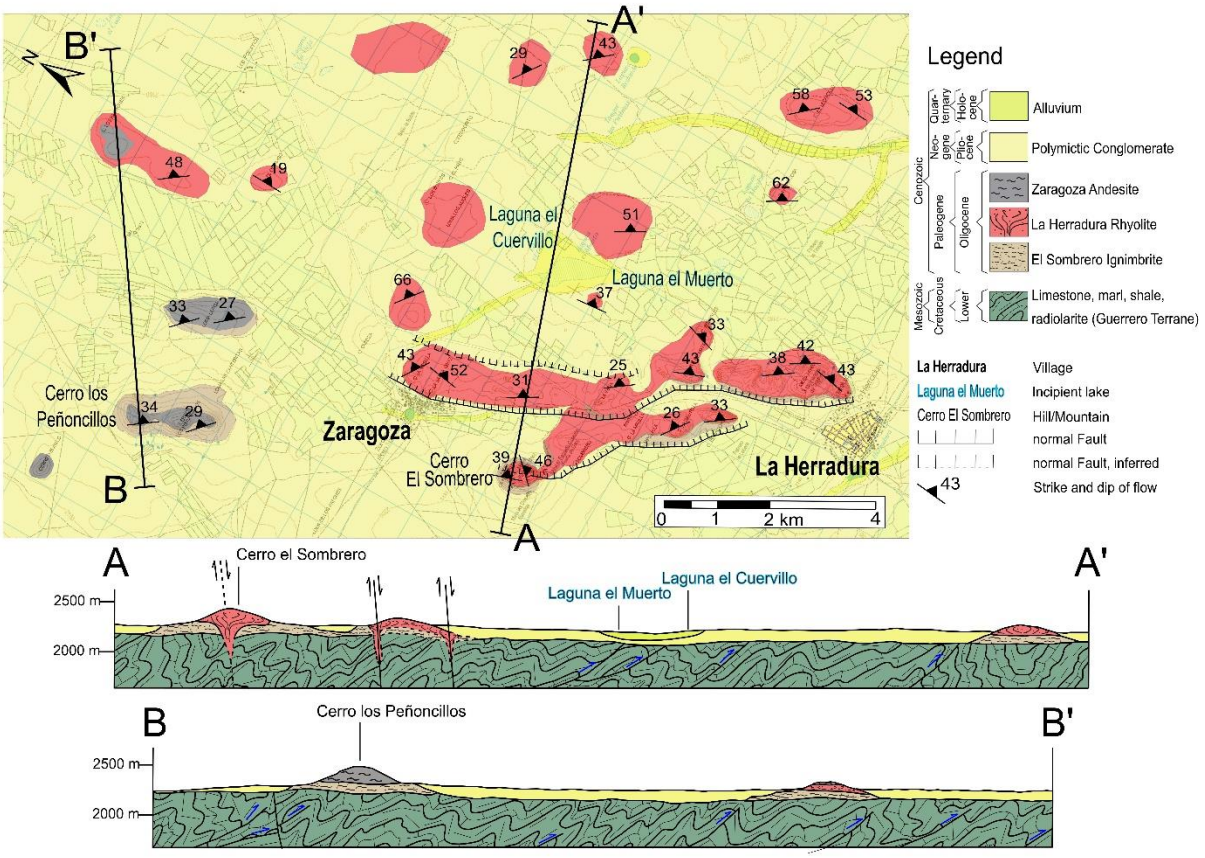

Figure 6: Geological map of La Herradura area and cross-sections through the study area.

This Oligocene volcanic activity was associated to a transtensive deformation regime that generated a set of several km-long NW-SE trending normal faults (e.g. the 9 km-long La Herradura fault and the 4.5 km-long Zaragoza fault), along which the Oligocene magmas flowed.

During the Pliocene-Pleistocene, 60 to 250 m-thick sandstones interlayered with conglomerates were deposited erosional discordant over both the lower Cretaceous and Oligocene volcanic rocks, and locally covered by Holocene gravels and silts, caliches, lacustrine materials and alluvium.

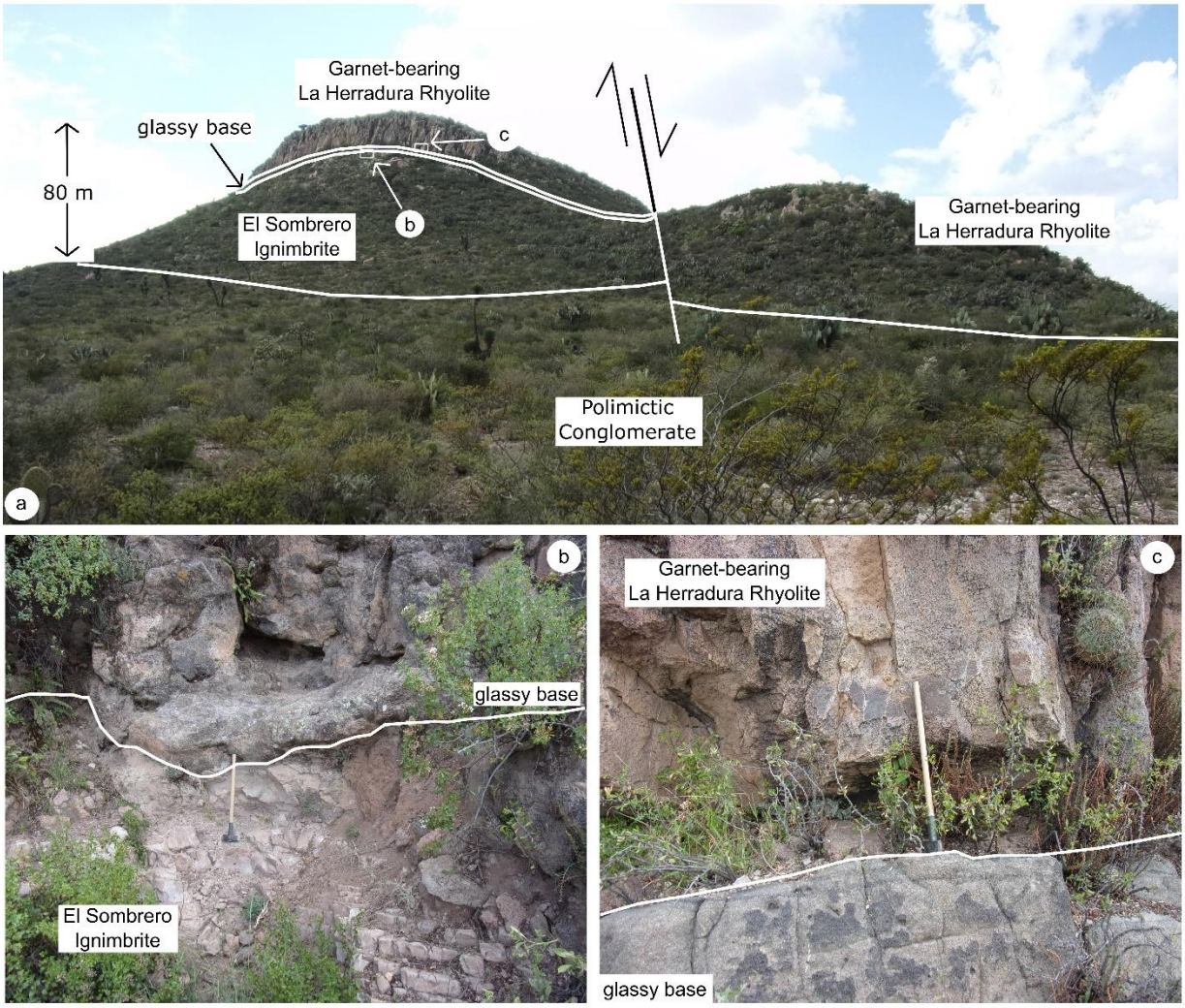

Figure 7: Field photography of the center part of the La Herradura area. a) Cerro El Sombrero in the center of the study area, marked are the geological contacts of the different units. b) Contact between the garnet-bearing La Herradura Rhyolite and its basal vitrophyre. c) Contact between the El Sombrero Ignimbrite and the basal vitrophyre of the La Herradura Rhyolite. The contact is erosive and parts of the ignimbrite are incorporated in the basal vitrophyre. Size of the hammer is 0.5 m.

4.4. Results

4.4.1. Stratigraphy and Petrography

The composite stratigraphic column of the study area is shown in Figure 8. Locally, the El Sombrero Ignimbrite consists of a light pink to gray, porphyritic, rhyolitic, and un-welded

ignimbrite (Figure 9 a), which contains quartz, plagioclase, K-feldspar, and pyroxene. The preserved estimated volume of the ignimbrite is 5 km^3.

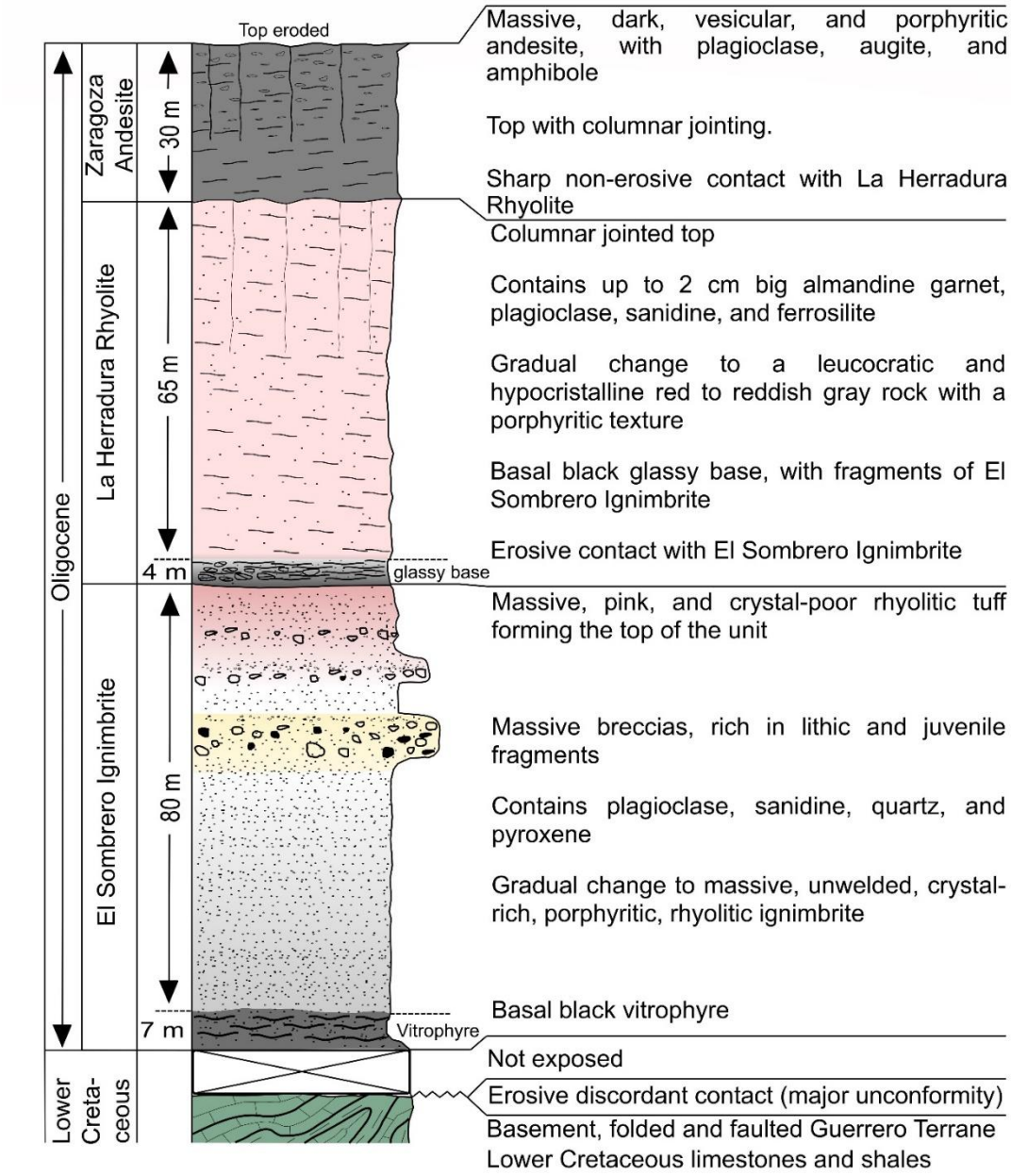

Figure 8: Composite stratigraphic column of the volcanic rocks from the La Herradura area showing the main lithostratigraphic units described in the text.

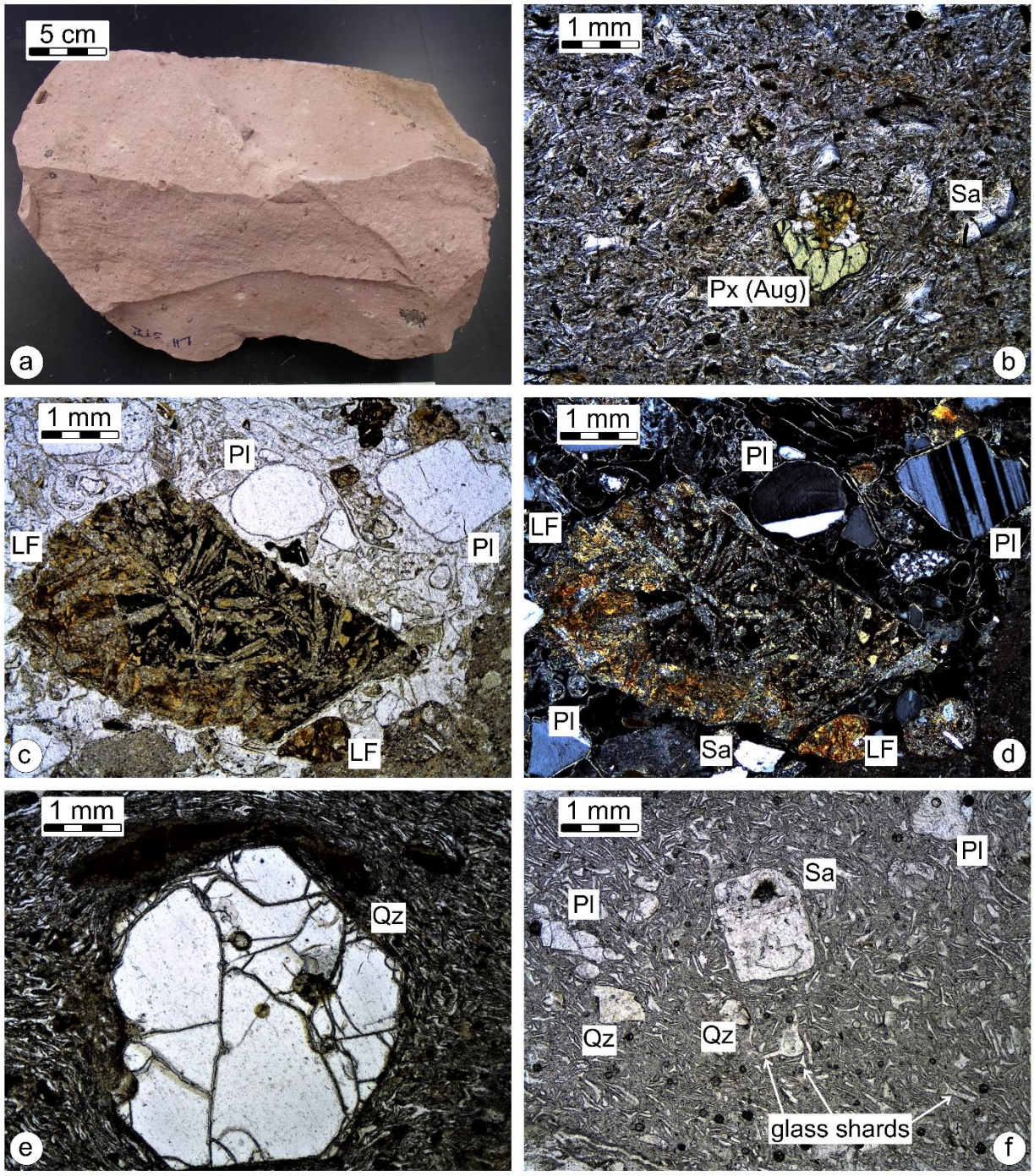

Figure 9: Hand specimen and thin section images of the El Sombrero Ignimbrite. a) Representative hand specimen of the El Sombrero Ignimbrite. b) – f) Thin section images of the El Sombrero Ignimbrite. b) Pyroxene (augite) and sanidine crystals in the fine-grained matrix of the El Sombrero Ignimbrite. c) and d) Thin section image of massive lithic and juvenile fragments-rich breccia. d) Picture taken with crossed nichols. e) Quartz crystal in the crystals in the fine-grained matrix of the El Sombrero Ignimbrite. f) Thin section image of the base of the El Sombrero Ignimbrite. Aug: augite, LF: lithic fragment, Pl: plagioclase, Px: pyroxene, Qz: quartz, Sa: Sanidine.

Angular to sub-angular and reddish, lithic clasts (~10 vol.% of the rock and up to 5 cm in size) are present. The base of the ignimbrite is formed by an up to 7 m thick vitrophyre, which gradually

turns into a gray, massive, porphyritic, rhyolitic ignimbrite. The rocks show no layering or graduation in grain size. Nevertheless, the upper part shows an increase of the juvenile clasts up to 15 vol.%, and can therefore be described as a massive lithic and juvenile fragments-rich breccia. At the top of the unit the porphyritic rhyolitic ignimbrites are brecciated and crosscut by quartz-filled fractures. In thin sections the light pink to gray porphyritic rhyolitic tuffs can be described as hypocrystalline with a porphyric texture. The fine-grained matrix that consists of calcite, hematite, glass shards and small amounts of clay minerals, contains xenomorphic quartz, hypidiomorphic plagioclase, hypidiomorphic sanidine, and rarely xenomorphic pyroxene (Figure 9 b-f). The lithic fragments consist mainly of xenomorphic quartz grains with a cover of hematite. The massive lithic- and juvenile-rich breccia shows the same composition as the gray massive porphyritic rhyolitic ignimbrite. In thin section the fractures, which are filled with secondary quartz, are crosscutting lithic fragments and the minerals.

The contact between the El Sombrero and the garnet-bearing rhyolitic lava is erosive and its base is formed by an up to 4 m thick glassy base (Figure 7 a and b). The glassy base can be described as leucocratic and hypocrystalline that gradually turns into a microcrystalline groundmass. The upper part of the glassy base is auto-brecciated. The La Herradura rhyolite has an actual estimated volume of 3 km^3 and is a leucocratic and hypocrystalline red to red-gray rock with a porphyric texture. In the glassy matrix of the base and in the microcrystalline groundmass of the rhyolite flow structures are recognizable (Figure 7 b and c). The rock contains hypidiomorphic to idiomorphic and up to 2 cm large red to reddish-brown garnets, as well as quartz, plagioclase, K-feldspar, and pyroxene (Figure 10 a-d). Garnet (Figure 10 b, Figure 11 a-c) is hypidiomorphic to idiomorphic, or rounded red and range in size from 0.25 to 3 mm and its modal abundance ranges between 3 % and 6 %.

In thin sections the garnet-bearing rhyolite can be described as seriate and hypocrystalline. The glassy matrix shows typical perlitic cracks and flow structures and gradually changes into a hyalopilitic groundmass consisting of, plagioclase and K-feldspar microlites. The garnets in thin sections are hypidiomorphic to idiomorphic red and poikilitic. Garnets contain inclusions of ilmenite, zircon, apatite, monazite, rutile, and rarely pyrite (Figure 10 d, Figure 11 c). Table 1 shows all minerals identified in the samples and except pyrite the setting of inclusions in garnet (ilmenite, zircon, apatite, monazite and, rutile) is also present in the groundmass. Furthermore,

corundum was identified in the microcrystalline groundmass and the samples of the glassy base have gap fillings of secondary barite.

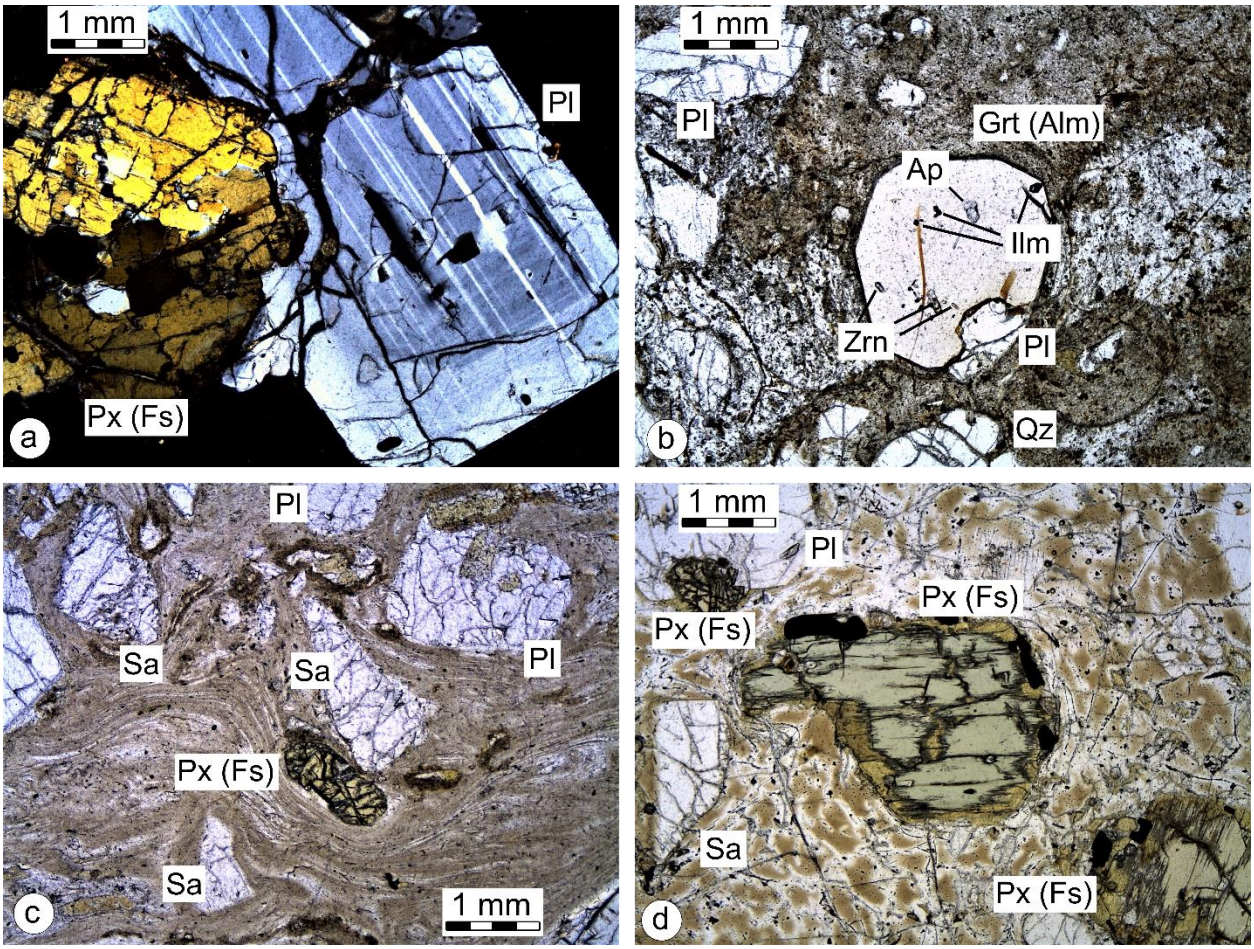

Figure 10: Thin section images of the garnet-bearing La Herradura Rhyolite. a) Idiomorphic plagioclase, with zoning, together with pyroxene (Ferrosilite) in the glassy matrix of the base from the garnet-bearing La Herradura Rhyolite. Picture taken with crossed nichols. b) Thin section image of a garnet crystal from the garnet-bearing La Herradura Rhyolite. Garnet contains inclusions of apatite, ilmenite and zircon. c) Thin section image of the glassy base of the garnet-bearing rhyolite. The glassy base shows flow-structures. d) Pyroxene (ferrosilite) with alteration rim in the glassy matrix of the glassy base of the garnet-bearing rhyolite. Alm: almandine, Ap: apatite, Fs: ferrosilite, Grt: garnet, Ilm: Ilmenite, Pl: plagioclase, Px: pyroxene, Sa: sanidine.

Quartz crystals in thin sections are xenomorphic with an average grain size of 3 mm. Sanidine crystals (~ 5 vol.%) are hypidiomorphic to xenomorphic and they show Carlsbad twinning. Hypidiomorphic to idiomorphic and in average 5 mm big plagioclase (~10 vol.%) crystals are also present in thin sections. They show the polysynthetic twinning and in base cuts a zoning is present. Plagioclase and pyroxene show very often a glomerophyric texture. Pyroxenes (~ 5 vol.%) have xenomorphic shape and an average grain size of 2 mm. Most of the grains show altered rims and a greenish to brownish pleochroism. The brecciated parts of the glassy base show the same mineral content as the non-brecciated parts; however, the minerals and the glassy matrix are crushed.

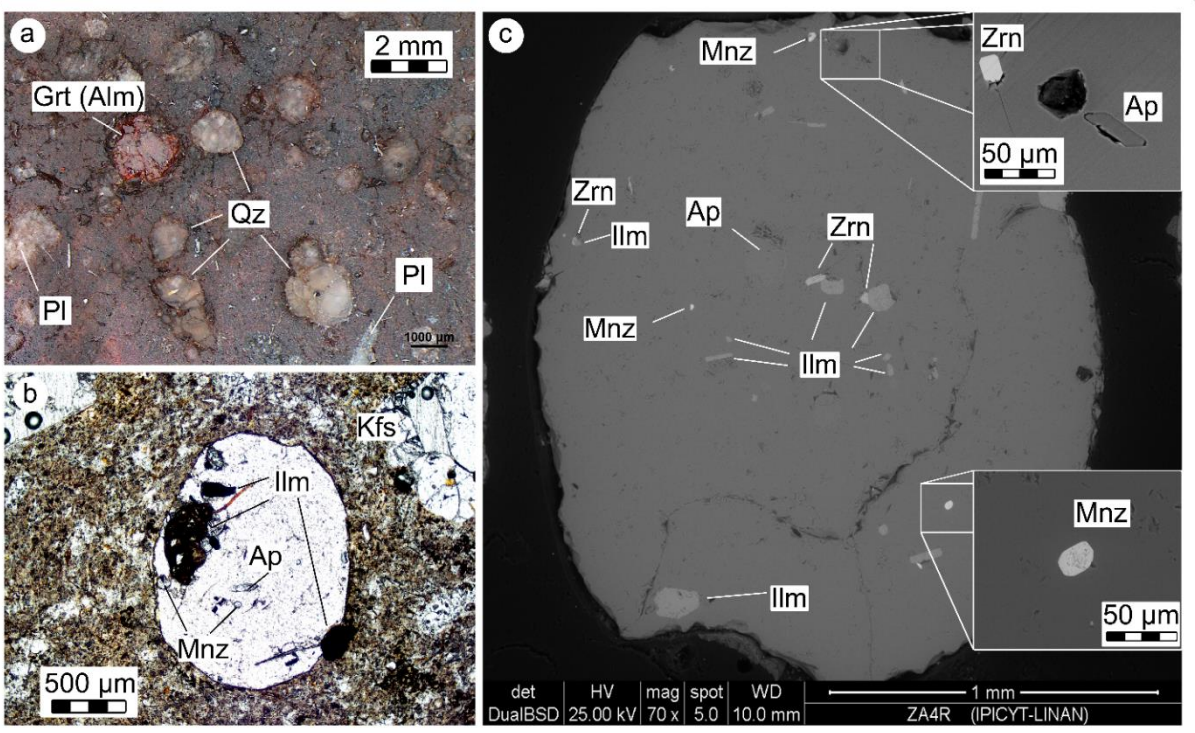

Figure 11: Almandine garnets of the La Herradura Rhyolite. a) Representative hand specimen from the base of the garnet-bearing La Herradura rhyolite. Hypidiomorphic garnet grain in the glassy matrix together with plagioclase and quartz. b) Thin section image of a garnet crystal from the garnet-bearing La Herradura rhyolite. Garnet contains inclusions of apatite, ilmenite and monazite. c) EDS image from garnet separates. The typical inclusion set-up consists of ilmenite, apatite, zircon, monazite, and, not visible in this grain, rutile and pyrite. Alm: almandine, Ap: apatite, Ilm: ilmenite, Kfs: K-feldspar, Mnz: monazite, Pl: plagioclase, Qz: Quartz, Zrn: zircon.

The contact between the Zaragoza Andesite (volume of 2 km^3; Figure 8, Figure 12 a) and the garnet-bearing rhyolite is non-erosive. The andesite is a massive, dark, vesicular rock, with a porphyritic texture. Pyroxene, amphibole, and plagioclase phenocrysts are present in the fine-grained matrix (Figure 12 b-d). In hand specimen and thin sections, the amphiboles show reaction rims (Figure 12 c, d, f).

In thin sections the rocks show a porphyritic, seriate and hypocrystalline texture. The groundmass consists of plagioclase microlites, which grain size decrease from the bottom to the top of the unit. Plagioclase microlites show a sub-parallel orientation (pilotaxitic texture), which indicates a flow of the magma. Plagioclase (~5 vol.%) and pyroxene (~5 vol.%) phenocrysts have both an average grain size of 1 mm and are hypidiomorphic to idiomorphic and together they form crystal accumulations (glomerophyric texture). Amphiboles (~ 2 vol.%) are xenomorphic to hypidiomorphic and show, the above described alteration rims. Vesicles are also present in the rocks, the number and size increase to the top of the unit. The vesicles at the top of the unit are lengthened and some of them are filled with secondary carbonate.

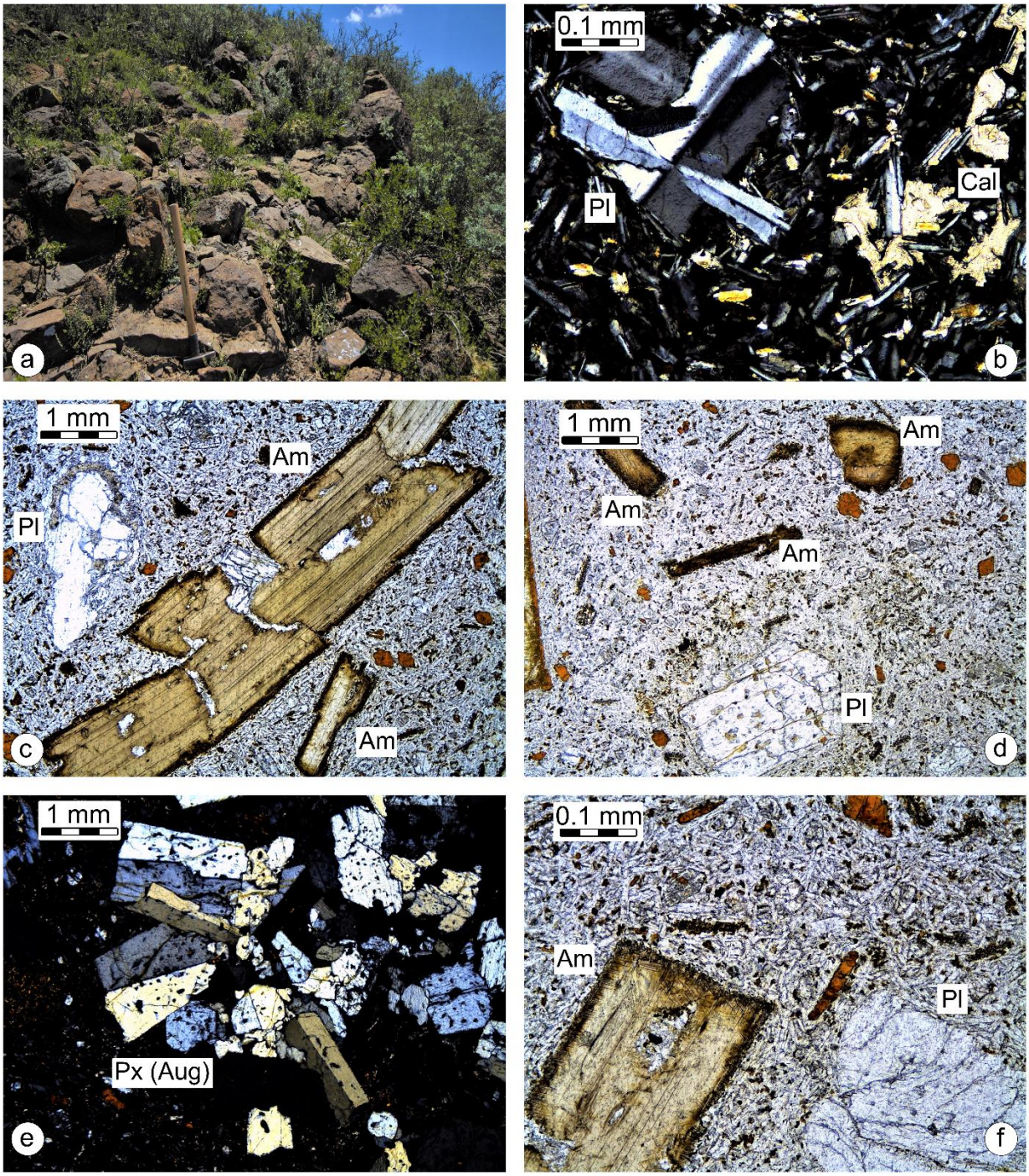

Figure 12: Field photography and thin section images of the Zaragoza Andesite. a) Exposure of Zaragoza Andesite on top of the Cerro los Peñoncillos in the northern part of the study area. Size of the hammer is 0.5 m. b) Micro-crystalline groundmass consisting of plagioclase microlites, vesicles are filled with secondary carbonate. Picture taken with crossed nichols. c) Amphibole xenocrystal with reaction rim consisting of opaque phases, pyroxenes and glass. d) Thin section image of the Zaragoza Andesite. Plagioclase and amphibole crystals in the fine-grained matrix. e) Agglomerate of hypidiomorphic augites in the fine-grained matrix. Picture taken with crossed nichols. f) Thin section image of the Zaragoza Andesite. Plagioclase and amphibole crystals in the fine-grained matrix. Am: amphibole, Aug: augite, Cal: calcite, Pl: plagioclase, Px: pyroxene.

Table 1: Minerals appearing in the groundmass and in the garnets of La Herradura rhyolite.

Mineral/Phase	Primary magmatic mineral (>1 vol.%)	Primary magmatic accessory mineral (<1 vol.%)	Inclusion in Garnet	Secondary mineral / Alteration mineral
Quartz	x	-	-	-
Plagioclase	x	-	-	-
K-Feldspar	x	-	-	-
Pyroxene	x	-	-	-
Garnet	x	-	-	-
Magnetite	-	x	-	-
Biotite	-	x	-	-
Barite	-	-	-	x
Corundum	-	x	-	-
Ilmenite	-	x	x	-
Zircon	-	x	x	-
Apatite	-	x	x	-
Monazite	-	x	x	-
Rutile	-	x	x	-
Pyrite	-	x	x	-

4.4.2. Whole-rock geochemistry

Analytical results are given in Table 2. Data processing and plots were carried out using GCDkit 4.1 (Janoušek et al., 2006; 2015).

For the geochemical analysis fresh, non-devitrified samples were used, the loss of ignition values (LOI at 1000°C) ranging from 1.19 wt.% for the La Herradura Rhyolite to 3.71 wt.% for the El Sombrero Ignimbrite. The garnet-bearing rocks of La Herradura show a relatively narrow range of SiO_2 (Figure 13 a, TAS diagram), varying between 69 and 73 wt.%. All samples of the garnet-bearing rhyolite and of the El Sombrero Ignimbrite have a rhyolitic composition. They are low in TiO_2 (< 0.5 wt.%) and MgO (< 2 wt.%). The composition of the Zaragoza andesite is basaltic andesitic. The volcanic rocks of the study area mostly correspond to the high-K calc-alkaline series, with a tendency towards shoshonitic (Figure 13 b). Likewise, the rocks of El Sombrero Ignimbrite and La Herradura Rhyolite are dominantly peraluminous and those of the Zaragoza

Andesite are metaluminous (Figure 13 c). TiO_2, Fe_2O_3, MgO, MnO, and CaO show negative correlations with increasing SiO_2 content, whereas K_2O and to a lesser extent Na_2O display positive correlations (Table 2).

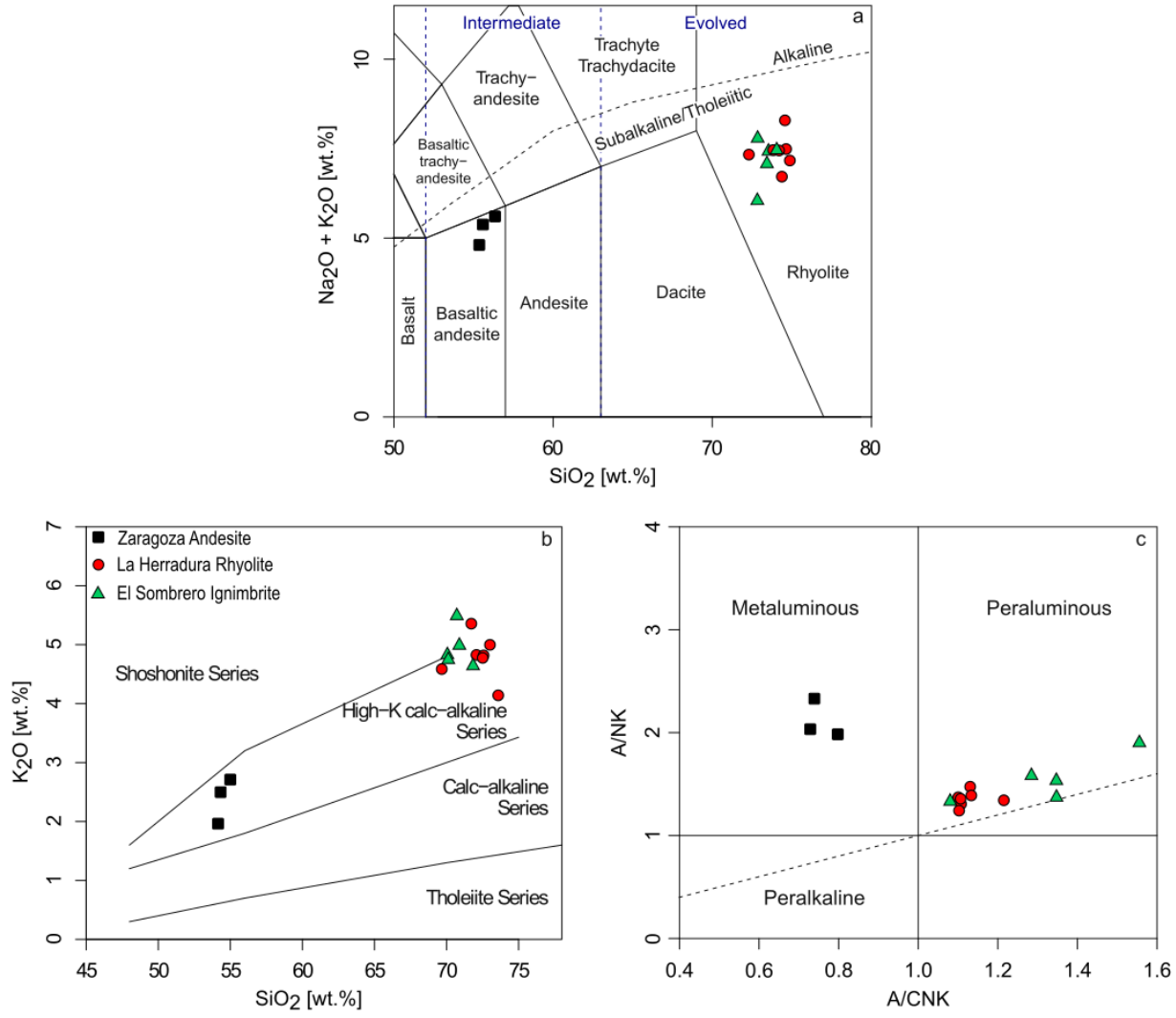

Figure 13: Major element results for La Herradura rocks. a) TAS classification diagram after Le Bas et al. (1986). Alkaline and subalkaline/tholeiitic fields after Miyashiro (1978). b) K_2O vs. SiO_2 diagram after Peccerillo and Taylor (1976). c) A/CNK vs A/NK plot after Shand (1943). A/CNK = $Al_2O_3/(CaO + Na_2O + K_2O)$, in molar ratios; A/NK = $Al_2O_3/(Na_2O+K_2O)$, in molar ratios.

Incompatible trace elements patterns, normalized to primitive mantle (McDonough and Sun, 1995), display a general negative slope (Figure 14), with negative anomalies of Nb, Ta, Sr and Ti and positive anomalies of U, Pb, Nd, Sm and enrichment in large ion lithophile elements (LILE) with respect to high field strength elements (HFSE).

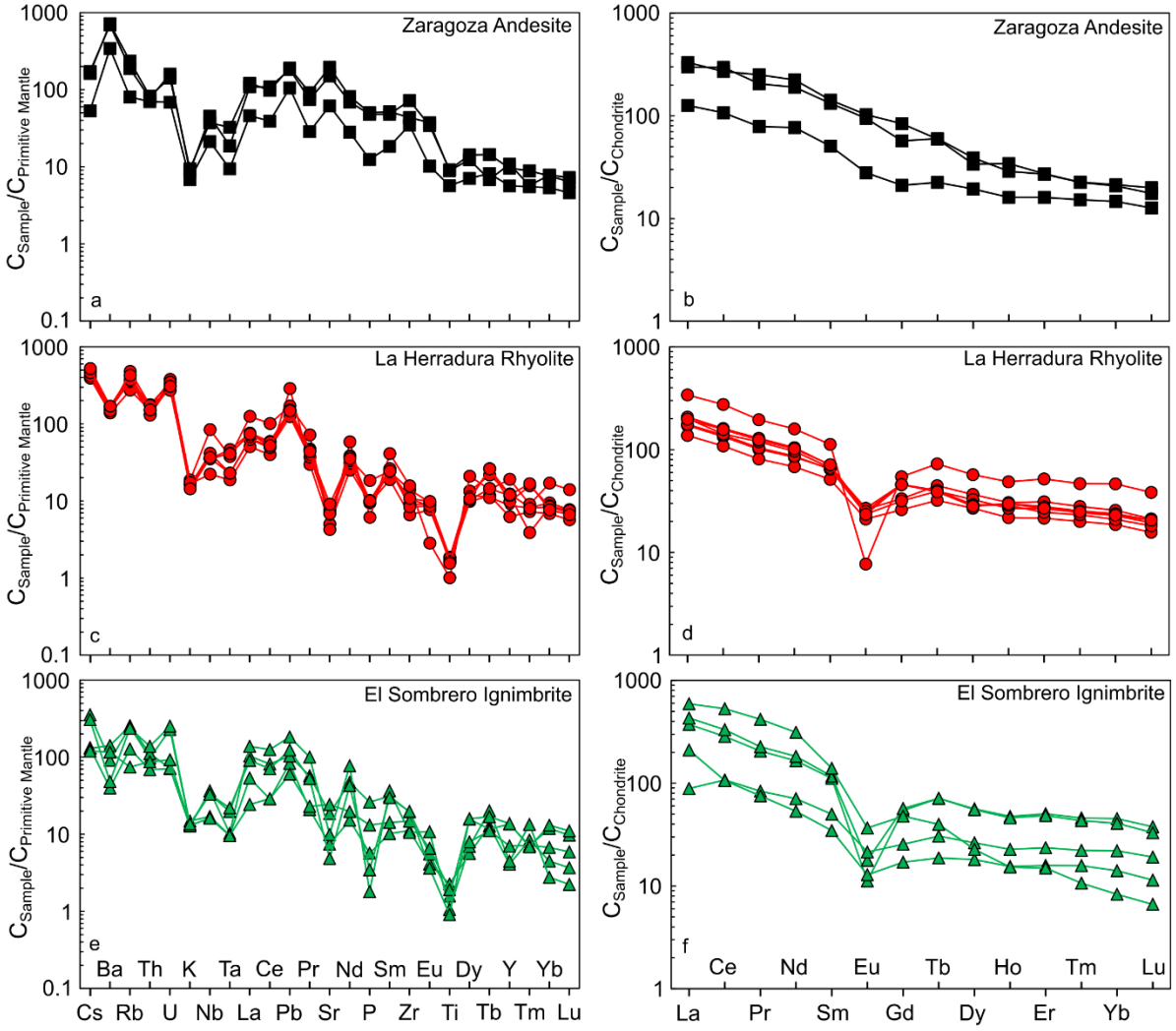

Figure 14: Trace element results for the La Herradura rocks of this study. a), c) and e) Chondrite-normalized REE plots for the volcanic rocks of the La Herradura area. b), d) and, f) Primitive mantle-normalized multielement plots for the volcanic rocks of the La Herradura area. Chondrite and primitive mantle composition after McDonough and Sun (1995).

Chondrite-normalized REE patterns show a marked enrichment in LREE with respect to HREE. A slightly to well-developed negative Eu anomaly is present in all samples of the garnet-bearing rhyolite and of the El Sombrero ignimbrite (Figure 14), with $(Eu/Eu^*)_N$ ($Eu^* = \sqrt{Sm_N \times Gd_N}$ and N denotes chondrite-normalized values) ranging from 0.09 and 0.60 (Table 2).

Table 2: Results of the XRF and ICPMS analyses. Eu* = $\sqrt{Sm_N \times Gd_N}$. Chondrite-normalized values after McDonough and Sun (1995).

Unit	Zaragoza Andesite			El Sombrero Ignimbrite				
Sample	EMA	LH3B	LH3A	ZATC21	ZATTC	ZATT	LHTT	LH3TR
Lat. N	23.14658°	23.12880°	23.07204°	23.07204°	23.07340°	23.07242°	23.04234°	23.13121°
Long W	101.8299°	101.8074°	101.7865°	101.7865°	101.7862°	101.7850°	101.7479°	101.8016°
SiO_2	54.23	54.41	55.07	70.2	70.14	70.78	71.91	70.98
TiO_2	1.14	1.83	1.79	0.41	0.33	0.49	0.21	0.18
Al_2O_3	15.56	14.91	14.97	13.38	13.18	13.08	12.93	12.17
Fe_2O_3	7.77	7.62	7.63	3.54	3.48	4.64	3.6	3.24
MnO	0.12	0.11	0.11	0.01	<0.007	<0.009	0.01	0.02
MgO	6.08	5.12	5.23	1.58	0.17	0.1	0.28	0.78
CaO	7.89	7.2	6.17	0.89	0.7	0.15	1.08	1.22
Na_2O	2.74	2.79	2.77	1.1	1.98	2.1	1.85	2.19
K_2O	1.98	2.51	2.73	4.77	4.84	5.51	4.66	5.01
P_2O_5	0.26	1.01	1.06	0.35	0.74	0.14	0.04	0.08
LOI	1.83	1.8	1.78	3.37	3.71	2.51	3.02	3.36
Total	99.6	99.32	99.31	99.6	99.26	99.5	99.6	99.22
Cs	1.12	3.61	3.42	3.89	12.63	4.33	4.24	10.83
Rb	48.41	113.01	140.79	65.89	244.88	118.59	252.4	234.03
K	8218	10418	11331	19799	20089	22870	19342	20795
Ba	2256.58	4567.96	4748.72	1184.35	901.69	365.3	1461.95	453.93
Sr	1226.83	2994.63	3899.23	645.8	480.36	177.55	242.71	111.69
Pb	15.78	27.51	28.57	6.46	13.6	4.43	5.57	13.8
Th	5.58	6.15	6.57	10.34	11.69	8.03	13.54	17.2
U	1.4	3.23	2.9	2.83	7.62	2.12	2.15	8.44
Zr	365.05	758.81	458.66	197.77	268.7	145.54	137.45	272.09
Hf	7.06	13.72	10.3	4.72	7.79	4.04	3.98	8.7
Ti	6832	10968	10728	2457	1977	2936	1258	1078
Ta	0.35	0.69	1.2	0.44	0.95	0.44	0.47	1.07
Y	24.33	41.22	46.54	36.1	74.1	20.02	21.97	74.99
Nb	14.01	29.74	24.49	13.71	30.03	14.41	33.18	29.79
Sc	18.64	16.77	42.07	4.93	7.99	6.12	7.37	8.35
Cr	262.19	99.41	161.72	10.83	4.35	22.59	24.99	4.6
Ni	67.58	32.22	51.78	6.82	1.29	1.44	14.27	2.79
Co	30.45	18.01	22.21	5.3	0.34	0.28	6.42	0.26
V	172.22	150.41	198.34	48.06	11.46	72.96	44.48	16.01
P	567	2203	2313	763	1614	305	87	174
La	29.85	70.67	78.47	21	101.97	49.72	140.21	88.27
Ce	65.44	181.78	165.34	65.83	202.66	64,83	324.61	174.64
Pr	7.28	19.04	23.28	7.76	20.98	6.99	38.73	1906
Nd	35.08	86.6	102.13	32.2	83.3	24.32	142.64	75.21
Sm	7.48	19.56	21.02	7.38	17.27	5.1	20.57	16.52
Eu	1.57	5.31	5.77	1.2	1	0.72	2.06	0.63
Gd	4.2	11.35	16.71	5.05	11.28	3.39	9.5	10.77
Tb	0.81	2.17	2.14	1.1	2.58	0.68	1.44	2.57
Dy	4.78	9.59	8.33	6.46	13.6	4.43	5.57	13.8
Ho	0.88	1.57	1.87	1.24	2.51	0.85	0.83	2.6
Er	2.57	4.32	4.37	3.76	7.72	2.53	2.38	8.07
Tm	0.38	0.55	0.56	0.55	1.06	0.39	0.26	1.13
Yb	2.37	3.35	3.45	3.54	6.55	2.26	1.33	7.27
Lu	0.31	0.43	0.49	0.47	0.81	0.28	0.16	0.93
$(La/Yb)_N$	8.574	14.333	15.466	4.031	10.572	14.926	71.486	8.245
$(Eu/Eu^*)_N$	0.917	1.087	0.938	0.602	0.218	0.675	0.449	0.144

Table 2: continued

Unit	El Sombrero Ignimbrite				
Sample	ZATC21	ZATTC	ZATT	LHTT	LH3TR
Lat. N	23.07204°	23.07340°	23.07242°	23.04234°	23.13121°
Long W	101.7865°	101.7862°	101.7850°	101.7479°	101.8016°
SiO_2	70.2	70.14	70.78	71.91	70.98
TiO_2	0.41	0.33	0.49	0.21	0.18
Al_2O_3	13.38	13.18	13.08	12.93	12.17
Fe_2O_3	3.54	3.48	4.64	3.6	3.24
MnO	0.01	<0.007	<0.009	0.01	0.02
MgO	1.58	0.17	0.1	0.28	0.78
CaO	0.89	0.7	0.15	1.08	1.22
Na_2O	1.1	1.98	2.1	1.85	2.19
K_2O	4.77	4.84	5.51	4.66	5.01
P_2O_5	0.35	0.74	0.14	0.04	0.08
LOI	3.37	3.71	2.51	3.02	3.36
Total	99.6	99.26	99.5	99.6	99.22
Cs	3.89	12.63	4.33	4.24	10.83
Rb	65.89	244.88	118.59	252.4	234.03
K	19799	20089	22870	19342	20795
Ba	1184.35	901.69	365.3	1461.95	453.93
Sr	645.8	480.36	177.55	242.71	111.69
Pb	6.46	13.6	4.43	5.57	13.8
Th	10.34	11.69	8.03	13.54	17.2
U	2.83	7.62	2.12	2.15	8.44
Zr	197.77	268.7	145.54	137.45	272.09
Hf	4.72	7.79	4.04	3.98	8.7
Ti	2457	1977	2936	1258	1078
Ta	0.44	0.95	0.44	0.47	1.07
Y	36.1	74.1	20.02	21.97	74.99
Nb	13.71	30.03	14.41	33.18	29.79
Sc	4.93	7.99	6.12	7.37	8.35
Cr	10.83	4.35	22.59	24.99	4.6
Ni	6.82	1.29	1.44	14.27	2.79
Co	5.3	0.34	0.28	6.42	0.26
V	48.06	11.46	72.96	44.48	16.01
P	763	1614	305	87	174
La	21	101.97	49.72	140.21	88.27
Ce	65.83	202.66	64,83	324.61	174.64
Pr	7.76	20.98	6.99	38.73	1906
Nd	32.2	83.3	24.32	142.64	75.21
Sm	7.38	17.27	5.1	20.57	16.52
Eu	1.2	1	0.72	2.06	0.63
Gd	5.05	11.28	3.39	9.5	10.77
Tb	1.1	2.58	0.68	1.44	2.57
Dy	6.46	13.6	4.43	5.57	13.8
Ho	1.24	2.51	0.85	0.83	2.6
Er	3.76	7.72	2.53	2.38	8.07
Tm	0.55	1.06	0.39	0.26	1.13
Yb	3.54	6.55	2.26	1.33	7.27
Lu	0.47	0.81	0.28	0.16	0.93
$(La/Yb)_N$	4.031	10.572	14.926	71.486	8.245
$(Eu/Eu^*)_N$	0.602	0.218	0.675	0.449	0.144

Compared to the La Herradura Rhyolite and the Zaragoza Andesite, the El Sombrero Ignimbrite show strong differences in the HREE. In addition, the negative anomalies in Sr and Eu are consistent with plagioclase fractionation during differentiation, while similar negative anomalies in Ti and P can be due to iron oxides and apatite fractionation, respectively. The samples of the Zaragoza andesite show no Eu anomalies with $(Eu/Eu^*)_N$ between 0.92 and 1.09. Moderate REE fractionation patterns is evident as well for most samples, and slightly higher ones for those from the Zaragoza andesite ($8.57 \leq (La/Yb)_N \leq 15.47$; Figure 14).

4.4.3. Mineral Chemistry

EPMA were performed to determine the end-member composition of plagioclases, pyroxenes, amphiboles, and garnet.

Plagioclases from El Sombrero Ignimbrite have a representative composition of Oligoclase to Andesine (An = 19.59 – 41.54%, Appendix B 1 - Appendix B 3, Figure 15 a). The orthoclase component is in between 3.76 and 12.17 %. Alkali feldspars are mostly Sanidine with an orthoclase component ranging from 59.65 to 68.42 %. All analyzed pyroxenes (Figure 15 b, Appendix C 1 - Appendix C 3) are augites. Compared to the pyroxenes of the Zaragoza Andesite, analyzed during this study, they contain more Fe and less Mg (molar magnesium numbers Mg# = 0.22 – 0.26).

The plagioclases of the La Herradura Rhyolite have an average andesine composition with an anorthite content in between 34.34 and 48.23 %. The orthoclase component lies between 3.41 and 6.49 %. All alkali feldspars of the rhyolite are sanidines, with higher orthoclase component (Or = 66.32 – 80.39 %) similar to sanidine from El Sombrero Ignimbrite. The analyzed pyroxenes are all ferrosilite with molar magnesium numbers slightly higher compared to the El Sombrero Ignimbrite (Mg# = 0.24 – 0.29). The composition of garnets from the La Herradura Rhyolite is shown in Table 3. All studied garnets consist of almandine (Figure 16; X_{alm} = 78.828 – 82.922 %), pyrope (X_{pyr} = 10.225 – 14.022 %), grossular (X_{gr} = 3.489 – 4.422 %), spessartine (X_{spess} = 2.489 – 3.340 %), and andradite (X_{and} = 0.019 – 0,249 %). Garnet grains are homogeneous and do not show significant chemical zoning.

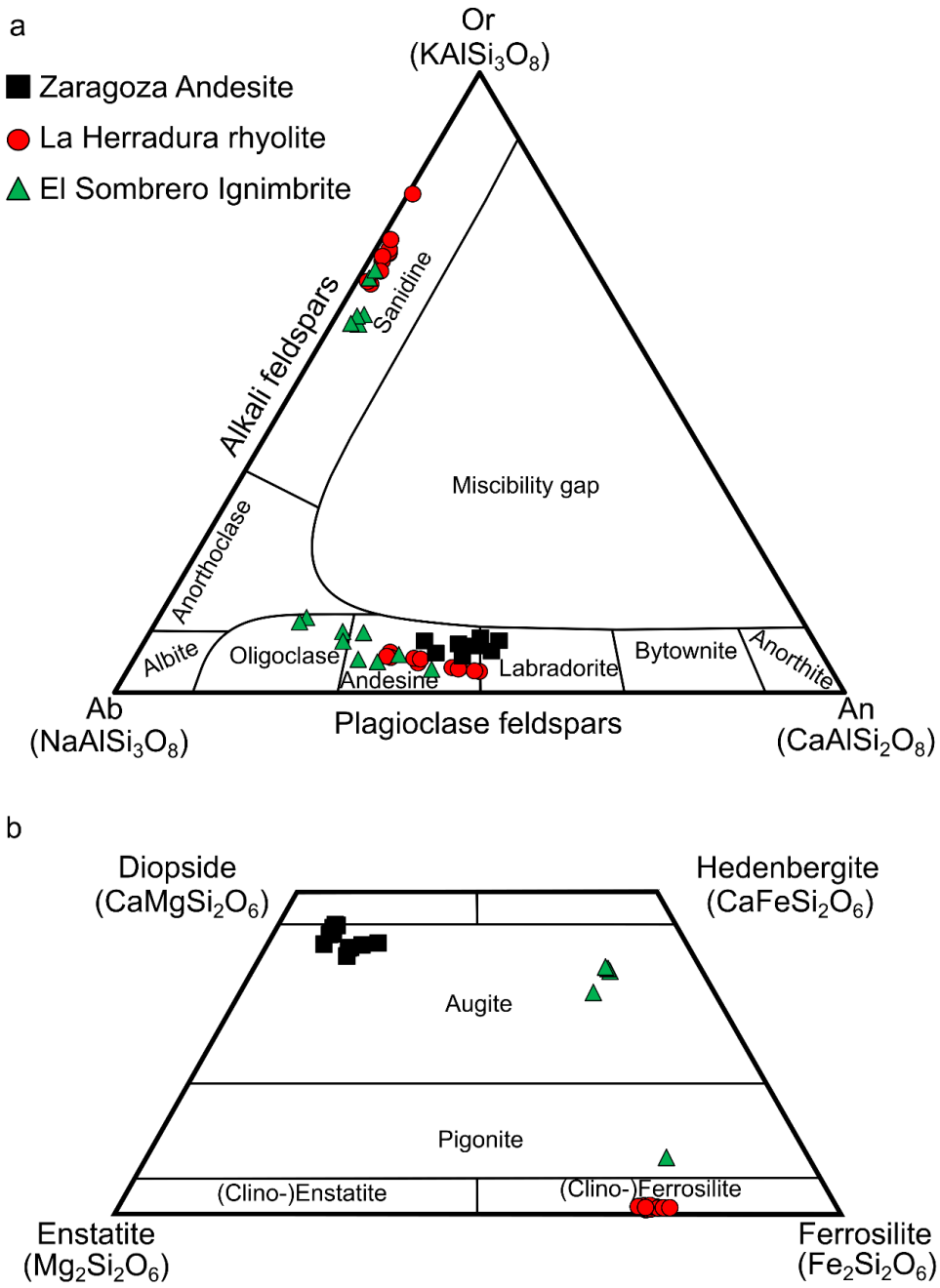

Figure 15: EPMA results of feldspars and pyroxenes. a) Ternary classification of feldspars from the La Herradura area. b) Classification of pyroxenes from the La Herradura area in the quaternary Ca-Fe-Mg-system after Morimoto (1988).

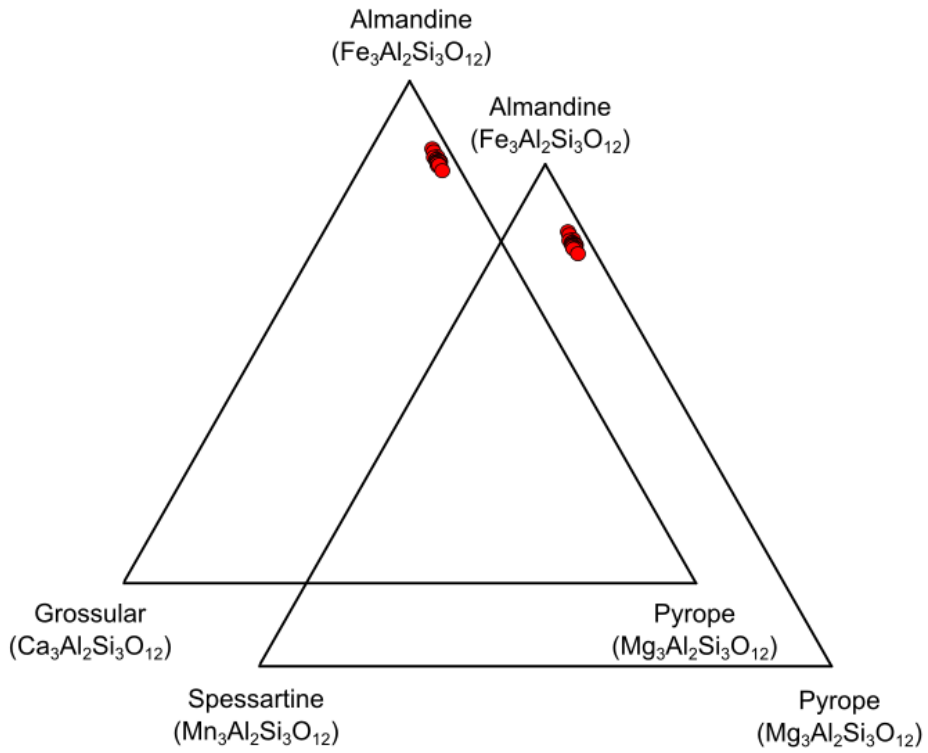

Figure 16: Ternary classification diagrams for garnets from the garnet-bearing La Herradura Rhyolite.

In addition, EPMA were performed to determine the end-member composition of plagioclases, pyroxenes, and amphiboles on the Zaragoza Andesite. Plagioclase crystals show an average composition of andesine to labradorite (anorthite (An) = 38.30 – 48.40%). The orthoclase component is generally in between 5.90 and 8.85. For pyroxenes, an average augite to slightly diopside composition was determined. The molar magnesium number (Mg#) of the pyroxenes ranges between 0.74 and 0.90. Amphiboles (Appendix D 1) show very high Al^{iv} (2.276 – 2.727) and furthermore a distinctive optical birefringence characteristic of high Fe or Mg contents. The molar magnesium numbers are in between 0.67 – 0.85. Black reaction rims (<15 µm) are developed around all amphibole crystals. In general, they consist of opaque phases, pyroxenes and glass.

Table 3: Representative chemical compositions of garnets from the garnet-bearing La Herradura Rhyolite.

Sample	ZA4R									
	Grt01		Grt02		Grt03		Grt04		Grt05	
	core	rim	core	rim	core	rim	core	rim	core	rim
SiO_2	37.12	36.82	37.00	36.99	37.24	37.07	36.75	36.79	37.08	37.16
TiO_2	0.04	0.06	0.02	0.05	0.02	0.06	0.03	0.08	0.10	0.10
Al_2O_3	20.02	19.82	20.65	20.68	20.11	20.55	20.14	19.60	19.90	20.63
Cr_2O_3	0.01	0.04	0.04	0.05	0.05		0.03	0.03	0.01	
FeO	37.14	36.57	36.35	35.70	36.61	36.14	36.39	37.05	36.85	36.49
MnO	1.20	1.31	1.28	1.40	1.32	1.20	1.35	1.16	1.44	1.09
MgO	3.16	3.20	2.99	2.79	3.27	3.11	3.01	3.14	3.11	2.96
CaO	1.47	1.52	1.45	1.52	1.54	1.47	1.46	1.39	1.49	1.55
Total	100.14	99.34	99.77	99.17	100.15	99.60	99.16	99.24	99.96	99.99
Cations based on 12 oxygens										
Si	2.997	2.995	2.994	3.012	3.002	3.002	2.995	3.000	3.000	3.001
Ti	0.002	0.004	0.001	0.003	0.001	0.004	0.002	0.005	0.006	0.006
Al	1.905	1.900	1.969	1.984	1.911	1.961	1.935	1.883	1.897	1.963
Cr	0.001	0.002	0.002	0.003	0.003		0.002	0.002		
Fe^{3+}	0.097	0.100	0.038		0.080	0.026	0.069	0.105	0.090	0.023
Fe^{2+}	2.410	2.388	2.421	2.431	2.388	2.421	2.411	2.422	2.403	2.441
Mn	0.082	0.091	0.088	0.096	0.090	0.082	0.093	0.080	0.099	0.075
Mg	0.380	0.387	0.360	0.338	0.393	0.375	0.365	0.382	0.375	0.356
Ca	0.127	0.133	0.126	0.133	0.133	0.128	0.128	0.122	0.129	0.134
Mole fraction end-members in %										
X_{alm}	80.377	79.643	80.849	81.081	79.522	80.557	80.448	80.600	79.969	81.210
X_{pyr}	12.670	12.922	12.028	11.284	13.077	12.475	12.187	12.704	12.474	11.857
X_{gr}	4.023	4.197	4.110	4.422	4.234	4.182	4.110	3.818	4.081	4.393
X_{spess}	2.725	3.019	2.934	3.214	2.990	2.729	3.108	2.666	3.281	2.489
X_{and}	0.205	0.220	0.080		0.177	0.056	0.147	0.212	0.195	0.051

Table 3: continued

Sample	LH5R									
	Grt01		Grt02		Grt03		Grt04		Grt05	
	core	rim	core	rim	core	rim	core	rim	core	rim
SiO_2	36.85	37.18	37.04	37.02	36.84	36.80	37.15	37.25	36.99	37.23
TiO_2	0.03	0.08	0.02	0.04	0.05	0.02	0.05	0.05	0.12	0.06
Al_2O_3	19.84	19.80	20.75	20.26	20.11	20.59	19.89	20.24	19.95	20.32
Cr_2O_3	0.02		0.03		0.01				0.01	0.02
FeO	36.71	36.99	36.91	36.73	36.62	36.12	36.61	36.90	36.73	36.68
MnO	1.32	1.29	1.16	1.29	1.33	1.17	1.34	1.38	1.46	1.11
MgO	3.10	3.26	2.54	3.08	2.94	2.64	3.50	3.07	3.20	3.19
CaO	1.60	1.57	1.46	1.35	1.54	1.35	1.42	1.56	1.26	1.59
Total	99.45	100.16	99.91	99.77	99.44	98.69	99.96	100.44	99.73	100.20
Cations based on 12 oxygens										
Si	2.995	3.001	3.000	2.998	2.996	3.015	2.999	2.998	2.998	2.999
Ti	0.002	0.002	0.005	0.002	0.003	0.001	0.003	0.003	0.007	0.003
Al	1.901	1.884	1.980	1.934	1.927	1.988	1.892	1.920	1.906	1.929
Cr	0.001		0.002		0.001				0.001	0.001
Fe^{3+}	0.104	0.110	0.009	0.065	0.074		0.105	0.078	0.081	0.066
Fe^{2+}	2.392	2.387	2.491	2.423	2.416	2.474	2.366	2.405	2.409	2.405
Mn	0.091	0.088	0.080	0.089	0.092	0.081	0.092	0.094	0.100	0.076
Mg	0.375	0.392	0.307	0.372	0.357	0.322	0.421	0.368	0.387	0.384
Ca	0.140	0.136	0.127	0.117	0.134	0.119	0.123	0.134	0.110	0.137
Mole fraction end-members in %										
X_{alm}	79.804	79.500	82.922	80.748	80.580	82.594	78.828	80.138	80.140	80.132
X_{pyr}	12.524	13.053	10.225	12.406	11.902	10.750	14.022	12.262	12.883	12.776
X_{gr}	4.409	4.264	4.179	3.762	4.295	3.958	3.881	4.292	3.489	4.419
X_{spess}	3.021	2.935	2.656	2.958	3.057	2.698	3.054	3.133	3.340	2.523
X_{and}	0.241	0.249	0.019	0.127	0.166		0.215	0.175	0.149	0.150

4.4.4. Rhyolite-MELTS crystallization models

Geochemical modeling of the volcanic rocks from the La Herradura area was carried out using rhyolite-Melts (Gualda et al., 2012). The aim in using the rhyolite-MELTS simulations is not to model in detail the crystallization of La Herradura volcanic rocks, but rather to obtain important information on over which crystallization can take place and which minerals can crystallize from the magmas that originated the La Herradura volcanic rocks. Isobaric simulations were run with variable initial water contents between 0.25 and 1.00 wt.% for the andesitic magmas and between 2.00 and 7.00 wt.% for the rhyolitic magmas to explore a wide range of crystallization conditions. The crystallization pressure of the rhyolitic magmas is constrained to be 7 kbar or higher considering that garnet can crystallize at these pressures (Green and Ringwood, 1968, 1972; Wood, 1974; Green, 1992; Harangi et al., 2001). Crystallization models of the Zaragoza Andesite were carried out with the pressure condition (8 kbar) described for the lower crust and upper mantle for San Luis Potosí (Schaaf et al., 1994), assuming an uppermost mantle origin for the andesitic magma as described in Aguillón-Robles et al. (2014) for the origin of the mafic magmas (31.2 ± 0.7 Ma) associated to bimodal volcanism from the nearby San Luis Potosí Volcanic Field.

Rhyolite-MELTS simulations with the rhyolitic lavas from the La Herradura area (ZATT, El Sombrero Ignimbrite; LH5R, La Herradura Rhyolite) reveal nearly similar results as the mineral assemblage present in the rocks. The simulations show that garnet can crystallize from rhyolitic magmas at pressures of ≥ 7 kbar, but compared to the EPMA results (Table 3, 78.8 - 82.9 wt.% almandine), the simulated almandine content is higher (~ 85 wt.% almandine, Appendix E). The mineral assemblage and mineral composition are the same for all investigated total water contents (2, 3, 5 and 7 wt.% H_2O). Liquidus temperatures decrease with increasing total water (Figure 17 a and b), directly controlling the range of temperature over which crystallization can take place. In addition, the simulations for the El Sombrero Ignimbrite reveals that garnet could have crystallized from these magmas at higher pressures (≥ 7 kbar) and became unstable at lower pressures (≤ 7 kbar), simulating a storage in a shallow magma chamber.

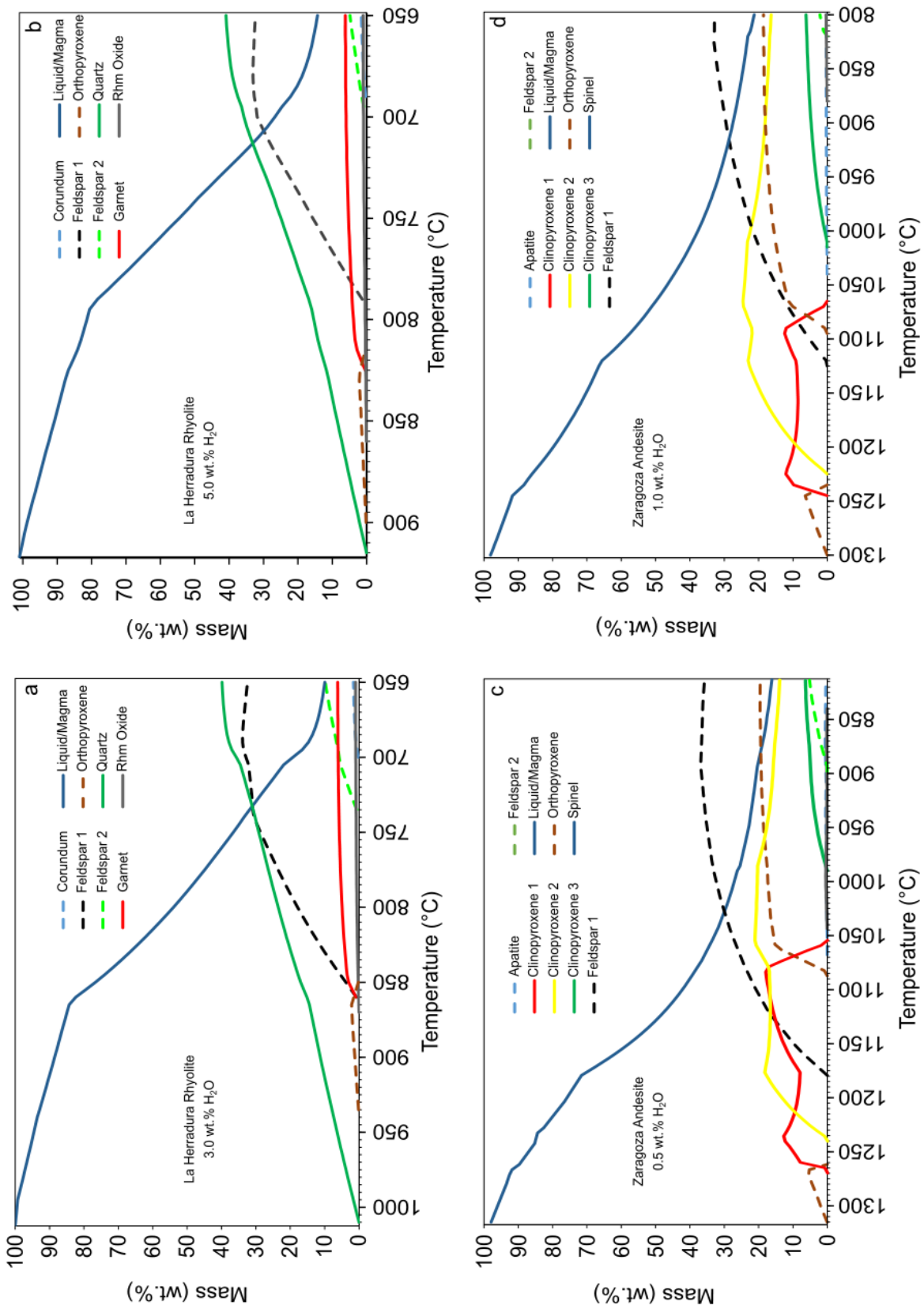
a
La Herradura Rhyolite
3.0 wt.% H2O
Corundum
Feldspar 1
Feldspar 2
Garnet
Liquid/Magma
Orthopyroxene
Quartz
Rhm Oxide
b
La Herradura Rhyolite
5.0 wt.% H2O
c
Zaragoza Andesite
0.5 wt.% H2O
Apatite
Clinopyroxene 1
Clinopyroxene 2
Clinopyroxene 3
Feldspar 1
Feldspar 2
Liquid/Magma
Orthopyroxene
Spinel
d
Zaragoza Andesite
1.0 wt.% H2O
Mass (wt.%)
Temperature (°C)

Figure 17: Rhyolite-MELTS crystallization models for the La Herradura rhyolite and the Zaragoza Andesite. a) Crystallization model of the La Herradura Rhyolite containing 3.0 wt.% H_2O. b) Crystallization model of the La Herradura Rhyolite containing 5.0 wt.% H_2O. c) Crystallization model of the Zaragoza Andesite containing 0.5 wt.% H_2O. d) Crystallization model of the Zaragoza Andesite containing 1.0 wt.% H_2O.

Simulations on the crystallization of the andesitic magmas of the La Herradura area show different results compared to the mineral assemblage in the rock. For all investigated water contents (0.25, 0.50, 0.75 and 1.00 wt.% H_2O) amphiboles rich in Ti and Mg, like in the Zaragoza Andesite, cannot crystallize from these magmas. Both, plagioclase and pyroxene, crystallize in the simulations from the magma with decreasing temperature. Pyroxene become unstable during crystallization in the simulations, resulting a replacement of pyroxenes with different compositions (Figure 17 c and d). At lower temperatures (e.g. > 900 °C for 0.5 wt.% H_2O) K-feldspar, that are not present in the mineral assemblage, crystallize from the andesitic magmas. Similar to the simulations of the rhyolitic magmas the liquidus temperatures decrease with increasing total water content, directly controlling the range of temperature over which crystallization can take place.

4.4.5. Formation temperature of La Herradura volcanic rocks

Formation temperature of the rhyolitic volcanic rocks of La Herradura was carried out using two-feldspar thermometer after Putirka (2008). Therefore, transects from the alkali feldspars through the plagioclase inclusions within and in case of intergrowth from alkali feldspar to plagioclase were measured. Two samples from the El Sombrero Ignimbrite and three samples of the La Herradura rhyolite were analyzed. The crystallization pressure of the rhyolitic magmas is constrained to be 7 kbar or higher considering that garnet can crystallize at these pressures (Green and Ringwood, 1968, 1972; Wood, 1974; Green, 1992; Harangi et al., 2001). The calculations were carried out using the Excel worksheet presented by Hora et al. (2013). For the El Sombrero Ignimbrite temperatures between 837 ± 43 °C and 920 ± 53 °C (Appendix F 1 - Appendix F 4) garnet-bearing La Herradura Rhyolite temperatures between 807 ± 50 °C and 1024 ± 53 °C (Appendix F 5 - Appendix F 10).

4.4.6. Geothermobarometric constrains on the crystallization of almandine garnets from the La Herradura Rhyolite

Garnet crystals from two samples of the garnet-bearing La Herradura Rhyolite (LH5R and ZA4R) were separated and analyzed to determine the formation pressure and temperature. Table 4 shows

the results of the formation temperature and pressure from the almandine garnets from the garnet-bearing La Herradura Rhyolite.

Table 4: Results of the determination of the formation pressure and temperature of almandine garnets from the garnet-bearing La Herradura Rhyolite.

Sample	Analyzed mineral pair	T (°C)	2 σ error (°C)	P (kbar)	2 σ error (kbar)
LH5R_Line1	Ilm08-Grt01	775	45	7.698	1.752
LH5R_Line2	Ilm16-Grt01	854	50	10.436	2.057
LH5R_Line3	Ilm11-Grt01	775	43	7.715	1.754
ZA4R_Line1	Ilm01-Grt03	807	45	8.991	1.867
ZA4R_Line1	Ilm02-Grt04	702	43	5.785	1.488
ZA4R_Line2	Ilm04-Grt01	886	55	11.887	2.181
ZA4R_Line3	Ilm01-Grt01	712	44	6.051	1.521

Formation temperature of the almandine crystals were determined using the garnet-ilmenite cation exchange thermometer (see chapter 3.4.3. Garnet-ilmenite cation exchange thermometer). Temperatures were calculated for mineral pairs of ilmenite and garnet (Figure 18) close to the contact to each other, assuming that the minerals are in equilibrium at the direct contact to each other. For the sample LH4R temperatures between 775 ± 45 °C and 854 ± 50°C (Table 4) and for the sample ZA4R temperatures 702 ± 43 °C and 886 ± 55°C were calculated (Appendix G 1 - Appendix G 12). Formation pressures were calculated using the apatite in garnet geobarometer after Ashley et al. (2017). Therefore, the Raman spectra of exposed apatite from the surface of the garnet and fully in garnet encapsulated apatite were measured in order to determine $\Delta\nu_{964}$, the shift of the Raman band at ca. 964 cm^{-1}. The $\Delta\nu_{964}$ was calculated individually for both samples from the Raman spectra analysis of each sample. The results of the measurements are shown in Appendix H. For the sample LH5R a maximum $\Delta\nu_{964}$ of 1.028 cm^{-1} and for the sample ZA4R maximum $\Delta\nu_{964}$ of 1.129 cm^{-1} was determined. The resulting formation pressures calculated with the temperatures from the garnet-ilmenite cation exchange thermometer yielded in pressures between 7698 ± 1752 bar and 10436 ± 2057 bar for the almandines from the sample LH5R and 5785 ± 1488 bar and 11887 ± 2181 bar for the sample ZA4R.

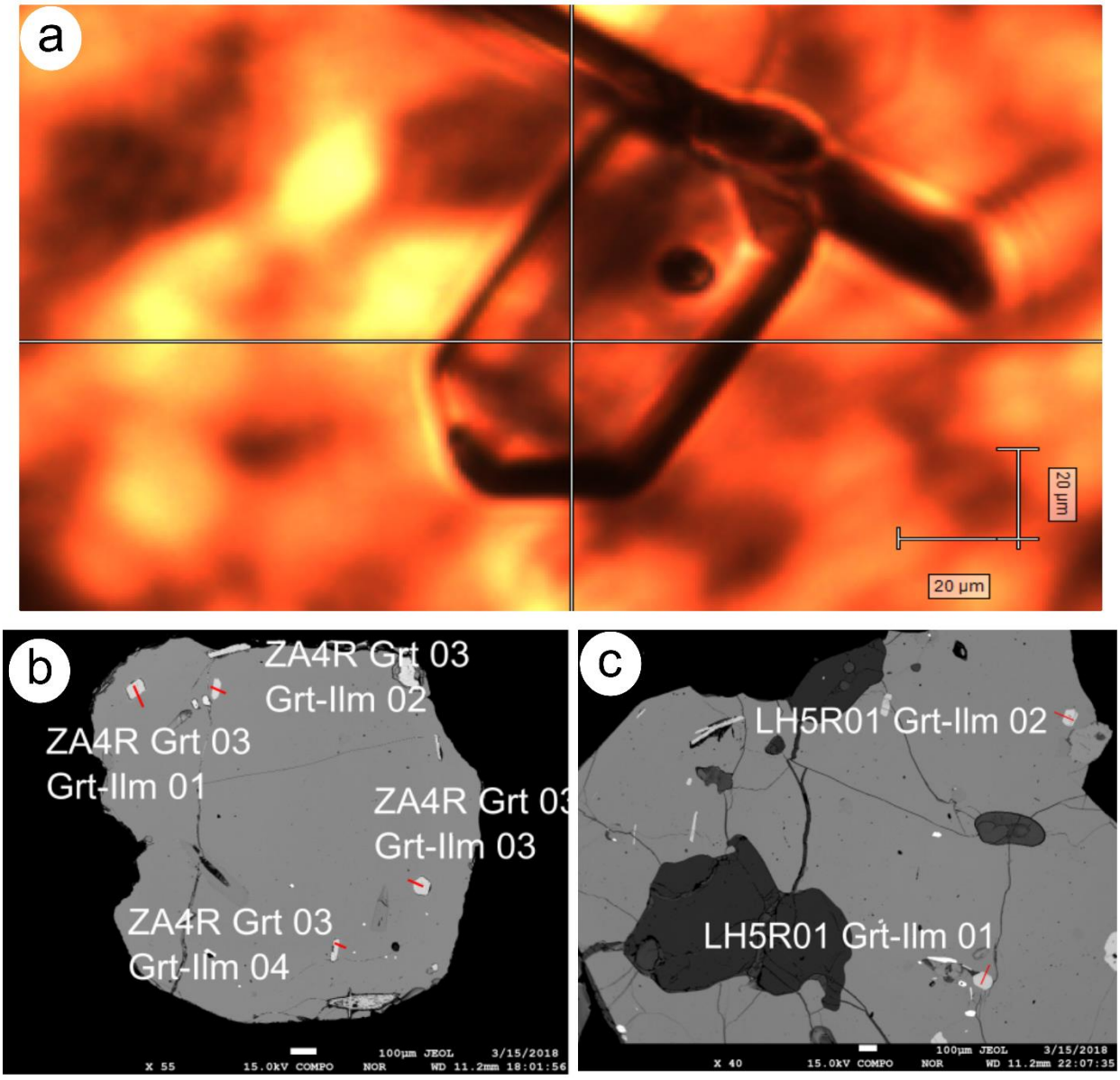

Figure 18: a) Apatite inclusion in garnet analyzed by Raman spectroscopy b) and c) Analyzed ilmenite inclusions in garnet by EPMA.

4.4.7. Geochronology

Geochronological data are summarized in Figure 19: Summary of the results of the U-Pb zircon crystallization ages and K-Ar eruption ages from the studied rocks. Results are shown with uncertainties. Figure 19 (a). In all samples, cathodoluminescence images (Figure 19) display zircons that are dominantly prismatic and exhibit oscillatory zoning, pointing to a magmatic origin. Cores showing oscillatory or sector zoning are locally observed as well.

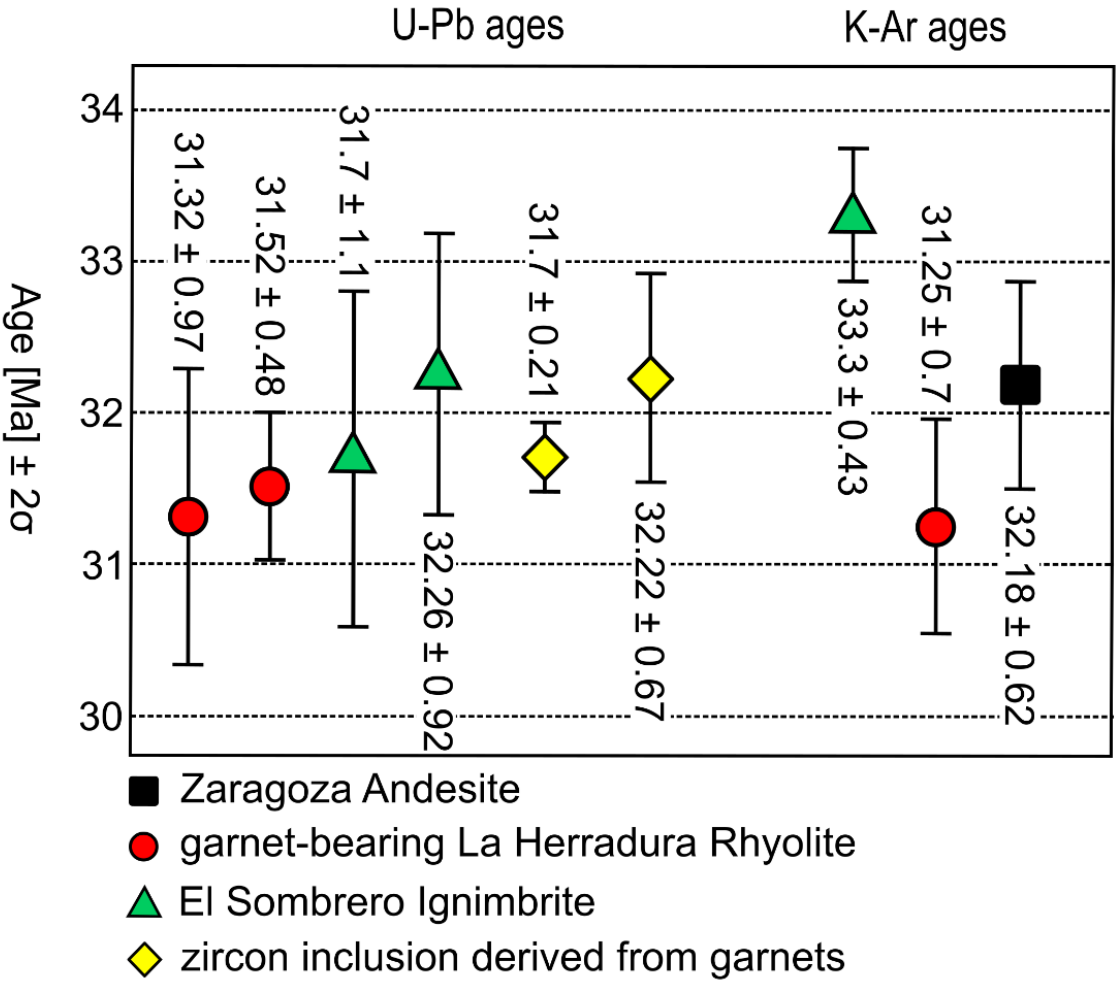

Figure 19: Summary of the results of the U-Pb zircon crystallization ages and K-Ar eruption ages from the studied rocks. Results are shown with uncertainties.

Crystallization ages within the range of ca. 32.26-31.32 Ma were obtained for all samples. Ages of 31.32 ± 0.97 (n=15, MWSD=4.6; LHVT; see Figure 20 and Appendix I 1) and 31.52 ± 0.48 Ma (n=11, MWSD=0.67; ZARTO; Figure 21 and Appendix I 2) were calculated for the samples of the garnet-bearing La Herradura rhyolite in the southern and central part of the study area and ages of 32.26 ± 0.92 Ma (n=25, MWSD=1.3; ZATT; see Figure 22 and Appendix I 3) and 31.7 ± 1.1 Ma (n=21, MWSD=6.4; LH3TR; see Figure 23 and Appendix I 4) for the El Sombrero Ignimbrite.

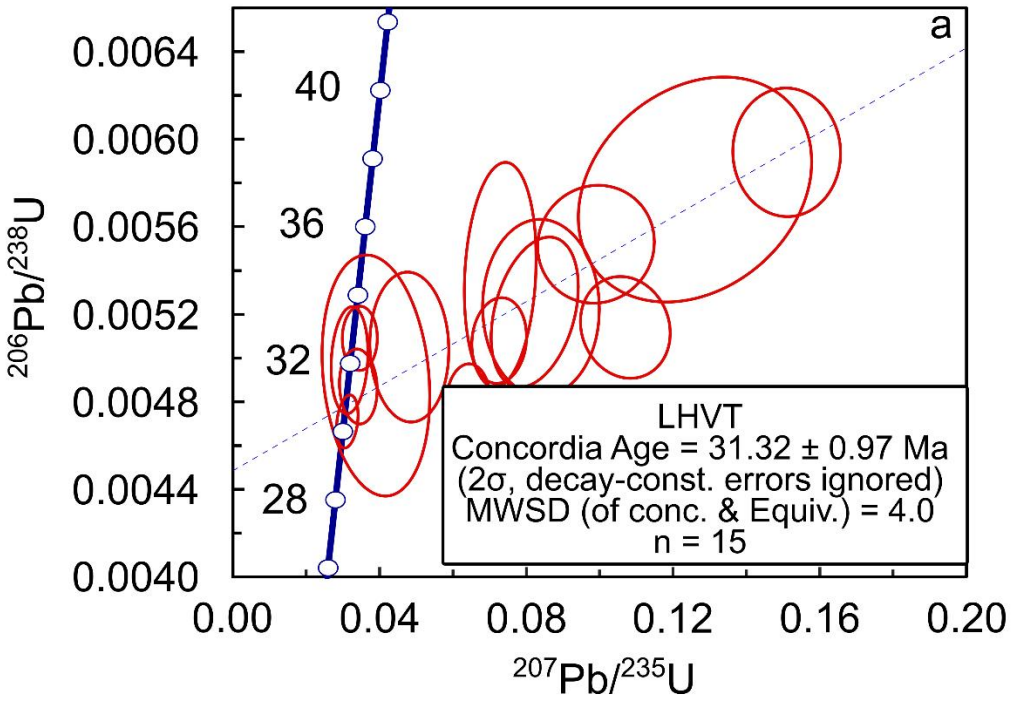

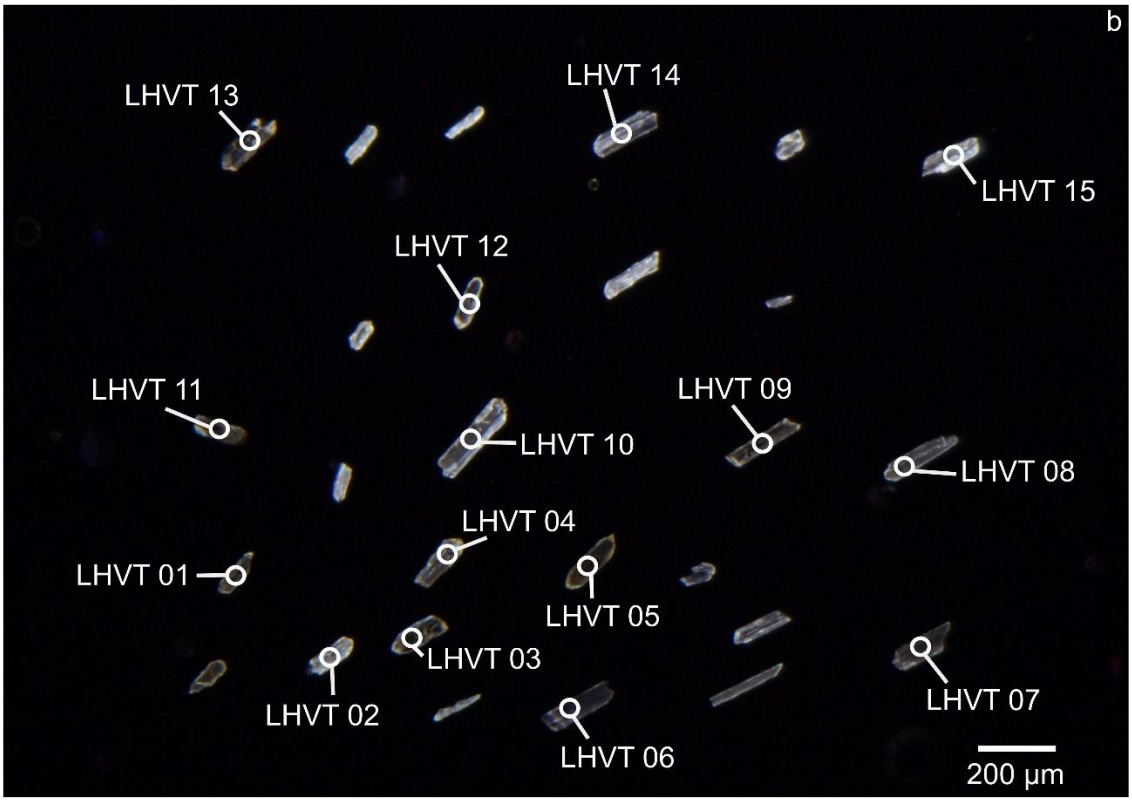

Figure 20: Concordia diagram and cathodoluminescence images of zircons form the sample LHVT. a) U-Pb diagrams. Red ellipses indicate data used for age calculations and concordia age, respectively. Errors depicted at the 2σ level. b) Cathodoluminescence images of analyzed zircons of the sample LHVT. Analytical data are presented in Appendix I 1.

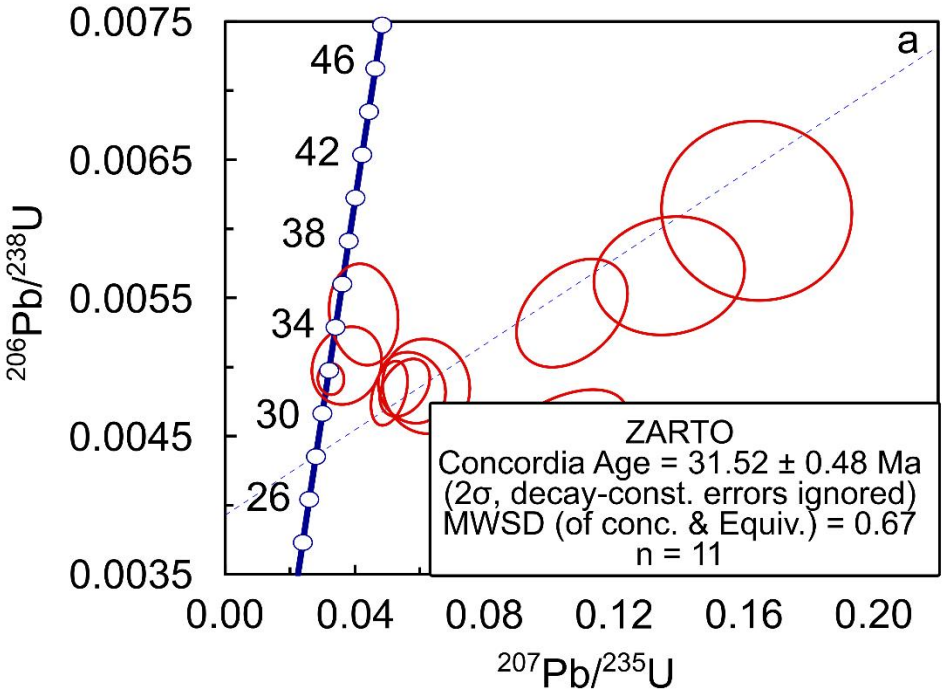

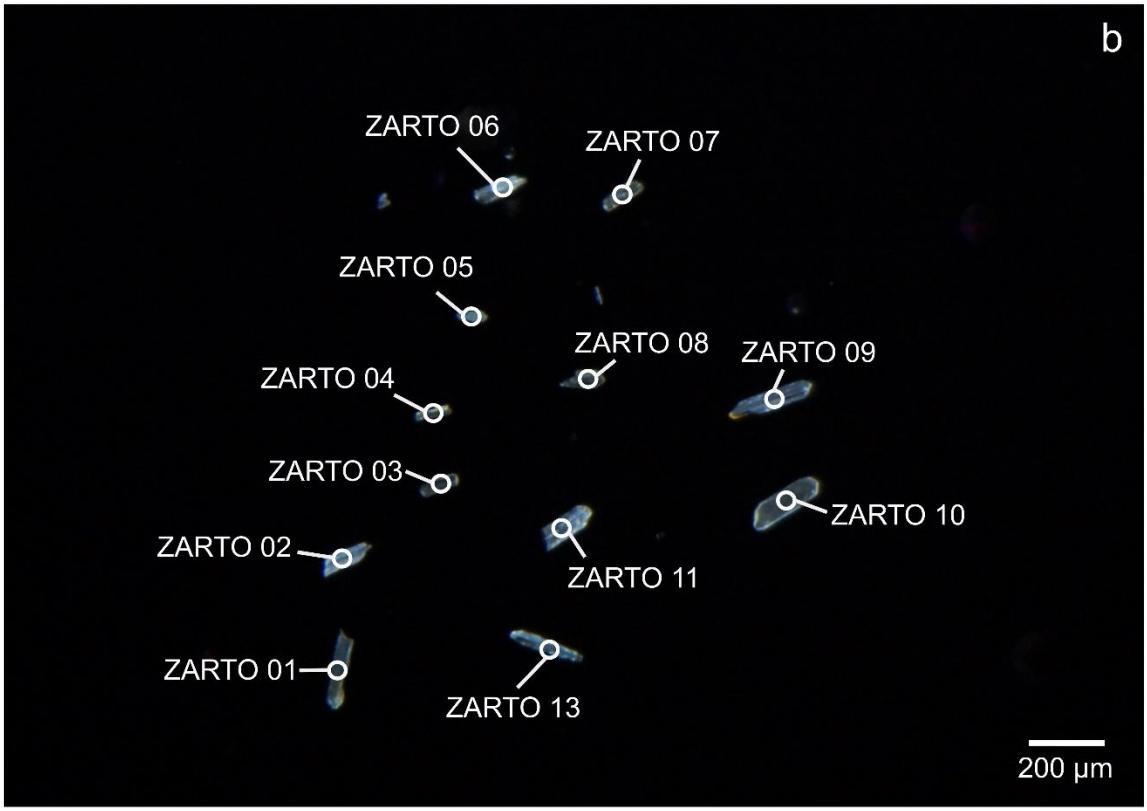

Figure 21: Concordia diagram and cathodoluminescence images of zircons form the sample ZARTO. a) U-Pb diagrams. Red ellipses indicate data used for age calculations and concordia age, respectively. Errors depicted at the 2σ level. b) Cathodoluminescence images of analyzed zircons of the sample ZARTO. Analytical data are presented in Appendix I 2.

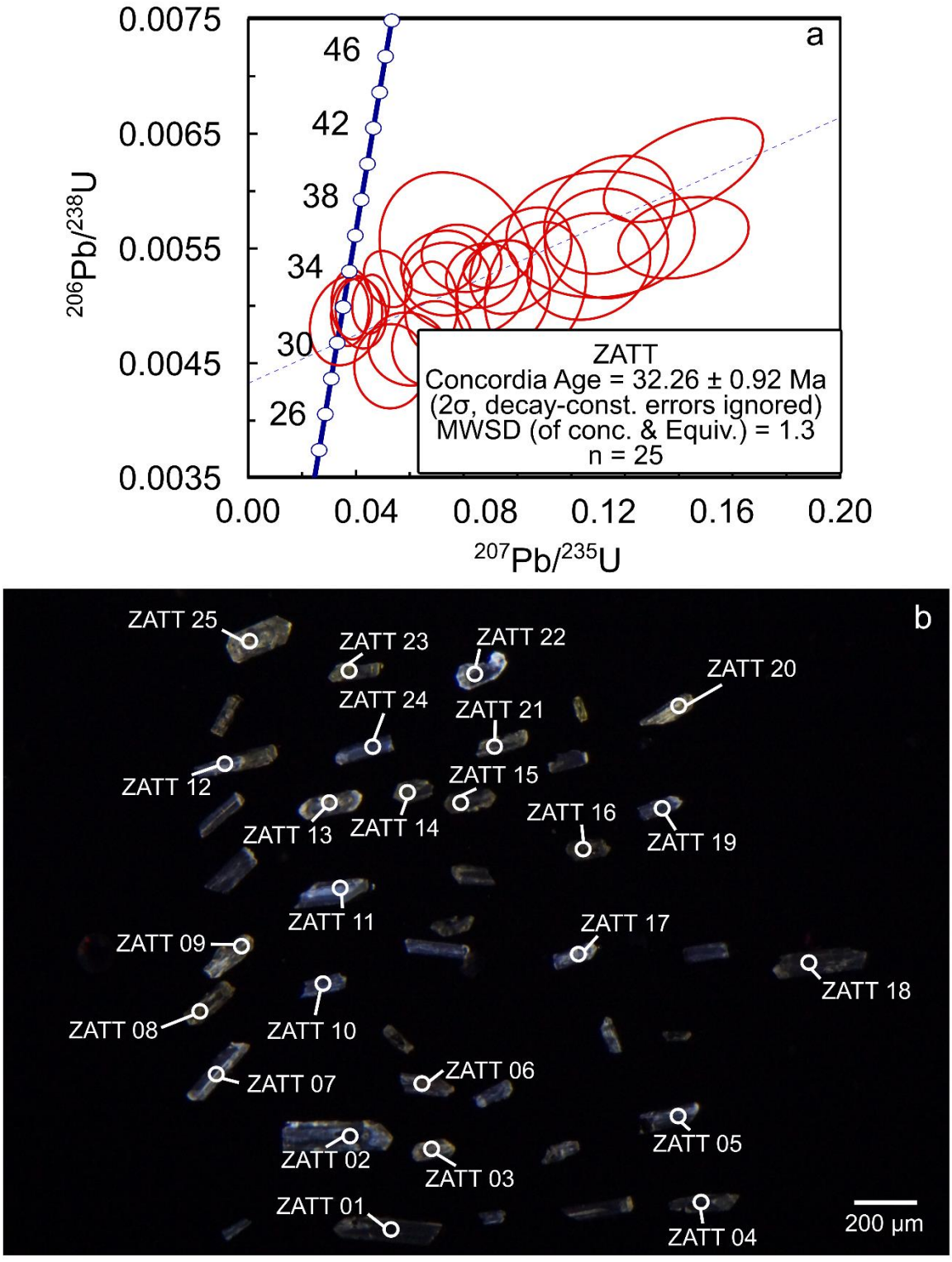

Figure 22: Concordia diagram and cathodoluminescence images of zircons form the sample ZATT. a) U-Pb diagrams. Red ellipses indicate data used for age calculations and concordia age, respectively. Errors depicted at the 2σ level. b) Cathodoluminescence images of analyzed zircons of the sample ZATT. Analytical data are presented in Appendix I 3.

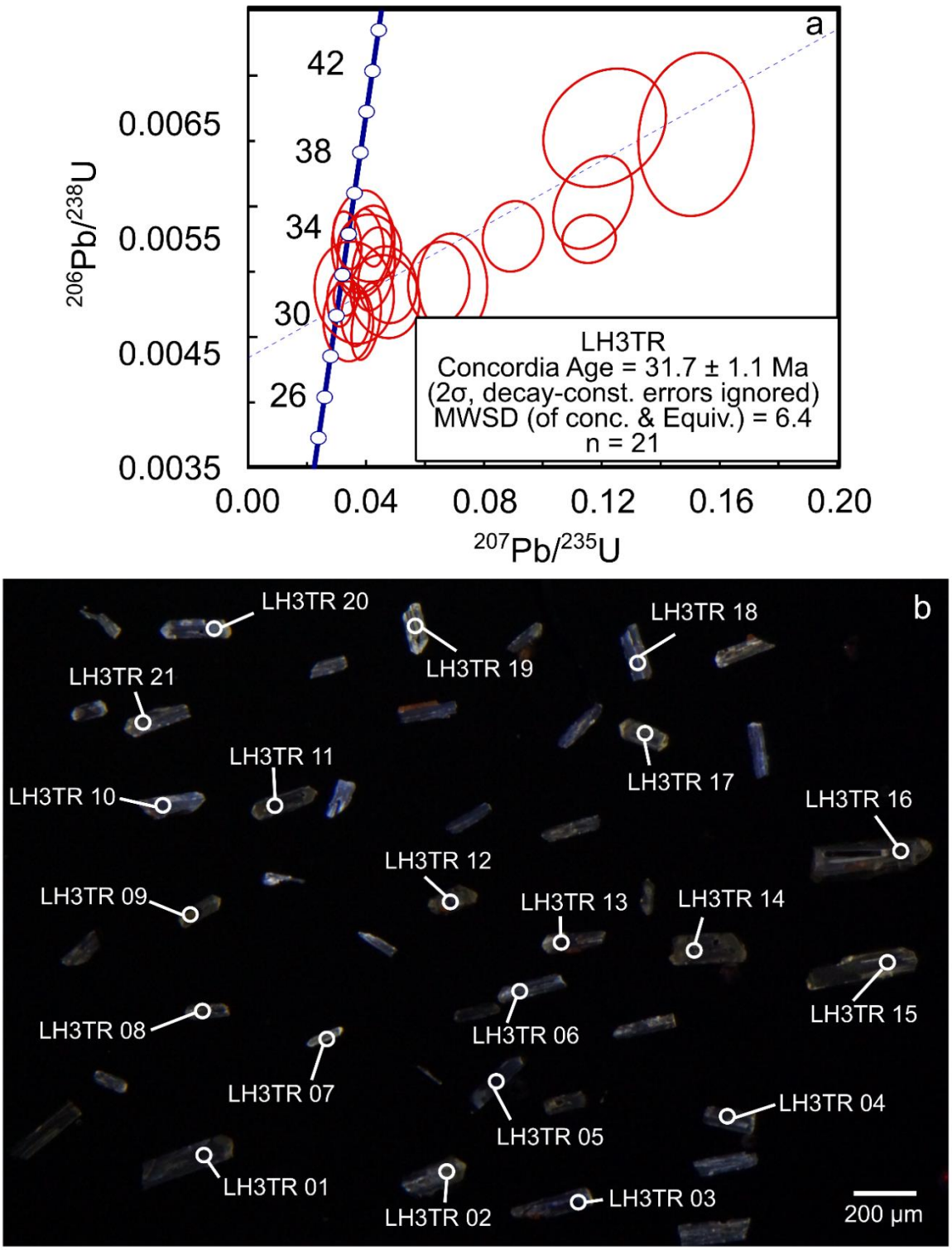

Figure 23: Concordia diagram and cathodoluminescence images of zircons form the sample LH3TR. a) U-Pb diagrams. Red ellipses indicate data used for age calculations and concordia age, respectively. Errors depicted at the 2σ level. b) Cathodoluminescence images of analyzed zircons of the sample LH3TR. Analytical data are presented in Appendix I 4.

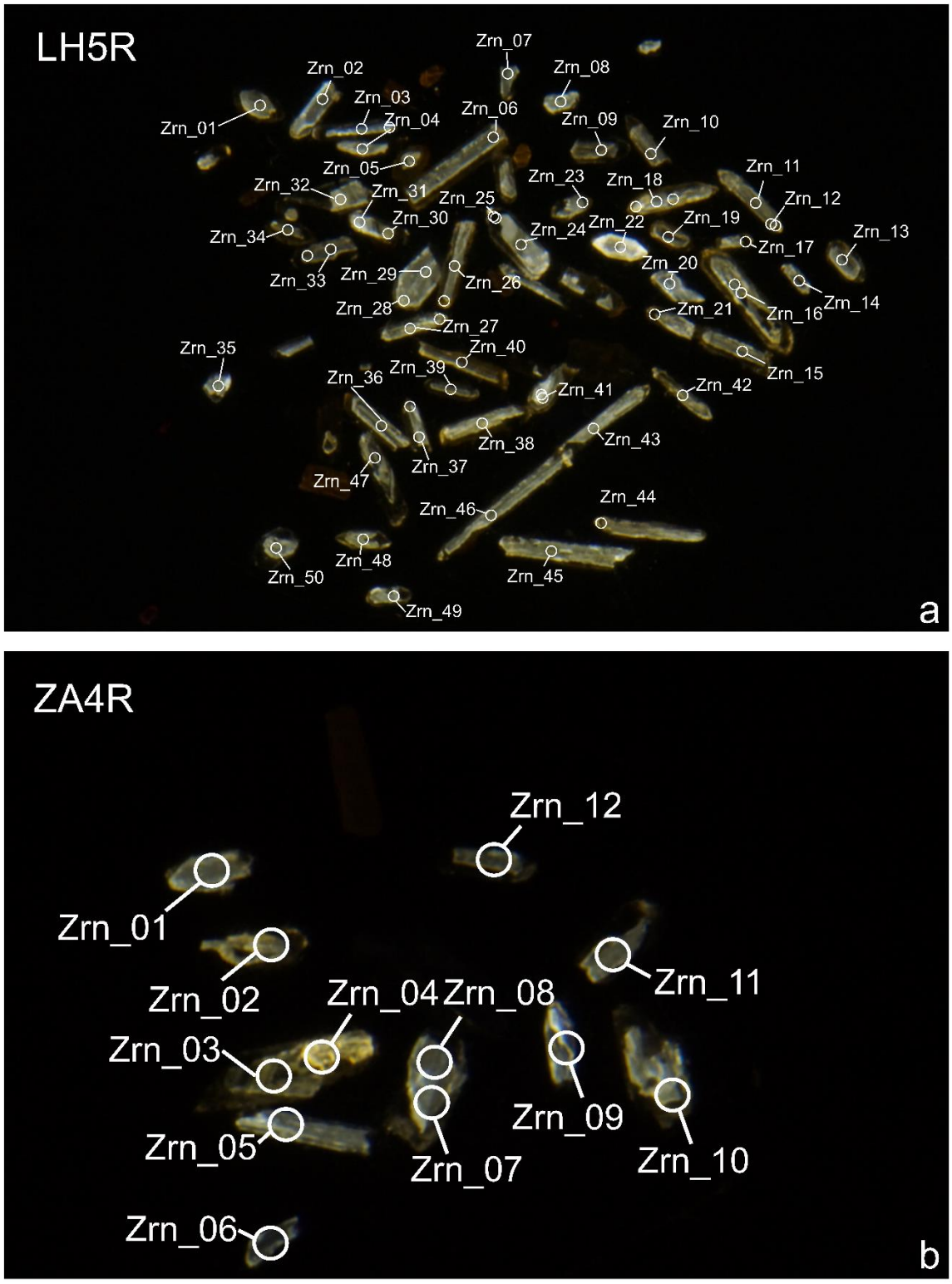

Figure 24: Cathodoluminescence images of analyzed zircons derived from garnets. a) Sample LH5R, Zrn_01 – Zrn_50 corresponds to the analytical data shown in Appendix I 5. b) Sample ZA4R, Zrn_01 – Zrn_50 corresponds to the analytical data shown in Appendix I 6.

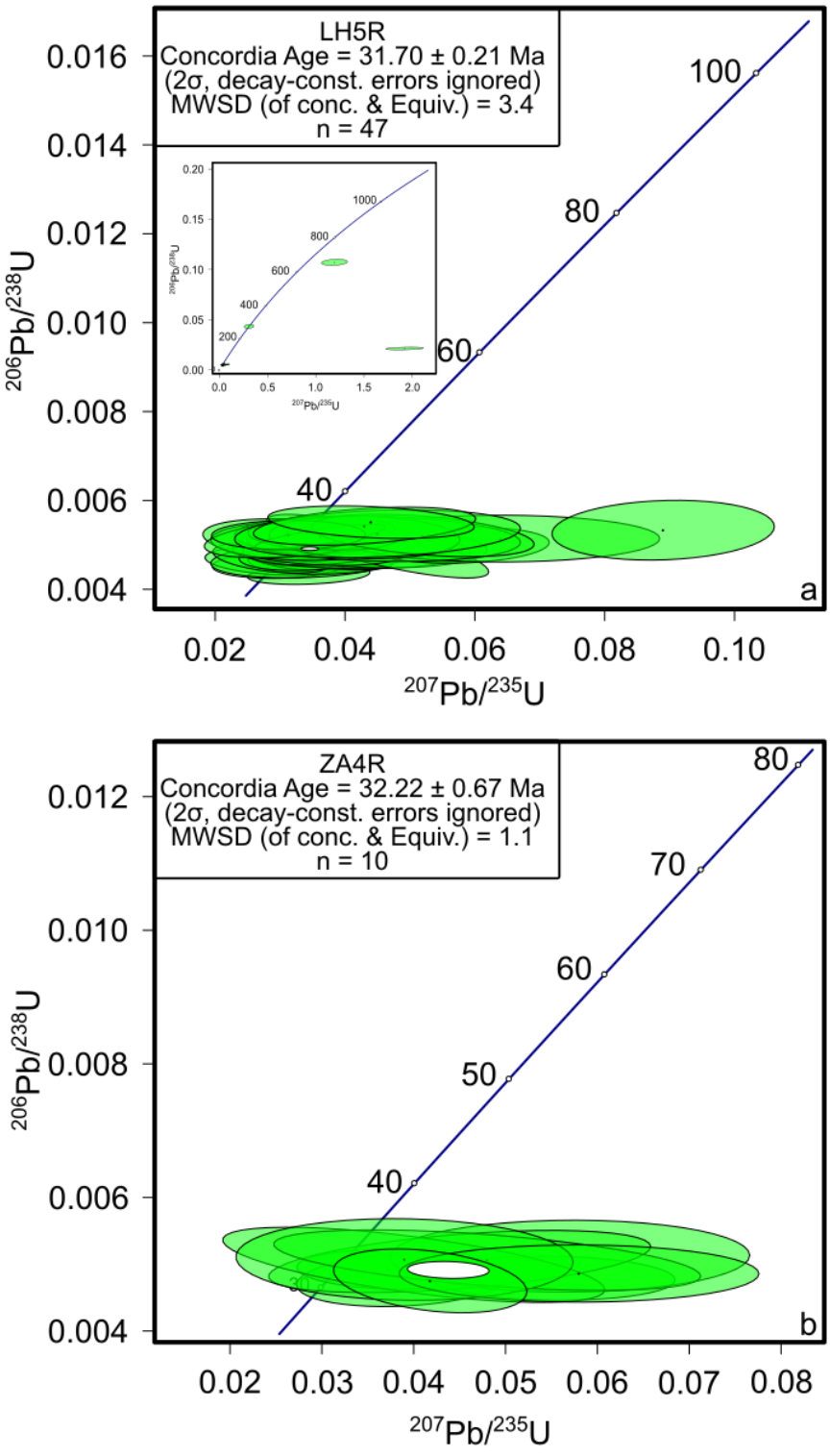

Figure 25: Concordia diagrams of analyzed zircons derived from garnets. a) U-Pb diagram of zircon inclusions derived from garnets of the sample LH5R. Green ellipses indicate data used for age calculations and concordia age, respectively. Errors depicted at the 2σ level. b) a) U-Pb diagram of zircon inclusions derived from garnets of the sample ZA4R. Analytical data of a) are shown in Appendix I 5 and b) are presented in Appendix I 6.

In order to determine the origin of the garnets, zircon inclusions in garnet of the samples LH5R and ZA4R were separated and analyzed. Cathodoluminescence images of the zircon inclusion derived from the garnets are, similar to the whole rock samples, dominantly prismatic and show exhibit oscillatory zoning, pointing to a magmatic origin For the sample LH5R a crystallization of 31.70 ± 0.21 (n=47, MWSD=3.4; Figure 25 a and Appendix I 5) and for the sample ZA4R a crystallization age of 32.22 ± 0.67 Ma (n=10, MWSD=1.1; Figure 25 b and Appendix I 6). Three zircon grains show inherited ages. The inherited ages (see Figure 24 and Appendix I 5) are derived from the core of these three zircon grains.

A K-Ar whole rock age of 33.3 ± 0.43 Ma was obtained for the El Sombrero ignimbrite. For the garnet-bearing La Herradura rhyolite an age of 31.25 ± 0.7 Ma (± 2σ) was calculated, whereas an age of 32.18 ± 0.62 Ma (± 2σ) was obtained for the Zaragoza andesite (Table 5).

Table 5: Measurement conditions and results of the K-Ar whole rock age determination form the La Herradura volcanic rocks.

K/Ar - Age Determinations

Ar - Isotopic Abundance	Spike-Isotopic Comp.	Decay Constants [1/a]:	Potassium
		l e :	0.011670
40 Ar : 99.6%	40 Ar : 0.009998%	0.0000000000581	40K : %
		l b :	
38 Ar : 0.063%	38 Ar : 99.989%	0.0000000004962	K2O/K : 0.8302
			Atomic Weight [g/mol]:
36 Ar : 0.337%	36 Ar : 0.0009998%		
Standard Temperature Pressure (STP) 0° C; 760 mm Hg		l tot : 0.0000000005543	tot Ar : 39.9477
		Molar Volume	40Ar : 39.9624
Normal Atmosphere (DIN 1343) 273,15 K; 1013,25 mbar		[ml] : 22413.8	tot K : 39.1027

Unit	Sample	Spike	K_2O	^{40}Ar *	^{40}Ar *	Age	2σ-Error	2σ-Error
		[No.]	[Wt. %]	[nl/g] STP	[%]	[Ma]	[Ma]	[%]
Zaragoza Andesite	LH3B	5617	3.73	3.9	79.27	32.18	0.62	1.9
La Herradura Rhyolite	LH2RT	5615	4.42	4.5	54.33	31.25	0.7	2.3
El Sombrero Ignimbrite	LHTT	5616	4.92	5.33	82.31	33.3	0.43	1.3

4.5. Discussion

4.5.1 Tectonic framework

The development of the Sierra Madre Occidental and its SE portion, the Mesa Central can be split into three main tectono-magmatic stages. First, a long phase of mainly andesitic to dacitic arc volcanism (45 Ma – 31 Ma) connected to the subduction of the Farallon plate that lasted until Eocene-Oligocene (McDowell and Clabaugh, 1979; Aguirre-Díaz and McDowell, 1991; Ferrari et al., 2002; Ferrari et al., 2005). Second, an extension-related phase (32 – 25 Ma) overlapped with the Oligocene to Miocene Basin and Range extension events (McDowell and Clabaugh, 1979; Damon, 1981; McDowell and Mauger, 1994; Aguirre-Díaz and Labarthe-Hernández, 2003; Aguirre-Díaz et al., 2008). This extension-related phase produced mainly rhyolitic to dacitic calc-alkaline volcanism, which was associated to the transition from a subduction-related to an extensional regime, when crustal relaxation may have been dominant (McDowell and Clabaugh, 1979; Damon et al., 1983; Aguirre-Díaz and McDowell, 1991; Ferrari et al., 2002; Ferrari et al., 2005). The third stage corresponds to early Miocene (23-20 Ma) mafic magmatism that marked the evolution from a continental arc regime to intraplate volcanism (Aguirre-Díaz and McDowell, 1993; Aranda-Gómez et al., 2000; Gottsmann and Martí, 2008).

Regional geological and geophysical studies imply that in the southern part and central part of the Mesa Central the crust has a thickness of approximately 30 to 33 km, whereas the thickness of the crust to the west is 40 to 42 km and to the east 37 km (Fix, 1975; Smith and Jones, 1979; Nieto-Samaniego et al., 1999; Nieto-Samaniego et al., 2007). The thinning of the crust in this part was apparently due to the extension of the Basin and Range during the Oligocene to Miocene (Tristán-González et al., 2009 b). These may have favored the generation of the acidic magmas, due to decompression, and ascent of the rhyolitic and andesitic magmas from the La Herradura area through the crust. The eruption ages of the La Herradura volcanic units are consistent with those of other volcanic units from the San Luis Potosí Volcanic Field (whole rock and sanidine K-Ar ages between 31.6 ± 0.9 Ma and 29.1 ± 0.7 Ma; Tristán-González et al., 2009 a; Aguillón-Robles et al., 2012) or the Rio Santa María Volcanic Field (whole rock and sanidine K-Ar ages between 32.5 ± 0.8 Ma and 31.8 ± 0.7 Ma; Labarthe-Hernández et al., 1989; Tristán-González et al., 2009 a). The volcanic domes in the southern part of the Mesa Central, in the states of Aguascalientes

and Zacatecas show similar to slightly younger eruption ages (whole rock and sanidine K-Ar ages between 32.3 ± 0.5 Ma and 29.5 ±0.5 Ma; Aguillón-Robles et al., 2009).

The formation of the Oligocene to Miocene felsic and voluminous volcanic rocks in the MC and SMO is associated in space and time to the Basin and Range extensional province, which is delineated by normal faults and grabens with a general NW–SE to NE–SW orientation (Stewart, 1978; Labarthe-Hernández et al., 1982; Henry and Aranda-Gómez, 1992; Nieto-Samaniego et al., 1996; Stewart, 1998; Torres-Hernández et al., 2006; Nieto-Samaniego et al., 2007; Aguirre-Díaz et al., 2008; Aguillón-Robles et al., 2009; Tristán-González et al., 2009 b).

The concomitance of the felsic magmatic event and the extensional regime meant that fissure type volcanism occurred all over the MC and SMO and along some of the grabens and normal fault systems, the emplacement of rhyolitic ignimbrites and/or domes was associated with basaltic to andesitic lava flows forming bimodal volcanic suits (Tristán-González, 1986; Aguirre-Díaz and Labarthe-Hernández, 2003; Tristán-González et al., 2008; Rodríguez-Ríos and Torres-Aguilera, 2009; Aguillón-Robles et al., 2012).

4.5.2. Genesis of the La Herradura volcanic rocks

The main characteristic of bimodal volcanism is the coalescence in time and space of felsic and mafic magmas. The magmas can be derived from either the same kind of source, due to differentiation of mafic magma (e.g. Espinoza et al., 2008; Charlier et al., 2011) or different sources, likely lower crustal and upper mantle melts (Verma, 2001; Rodríguez-Ríos and Torres-Aguilera, 2009).

The volcanic rocks from La Herradura area show almost identical eruption ages, only the ages of the Zaragoza Andesite and El Sombrero Ignimbrite show slightly different ages. For the garnet-bearing La Herradura rhyolite an age of 31.25 ± 0.7 Ma was calculated, whereas an age of 32.18 ± 0.62 Ma was obtained for the Zaragoza Andesite and an age of 33.3 ± 0.43 Ma for the El Sombrero Ignimbrite. The ages of the Zaragoza andesite and of the garnet-bearing La Herradura are within uncertainty of each other (Figure 19) although field relationships (Figure 6, Figure 8) indicate that the rhyolite has to be slightly older. Furthermore, the La Herradura Rhyolite and the Zaragoza Andesite form domes and plateaus along NNW-SSE trending normal faults, which might have acted as channels for magma ascent, as already suggested for volcanic rocks close to the study area and that NNW-SSE trending is similar to the Basin and Range extension (Aguillón-

Robles et al., 2009; Rodríguez-Ríos and Torres-Aguilera, 2009; Tristán-González et al., 2009 a; Aguillón-Robles et al., 2014).

The samples of the Zaragoza Andesite show enrichment in Cr, Ni, and Ba, while Sr and La show a depletion with increasing Mg#. The high contents of Cr and Ni in the Zaragoza Andesite are preserved characteristics from mantle-derived magma (Aguillón-Robles et al., 2014). Aguillón-Robles et al. (2014) showed that high Ba, Sr, U, and minor Th values, like the Zaragoza Andesite, from the nearby San Luis Potosí Volcanic Field were derived from assimilation of calc-alkaline affine lower crustal material into the mafic magmas. These features, together with the strong negative anomaly in Nb and Ta (Figure 14), indicate that the parental magma was derived from partial melting (Figure 26) in the uppermost mantle and that it stagnated at the mantle-crust boundary.

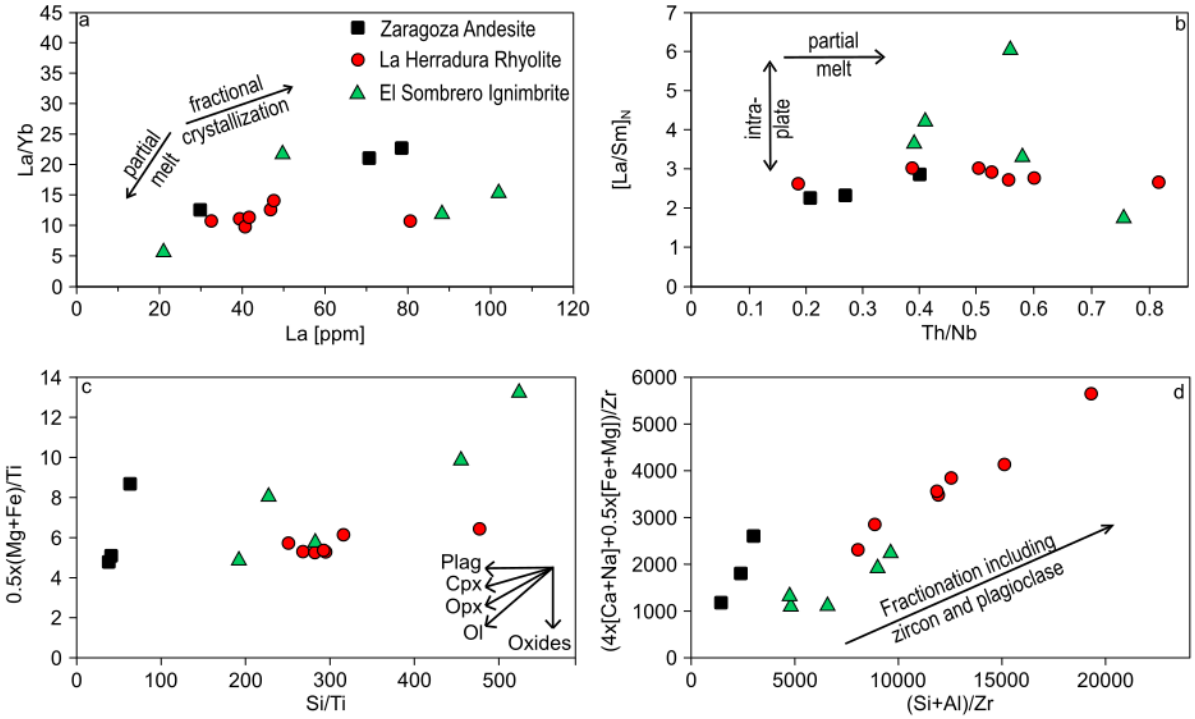

Figure 26: a) and b) Bi-element variation diagrams for samples of the La Herradura area. N denotes chondrite-normalized values after McDonough and Sun (1995). c) and d) Pearce Element ratio diagrams (after Pearce, 1968; Pearce and Cann, 1973; Bradshaw, 1992) showing crystal fractionation trends for the volcanic rocks from the La Herradura area.

Crystallization simulations of the Zaragoza Andesite with the pressure and temperature condition described in Schaaf et al. (1994) show that the amphibole crystals with high Mg and Ti content, like the ones from the Zaragoza Andesite cannot crystallize from the magma (Figure 17). The amphiboles xenocrystals imply that at the crust-mantle boundary or in the lower mantle the partial

assimilation of the lower crust took place. The reaction rims, consisting of opaque phases, pyroxenes and glass (Figure 12 c, d, f) indicate that the amphiboles were not in equilibrium with the melt. Amphiboles xenocrystals are also reported from quaternary volcanism in San Luis Potosí (Schaaf et al., 1994) and from Oligocene andesites in San Lorenzo in the northern portion of the San Luis Potosí Volcanic Field (32.2 ± 0.8 Ma, K-Ar whole-rock data, unpublished data, Aguillón-Robles personal communication, 2019).

The relatively high SiO_2, low MgO, Cr and Ni contents indicate an evolved magma for the garnet-bearing La Herradura rhyolite and the El Sombrero Ignimbrite. The depletion of HREE as well as the Ba, Sr, Eu and K anomalies of the garnet-bearing rocks indicates the fractionation of plagioclase, garnet and pyroxene (Figure 14, Figure 26). Additionally, the decreasing Zr content with increasing SiO_2 content (Figure 26 d) indicates the fractionation of zircon during the evolution of the magma. Based mainly on the behavior of Nb, Ta and Th the rhyolitic magmas of the La Herradura area are produced in an intra-plate setting. If the magma source was a subduction related, then these elements would be more depleted due to differentiation (Gill, 1981). The REE have light negative patterns which indicate intra-plate signatures, whereas strong negative patterns are typical for subduction related magmas (Wilson, 1989). The different HRRE values of the El Sombrero Ignimbrite can be explained due to the influence of the lithic clasts. The trace element behavior in the multi-element plots (Figure 14) imply that the rhyolitic volcanic rocks were the result of a process involving partial melting of the crust and fractional crystallization. The fractional crystallization is confirmed in the change in composition of K-feldspars, plagioclases, and pyroxenes (Figure 15). During the fractional crystallization of the acidic magmas of the El Sombrero Ignimbrite to the La Herradura Rhyolite, the magma becomes enriched in K and enriched in Fe and depleted in Na, resulting in the crystallization of K-rich K-feldspar and Fe-rich pyroxene and in the crystallization of mainly andesine. The zoning of plagioclase (Figure 10 a) confirm the evolution to higher andesine content form the core to the rim. Furthermore, this is particularly evident in the La vs. La/Yb, Th/Nb vs. $[La/Sm]_N$ and Pearce Element Ratio diagrams of Figure 26.

Our results are in good agreement to geochemical works near the study area in the states of Zacatecas, San Luis Potosí, and Aguascalientes (Verma, 1984; Orozco-Esquivel et al., 2002; Rodríguez-Ríos et al., 2007; Rodríguez-Ríos and Torres-Aguilera, 2009).

In summary, the geochemical data show that the rhyolitic magmas were formed by a process involving partial melting of the lower crust most likely with the presence of fluids enriched in HFSE and LILE that show signatures of an intraplate fertile lithosphere and fractional crystallization of the magma during the ascent. In contrast, the andesitic magmas derived from partial melting of the upper-most mantle and that during the ascent the magma stagnated at the crust-mantle boundary or the lower crust, where assimilation and fractional crystallization took place.

4.5.3. Origin of La Herradura rhyolite garnets

Almandine-rich garnets from volcanic rocks can crystallize directly from Al-rich (peraluminous) silicic magmas as a liquidus or near liquidus phase at high pressures (9-18 kbar; e.g. Green and Ringwood, 1968, 1972) and temperatures (~950 – 1050°C; e.g. Wood, 1974), corresponding to depths of >25 km. An alternative possibility is that the garnets can represent xenocrystals or residual phases derived from partial melting of metamorphic rocks (Chappell and White, 1991; Sheibi et al., 2010). Primary igneous garnet is a rare phase and their crystallization is restricted to special conditions; therefore, they give valuable information about the pressure and temperature conditions as well as the geodynamic affinity of the magma (Green, 1977; Harangi et al., 2001).
The almandine garnet-bearing La Herradura Rhyolite do not contain any metamorphic crustal xenoliths and the garnets do not have any inclusions of metamorphic minerals (e.g. sillimanite, staurolite, and/or muscovite) that could indicate residual origin. Furthermore, the garnets have in general sharp margins and are either euhedral or have rounded shapes. Almandine garnets poor in MnO, like the ones from La Herradura, are not stable at shallow depths (Green, 1977). To preserve them, a rapid ascent of the magma is necessary. The U-Pb crystallization ages, from the zircons crystallized from the rhyolitic magma, and the K-Ar whole rock ages of the garnet-bearing rhyolite indicate a short time between the cooling from the closure temperature of zircons (> 900 °C; Lee et al., 1997) and the eruption, corresponding to the closure temperature the K-Ar system (350 ± 50 °C; Purdy and Jäger, 1976) of the rhyolite magma.
Garnets with low MnO (<2 wt.%) and relatively high CaO-content (>5 wt.%) are derived from partial melts of the upper mantle and partial melts of igneous rocks (Green, 1977, 1992; Harangi et al., 2001). If the garnet is a primary phase it limits the pressure and temperature conditions as well as the composition under that the magma can form at (Green, 1977, 1992). In contrast, garnets

derived from partial melts of metapelites or meta-sediments have low CaO- content (<4 wt.%) and variable MnO content (Harangi et al., 2001). The La Herradura garnets plot in the intersect of the fields for the garnets crystallized from melts/partial melts of meta-sediments magmas and the field of garnets derived from metapelitic rocks within a CaO vs. MnO diagram, including the discrimination fields after Harangi et al. (2001) (Figure 27).

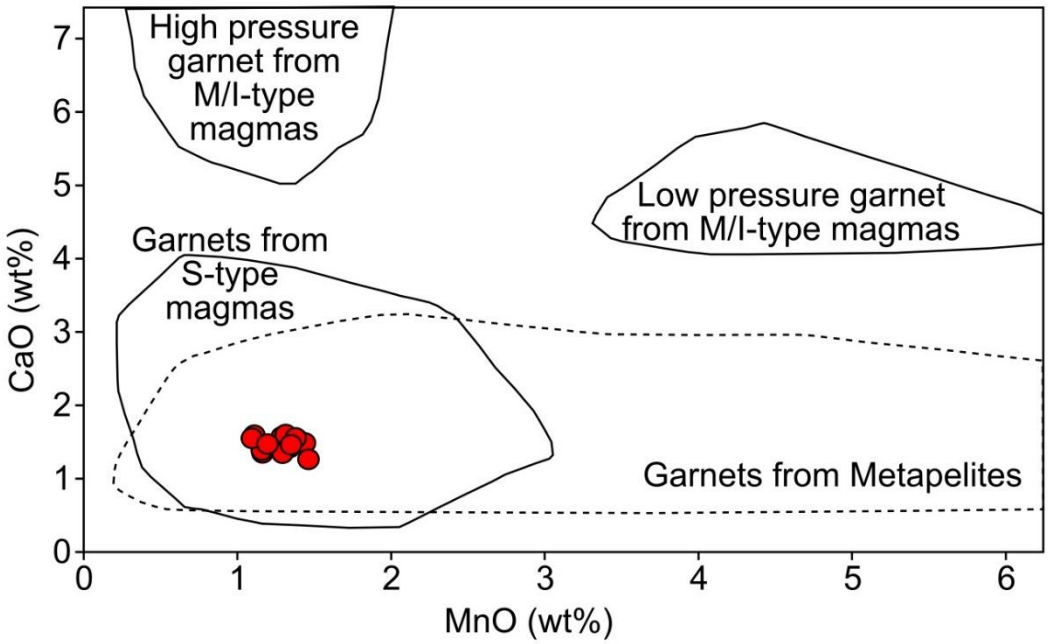

Figure 27: CaO vs MnO plot for almandine garnets from La Herradura, from the samples Za4R and LH5R. Results for the samples ZA4R and LH5R are shown in Table 3. Fields for the origin of garnets from Harangi et al. (2001).

Previous experiments indicate that only spessartine-rich (Mn-rich) garnets can crystallize at P < 5-7 kbar in intermediate to silicic melts, whereas other garnets, such as almandine-rich garnets, only from at P ≥ 7 kbar (Green and Ringwood, 1968; Green, 1976, 1977; Clemens and Wall, 1984; Green, 1992). As mentioned above, the garnets within the La Herradura rhyolite are mainly composed of almandine and pyrope and are low in MnO (1.09 – 1.46 wt.%), indicating crystallization at pressures above 7 kbar. Using the minimum pressure of 7 kbar for feldspar crystallization temperature calculations with the two-feldspar thermometer (equation 27b in Putirka, 2008) yielded in minimum crystallization temperatures between 807 ± 50 °C and 1024 ± 53 °C for the garnet-bearing rhyolite and 837 ± 43 °C and 920 ± 53 °C for the El Sombrero Ignimbrite. Additionally, the upper zircon saturation temperature calculations (Boehnke et al., 2013) for the garnet-bearing rhyolite and the ignimbrite are slightly lower and range between 875

± 50°C and 750 ± 50°C. Among the geothermometers and geobarometers that use the mineral assemblage characteristic for the garnet-bearing La Herradura Rhyolite the garnet-ilmenite cation exchange thermometer (Pownceby et al., 1987, 1991) and the apatite in garnet barometer (Ashley et al., 2017) appear to be appropriate for the considering the conditions of calibration. The calculations lead to formation temperature (Table 4) between ~ 775 ± 45 °C and ~ 854 ±50 °C for the sample LH5R and ~ 702 ± 43 °C and ~ 886 ± 55 °C for the sample ZA4R. The results of the formation pressures are between ~ 5785 ± 1500 kbar and ~ 10440 ± 2060 kbar for the sample LH5R and ~ 9000 ± 1870 kbar and ~11890 ± 2180 kbar. The temperatures derived from the garnet-ilmenite thermometer are comparable with the zircon saturation temperatures and the two feldspar. Formation pressures are with exception of two analysis from the sample of ZA4R, which are within their error above 7 kbar, confirming the experimental results (Green and Ringwood, 1968, 1972; Wood, 1974; Green, 1992) that garnets can crystallize from Al-rich silicic magmas as a liquidus or near liquidus phase at high pressures ≤ 7 kbar. These temperature and pressure conditions are in the range of the above-mentioned authors, indicating crystallization in the lower continental crust. In addition, rhyolite-MELTS simulations on the crystallization of the rhyolitic magmas show that garnet can crystallize from rhyolitic melts (3 wt.% H_2O) at pressures P ≥ 7 kbar at ~ 860 °C. Crystallization temperatures of garnets decrease with increasing total water content in the magma. These temperatures are comparable to the upper zircon saturation temperature and the results from the garnet-ilmenite thermometer and the apatite in garnet barometer, referring to that zircons and garnets crystallized at the same time.

The U-Pb ages derived from zircon inclusions in garnet are similar or within the error to the U-Pb ages of the whole rock samples (Figure 19). This indicates that both, crystallized at the same time from the magma chamber. Nevertheless, the calculated ages of zircon inclusion in garnets are derived from the $^{206}Pb/^{238}U$ age and it is not clear if the ages are concordant, the zircon ages might have been reset due to a reheating above more than 800 °C (Pristiner Zircon; Mezger and Krogstad, 1997). The simulations for the El Sombrero Ignimbrite show similar results (Appendix E) to the garnet-bearing rhyolite. Garnets could have crystallized from rhyolitic melts, with the composition of the El Sombrero Ignimbrite (3 wt.% H_2O) at pressures P ≥ 7 kbar at ~ 890 °C, whereas the crystallization temperatures of garnets, like in the garnet-bearing rhyolite, decreases with increasing total water content in the magma. The simulation also showed that at lower pressures garnets become instable and disappear. An example for this scenario would be the generation of

the magma at lower crustal depth, where the garnet crystallizes and a storage in a shallow magma chamber, which is required for the ignimbrites in the MC and SMO (Aguirre-Díaz and Labarthe-Hernández, 2003; Aguirre-Díaz et al., 2008).

Considering the garnet is an early magmatic phase that was in equilibrium with the rhyolitic melt and is only present in the rhyolite, it is inferred that the garnet did not crystallize in a basic or intermediate magma and that the rhyolite could not have been derived from a basic magma by crystal fractionation.

The geochemical features as well the set of inclusions in garnets from the La Herradura Rhyolite are rather similar to those of the garnets in rhyolites from the Deh-Salm area, Iran (Mirnejad et al., 2008) and the garnets derived from ignimbrites in the Violet Town volcanic rocks, Victoria, Australia (Clemens and Wall, 1984) that crystallized from peraluminous magmas under medium to high pressure conditions. Dahlquist et al. (2007) also reported the direct crystallization of garnets in the Peñón Rosado granite, Argentina from a peraluminous magma. These similar features of the garnets and the garnet-bearing rocks described by other authors tighten that garnets crystallized from the rhyolitic magma in the La Herradura area.

4.5.4. Geodynamic implications of the eruption and emplacement of La Herrradura garnet-bearing rhyolite

Almandine garnet-bearing volcanic rocks are uncommon (e.g. Table 1 in Harangi et al., 2001). Green (1977) showed that almandine garnets poor in Mn are not stable at shallow depths. To preserve the almandine garnets a rapid ascent is necessary. Therefore, a direct ascent of magmas from their generation zone at the base of the crust to the surface along deep-seated faults or tectonically weak zones and a tensional stress field is required. Besides that, almandine garnet crystallization is favored from silicate melts with high water content (Green and Ringwood, 1972). Such conditions can be found in areas where lithospheric extension followed active subduction, like the Basin and Range Province during the Oligocene in the Mesa Central (Aguirre-Díaz and McDowell, 1993; Nieto-Samaniego et al., 2007; Tristán-González et al., 2009 b). The felsic domes from the southern part of the Mesa Central, near the study area, were generated by direct ascent of magmas from their generation zone at the base of the crust to the surface without temporary storage at intermediate depths (Aguillón-Robles et al., 2009). Hildreth (1981) proposed a similar

mechanism according to which magmas produced by partial melting in the lower crust ascent by diapirism during episodic extensional events.

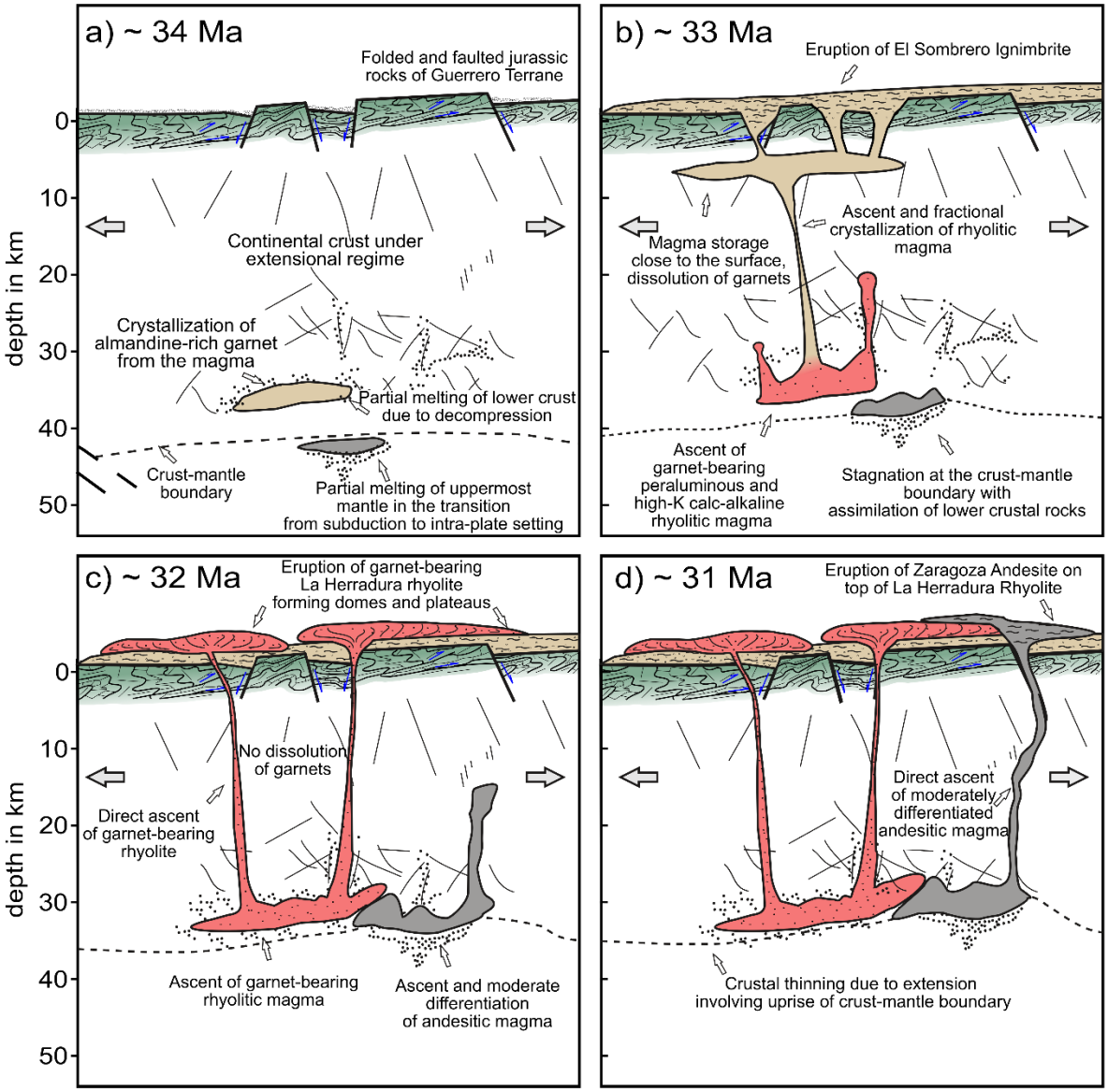

Figure 28: Schematic evolution of the La Herradura volcanic rocks between ca. 34 Ma and 31 Ma. a) Generation of andesitic magma in a post-subduction setting in the upper mantle and of a rhyolitic magma in an intra-plate extension-related setting in the lower crust. b) Ascent and accumulation of the rhyolitic magma. In the magma chamber volatiles are exsolved favoring explosive eruptions which emplaced the El Sombrero Ignimbrite. The storage time in the magma chamber was as long as necessary to dissolve the garnets, if they were in the melt before. During the rise of the rhyolitic magma, fractional crystallization took place. c) Direct ascent and eruption/emplacement of the garnet-bearing rhyolitic magma. Geochronological results indicate a time of ca. 300 ka between the crystallization and the eruption of the garnet-bearing rhyolite. d) Direct ascent and eruption/emplacement of Zaragoza Andesite. Field relations show that the Andesite was emplaced after the garnet-bearing rhyolite. Figure compared to Aguillón-Robles et al. (2014).

On the other hand, the El Sombrero ignimbrite is the result of a major explosive eruption, following a temporary storage in a shallow magma chamber in which volatiles were exsolved. Such ignimbrite-generating events occurred in many areas of the Mesa Central and in the adjacent Sierra Madre Occidental (Aguirre-Díaz and Labarthe-Hernández, 2003; Aguirre-Díaz et al., 2008). This storage might lead to garnet dissolution, which are confirmed by the rhyolites-MELT simulation on the crystallization of the EL Sombrero Ignimbrite (Appendix E). The andesitic magma of the Zaragoza Andesite was derived from partial melting in the uppermost mantle and then stagnated at the mantle-crust boundary or in the lower crust where assimilation took place (Figure 28). The high Mg# values of pyroxenes support an origin of a mantle origin from a less differentiated magma. Many authors describe similar geological settings for garnet-bearing volcanism worldwide. For example, Gilbert and Rogers (1989) described a garnet-bearing volcanism in the Pyrenees, which is formed during the Hercynian orogeny, when extension followed collision. In the Northern Pannion Basin garnet-bearing volcanism occurred during a phase of extension, after the ending of the subduction phase (Harangi et al., 2001).

The regional geological setting and the geochemical features of the studied rocks are widespread in the SMO and its south-eastern part, the MC (Aguirre-Díaz and McDowell, 1993; Nieto-Samaniego et al., 2007; Tristán-González et al., 2009 b). The results show that garnets can crystallize from a rhyolitic magma at lower crustal depth and that they can be persevered if the magma ascent is fast. However, there are no reports about garnet-bearing volcanism in the Mesa Central published. This might have three reasons, first, pressure and temperature conditions are slightly different yielding in no crystallization of garnets. Second, garnets dissolved during a slow ascent of the magma or during magma storage in a shallow magma chamber that is required for the eruptions of the large ignimbrites of the SMO (Aguirre-Díaz and Labarthe-Hernández, 2003; Aguirre-Díaz et al., 2008). Third, the garnet-bearing rhyolites of the study area have a small volume compared to the large ignimbrites and rhyolitic domes of the SMO and its south-eastern part, the MC, and they might have not been discovered yet. The garnet-bearing rhyolites and their associated bimodal suit reflect the early magmatic evolution of the rhyolitic volcanic rocks in the Sierra Madre Occidental and its southeastern part the Mesa Central.

4.6. Conclusions

Four major phases (Figure 28 a-d) formed the bimodal volcanism of the La Herradura area. First, the formation of andesitic magma, where the parental magma was probably derived from partial melting in the uppermost mantle within a post-subduction setting and that it stagnated at the mantle-crust boundary or in the lower crust. Geochemical data as well as rhyolite-MELTS simulations on the crystallization show that there partial assimilation of the lower crust took place. During the same time partial melting of the lower crust, close to the crust-mantle boundary, took place due to the Basin and Range extension associated thinning of the crust. The geochemical results confirm an intra-plate origin of the magmas by partial melting of the base of the continental crust, involving fluids enriched in HFSE and LILE. In addition, the stagnated andesitic magma might have favored the partial melting of the lower crust. Simulations on the crystallization shows that garnet crystallize as a primary phase form the rhyolitic magma at pressures > 7kbar. Confirmed is the crystallization of garnet by the similar results of the U-Pb age analysis of zircons derived from the garnet-bearing rhyolite and zircon inclusions derived from garnet. The rhyolitic magma uprose through the brittle crust and was temporarily stored in a shallow magma chamber, where garnets were dissolved, confirmed by the rhyolite-MELTS simulations on the crystallization of the EL Sombrero Ignimbrite, and volatile exsolution generated explosive eruptions which emplaced the El Sombrero Ignimbrite. The third phase involved the direct ascent and emplacement of the garnet-bearing La Herradura rhyolitic magma. The last stage involved the direct ascent and eruption of Zaragoza Andesite, which according to field relationships was emplaced after the garnet-bearing rhyolite. The direct ascend from the lower crust, where the magmas were generated, is favored by the intense extensional regime and is necessary to preserve the garnets.

5. Stratigraphy and geochemical, petrological and geochronological constraints on the evolution of the Oligocene Villa Garcia Ignimbrite complex in the southern Mesa Central of Mexico.

5.1. Introduction

The Oligocene Villa Garcia Ignimbrite complex lies in the NE of the Mexican state of Aguascalientes and SE of the Mexican state of Zacatecas (Figure 29), covering an area of 550 km^2, located in the southeastern portion of Sierra Madre Occidental (SMO), the Mesa Central (MC). The Sierra Madre Occidental (SMO) is an Eocene–Miocene silicic large igneous province, which consists of mainly Oligocene to Miocene rhyolitic ignimbrites, lava flows and domes (McDowell and Clabaugh, 1979; Damon, 1981; Aguirre-Díaz and McDowell, 1991, 1993; Aguirre-Díaz et al., 2008; Tristán-González et al., 2009 a; Ferrari et al., 2018). The Oligocene high-silica rhyolitic ignimbrites and lavas are common in the MC (McDowell and Clabaugh, 1979; Swanson and McDowell, 1984; Aguirre-Díaz and Labarthe-Hernández, 2003), but not all have been studied in detail.

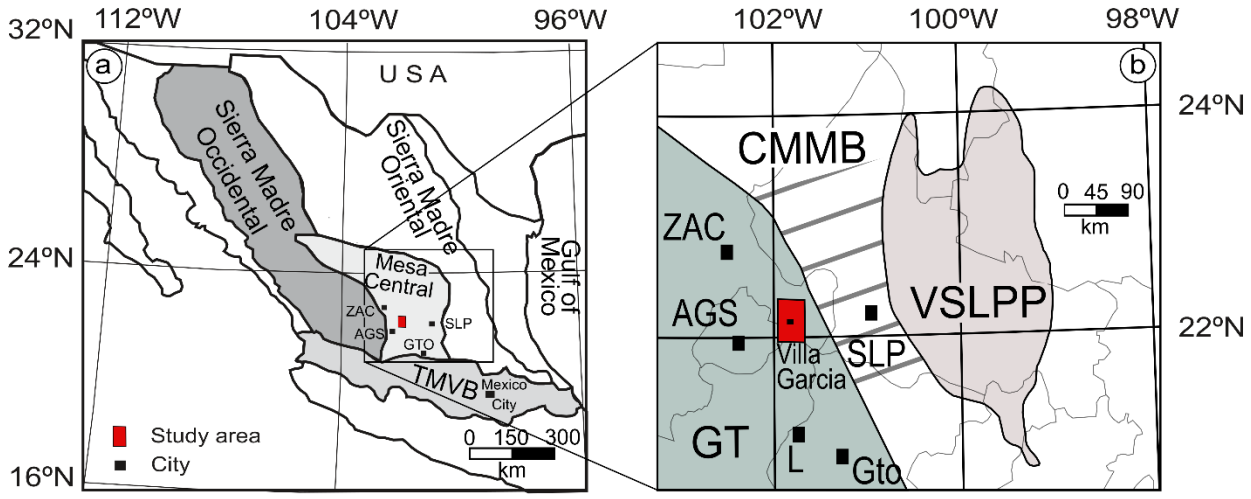

Figure 29: Location of the Villa Garcia volcanic succession. a) Spatial relationship with the main geological provinces of northern Mexico. b) Location of volcano-tectonic features of San Luis Potosí and Zacatecas. a) and b) modified after Mortensen et al. (2008) and Aguillón-Robles et al. (2014). ZAC: Zacatecas city; AGS: Aguascalientes city; GTO: Guanajuato city; SLP: San Luis Potosí city; L: Leon; TMVB: Trans Mexican Volcanic Belt; GT: Guerrero Terrane; CMMB: Central Mexico Mesozoic Basin; VSLPP: Valles-San Luis Potosí Platform.

Previous works on the stratigraphy in southern and central part of the Mesa Central showed that the volcanism initiated with andesites (~44 Ma Casita Blanca Andesite) followed by a 32–27 Ma rhyolitic to dacitic volcanism that produced mainly ignimbrites and lava domes and subordinated with andesites forming a bimodal succession (Labarthe-Hernández et al., 1982; Rodríguez-Ríos and Torres-Aguilera, 2009; Tristán-González et al., 2009 a). The last volcanic stages in the southern and central portion of the Mesa Central consists of Middle Miocene and Plio-Pleistocene alkaline basalts and andesites (Luhr et al., 1989; Aranda-Gómez et al., 2005; Nieto-Samaniego et al., 2007). The Oligocene to Miocene volcanism in the area was mainly controlled by NW–SE normal faults that are associated to the Basin and Range extension in Mexico (Tristán-González et al., 2008; Tristán-González et al., 2009 b).

Previous studies in the area date back to the last decade, Aguillón-Robles et al. (2009) published a brief description of the geology and geochemistry of the Villa Garcia Ignimbrite complex, as part of the dome volcanism in the southern Mesa Central and the geologists of the Mexican Geological Survey (SGM) did basic geological mapping I the study area. Despite all these studies, the stratigraphy, the timing of the volcanism as well as processes involved in the formation, the ascent and the eruption of the Villa Garcia Ignimbrite complex are not well constrained. Prior to this work there were only four K-Ar ages reported, between 29.5 ± 0.5 Ma (1σ) and 32.3 ± 0.5 Ma (1σ) by Aguillón-Robles et al. (2009), however, they do not report to which unit the ages belong.

This work provides first and new high precision radiometric ages ($^{40}Ar - ^{39}Ar$ age data), major and trace element geochemistry and mineral studies in order to reconstruct the temporal and magmatic evolution and tectonic processes that took place during the formation, ascent, and eruption of the Oligocene high-silica rhyolitic ignimbrites and lavas in the area of Villa in the southern MC. In order to understand better, the origin of the rhyolitic explosive and effusive rocks of the Villa Garcia Ignimbrite complex, we combine geochemical data with well constrained geological, stratigraphical and geochronological data, which are the basis of this work.

The aim of this study is to investigate and understand the origins of the voluminous effusive and explosive rhyolitic rocks based on the study of their geological, petrographic, geochemical and geochronological features. The interpretation of these dataset provides new information on the origin of the Oligocene high-silica rhyolitic ignimbrites and lavas in the Mesa Central.

5.2. Geological and tectonic setting

The oldest rocks exposed are a volcano-sedimentary sequences with interlayered limestones (Figure 31 a and b) of the Guerrero terrane (Centeno-García et al., 2008; Aguillón-Robles et al., 2009; Centeno-Garcia et al., 2011). Both are strongly deformed and slightly metamorphosed during the Laramide Orogeny (Centeno-García et al., 2008; Aguillón-Robles et al., 2009; Centeno-Garcia et al., 2011). Discordantly, the early Cretaceous sedimentary succession is overlain by younger continental red sediments and conglomerates, with tourmaline- and muscovite-bearing intrusive clasts, that were not affected by the orogeny and are up to 200 m thick. The continental sedimentary succession is interlayered by a red and massive rhyolitic lava flow and a pumice-bearing volcanoclastic succession (Figure 31 c). Aranda-Gómez et al. (2007) described a similar succession in the Pinos area, close to the study area. The interlayered rhyolitic lava flow with glassy base and 20 vol.% of crystals (quartz, sanidine, plagioclase, biotite and pyroxene) initiates the volcanic sequence, which is directly overlain by a volcanoclastic sequence. This volcanoclastic sequence is exposed around the Granadas village, it is up to 80 m thick and it may present distal explosive volcanic products emplaced within an ephemeral lake, forming a sub-parallel succession of mainly pumice-bearing sand- and siltstones with abundant subaqueous sedimentary structures. Two voluminous Ignimbrites form the top of the composite stratigraphy (Figure 31 d). First, the lower Villa Garcia Ignimbrite is a densely welded, massive, reddish, up to 130 m thick, and lava-like to rheomorphic ignimbrite, with a basal vitrophyre. Second, the Loreto Ignimbrite shows similar internal stratigraphy to the Villa Garica Ignimbrite, with a basal black vitrophyre, followed by a massive and densely welded, lava-like to rheomorphic ignimbrite. In-between the two ignimbrites an up to 10 m thick conglomerate was deposited erosive discordant on the Villa Garcia Ignimbrite and the top of the conglomerate is built up by a lithified paleosol. An andesitic, black lava flow was emplaced after or at the same time as the Loreto Ignimbrite forming a possible bimodal series. This Oligocene activity was associated to a transtensive deformation regime that generated a set of several km-long NW-SE trending normal faults. During the Pliocene-Pleistocene, 40 to 100 m-thick sandstones interlayered with conglomerates were deposited in erosional discordance over both the lower Cretaceous and Oligocene volcanic rocks, and locally covered by Holocene gravels and silts, caliches, lacustrine materials and alluvium

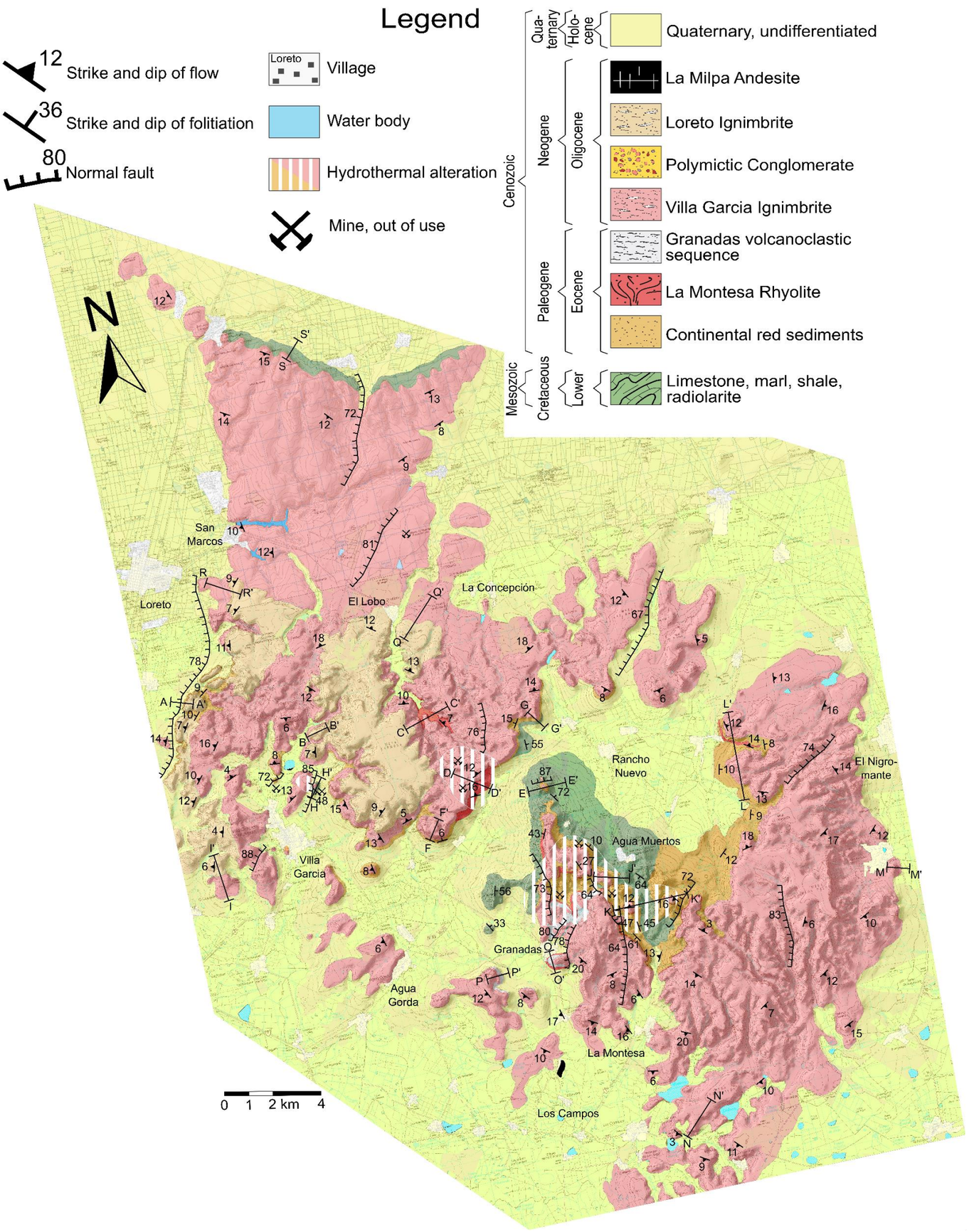

Figure 30: Geological map of the Villa Garcia volcanic succession complex. A-A' to S-S' are the logged sections shown in Appendix J.

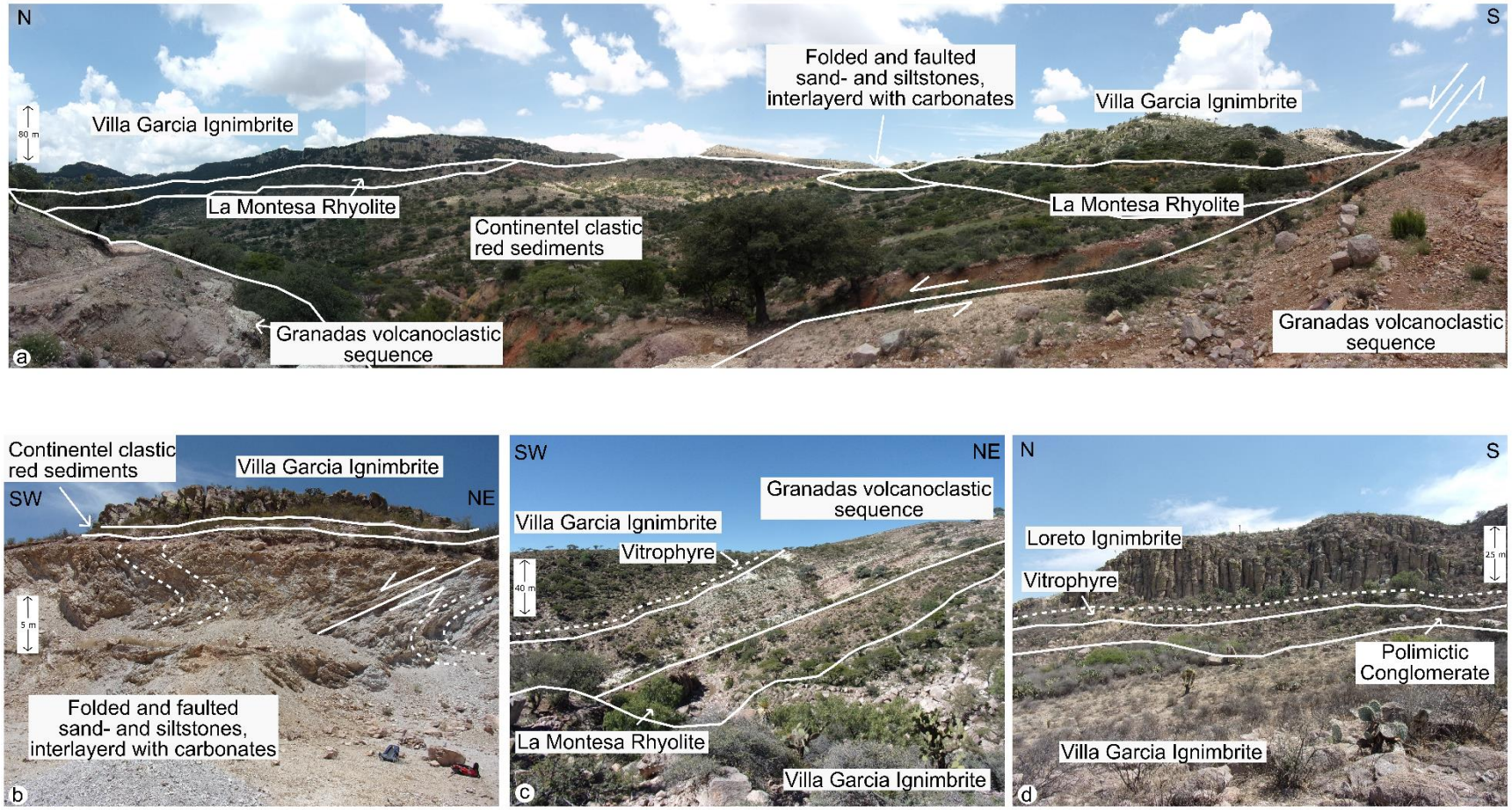

Figure 31: Field photography from the Villa Garcia Ignimbrite complex. a) Center of the study are northeast of Granadas, marked are the geological contacts of the different units and a major normal fault. b) Western center of the study area, northeast of Villa Garcia, marked are the geological contacts of the different units, as well as the foliation of the folded and faulted basement. c) Center of the study are north of Granada, marked are the geological contacts of the different units and the basal vitrophyre of the Villa Garcia Ignimbrite. d) Northern portion of the study area, west of Loreto, marked are the geological contacts of massive lithic rich breccia at the top of the Villa Garcia Ignimbrite with the polymictic conglomerate and the Loreto Ignimbrite, as well as the basal vitrophyre of the Loreto Ignimbrite.

5.3. Methodology

Mapping and logging of sections were done in twelve field work campaigns of three days each. During the campaigns 18 sections were logged and the study area was mapped. The location of the logged sections is given in Figure 30. In addition, 34 samples were taken from the different units in the logged sections, the coordinates of the sample location are shown Table 6. From two samples of the Granadas volcanoclastic sequence pumice clast were separated for the geochemical analysis. Sample preparation for the geochemical analysis, the petrographic analysis, the EPMA and the $^{40}Ar - ^{39}Ar$ age determinations and was carried out in the Laboratorio de Petrografía in the IPICYT. The analytical methods for the sample preparation, the determination of the major and trace elements, EPMA as well as the $^{40}Ar - ^{39}Ar$ age determinations is described in Chapter 3. Analytical Methods.

5.4. Results

5.4.1. Stratigraphy and Petrography

The Mesozoic Basement

The composite stratigraphic column of the study area is shown in Figure 32. Locally, the basement is formed by a volcano-sedimentary sequences of the Guerrero terrane. In the eastern part of the study area, the basement is built up by a folded Mesozoic marine sequence, mainly carbonates containing fossils, mainly rudists. The thick marine sediments are interlayered with thin layers of shales and siltstones. In the western and central part of this area the sequence includes andesites that are slightly metamorphosed, sandstones and shales, interlayered with reef limestones. The ages of the are Upper Cretaceous, more precisely Barremian to Aptian (Tristán-González et al., 1994). Both, the sediments of the Sierra Madre terranes and the Guerrero terrane strongly folded and faulted and effected by intense erosion. The Mesozoic basement is discordantly overlain by a succession of continental red sediments.

Continental clastic red sediments

The thickness of the continental clastic red sediments varies from up to 200 m, in basins within the basement, to a few meters or are not present on top of basement highs. The continental red sediments are mainly well lithified sand- and siltstones (Figure 33 a - c) and to the top of the sequence well-lithified conglomeratic sandstone and matrix-supported fine-grained to medium-grained polymictic conglomerate.

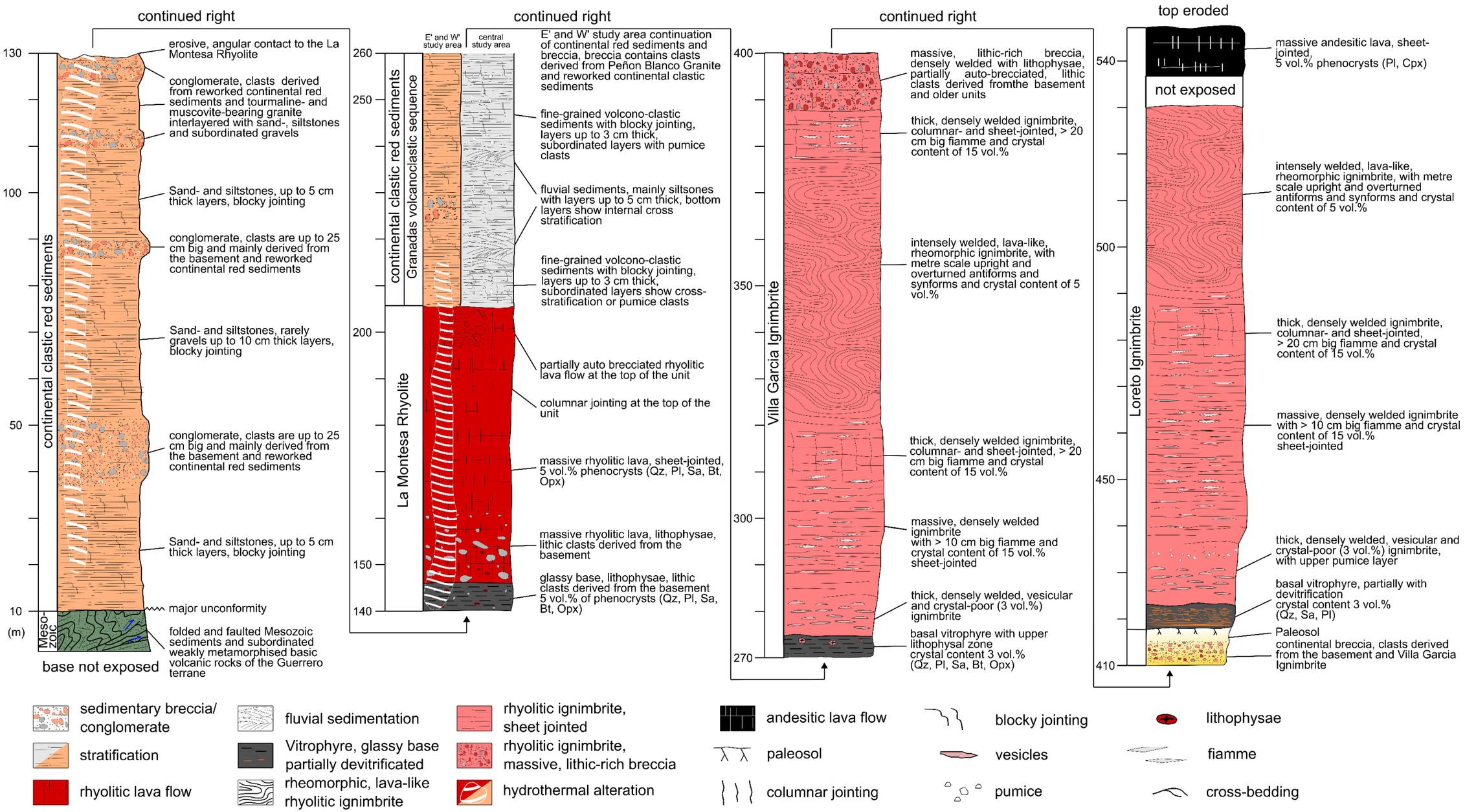

Figure 32: Composite stratigraphic column of the Villa Garcia Ignimbrite complex showing the main lithostratigraphic units described in the text. Bt – biotite; Qz – quartz; Pl – plagioclase; Px – pyroxene; Sa – sanidine. The composite stratigraphic column is the result of the measured sections shown in Appendix J.

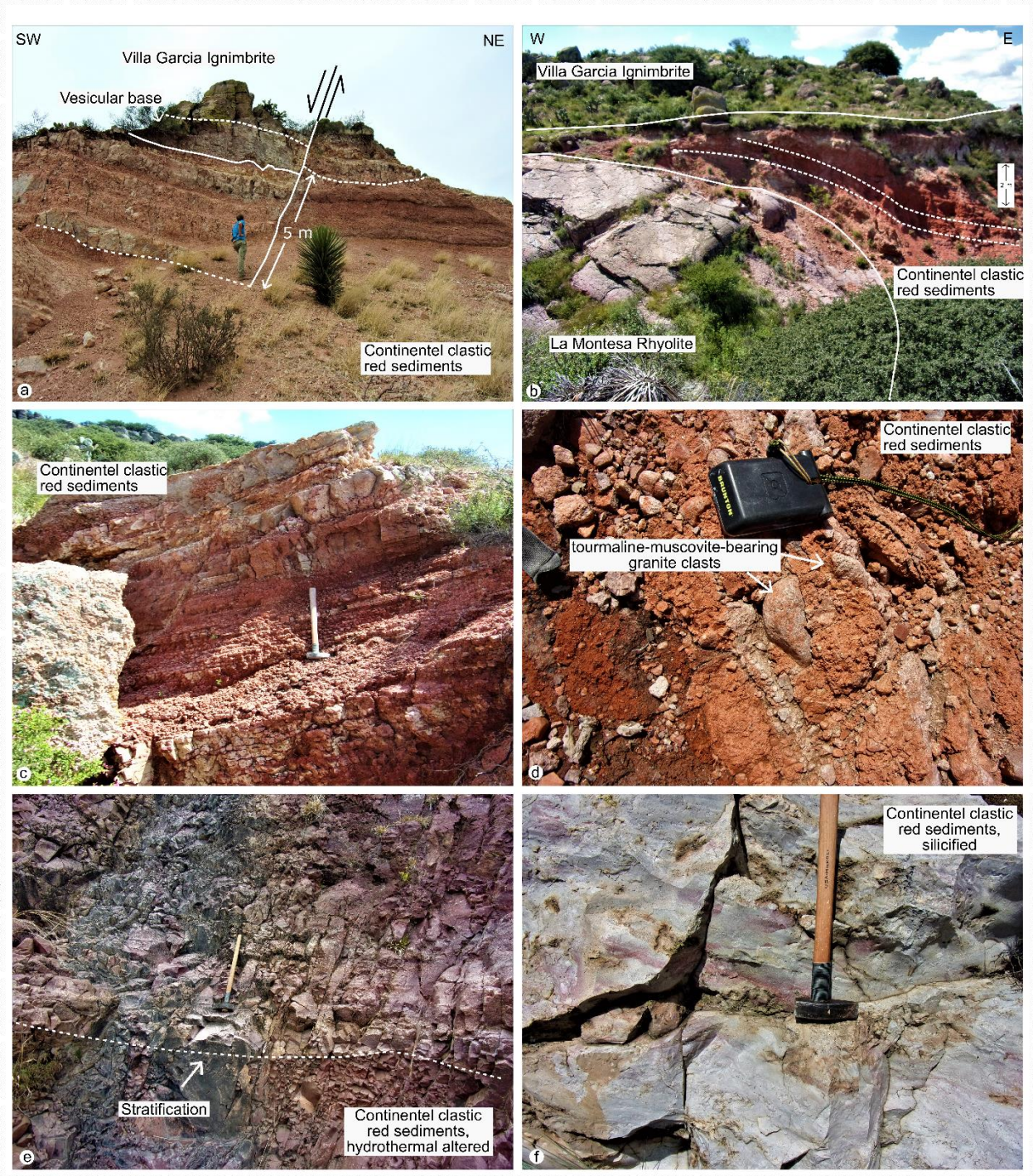

Figure 33: Field photography from the Villa Garcia Ignimbrite complex. a) Center of the study area, north of Villa Garcia. The continental clastic red sediments and the Villa Garcia Ignimbrite are displaced by a minor normal fault. b) Center of the study area, south of Granadas, marked are the geological contacts between the different lithological units. c) Continental clastic red sediments in the eastern part of the study area. Size of the Hammer is 0.5 m. d) Tourmaline- and muscovite-bearing clast in the continental clastic red sediments close to the contact with the La Montesa Rhyolite in the center part of the study area e) and f) Silicified continental read sediments in the central part of the study area. Size of the Hammer is 0.5 m.

Clasts in the red beds were derived from the Mesozoic basement, subaerial felsic volcanic rocks of unknown provenance, and tourmaline-bearing muscovite granite (Figure 33 d) similar to the Peñón Blanco Granite (Aranda-Gómez et al., 2007).

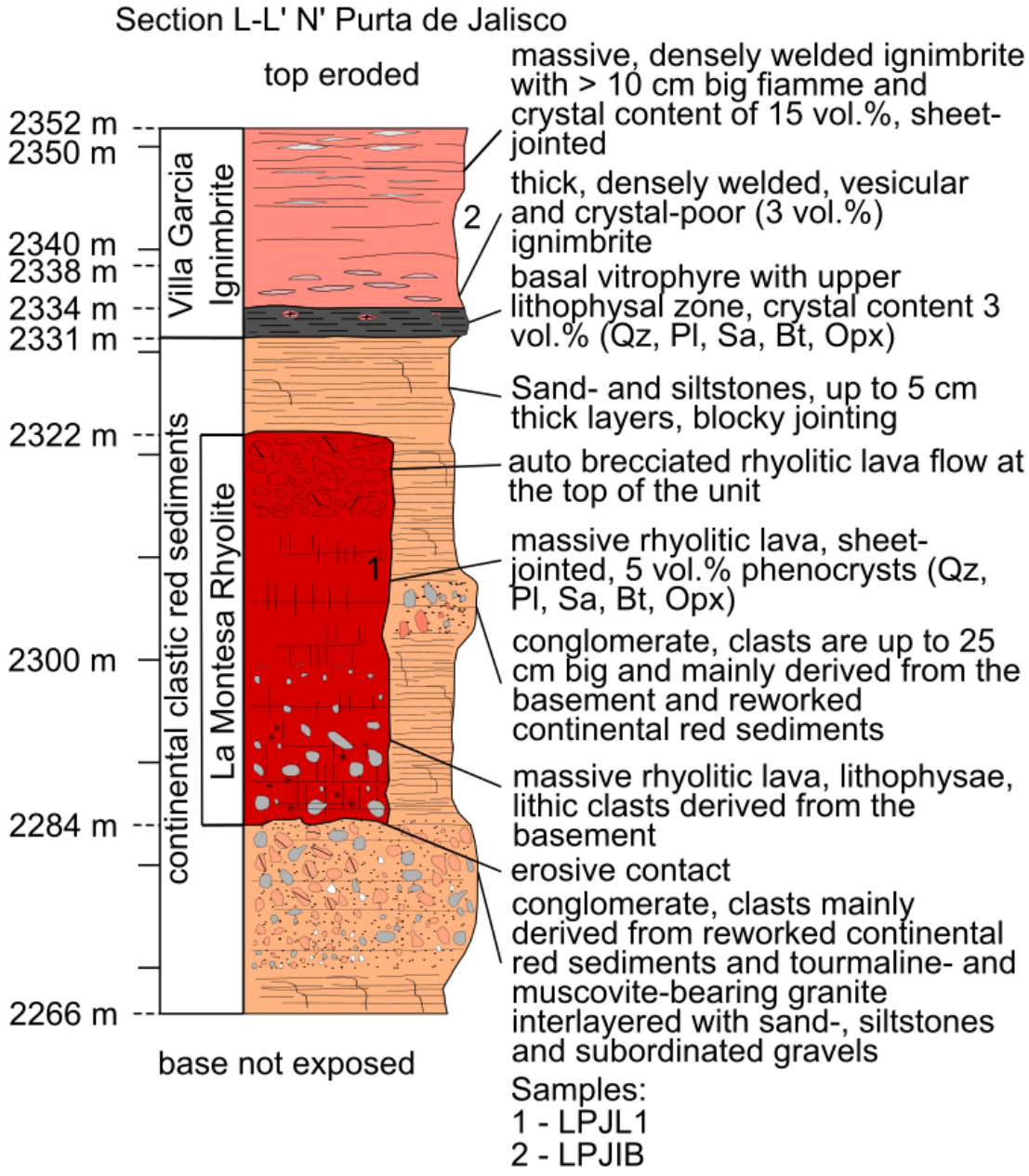

Figure 34: Logged section L-L' north Puerta de Jalisco (Zacatecas), showing the relationship between the continental clastic red sediments, the La Montesa Rhyolite and Villa Garcia Ignimbrite in the eastern study area and their lithological feautures. The labels correspond to the sections indicated in the geological map shown in Figure 30. Symbols and stratigraphy are explained in Figure 32. Bt: biotite, Opx: orthopyroxene, Pl: plagioclase, Qz: quartz, Sa: sanidine.

The sedimentary succession is interlayered by rhyolitic volcanic rocks including a rhyolitic lava (Figure 33 b), ash-fall tuffs, and water-laid or reworked pyroclastic material. In the eastern part of the study area the continental red sediments, mainly the conglomerates at the top of the sequence are silicified, oxidized and argilized due to hydrothermal activity (Figure 33 e and f). The contact of the interlayered rhyolitic lava flow, herein named La Montesa Rhyolite, with the continental red sediments is erosive discordant (Figure 34).

La Montesa Rhyolite

The La Montesa Rhyolite is a red and massive rhyolitic lava flow present in the eastern and central part of the study area. The base of the rhyolite is built up by an up to 6 m thick and black glassy base (Figure 35 a). The glassy base can be described as leucocratic and hypocrystalline and the upper part shows auto-brecciation features and it turns gradually into a microcrystalline groundmass. Macroscopically the glassy base contains up to 5 vol.% phenocrysts of plagioclase, sanidine, quartz, and biotite as well as lithic clasts of the Mesozoic basement and the continental red sediments. The rhyolitic lava flow (Figure 35 b) is a leucocratic and hypocrystalline red to red-gray rock with a porphyric texture, up to 60 m thick and contains up to 5 vol.% plagioclase, sanidine, and quartz. At the base the lava contains up to 5 vol.% lithic fragments, mainly carbonate clasts. Like the continental red sediments, La Montesa Rhyolite is affected by intense hydrothermal alteration, mainly argilization in the eastern and central part of the study. Furthermore, the lava flow is crosscut by silicified oxidized and argilized fractures. In thin sections the glassy matrix of the base show flow structures (Figure 35 c) and typical perlitic cracks. The glassy matrix gradually turns into a hyalopilitic groundmass consisting of K-feldspar microlites. The auto-brecciated part of the glassy base (Figure 35 d) contains the same mineral content as the non-brecciated part. The rhyolitic lava is rather fresh and show a beginning to intense alteration and it can be described as seriate, hypocrystalline. The mineral content of the glassy base is similar to the rhyolitic lava (Figure 35 e and f). Quartz crystals (~ 10 vol.%) in thin sections are xenomorphic with an average grain size of 2 mm. Sanidines (~ 5 vol.%) have an average grain size of 3 mm, the shape is hypidiomorphic to xenomorphic and they show Carlsbad twinning. Hypidiomorphic to idiomorphic and in average 4 mm big plagioclase (~5 vol.%) crystals with polysynthetic twinning and in base cuts a zoning is present (Figure 35 e and f) are also present in thin sections.

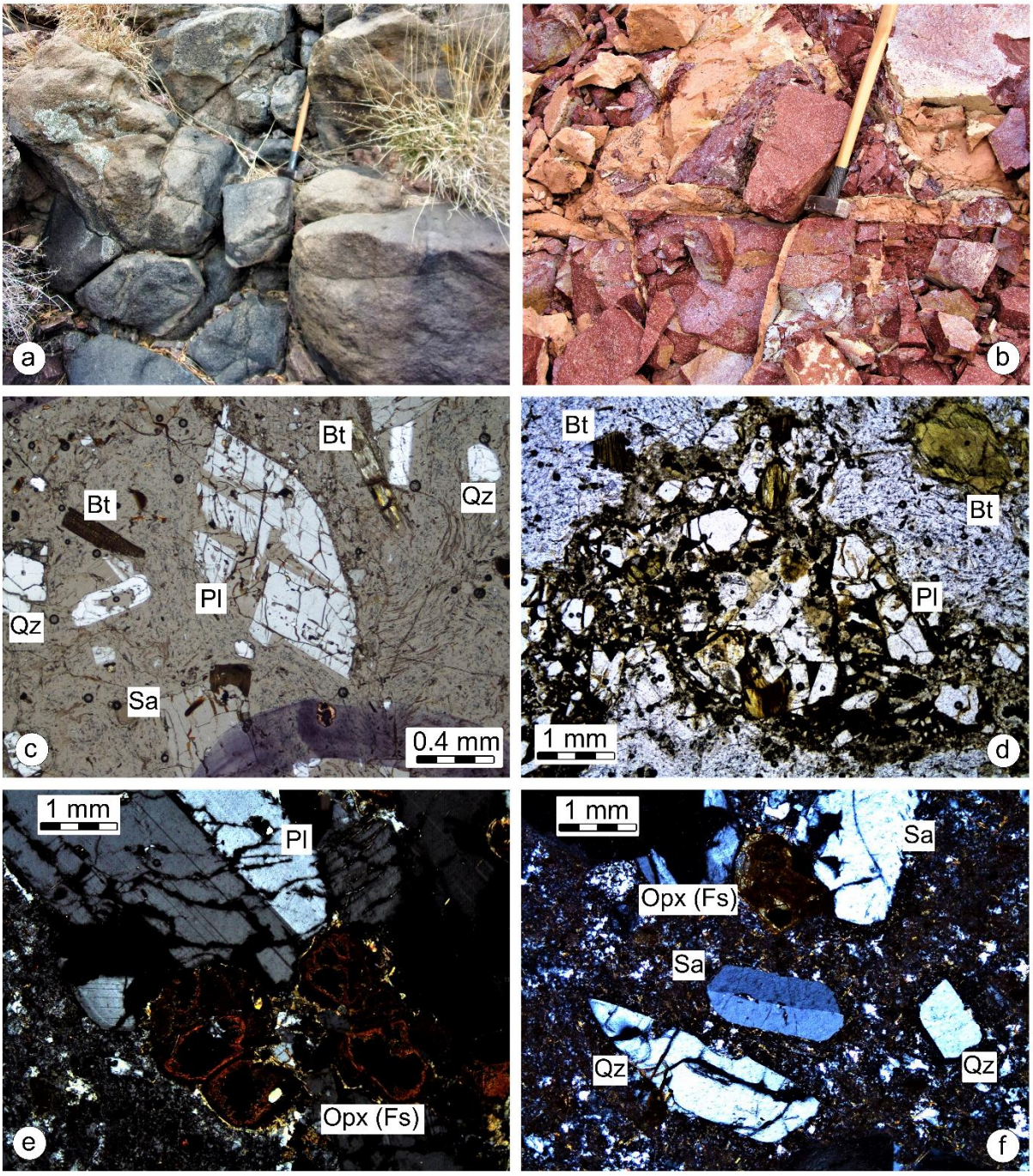

Figure 35: Representative outcrop and thin section images of the La Montesa Rhyolite. a) Representative outcrop of the glassy base of the La Montesa Rhyolite in the central part of the study area. Size of the hammer is 0.5 m. b) Representative outcrop of the La Montesa Rhyolite in the central part of the study area. Size of the hammer is 0.5 m. c) Thin section image of the glassy base of La Montesa Rhyolite. hypidiomorphic plagioclase, with twinning, together with biotite and quartz crystals in the glassy matrix. One biotite shows intense alteration (chloritization). Picture taken with crossed nichols d) Brecciated part of the glassy base; crystals and matrix are fractured due to the flow of the rhyolitic lava. e) and f) Thin section images of the La Montesa Rhyolite showing the typical mineral content. Pyroxene crystals show intense alteration. Picture taken with crossed nichols. Bt: Biotite, Fs: ferrosilite, Opx: orthopyroxene, Pl: plagioclase, Qz: Quartz, Sa: sanidine.

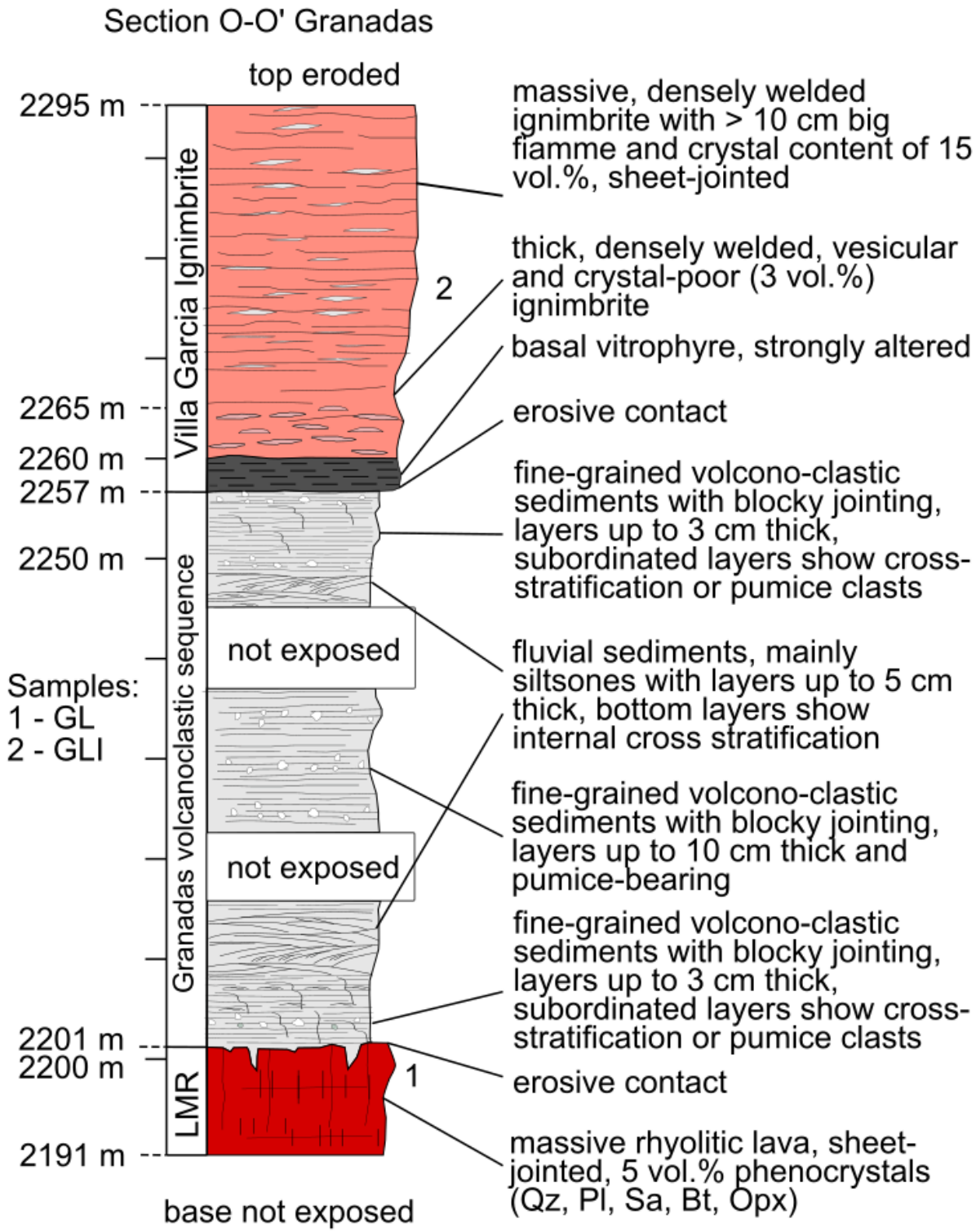

Figure 36: Logged section O-O' near Granadas (Zacatecas), showing the relationship between the La Montesa Rhyolite, the Granadas volcanoclastic sequence, and Villa Garcia Ignimbrite in the center study area and their lithological features. The labels correspond to the sections indicated in the geological map shown in Figure 30. Symbols and stratigraphy are explained in Figure 32. LMR: La Montesa Rhyolite. Bt: biotite, Opx: orthopyroxene, Pl: plagioclase, Qz: quartz, Sa: sanidine.

Pyroxenes (~ 2 vol.%) have xenomorphic shape and an average grain size of 1 mm. Most of the grains are intense altered and show a greenish to brownish pleochroism. Plagioclase and pyroxene show very often a glomerophyric texture. Biotite crystals (3 vol.%) are xenormorphic and have an average grain size of 1 mm. They show the typical brownish-greenish pleochroism and a beginning to intensive chloritization. Furthermore, ilmenite, zircon, apatite, and monazite are present in the groundmass. The La Montesa Rhyolite is discordant overlain by an 80 m thick volcanoclastic sequence (Figure 36).

Granadas volcanoclastic Sequence

The volcanoclastic sequence, herein named Granadas volcanoclastic sequence, is thin-layered (cm thick; Figure 37 a), generally sub-parallel and contains tabular to irregular packages of volcanic material as well as fossil-free sedimentary layers with cross stratification. The clastic heterogeneity constituted by pumice clasts (subangular to rounded), lithics, lapilli and loose crystals of volcanic origin (quartz, biotite, sanidine, and plagioclase). Granulometrically, the succession is characterized by an ash matrix and sporadic layers of pumice clasts. The layers of the lower part of the succession show coarsening upward sequences, with fine to very fine ash matrix layers at the base and furthermore, sedimentary or injected dykes. The middle part of the volcanoclastic sequence is built up by an intercalation of fine-grained ash and coarser sediments that are characterized by a zone of fossil-free and fluvial sedimentary structures (Figure 37 b) such as parallel lamination, cross lamination and undulated lamination.

In addition, the succession shows a pervasive zeolitization (heulandite, clinoptilolite, mordenite and sepiolite). In thin sections, the fine-grained matrix that consists of calcite, hematite, and clay minerals, contains xenomorphic quartz, hypidiomorphic plagioclase, hypidiomorphic sanidine, and rarely xenomorphic pyroxene (Figure 37 c - f). The lithic fragments consist mainly of xenomorphic quartz grains with a cover of hematite. In summary, the Granadas Volcanoclastic Sequence can be described as a succession of deposits of a distal density pyroclastic flows or currents, together with ash fall from eruptive columns of rhyolitic composition that were deposit in a shallow and intermittent water body.

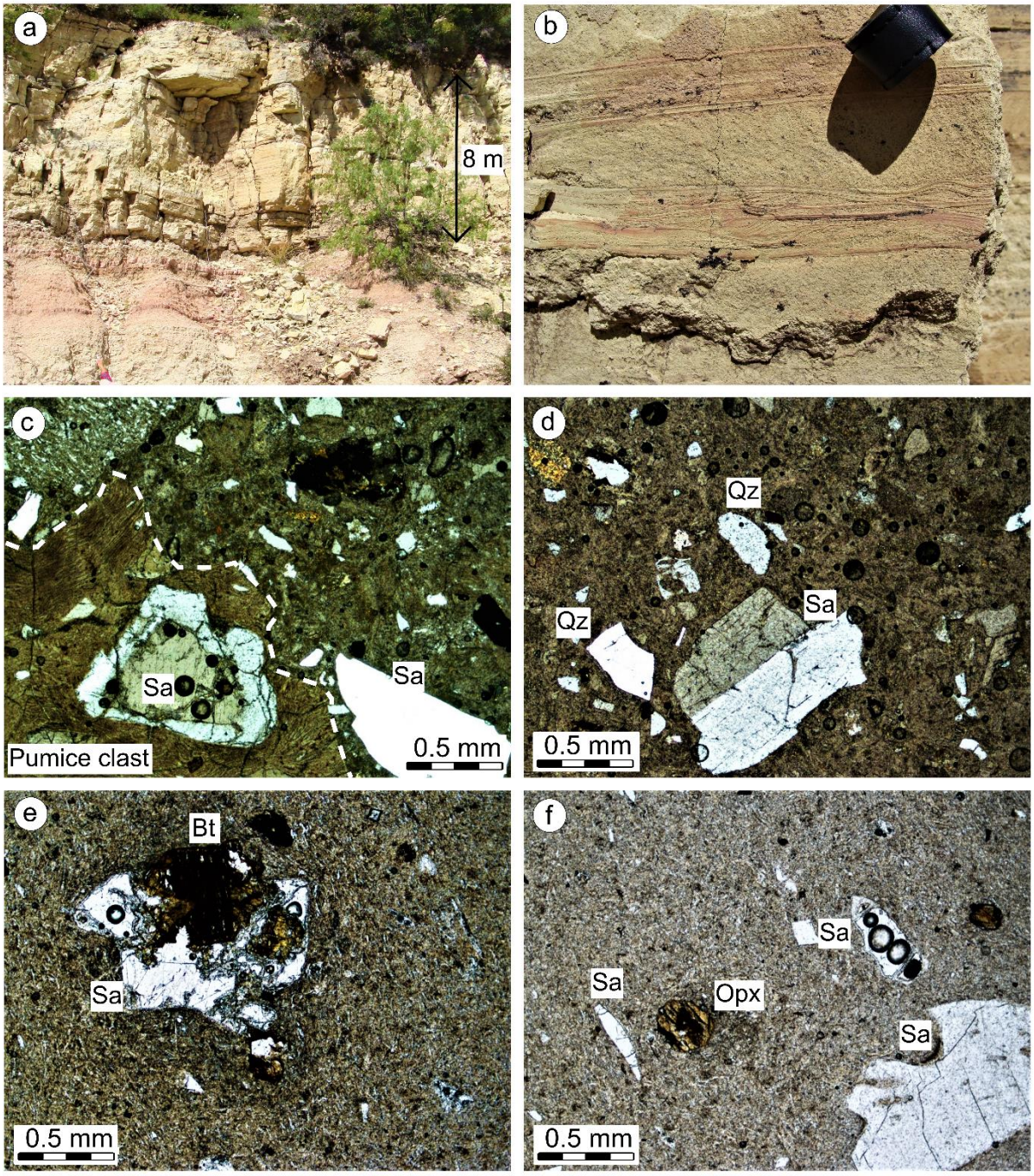

Figure 37: Field photography and thin section images of the Granadas Volcanoclastic sequence. a) Representative exposure of the Granadas Volcanoclastic sequence in the central part of the study area north of Granadas. b) Cross lamination in the middle part of the Granadas Volcanoclastic sequence. c)-f) Thin section image of the Granadas Volcanoclastic Sequence. c) Pumice clast with sanidine crystal in the fine-grained matrix from the lower part of the volcanoclastic sequence. Picture taken with crossed nichols. d) Xenomorphic quartz and sanidine crystals in the fine-grained matrix. Picture taken with crossed nichols. e) Agglomerate of sanidine and altered biotite in the fine-grained matrix. Picture taken with crossed nichols. f) Xenomorphic sanidine crystals and altered pyroxene crystal in the fine-grained matrix. Bt: Biotite, Opx: orthpyroxene, Pl: plagioclase, Qz: Quartz, Sa: sanidine.

Villa Garcia Ignimbrite

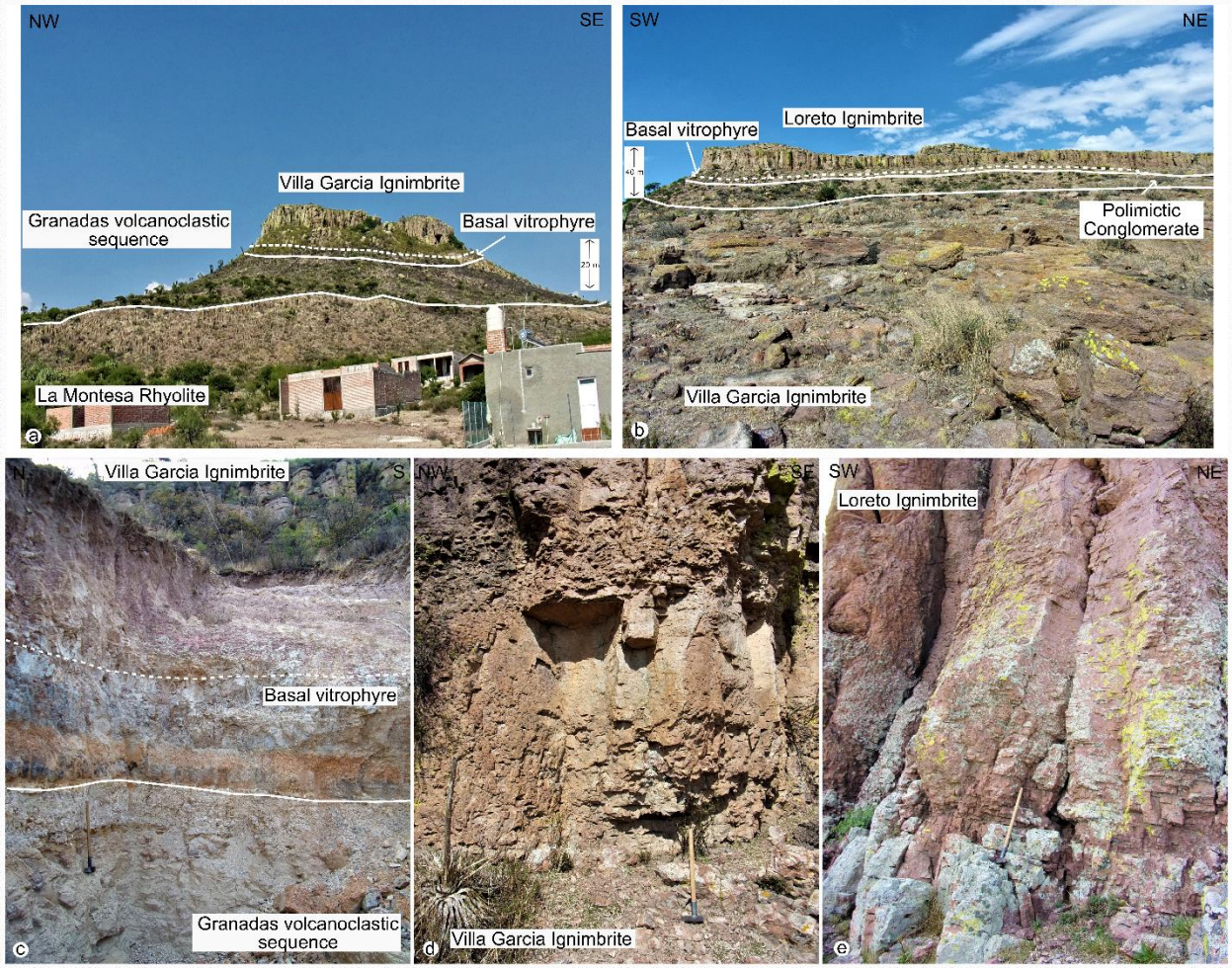

Figure 38: Field photography of the Villa Garcia and Loreto Ignimbrite. a) Western portion of the study area, northwest of El Nigromante, marked are the geological contacts between the different lithological units. The photography shows the rim of the La Montesa Rhyolite and the continuing sedimentation of the continental clastic red sediments after the emplacement of the lava flow. Dashed line marks the stratification of the sediments. b) Center of the study area, northeast of Villa Garcia, marked are the geological contacts between the different lithological units. c) Contact of the Granadas volcanoclastic sequence with the Villa Garcia Ignimbrite in a construction site in the center of the study area, marked are the geological contacts between the different lithological units. The basal vitrophyre shows intense alteration. Size of the Hammer is 0.5 m. d) Vesicular base of the Villa Garcia Ignimbrite in the northern portion of the study area. Size of the Hammer is 0.5 m. e) Vesicular base of the Loreto Ignimbrite in the southwestern portion of the study area. Size of the Hammer is 0.5 m.

The Villa Garcia Ignimbrite (Figure 38 a – d) covers the underlying continental red sediments and volcano-sedimentary rocks erosively discordant (Figure 38 a and c; Figure 39 a) all over the study area. The base of the Villa Garcia Ignimbrite is built up by an up to 3 m thick and crystal poor (3 vol.% of phenocrysts, mainly quartz, sanidine, plagioclase, and biotite) black vitrophyre (Figure 39 b). In thin section, the basal vytrophyre (Figure 39 c – e) can be described as seriate, holocrystalline and it shows perlitic cracks, flow structures, as well as a beginning devitrification. Quartz crystals (~ 1 vol.%) in thin sections are xenomorphic with an average grain size of 1 mm.

Sanidines (~ 2 vol.%) have an average grain size of 0.5 mm, the shape is hypidiomorphic to xenomorphic and they show Carlsbad twinning. Plagioclase crystals (2 vol.%) are hypidiomorphic

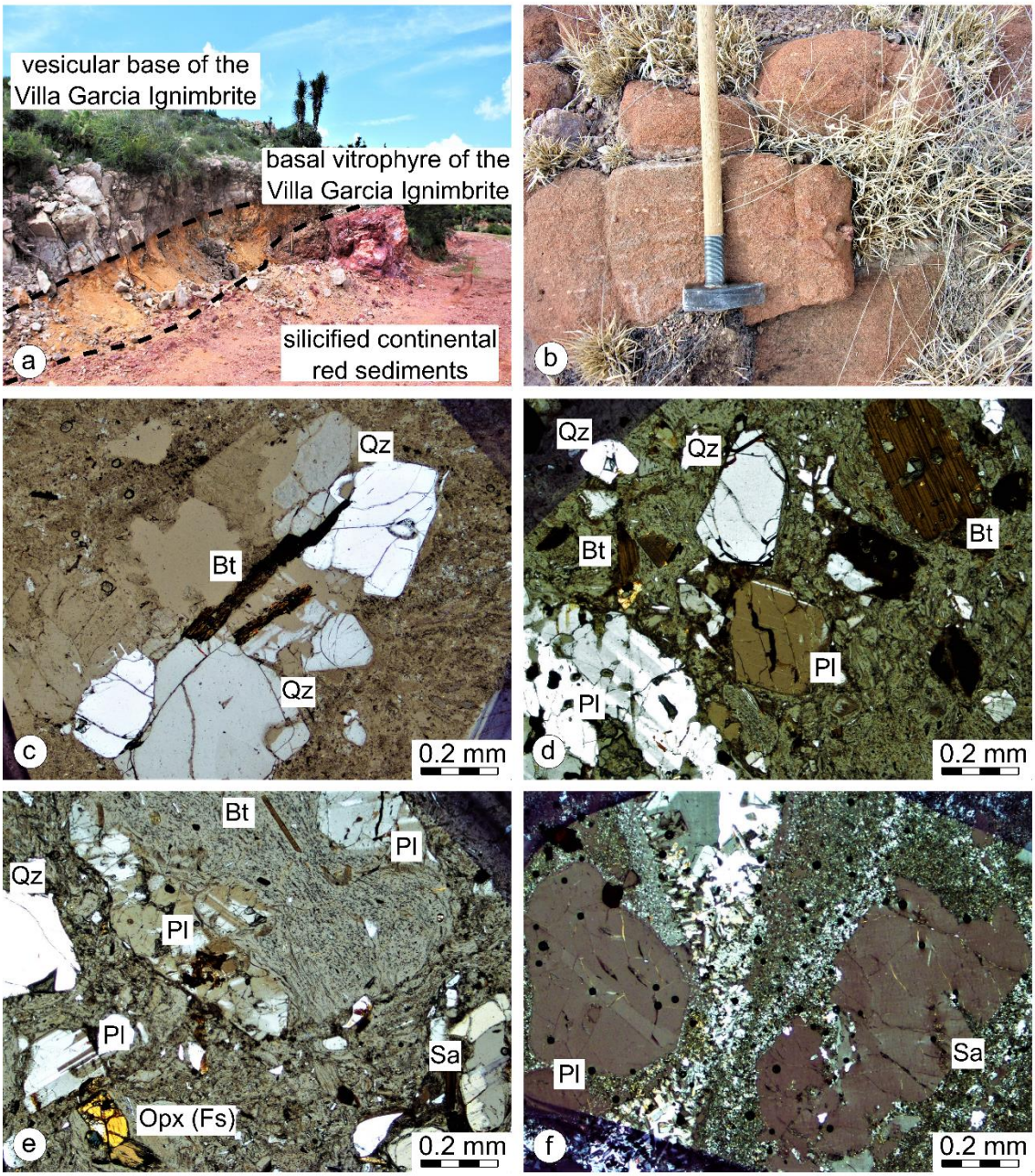

Figure 39:Field photography and thin section images of the base of the Villa Garcia Ignimbrite. a) and b) Representative field picture of the exposure of the Villa Garcia Ignimbrite. a) Exposure of the contact of the hydrothermal altered continental red sediments with Villa Garcia Ignimbrite in the central part of the study area, north of Granadas. The basal vitrophyre is intense altered. b) Representative outcrop of the basal vitrophyre of the Villa Garcia Ignimbrite, in the central part of the study area northeast of Villa Garcia. Size of the hammer is 0.5 m. c)-f) Thin section images of the Villa Garcia Ignimbrite. c) Agglomerate of quartz and biotite in the glassy matrix. Picture taken with crossed nichols. d) Plagioclase, quartz and biotite crystals in the glassy matrix of the basal vitrophyre. Picture taken with crossed nichols. e) Brecciated part of the vitrophyre of the Villa Garcia Ignimbrite. Picture taken with crossed nichols. f) Plagioclase and sanidine crystals separated by a fiamme, consisting of mainly quartz. Picture taken with crossed nichols. Bt: Biotite, Fs: ferrosilite, Opx: orthopyroxene, Pl: plagioclase, Qz: Quartz, Sa: sanidine.

to xenomorphic with an average grain size of 0.2 mm. Biotite crystals (> 1 vol.%) are xenormorphic and have an average grain size of 1 mm and show the typical brownish-greenish pleochroism and a beginning chloritization. The vitrophyre shows no layering or graduation in grain size and gradually turns into a pale reddish massive and densely welded porphyritic rhyolitic ignimbrite.

Its base (~ 6 m) is crystal poor (approximately 3 vol.% of quartz, sanidine, and plagioclase phenocrysts), and vesicular. Vesicles in the base of the unit have a maximum extend of 20 cm and their size and number decrease to the top, whereas the amount of crystals increase in the same direction. At the point where the vesicles are no longer present, fiammes appear and the rocks can be described as densely-welded and crystal-rich ignimbrite. The densely-welded and massive ignimbrite is pale reddish to gray, up to 35 m thick and shows up 4 cm thick and 25 cm long fiammes. The amount and size of the fiammes increases to the top of the sub-sequence. The ignimbrite contains around 15 vol.% phenocrysts, mainly quartz and sanidine, subordinate plagioclase and pyroxenes. In thin section the sub-sequence of this ignimbrite can be described as seriate and holocrystalline and a beginning devitrification of the matrix is observable. The matrix consists mainly of collapsed and elongated ash and glass particles. Sanidine (Figure 39 f) has a percentage of ~ 5 vol.% and an average grain size of 3 mm, the shape is hypidiomorphic to xenomorphic and they show Carlsbad twinning. Xenomorphic quartz crystals (~ 5 vol.%) with an average grain size of 0.5 mm and hypidiomorphic to idiomorphic and in average 0.5 mm big plagioclase (~3 vol.%) crystals, with polysynthetic twinning, are also present in thin sections. Pyroxenes (~ 2 vol.%) have xenomorphic shape and an average grain size of 0.2 mm.

In the upper part the densely welded Villa Garcia changes into an intensely welded and rheomorphic to lava-like ignimbrite (Figure 40 a), with a minimum thickness of 50 m, exposed in the central and southern part of the study area. The rocks are massive to flow-laminated, lava-like and lithic-poor, with ubiquitous meter-scale rheomorphic folds and platy joints. Fiammes are not observable in the rheomorphic ignimbrite. Its mineralogy is similar to the rest of the unit, but crystals are conspicuously larger. In thin sections the rocks can be described as holohyaline to hypocrystalline. Furthermore, flow structures and a beginning devitrification are observable in the glassy matrix. Mineral characteristics are similar to the densely-welded and crystal-rich ignimbrite (Figure 40 b and c), but the abundances are lower.

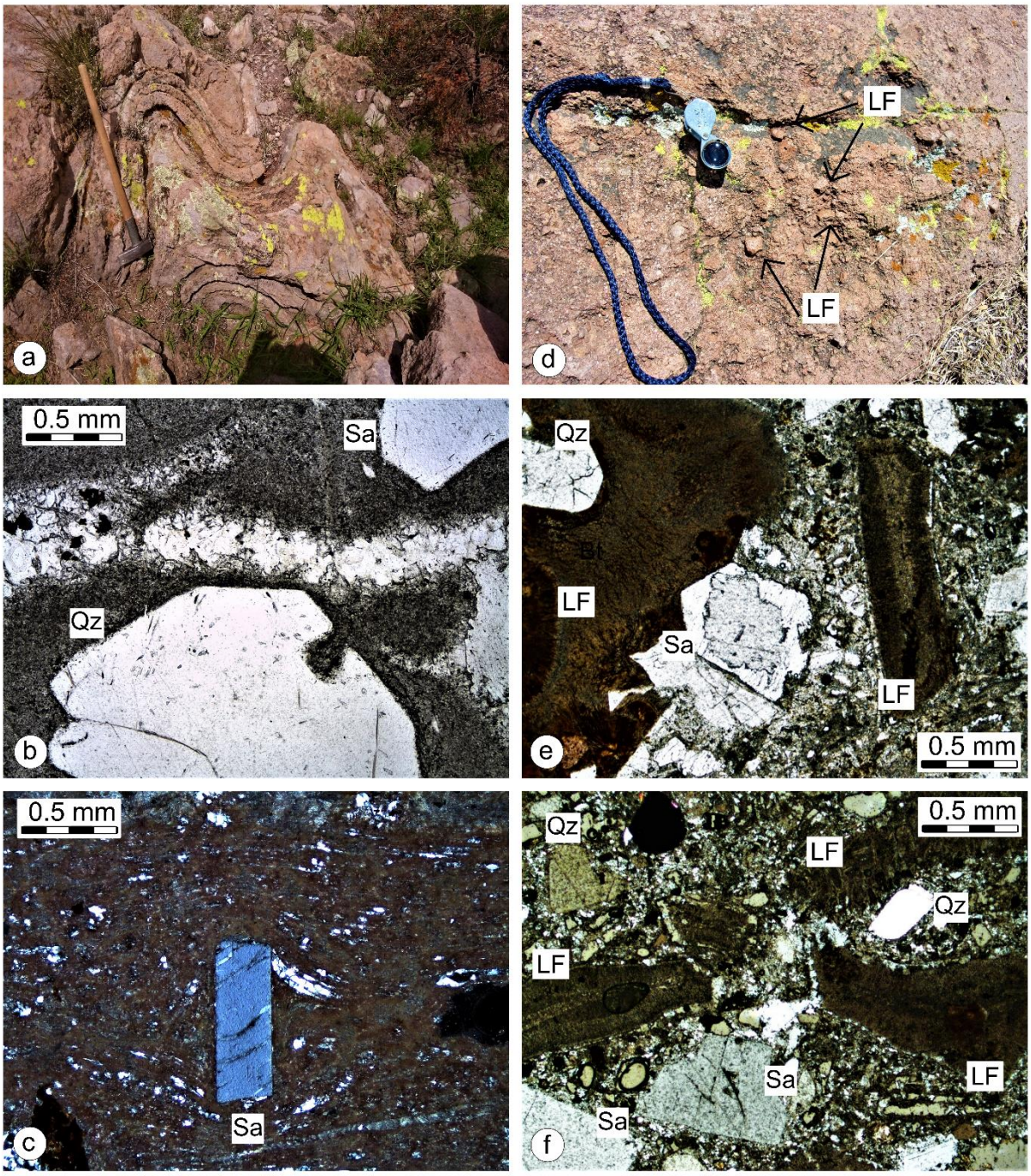

Figure 40: Field photography and thin section images of the top of the Villa Garcia Ignimbrite. a) and d) Representative field picture of the exposure of the Villa Garcia Ignimbrite. b), c), e) and f) Thin section images of the Villa Garcia Ignimbrite a) Rheomorphic, lava-like and crystal-poor ignimbrite showing rheomorphic folds. Size of hammer is 0.5 m. b) Quartz and sanidine crystals separated by a fiamme, consisting of mainly quartz. c) Rotated sanidine crystal in the fine-grained matrix of the lava-like, rheomorphic ignimbrite. d) Field picture of the massive lithic rich breccia from the top of the Villa Garcia Ignimbrite. e) Thin section image of the massive lithic-rich breccia from the top of the Villa Garcia Ignimbrite. f) Thin section image of the massive lithic-rich breccia from the top of the Villa Garcia Ignimbrite. Picture taken with crossed nichols. LF: lithic fragment, Qz: Quartz, Sa: sanidine.

In addition, xenomorphic quartz crystals and hypidiomorphic sanidine crystals often form granophyric intergrowths. The top of the Villa Garcia Ignimbrite is formed by an up to 10 m thick massive lithic rich breccia (Figure 40 d), which is only present in the northwestern portion of the study area. The breccia is thin and discontinuous and is not associated to a caldera collapse breccia. Besides the above-mentioned phenocrysts, the breccia contains in-situ ignimbrite clasts as well as carbonate, sand- and siltstone clasts (Figure 40 e and f). Like the other sections of the ignimbrite described above, the glassy matrix of the massive lithic breccia shows beginning devitrification.

Polymictic conglomerate

In-between the Villa Garcia and the Loreto Ignimbrite (Figure 38 b, Figure 41) an, up to 10 m thick continental sedimentary conglomerate, was deposited. The contact between the polymictic conglomerate and the Villa Garcia ignimbrite is erosive discordant. The polymictic conglomerate is matrix-supported, generally fine-grained to medium-grained. Clasts in the polymictic conglomerate were derived mainly from the Villa Garcia Ignimbrite and the Mesozoic basement. The polymictic conglomerate is only present in the center and western part of the study area and the top is built up by a paleosol.

Loreto Ignimbrite

The polymictic conglomerate and paleosol are erosively covered by the Loreto Ignimbrite (Figure 42 a – c). The Loreto Ignimbrite is mainly exposed in the western portion of the area and its base is formed by a black and crystal poor (3 vol.% of phenocrystals, mainly quartz and sanidine) vitrophyre that shows a starting to intensive devitrification (Figure 42 a). In thin sections the basal vitrophyre can be described as seriate, holocrystalline and it shows perlitic cracks, flow structures, as well as a beginning to intense devitrification (Figure 42 d and e). Quartz crystals (~ 1 vol.%) are xenomorphic with an average grain size of 1 mm. Sanidines (~ 2 vol.%) have an average grain size of 0.5 mm, the shape is hypidiomorphic to xenomorphic and they show Carlsbad twinning. The vitrophyre show no layering or graduation in grain size and gradually turns into a pale reddish massive and densely welded porphyritic rhyolitic and vesicle-rich ignimbrite.

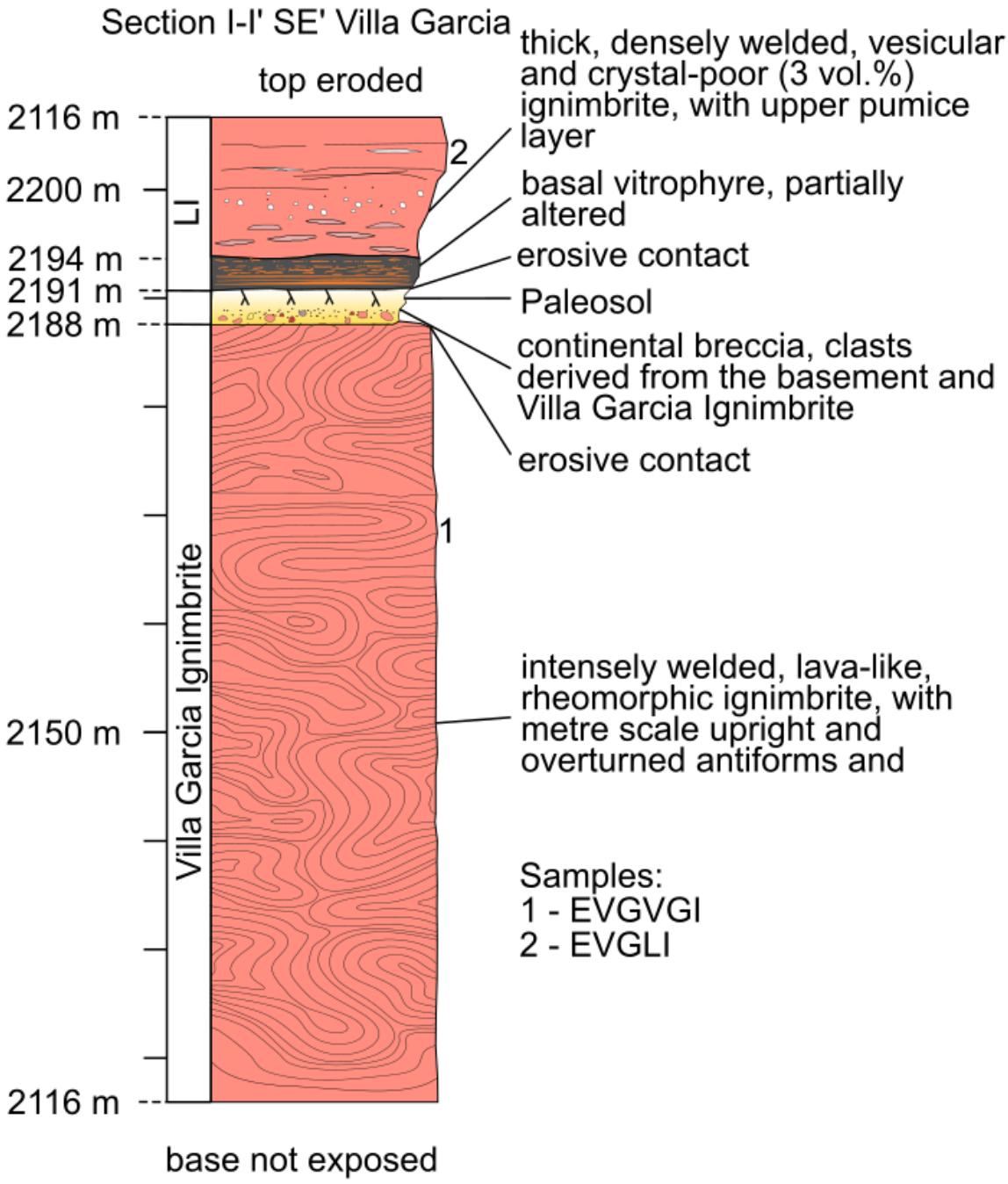

Figure 41: Logged section I-I' southeast of Villa Garcia (Zacatecas), showing the relationship between the Villa Garcia Ignimbrite, the interlayered sediments and the Loreto Ignimbrite and their lithological features. The labels correspond to the sections indicated in the geological map shown in Figure 30. Symbols and stratigraphy are explained in Figure 32. LI: Loreto Ignimbrite.

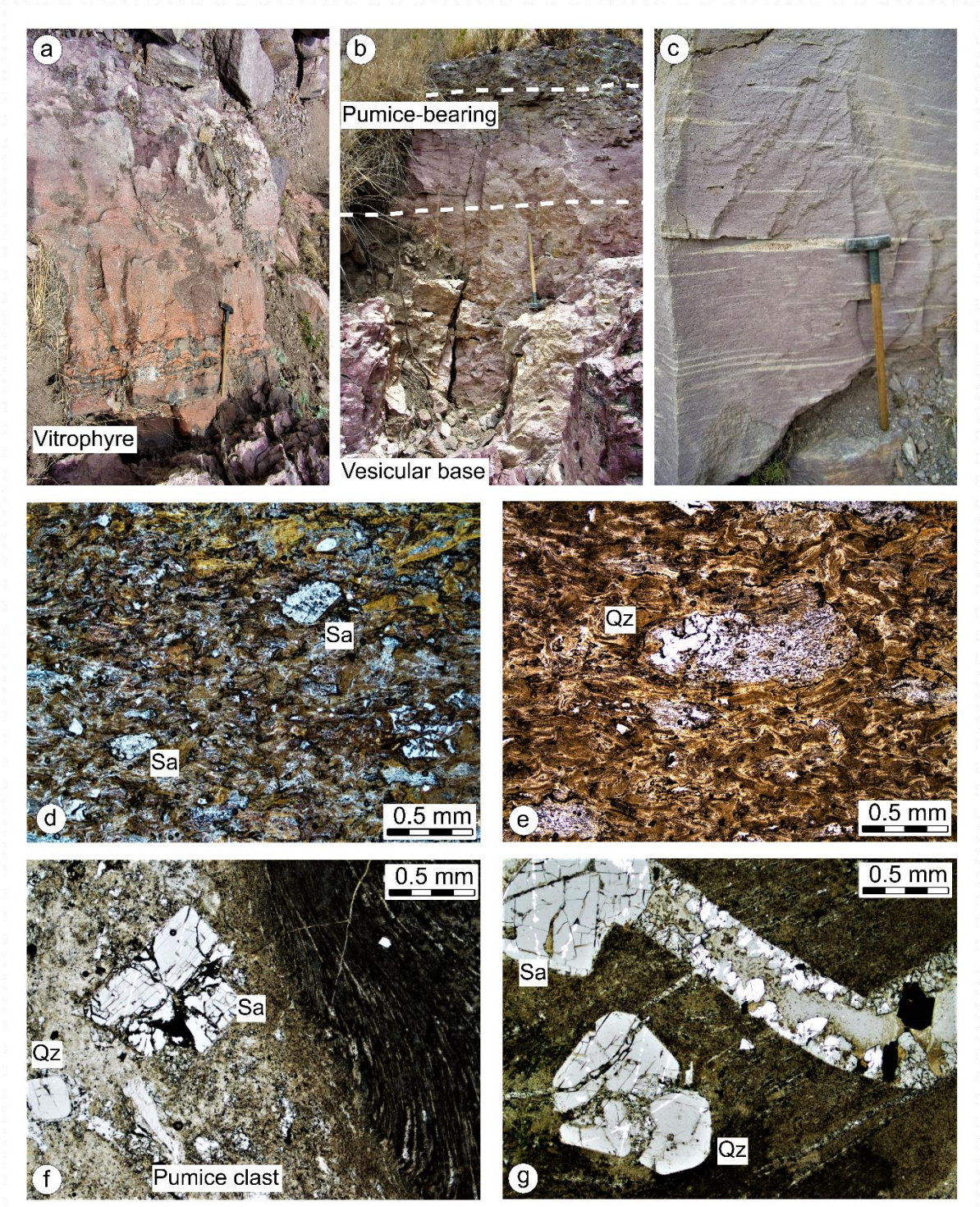

Figure 42: Field photography and thin section images of the Loreto Ignimbrite. a) -c) Representative field picture of the exposure of the Loreto Ignimbrite. a) Vitrophyre of the Loreto Ignimbrite in the western part of the study area, southeast of Loreto. Size of the hammer is 0.5 m. b) Representative outcrop of the vesicular base of the Loreto Ignimbrite in the western part of the study area, southeast of Loreto. Size of hammer is 0.5 m. c) Representative exposure of the densely welded Loreto Ignimbrite. Size of the hammer is 0.5 m. d) – g) Thin section images of the Loreto Ignimbrite. d) Sanidine crystals in the devitrified glassy matrix of the basal vitrophyre. Picture taken with crossed nichols. e) Quartz crystal in the devitrified matrix of the basal vitrophyre. f) Contact of a pumice clast and the fine-grained matrix. Pumice clast contains hypidiomorphic sanidine and xenomorphic quartz crystals. g) Sanidine and quartz in the fine-grained matrix. Picture taken with crossed nichols. Qz: quartz, Sa: Sanidine.

The lower part of the Loreto Ignimbrite is pale reddish, up to 7 m thick, densely welded and crystal-poor (approximately 3 vol.% of quartz and sanidine phenocrysts). The elliptical vesicles in the base of the unit decrease in number and size to the top, transforming into a densely welded ignimbrite. At the point, where the vesicles are no longer present appears a 40 cm thin and crystal poor layer, with up to 5 cm spherical pumice clasts. This pumice clast rich layer forms the top of the sub-sequence. Pumice clasts show the same mineral content but the modal abundances are higher (quartz, 10 vol.%; sanidine, 15 vol.%; plagioclase, 10 vol.%; Figure 42 f).

After the disappearance of pumice clasts, the Loreto Ignimbrite can be described as a densely-welded and massive ignimbrite. It is pale reddish to gray, up to 45 m thick and shows up 10 cm thick and 75 cm long fiammes. From the base of the sub-sequence of the densely-welded and massive ignimbrite the amount and size of the fiammes increases. The ignimbrite contains around 15 vol.% phenocrysts, mainly quartz and sanidine, subordinated plagioclase. In thin section, the ignimbrite can be described as seriate and holocrystalline and a beginning devitrification of the matrix is observable (Figure 42 g). Like the matrix of the Villa Garcia Ignimbrite, it consists mainly of collapsed and elongated ash and glass particles. Sanidine crystals (~ 6 vol.%) have an average grain size of 3 mm, the shape is hypidiomorphic to xenomorphic and they show Carlsbad twinning. Xenomorphic quartz crystals (~ 6 vol.%) with an average grain size of 0.5 mm and hypidiomorphic to idiomorphic and in average 0.5 mm big plagioclase (~3 vol.%) crystals, with polysynthetic twinning, are also present in the samples. The densely welded ignimbrite (Figure 43) turns into lava-like and rheomorphic ignimbrite that do not have fiammes and show a stronger devitrification of the matrix compared to the densely welded ignimbrite. In thin sections the rocks show comparable to the rheomorphic sequence of the Villa Garcia Ignimbrite. The ignimbrite in this part is massive to flow-laminated and lava-like, with ubiquitous metre-scale rheomorphic folds and platy joints. As in the rheomorphic sequence of the Villa Garcia Ignimbrite fiammes are not observable and its mineralogy is similar to the rest of the unit, but crystals are conspicuously larger. In thin sections, the rocks can be described as holohyaline to hypocrystalline with a vitrophyric structure. Furthermore, flow structures and an intense devitrification of the matrix is observable. Mineral characteristics are similar to the densely-welded and crystal-rich ignimbrite, but the abundances are lower. In addition, xenomorphic quartz crystals and hypidiomorphic sanidine crystals often form granophyric intergrowths. The top of the Loreto Ignimbrite is eroded and not exposed in the study area.

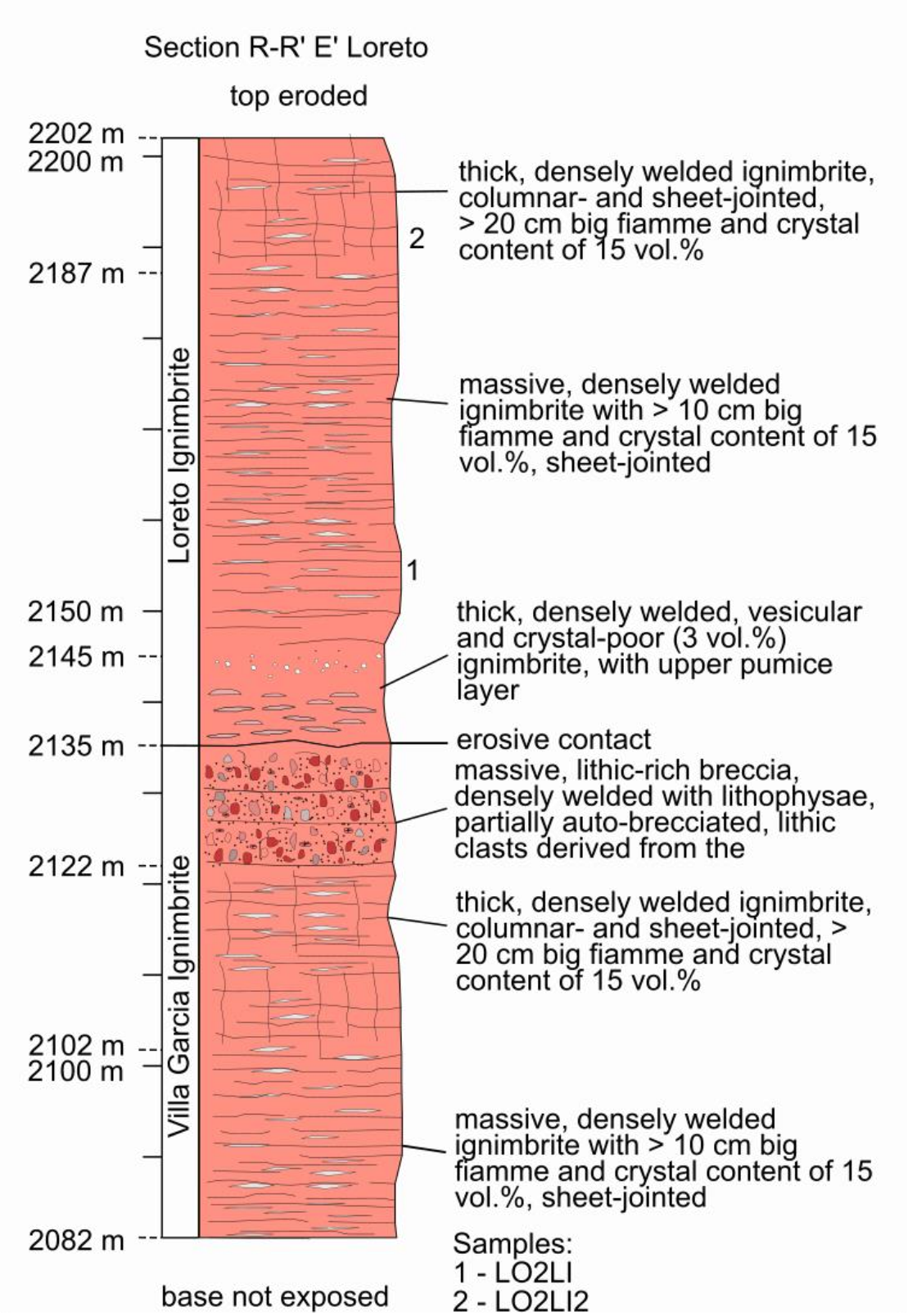

Figure 43: Logged section R-R' east of Loreto (Zacatecas), showing the relationship between the Villa Garcia and Loreto Ignimbrite in the western portion of the study area and their lithological features. The labels correspond to the sections indicated in the geological map shown in Figure 30. Symbols and stratigraphy are explained in Figure 32.

La Milpa Andesite

The Oligocene volcanic activity of the Villa Garcia ignimbrite complex terminated with the eruption of the La Milpa Andesite (Figure 44 a and b).

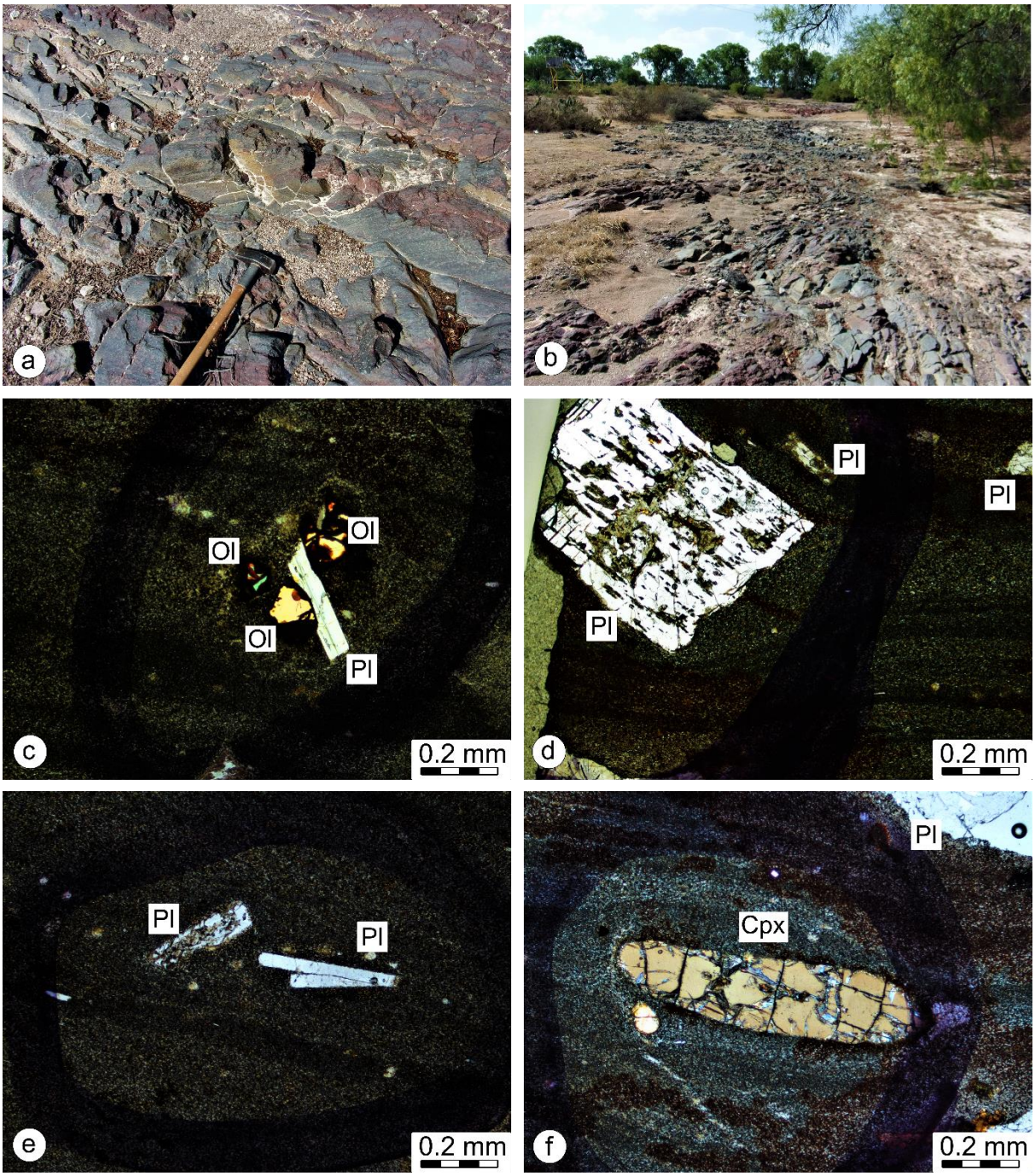

Figure 44: Field photography and thin section images of the La Milpa Andesite. a) and b) Representative field picture of the exposure of the La Milpa Andesite in the southern portion of the study area. Size of the hammer is 0.5 m. c)-f) Thin section images of the La Milpa Andesite. c) Olivine crystals with alteration rim forming together with plagioclase crystal accumulations. d) Altered plagioclase crystal in the fine-grained matrix. e) Plagioclase crystals in the fine-grained matrix. f) Xenomorphic pyroxene crystal in the fine-grained matrix. Cpx: clinopyroxene, Pl: plagioclase, Ol: olivine.

The contact of the Andesite to Loreto Ignimbrite is not exposed in the study area. The andesite is a massive, dark, vesicular rock, with a porphyritic texture and only present isolated in the southern portion of the study area. Pyroxene, olivine, and plagioclase phenocrysts are present in the fine-grained matrix. In thin sections (Figure 44 b – f), the rocks show a porphyritic, seriate and hypocrystalline texture. The groundmass consists of plagioclase microlites, which grain size decrease to the top of the unit. Plagioclase microlites show a pilotaxitic texture. Plagioclase (~3 vol.%) and pyroxene (~2 vol.%) phenocrysts have both an average grain size of 0.5 mm and are hypidiomorphic to xenomorphic. Olivine crystals (1 vol.%) are xenomorphic to hypidiomorphic and in average 0.2 mm big. Olivine and plagioclase crystals form together crystal accumulations (glomerophyric texture).

5.3.2. Whole-rock geochemistry

Analytical results are given in Table 6. Data processing and plots were carried out using GCDkit 4.1 (Janoušek et al., 2006; 2015).

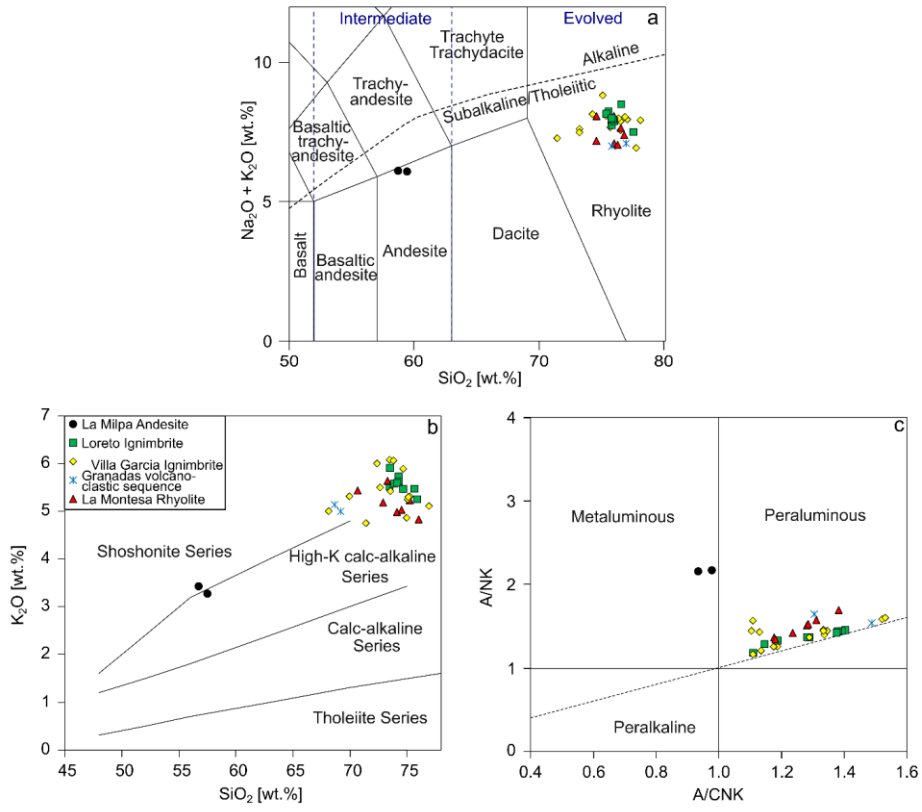

Figure 45: Major element results for Villa Garcia volcanic rocks. a) TAS classification diagram after Le Bas et al. (1986). Alkaline and subalkaline/tholeiitic fields after Miyashiro (1978). b) K_2O vs. SiO_2 diagram after Peccerillo and Taylor (1976). c) A/CNK vs A/NK plot after Shand (1943). A/CNK = $Al_2O_3/(CaO + Na_2O + K_2O)$, in molar ratios; A/NK = $Al_2O_3/(Na_2O+K_2O)$, in molar ratios.

For the geochemical analysis fresh, non-devitrified samples were used, the loss of ignition values (LOI at 1000°C) ranging from 0.56 wt.% for the Loreto Ignimbrite to 3.62 wt.% for the Villa Garcia Ignimbrite. For the two samples of the Granadas volcanoclastic sequence pumice clasts were separated, prepared and analyzed, the LOI values are, compared to the other samples, with values of 9.97 and 9.23 wt.%, higher. The samples of the Loreto Ignimbrite show a relatively narrow range of SiO_2 content (Figure 45 a, TAS diagram), varying between 73.5 and 75.9 wt.%, whereas the samples of the Villa Garcia Ignimbrite range between 68.2 and 76.9 wt.% and the La Montesa Rhyolite between 70.7 and 76.0 wt.%.

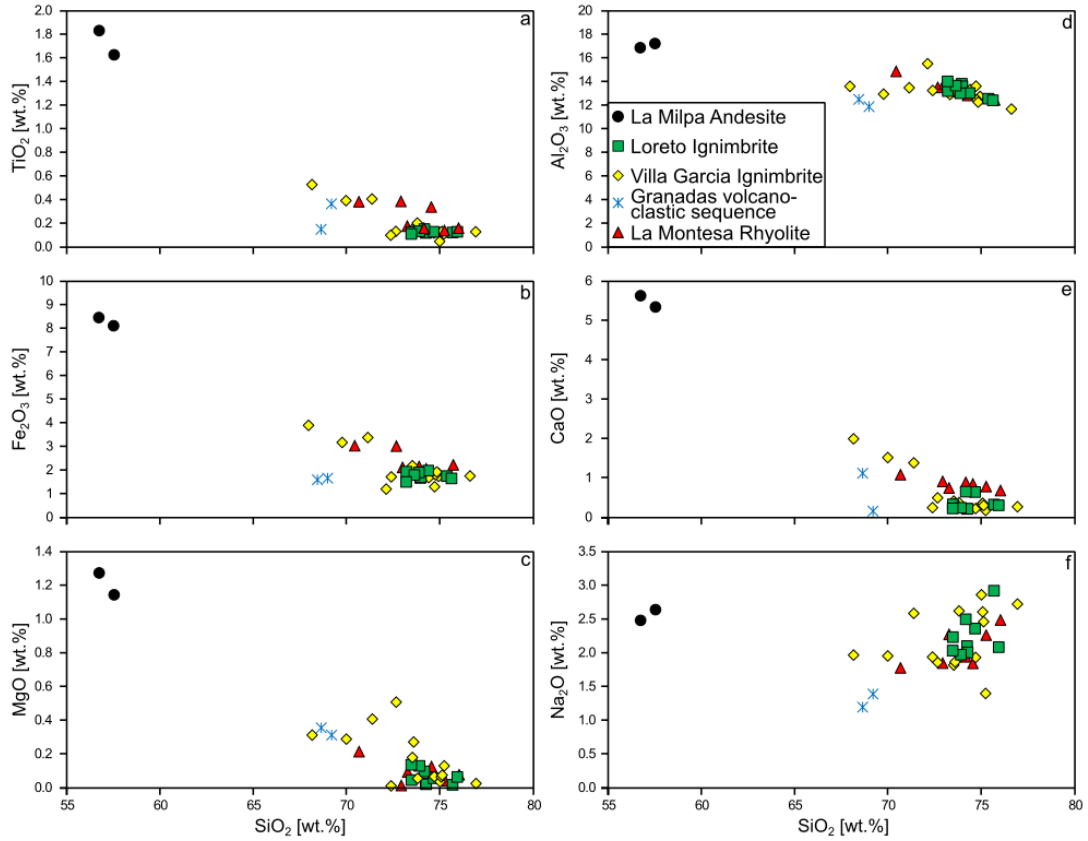

Figure 46: Harker variation diagrams after Harker (1909) with selected major elements for the volcanic rocks of the Villa Garcia Ignimbrite complex.

All samples of the La Montesa Rhyolite, Granadas volcanoclastic sequence, Villa Garcia Ignimbrite, and the Loreto Ignimbrite have a rhyolitic composition and the composition of the La Milpa Aandesite is andesitic. The volcanic rocks of the study area mostly correspond to the high-K calc-alkaline series, with a tendency towards shoshonitic (Figure 45 b). Likewise, the rocks of La Montesa Rhyolite, Granadas volcanoclastic sequence, Villa Garcia Ignimbrite, and the Loreto

Ignimbrite are dominantly peraluminous and those of the La Milpa Andesite are metaluminous (Figure 45 c).

The rhyolitic rocks are low in TiO_2 (< 0.6 wt.%) and MgO (< 0.6 wt.%). In general, the major elements show negative correlations with increasing SiO_2 content, whereas K_2O and to a lesser extent Na_2O display positive correlations (Figure 46 a – f).

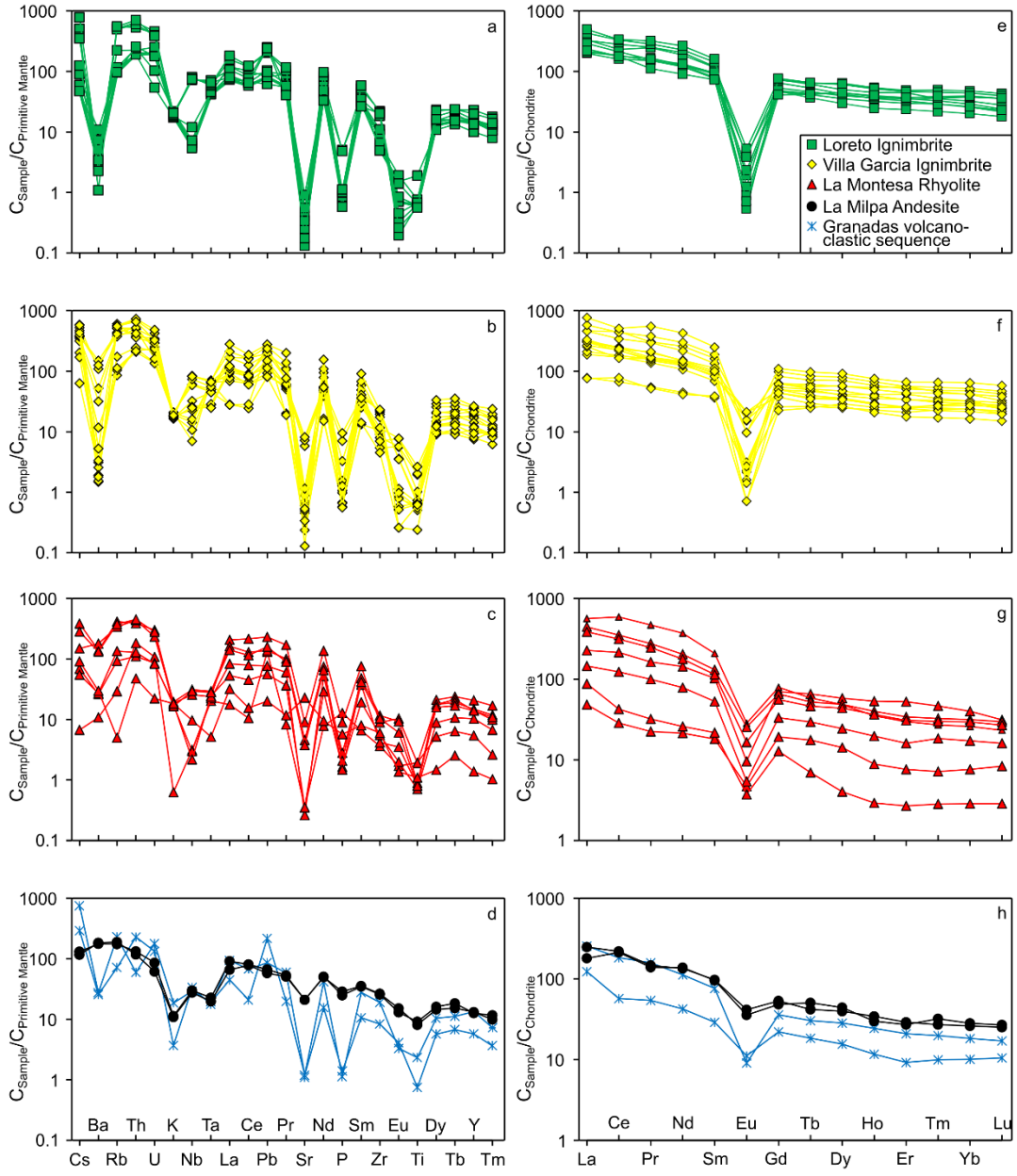

Figure 47 Trace element results for the Villa Garcia ignimbrite complex rocks of this study. a) – d) Primitive mantle-normalized multielement plots for the volcanic rocks of the Villa Garcia area. e) - h) Chondrite-normalized REE plots for the volcanic rocks of the Villa Garcia area. Chondrite and primitive mantle composition after McDonough and Sun (1995).

Table 6: Results of the XRF and ICPMS analyses. Eu* = $\sqrt{Sm_N \times Gd_N}$. Chondrite-normalized values after McDonough and Sun (1995).

Unit	La Montesa Rhyolite							Granadas Volcanoclastic sequence		Villa Garcia Ignimbrite	
Sample	IZVR	ICVI1	LPJL1	ELSL1	ELSL2	GL	IC3B1-1	IZTB	ELST	LORI	LCIB
Lat. N	22.0957	22.0954	22.0922	22.1151	22.1145	22.0552	22.0944	22.1008	22.1132	22.1224	22.1234
Long. W	101.5235	101.5235	101.4621	101.5524	101.5334	101.5151	101.5233	101.523	101.5335	101.5947	101.5604
SiO_2	72.93	70.67	73.27	74.16	75.26	76.02	74.55	69.21	68.65	73.79	73.51
TiO_2	0.39	0.38	0.18	0.16	0.14	0.16	0.34	0.37	0.15	0.20	0.15
Al_2O_3	13.52	14.88	13.83	13.09	12.71	12.46	12.84	11.90	12.50	13.13	13.80
Fe_2O_3	3.02	3.04	2.13	2.17	1.86	2.23	2.06	1.67	1.60	2.20	1.66
MnO	0.01	0.02	0.01	0.01	0.01	0.01	0.01	0.02	0.01	0.04	0.02
MgO	0.01	0.22	0.09	0.10	0.04	0.08	0.13	0.31	0.36	0.06	0.18
CaO	0.92	1.09	0.75	0.89	0.79	0.69	0.85	0.16	1.12	0.38	0.42
Na_2O	1.85	1.78	2.27	1.94	2.26	2.49	1.85	1.39	1.20	2.62	1.82
K_2O	5.18	5.42	5.63	4.98	5.23	4.81	5.02	5.01	5.15	6.07	6.08
P_2O_5	0.07	0.09	0.04	0.06	0.03	0.03	0.06	0.02	0.03	0.02	0.02
LOI	1.87	1.72	1.17	1.66	1.03	0.80	2.16	9.97	9.23	0.94	1.54
Sum	99.77	99.31	99.37	99.23	99.38	99.78	99.88	100.04	100.01	99.45	99.20
Cs	0.14	8.04	3.13	1.43	1.15	5.89	1.91	15.91	6.12	12.09	7.33
Rb	17.44	248.79	202.54	55.74	80.32	225.48	3.01	135.72	42.78	332.61	227.08
Ba	70.93	913.31	1176.67	171.76	179.44	871.22	196.70	180.58	168.83	11.89	343.90
Sr	7.00	178.12	91.07	5.20	7.00	75.18	452.23	23.85	24.09	10.61	17.66
Pb	19.50	34.36	20.59	11.39	8.34	23.79	2.99	32.53	12.86	35.44	29.07
Th	14.56	30.54	34.79	8.75	10.15	35.71	3.76	4.71	18.11	52.34	38.75
U	2.18	6.06	4.74	1.74	1.67	5.65	0.45	3.59	2.69	6.60	3.24
Zr	37.80	93.59	121.15	43.90	57.86	108.60	63.18	87.50	199.27	242.48	57.29
Hf	0.71	2.94	4.95	1.01	1.36	4.30	1.21	3.67	1.58	9.62	2.73
Ta	0.75	0.88	1.08	0.83	0.91	1.04	0.19	0.71	0.65	2.45	1.84
Y	23.23	60.58	63.41	89.14	44.04	59.48	5.91	24.48	57.48	40.41	85.31
Nb	2.06	16.84	20.34	1.96	1.43	19.38	6.37	19.15	21.62	54.14	40.02
Sc	34.70	13.02	13.13	8.29	8.39	12.45	14.01	7.49	22.28	5.73	8.17
Cr	15.87	5.62	11.17	22.09	32.19	6.90	16.06	10.71	51.14	1.57	8.43
Ni	6.82	2.17	2.61	9.53	7.44	1.57	0.99	8.87	45.71	0.65	1.91
Co	3.41	2.55	1.22	3.50	3.36	0.96	0.17	4.92	10.23	0.07	0.86
V	25.37	15.45	41.11	136.52	83.88	32.79	23.41	53.92	150.56	2.26	9.00
La	11.42	133.14	104.76	53.63	34.36	91.09	20.73	29.12	60.51	78.57	109.82
Ce	17.49	360.05	215.59	131.05	75.13	192.36	25.90	35.14	111.80	141.62	277.20
Pr	2.08	43.26	25.50	15.13	9.24	22.77	2.96	5.05	14.72	19.45	28.24
Nd	9.77	169.37	92.44	65.10	35.94	80.77	11.82	19.46	51.31	67.42	117.87
Sm	2.68	30.74	19.34	15.16	7.82	16.79	3.22	4.29	11.25	14.74	23.91
Eu	0.26	1.59	1.43	0.54	0.31	0.93	0.21	0.63	0.51	0.04	0.86
Gd	3.82	15.72	13.03	13.91	6.62	11.08	2.53	7.15	4.38	8.65	16.33
Tb	0.63	2.10	1.88	2.36	1.06	1.66	0.25	0.67	1.10	1.26	2.56
Dy	3.49	11.89	11.97	14.19	5.96	10.72	0.99	3.82	7.00	8.36	17.25
Ho	0.48	1.92	2.18	2.90	1.07	1.98	0.16	1.33	0.64	1.54	3.18
Er	0.41	4.75	5.45	8.41	2.56	4.92	0.43	3.34	0.88	4.10	8.13
Tm	0.18	0.67	0.80	1.14	0.46	0.74	0.07	0.25	0.49	0.66	1.19
Yb	1.23	4.17	5.09	6.40	2.77	4.75	0.46	1.63	2.95	4.38	7.65
Lu	0.20	0.57	0.73	0.77	0.40	0.66	0.07	0.26	0.42	0.63	1.04
Eu/Eu*	0.251	0.220	0.275	0.113	0.129	0.208	0.224	0.173	0.440	0.011	0.133
$(La/Yb)_N$	5.797	24.245	14.896	7.234	9.025	14.326	30.739	14.954	11.729	12.945	10.961

Table 6: continued

Unit	Villa Garcia Ignimbrite											
Sample	IC3Vi1	IC2I	CIB	LPJIB	NVGIB	EVGVGI	GLI	NG1VI	NG1VGI	NG2VI	NG2IB	NG3IB
Lat. N	22.1006	22.0905	22.0951	22.0955	22.1046	22.0901	22.0544	22.0628	22.0635	22.0623	22.0622	22.0715
Long. W	101.5237	101.5351	101.5103	101.4630	101.5624	101.5803	101.5139	101.5141	101.5139	101.5117	101.5113	101.5007
SiO_2	69.97	72.65	72.37	74.68	75.22	74.99	76.92	75.06	71.37	68.15	75.12	73.58
TiO_2	0.39	0.13	0.10	0.12	0.11	0.05	0.13	0.13	0.41	0.53	0.13	0.13
Al_2O_3	12.95	13.25	15.53	13.34	12.75	13.62	11.68	12.48	13.49	13.62	12.28	12.93
Fe_2O_3	3.18	1.72	1.20	1.70	1.75	1.31	1.76	1.82	3.39	3.91	1.93	1.75
MnO	0.15	0.01	0.01	0.01	0.01	0.02	0.02	0.01	0.02	0.03	0.01	0.01
MgO	0.29	0.51	0.01	0.07	0.13	0.04	0.03	0.07	0.41	0.31	0.08	0.27
CaO	1.52	0.50	0.25	0.23	0.18	0.33	0.28	0.36	1.39	2.00	0.31	0.36
Na_2O	1.96	1.86	1.94	1.93	1.40	2.86	2.73	2.61	2.59	1.97	2.46	1.87
K_2O	5.31	5.51	6.00	5.90	5.31	4.87	5.11	5.25	4.75	5.00	5.30	5.43
P_2O_5	0.15	0.01	0.07	0.01	0.02	0.01	0.03	0.01	0.03	0.20	0.03	0.01
LOI	3.50	3.14	1.54	1.35	2.44	1.34	0.80	1.58	1.58	3.62	1.80	2.97
Sum	99.37	99.31	99.02	99.34	99.33	99.45	99.48	99.38	99.42	99.34	99.43	99.31
Cs	6.66	11.04	4.27	3.56	1.32	7.62	12.31	7.83	9.86	8.03	8.22	9.11
Rb	225.44	311.63	51.34	104.33	62.39	67.67	362.65	338.26	305.97	262.43	247.41	338.20
Ba	209.65	719.81	77.32	20.59	16.94	22.03	34.77	9.78	12.67	989.22	825.95	10.17
Sr	22.91	116.32	23.00	14.00	9.00	12.00	4.73	2.57	6.73	144.11	161.99	9.92
Pb	28.86	18.89	13.93	17.15	12.09	12.16	31.86	38.34	29.73	22.41	16.87	41.55
Th	38.73	30.04	18.97	19.54	16.53	17.14	28.54	55.22	40.32	41.24	33.38	58.22
U	5.12	6.95	2.77	4.34	2.74	4.84	5.90	8.63	7.03	4.79	5.93	9.77
Zr	203.53	83.95	109.48	94.37	109.36	103.44	47.37	182.18	223.63	73.42	121.62	236.54
Hf	7.43	3.13	2.76	2.59	2.53	2.61	3.32	8.22	8.09	2.81	3.50	0.70
Ta	1.67	1.03	2.39	2.62	2.41	2.22	1.66	2.61	2.05	1.06	0.92	2.54
Y	61.07	52.58	79.70	103.28	45.47	73.27	32.27	106.30	90.78	34.31	51.12	113.26
Nb	38.49	14.88	9.35	4.59	10.53	7.04	21.20	54.23	48.24	17.03	16.30	55.30
Sc	8.32	11.52	9.76	7.34	9.86	7.97	19.63	7.13	6.36	13.30	12.71	6.65
Cr	11.87	7.24	7.83	9.71	18.44	12.66	8.64	5.65	3.17	7.76	8.08	4.04
Ni	1.35	2.20	6.35	5.42	6.78	6.73	3.87	0.94	0.41	2.03	1.65	0.67
Co	0.31	9.26	4.37	3.12	1.61	0.82	0.18	0.17	0.21	2.52	3.01	0.29
V	9.21	14.87	20.11	30.34	13.79	18.19	3.38	4.38	3.02	20.95	20.13	5.71
La	108.63	63.37	44.58	49.85	18.41	60.06	17.96	136.61	74.89	71.22	72.06	180.89
Ce	210.03	135.54	104.81	111.36	40.79	100.33	47.69	268.49	152.30	133.23	146.09	311.50
Pr	27.38	13.84	12.76	14.51	5.08	14.87	4.81	34.94	18.68	14.85	15.59	51.13
Nd	98.95	56.83	48.76	60.32	20.42	63.01	18.86	136.37	69.17	59.44	66.48	195.34
Sm	19.86	12.82	10.21	13.82	5.36	13.61	5.73	27.63	16.58	12.07	14.71	36.87
Eu	0.55	0.88	0.18	0.13	0.12	0.15	0.04	0.09	0.08	1.18	1.19	0.54
Gd	12.42	8.76	9.75	12.47	5.11	10.79	4.47	19.43	12.11	7.42	9.88	21.88
Tb	1.82	1.32	1.67	2.17	0.95	1.80	0.89	2.98	1.99	1.05	1.43	3.50
Dy	11.63	8.73	10.13	13.74	6.07	9.76	7.09	19.55	14.04	6.45	8.79	22.46
Ho	2.13	1.60	2.23	2.94	1.25	1.94	1.38	3.62	2.71	1.14	1.60	4.11
Er	5.39	4.05	6.69	8.86	3.34	5.53	4.02	8.95	7.01	2.82	3.85	10.53
Tm	0.81	0.61	0.88	1.13	0.56	0.75	0.68	1.33	1.07	0.42	0.55	1.62
Yb	5.17	3.79	5.16	6.63	3.88	4.68	4.77	8.28	6.70	2.64	3.48	10.36
Lu	0.74	0.54	0.60	0.80	0.49	0.59	0.67	1.15	0.94	0.37	0.48	1.43
Eu/Eu*	0.107	0.253	0.054	0.030	0.071	0.038	0.024	0.012	0.017	0.380	0.301	0.058
$(La/Yb)_N$	15.237	12.181	7.685	6.473	3.876	10.586	2.782	12.330	8.270	19.980	15.583	13.130

Table 6: continued

Unit	Loreto Ignimbrite									La Milpa Andesite	
Sample	LOVI	LOVIT	LOIT	LCIT	LO2LI	LO2LI2	ELSIB	NVGIT	EVGLI	LMAB1	LMAB2
Lat. N	22.1205	22.1203	22.1155	22.1235	22.1203	22.1415	22.1136	22.1112	22.0942	22.0331	22.0339
Long. W	101.5925	101.5924	101.5922	101.5557	101.5924	101.5657	101.5346	101.5528	101.5844	101.5204	101.5203
SiO_2	75.67	74.24	74.27	73.48	74.66	74.16	73.91	75.93	73.46	57.54	56.74
TiO_2	0.12	0.12	0.12	0.13	0.13	0.15	0.13	0.13	0.11	1.63	1.83
Al_2O_3	12.58	13.83	13.62	13.22	13.04	13.04	13.67	12.43	14.03	17.23	16.88
Fe_2O_3	1.75	1.67	1.70	1.93	1.98	1.91	1.80	1.65	1.50	8.12	8.47
MNO	0.02	0.02	0.02	0.01	0.01	0.01	0.01	0.01	0.01	0.12	0.13
MGO	0.02	0.03	0.02	0.05	0.06	0.10	0.13	0.07	0.14	1.14	1.27
CAO	0.33	0.22	0.22	0.33	0.65	0.66	0.24	0.31	0.23	5.35	5.64
NA_2O	2.92	2.10	2.01	2.24	2.36	2.50	1.98	2.09	2.04	2.64	2.48
K_2O	5.47	5.63	5.72	5.52	5.47	5.60	5.59	5.26	5.91	3.27	3.43
P_2O_5	0.01	0.02	0.02	0.02	0.02	0.04	0.02	0.02	0.02	0.60	0.61
LOI	0.56	1.47	1.60	2.16	0.96	0.96	1.88	1.46	1.75	1.59	1.77
Sum	99.45	99.34	99.33	99.08	99.35	99.12	99.36	99.35	99.21	99.23	99.26
Cs	10.50	1.06	1.89	7.79	1.25	0.99	16.36	2.61	7.31	2.74	2.43
Rb	327.55	56.94	133.25	304.99	69.64	69.51	295.33	57.91	330.47	104.81	112.94
Ba	7.11	19.73	22.80	22.29	70.98	47.85	22.40	33.59	14.86	1163.06	1201.95
Sr	2.62	5.00	18.00	10.91	6.98	8.00	6.71	11.00	3.49	415.44	417.88
Pb	30.11	12.05	15.43	37.34	9.25	12.05	31.61	14.62	35.83	9.94	8.65
Th	42.10	15.24	17.75	51.27	15.10	19.07	47.44	20.35	55.73	10.51	9.30
U	8.61	3.99	5.08	9.24	1.09	2.08	7.93	3.57	7.73	1.73	1.24
Zr	230.21	97.05	114.50	192.75	57.61	69.06	220.98	51.36	211.15	276.84	268.42
Hf	8.30	2.31	2.94	9.44	1.32	1.75	9.08	1.40	9.07	7.29	7.13
Ta	2.15	1.53	1.64	2.64	1.68	1.70	2.27	1.68	2.42	0.84	0.73
Y	98.12	65.71	68.58	56.55	42.58	68.04	85.49	61.25	57.45	56.66	54.09
Nb	52.59	3.88	4.28	47.26	3.52	4.73	49.48	7.89	48.70	19.59	18.17
Sc	7.22	6.68	6.99	5.46	5.14	7.03	5.83	8.15	5.87	27.78	25.92
Cr	10.74	22.10	7.34	3.91	14.17	15.18	2.97	19.32	3.15	9.52	10.78
Ni	0.89	5.01	5.04	0.64	6.03	6.48	0.79	5.37	0.62	1.98	2.29
Co	0.13	0.42	0.28	0.46	0.16	0.19	0.12	0.14	0.09	15.42	14.86
V	5.58	13.82	15.89	2.29	16.72	16.84	4.38	18.64	4.23	106.06	103.17
La	101.16	46.93	55.36	68.08	48.48	76.77	116.42	78.51	51.35	58.76	42.56
Ce	200.35	97.44	108.92	128.22	112.74	171.52	204.77	141.23	107.95	134.71	130.56
Pr	26.07	14.01	15.35	14.56	13.84	23.04	29.46	22.65	10.26	13.56	12.87
Nd	102.63	54.64	58.00	60.18	57.20	92.66	119.89	85.23	40.93	61.81	62.82
Sm	21.04	11.27	13.28	13.99	11.78	17.58	23.57	17.06	10.69	14.42	14.14
Eu	0.03	0.11	0.13	0.05	0.23	0.30	0.07	0.22	0.04	2.34	2.01
Gd	14.33	9.17	10.55	9.56	9.34	14.53	15.13	12.81	8.11	10.59	9.64
Tb	2.28	1.48	1.66	1.56	1.32	2.20	2.33	1.91	1.50	1.51	1.82
Dy	15.59	8.70	9.67	10.84	7.25	12.24	14.92	10.28	10.84	9.75	10.87
Ho	2.93	1.75	2.00	2.09	2.45	1.34	2.81	1.94	2.16	1.87	1.89
Er	7.77	4.76	5.73	5.56	7.04	3.75	7.32	5.19	5.86	4.63	4.60
Tm	1.21	0.71	0.80	0.90	0.53	0.87	1.11	0.71	0.95	0.67	0.79
Yb	7.62	4.11	4.65	6.04	3.23	5.21	7.01	4.19	6.29	4.22	4.53
Lu	1.05	0.53	0.58	0.88	0.44	0.68	0.97	0.56	0.88	0.62	0.66
Eu/Eu*	0.005	0.032	0.033	0.013	0.068	0.056	0.011	0.044	0.013	0.577	0.525
$(La/Yb)_N$	10.000	9.191	9.839	8.030	11.476	11.686	12.458	14.525	6.057	9.837	6.693

Incompatible trace elements patterns, normalized to primitive mantle (McDonough and Sun, 1995), display a general negative slope (Figure 47 a- d), with negative anomalies of Ba, Nb, Ta, Sr, Eu, and Ti and positive anomalies Pb, Nd, and Sm and enrichment in large ion lithophile elements (LILE) with respect to high field strength elements (HFSE). Chondrite-normalized REE patterns show a marked enrichment in LREE with respect to HREE. A well-developed negative Eu anomaly is present in all samples of La Montesa Rhyolite, Granadas volcanoclastic sequence, Villa Garcia Ignimbrite, and the Loreto Ignimbrite (Figure 47 e -h), with $(Eu/Eu^*)_N$ (Eu* =

$\sqrt{Sm_N \times Gd_N}$ and N denotes chondrite-normalized values) ranging from 0.05 and 0.440 (Table 6). In contrast the La Milpa Andesite show a slight Eu anomaly ($0.525 \leq (Eu/Eu^*)_N \leq 0.577$). In all samples the light REE (LREE) are more fractionated with respect to the heavy REE (HREE). In general, the HREE have more horizontal pattern compared to the LREE. Moderate REE fractionation patterns is evident as well for most samples, and slightly lower ones for those from the Zaragoza andesite ($2.782 \leq (La/Yb)_N \leq 30.739$; Figure 47 e – h, Table 6).

5.3.3. Mineral Chemistry

EPMA were performed to determine the end-member composition of K-feldspar, plagioclase, pyroxene, and olivine.

The composition of K-feldspars from the studied rhyolitic rocks show comparable results (Figure 48, Appendix K).

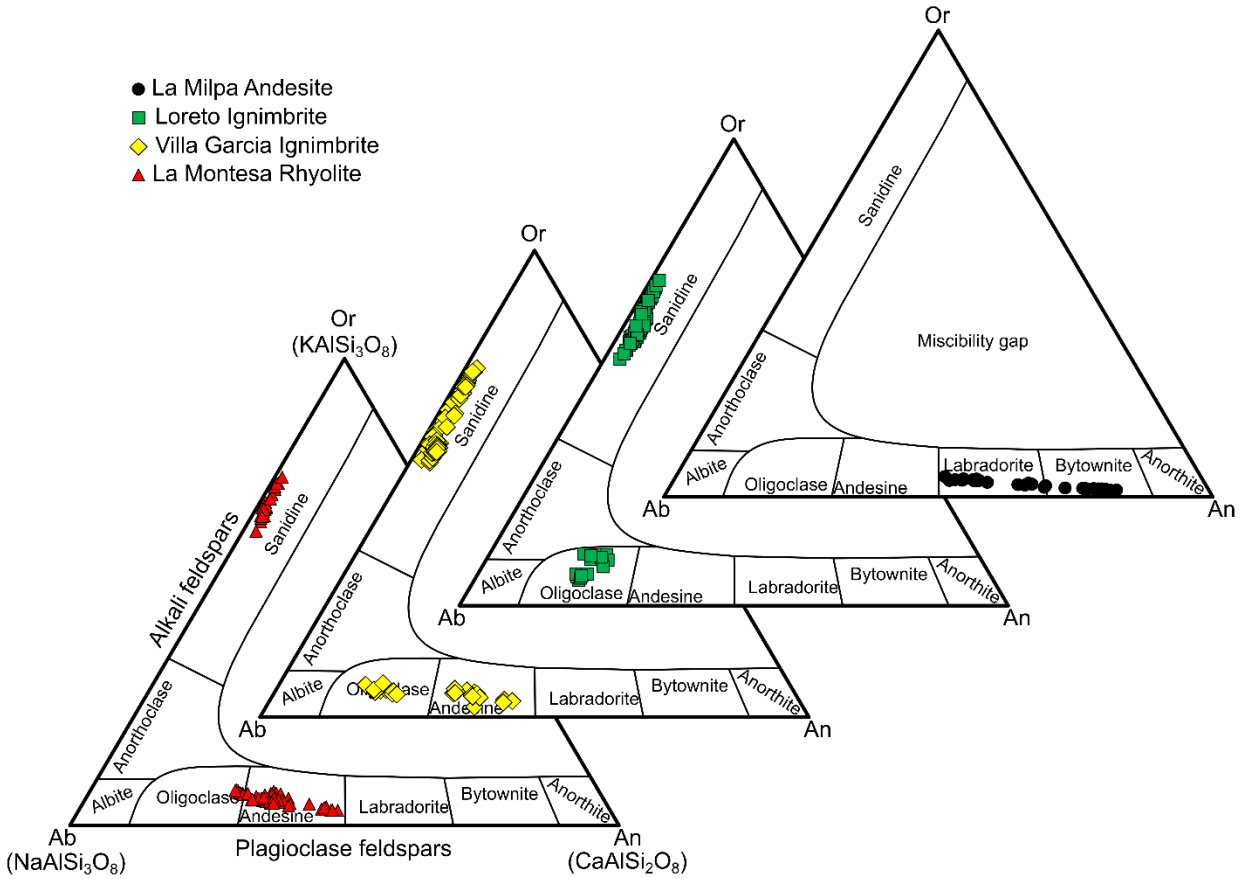

Figure 48: Ternary classification of feldspars from the Villa Garcia Ignimbrite complex.

All analyzed K-Feldspars are sanidines with an orthoclase component between 54.39 and 74.66 %. The analyzed plagioclases show a change in composition from the La Montesa Rhyolite, with

mainly andesine composition (An = 26.40 – 47.17 %) through the plagioclases of the Villa Garcia Ignimbrite, mainly andesine – oligoclase composition (An = 15.82 – 44.30 %) to the plagioclase of the Loreto Ignimbrite that are oligoclase (An = 16.86 – 22.09 %). The plagioclases from the La Milpa Andesite show composition between bytownite and labradorite. Significant changes in plagioclase composition perpendicular to the zonation were not observed.

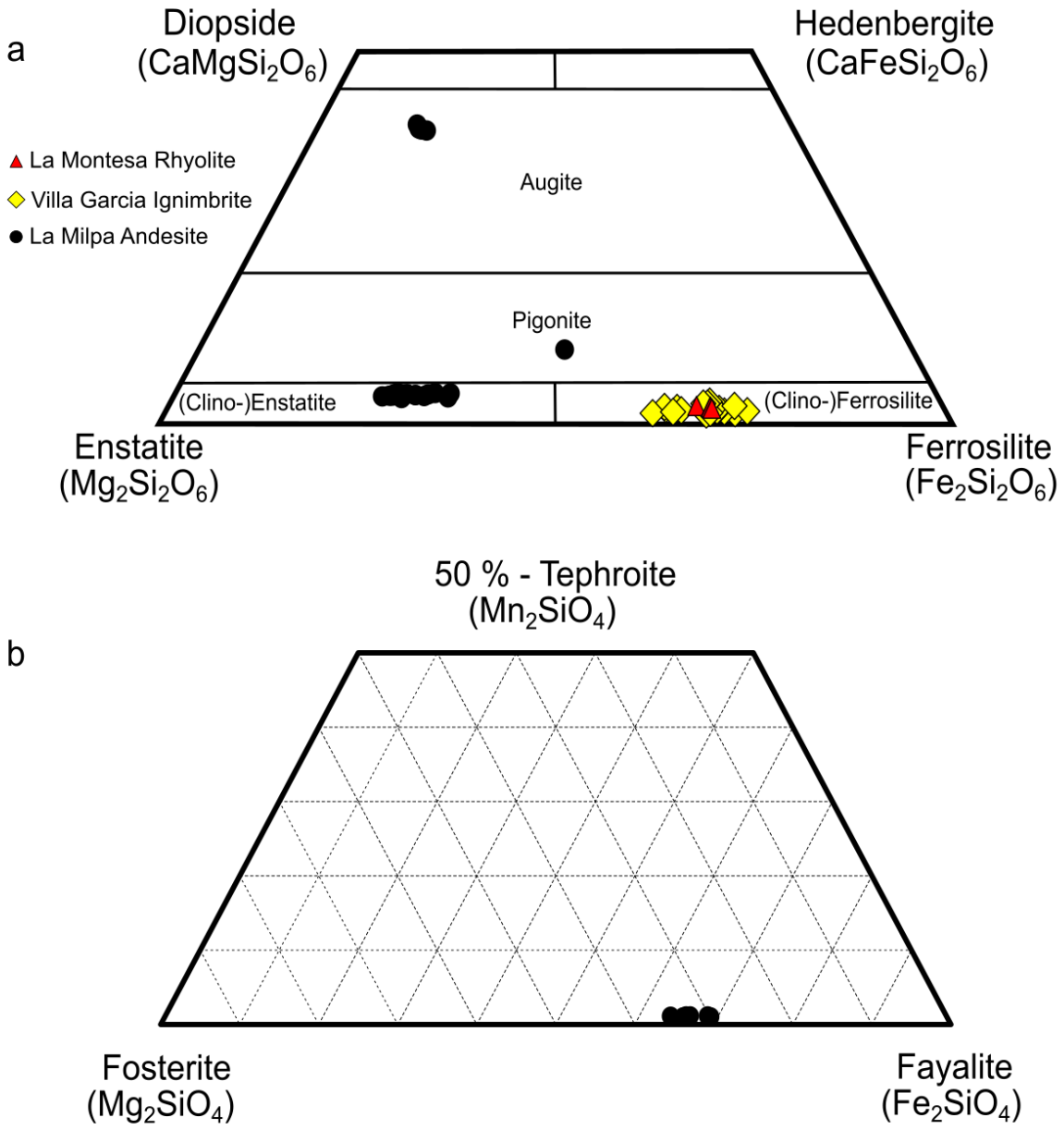

Figure 49: Classification of pyroxenes and olivines from Villa Garcia area. a) Classification of pyroxenes from the La Herradura area in the quaternary Ca-Fe-Mg-system after Morimoto (1988). b) Ternary olivine classification diagram in the system Forsterite-Fayalite-Tephroite.

Orthopyroxene crystals from the La Montesa Rhyolite and the Villa Garcia Ignimbrite show a ferrosilite composition (Figure 49 a, Appendix K). Compared to the orthopyroxenes of the rhyolitic rocks, the analyzed clinopyroxene crystals of the La Milpa Andesite have higher Mg-contents and they are mainly enstatites. Three analyzed pyroxene crystals show augite composition and one pigonite composition. The molar magnesium numbers of the analyzed pyroxenes from the rhyolitic rocks of the study area range between 0.26 and 0.38 (Appendix K). In comparison, pyroxenes from the La Milpa Andesite have higher molar magnesium numbers as the ones of the rhyolitic rocks (Mg# = 0.65 – 0.81).

Olivine is only present in the La Milpa Andesite, the composition of the analyzed olivine crystals is mainly fayalite (63.96 wt.% ≤ Fayalite ≤ 69.05 wt.%; Figure 49 b, Appendix K).

5.3.4. Ar-Ar age determination of sanidine

^{40}Ar-^{39}Ar analytical results are summarized and illustrated in Figure 50.

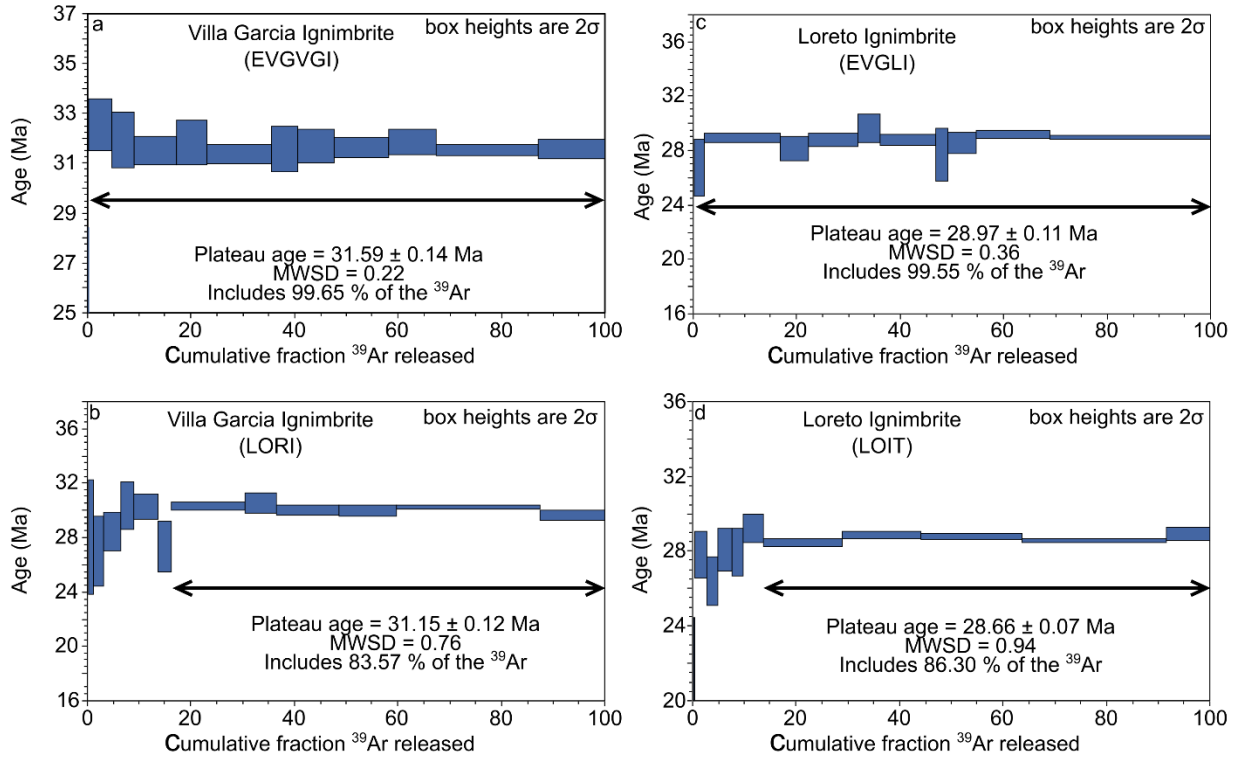

Figure 50: ^{40}Ar/^{39}Ar age spectrum for sanidines from the Villa Garcia area. a) Results of the sanidines from the Villa Garcia Ignimbrite sample EVGVGI. b) Results of the sanidines from the Villa Garcia Ignimbrite sample LORI. c) Results of the sanidines from the Loreto Ignimbrite sample EVGLI. d) Results of the sanidines from the Loreto Ignimbrite sample LOIT.

For this study, a plateau age is defined as a sequence that includes five or more consecutive steps corresponding to at least 60% of the total ^{39}Ar released that yield apparent ages reproducible at the

95% confidence level (2σ). The two samples from the Villa Garcia Ignimbrite resulted in two sharp plateau ages at 31.59 ± 0.14 Ma (sample EVGVGI, Figure 50 a) and 31.15 ± 0.12 Ma (sample LORI, Figure 50 b). The sample EVGVGI contains 11constant steps including 99.65 % of the released ^{39}Ar and in contrast the second sample of the Villa Garcia Ignimbrite, sample LORI covers 6 constant steps including 83.57 % of the released ^{39}Ar. The two samples from the Loreto Ignimbrite yielded two sharp plateau ages 28.97 ± 0.11 Ma (sample EVGLI, Figure 50 c) and 28.66 ± 0.07 Ma (sample LOIT, Figure 50 d). The sample EVGLI contains 10 constant steps including 99.55 % of the released ^{39}Ar and in contrast the second sample of the Loreto Ignimbrite, sample LORI covers 5 constant steps including 86.30 % of the released ^{39}Ar. The spectra of the samples EVGVGI and EVGLI that the loss of argon and the excess of argon did not occur in the samples. In comparison, the spectra samples LORI and LOIT suggest that argon loss and excess argon occurred during the geological history of the sample.

5.4. Discussion

5.4.1. Genesis of the volcanic rocks from the Villa Garcia Ignimbrite complex

The studies on the origin of the rhyolitic magmas in the Mesa Central are rare and are mainly from the last decades. Most works on the rhyolitic Oligocene rocks in the Mesa Central are restricted to general geochemical classifications without information regarding the genesis and evolution of the magmas. A first petrogenic study was carried out by Verma (1984) who concluded that the felsic domes in Zacatecas were derived from partial melting of the continental crust. The first detailed geochemical and petrological study to present a generalized model of the magmatic evolution in the Mesa Central was carried out by Orozco-Esquivel et al. (2002), resulting in a formation model including the generation of rhyolitic magmas by partial melting of the continental crust. In the study area Aguillón-Robles et al. (2009) presented a detailed model of the origin and evolution of the rhyolitic domes in the southern Mesa Central indicating an origin by partial melting of the base of the continental crust in an intra-plate setting, and fractional crystallization during magma ascent, but due to a poor stratigraphic control in their study, it is not clear which volcanic units corresponds to which magmatic process and in addition they base their results in only a few geochemical analysis. This work obtains a large set of trace element data and number of samples in order to reconstruct the magmatic evolution of the Villa Garcia ignimbrite complex.

The Villa Garcia ignimbrite complex was previously assigned to the Oligocene dome volcanism in the southern Mesa Central that is associated to the Ignimbrite flare up of the Sierra Madre Occidental large silicic province (Nieto-Samaniego et al., 2007; Aguirre-Díaz et al., 2008; Aguillón-Robles et al., 2009; Tristán-González et al., 2009 a; Ferrari et al., 2018). Aguillón-Robles et al. (2009) presented four K-Ar ages between 29.5 ± 0.5 Ma (1σ) and 32.3 ± 0.5 Ma (1σ), however not indicating from which unit the ages were derived. But, since the previous works and mapping, the debate on the stratigraphic position has continued. This work shows that the Villa Garcia volcanic succession comprises at least five volcanic units, separated by clear contacts, and which some have not been reported before. The new stratigraphy, combined with the major element geochemistry shows that the volcanism in the Villa Garcia area initiated with a rhyolitic lava flow (La Montesa Rhyolite), former described as dacite. Both, the Villa Garcia and the Loreto Ignimbrite are described in detail.

In comparison to the major ignimbrites in the San Luis Potosí and Santa Maria del Rio volcanic fields and the Salinas volcanic field (Figure 51 a – f), the rhyolitic volcanic rocks show similarities to the El Sombrero Ignimbrite (see 4.4.2. Whole-rock geochemistry) and the Guanamé Ignimbrite (Cruz-Castillo, 2019) from the Salinas volcanic field north of the study area and to the Cantera Ignimbrite as well as the Santa Maria ignimbrite form the San Luis Potosí volcanic field. In addition, both ignimbrites show similar trace element and REE patterns as the San Miguelito Ignimbrite of the Pinos volcanic field northeast of the study area (Tristán-González, 2008; Tristán-González et al., 2009 a).

The obtained Ar-Ar ages of Villa Garcia Ignimbrite (Figure 50 a and b) are younger than the ages of the El Sombrero Ignimbrite (see 4.4.7. Geochronology, 33.3 ± 0.43 Ma) and older than the Guanamé Ignimbrite (30.12 ± 0.45 Ma, 2 σ; Cruz-Castillo, 2019). The eruption ages derived from the Santa Maria Ignimbrite in the Rio Santa Maria volcanic field (ages between 32.8 ± 0.5 Ma and 31.3 ± 0.7 Ma, 1 σ; Tristán-González et al., 2009 a) and in the Villa Hidalgo volcanic field (ages between 31.7 ± 0.7 Ma and 31.0 ± 0.7 Ma, 1 σ; Tristán-González et al., 2009 a) as well

Cantera ignimbrite in the Villa Hidalgo volcanic field (ages between 31.7 ± 0.8 Ma and 31.0 ± 0.7 Ma, 1 σ; Tristán-González et al., 2009 a) indicate a contemporaneous emplacement of the ignimbrites.

In addition, both, the Villa Garcia Ignimbrite and the Loreto Ignimbrite are contemporaneous with the eruption of the San Miguelito ignimbrite in the Pinos volcanic field, close to the study area

(ages between 33.1 ± 0.8 Ma, 1 σ and 28.7 ± 0.8 Ma, 1 σ; Tristán-González et al., 2009 a). The ages from the ignimbrite in the Pinos vocanic field as well as the geochemical results are similar to the ignimbrites of the Villa Garcia Ignimbrite complex, and might correspond to the same eruptions. Previous studies on the Ignimbrites in the Pinos volcanic field describe those as high grade and densely welded ignimbrites with rheomorphic features similar to the Villa Garcia and Loreto Ignimbrite (Rocha-Echavarría et al., 2006; Torres-Hernández et al., 2006). Torres-Hernández et al. (2006) mention an NW-SE orientated extension of the ignimbrite and that they might be emplaced through faults but they do not show clear evidence.

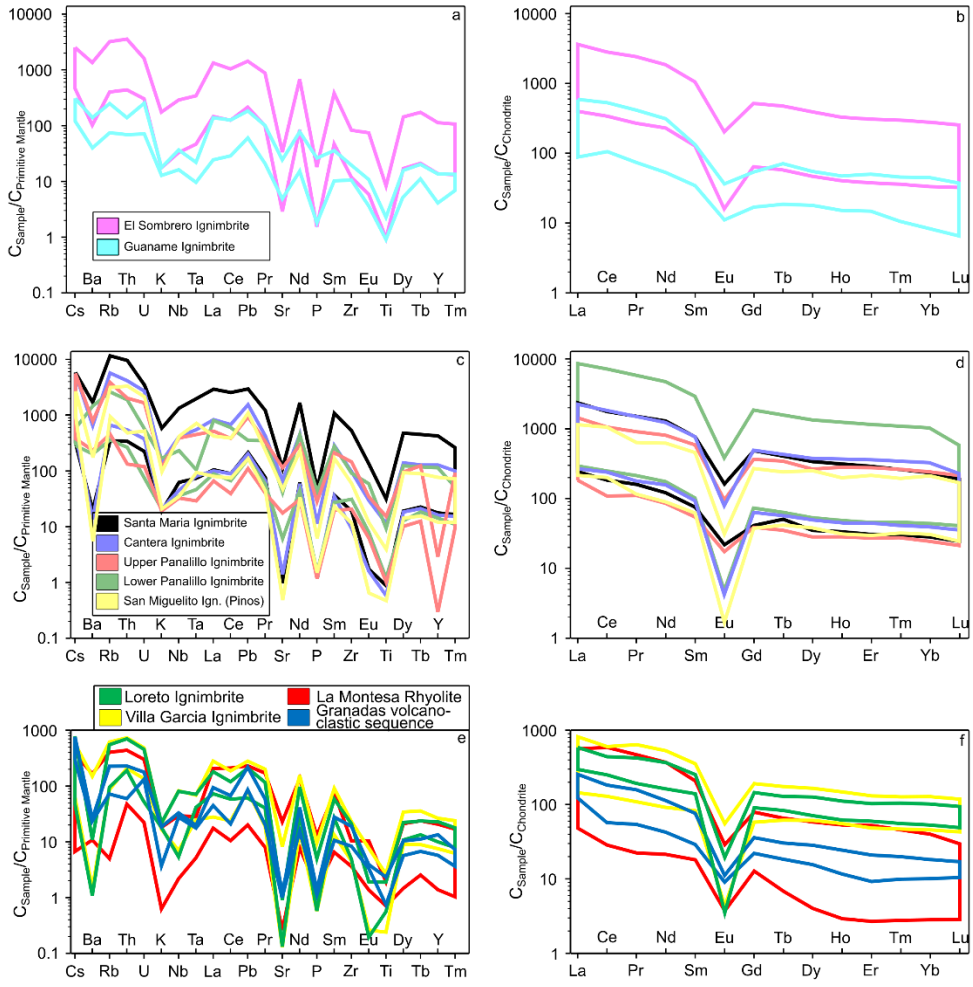

Figure 51: Trace element composition of rhyolitic volcanic rocks from the Salinas Volcanic field a) and b), the San Luis Potosí and Rio Santa Maria volcanic fields c) and d) and results for the Villa Garcia ignimbrite complex rocks of this study e) and f). a), c) and e) Primitive mantle-normalized multielement plots. b), d) and f)) Chondrite-normalized REE plots. Chondrite and primitive mantle composition after McDonough and Sun (1995). Data derived from Idier (2003); Tristán-González (2008); Villegas-Grimaldo (2015); Serna-Bafún (2018); Cruz-Castillo (2019) and Aguillón-Robles personal communication (2019).

All rhyolitic samples have relatively high SiO_2, low MgO, Cr and Ni contents indicating an evolved magma. In addition, all rhyolitic samples are peraluminous, pointing out a saturation of Al_2O_3, and they belong a high-K calc-alkaline to shoshonitic series with ferroan character, which is related to the generation and evolution of magmas under reducing conditions, leading to iron enrichment (Frost and Frost, 2008). In the multielement plots (Figure 47) large ion lithophile elements like Rb, Th, U are enriched and Nb, Ta and the feldspar compatible elements Ba, Sr and Eu show negative anomalies.

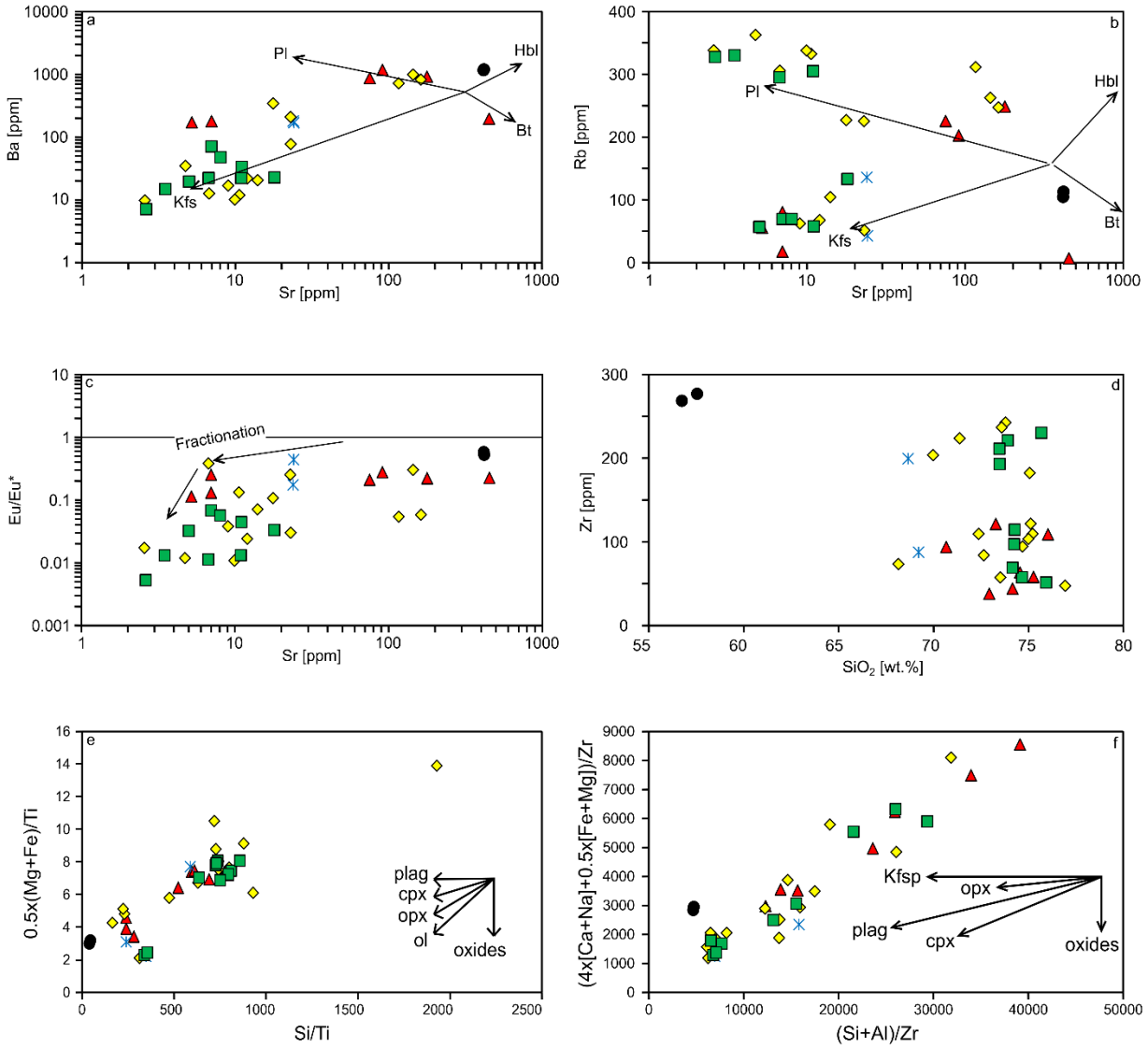

Figure 52: Co-variations of element concentrations and elemental ratios diagrams of the volcanic rocks of the Villa Garcia ignimbrite complex. a) Ba vs. Sr; b) Rb vs. Sr; c) Eu/Eu* vs. Sr; d) Zr vs. SiO_2. e) and f) Pearce Element ratio diagrams (after Pearce, 1968; Pearce and Cann, 1973; Bradshaw, 1992) showing crystal fractionation trends for the volcanic rocks from the Villa Garcia ignimbrite complex.

Enrichment of incompatible elements and depletion of compatible elements also indicate the role of fractionation in the generation of these rocks, possibly in a magma chamber prior to the eruption and/or during the ascent of the magma. Correlations between Rb and Ba with Sr indicate that K-feldspar and plagioclase were the main fractionating phases during the evolution of these rocks (Figure 52 a-c). The concentrations of zirconium in the volcanic rocks of the Villa Garcia volcanic succession are quite variable but low (< 300 ppm) and not correlated to the SiO_2 concentration of the rocks (Figure 52 d). However, the differences in the contents of elements like Ba, Sr, P and Ti in the different rhyolitic volcanic rocks indicate different degrees of mineral fractionation, i.e., the feldspars and accessory minerals. In addition, the Pearce ratio diagrams show that the fractionation of orthopyroxene took place during the evolution of magmas in the lower crust (Figure 52 e and f). The fractional crystallization is confirmed in the change in composition of K-feldspars and plagioclases of the different volcanic units of the Villa Garcia ignimbrite complex (Figure 48) as well in the disappearance of orthopyroxenes from the oldest to youngest rocks. During the fractional crystallization of the felsic magmas of the La Montesa Rhyolite over the Villa Garcia Ignimbrite to the Loreto Ignimbrite the magma becomes enriched in Na and slightly depleted in Fe and K, resulting in the crystallization of sanidine, with lower K concentrations, the crystallization of mainly oligoclase instead of andesine and the disappearance of Fe-rich orthopyroxenes (Figure 46; Figure 48; Figure 49a). A well-developed to strong Eu anomalies is present in all rhyolitic samples of the Villa Garcia ignimbrite complex (Figure 47) proving the fractionation process of plagioclase during the evolution of the rhyolitic magmas.

The trace element behavior in the multi-element plots (Figure 47) imply that the rhyolitic volcanic rocks were the result of a process involving partial melting of the lower crust and fractional crystallization. Based mainly on the behavior of Nb and Ta the rhyolitic magmas of the Villa Garcia rhyolitic rocks are produced in an intra-plate setting and confirmed by the bi-element variation diagrams shown in Figure 53 (a-d). If the magma source was a subduction related, then these elements would be more depleted due to differentiation (Gill, 1981). The REE have light negative patterns which indicate intra-plate signatures, whereas strong negative patterns are typical for subduction related magmas (Wilson, 1989). In addition, the behavior of the trace elements Ba, Th and Nb indicate a generation of the rhyolitic magmas in the lower crust (Figure 53 d). The different HRRE values of the La Montesa Rhyolite can be explained due to the influence of the lithic clasts and the partially intense alteration.

In summary, the results of the geochemical and mineralogical results and the related variations in the multi-element plots as well as mineral composition plots indicate that the silicic rocks of the Villa Garcia volcanic succession were derived by a process that includes the partial melting of the lower continental crust, possibly metasomatized and fractional crystallization in a magma chamber.

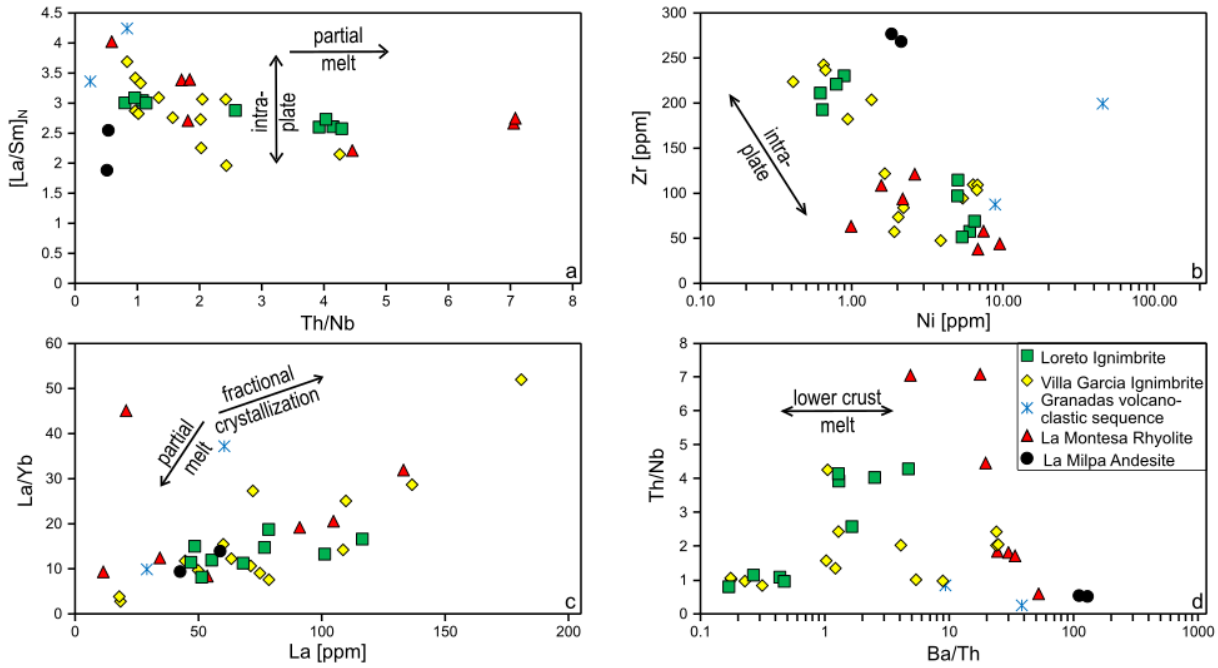

Figure 53: Bi-element variation diagrams for samples of the Villa Garcia ignimbrite complex. a) $[La/Sm]_N$ vs. Th/Nb; N denotes chondrite-normalized values after McDonough and Sun (1995). b) Zr vs. Ni. c) La/Yb vs. La. d) Th/Nb vs. Ba/Th.

Due to the small and limited exposure of the La Milpa Andesite it is still difficult to determine its origin. Nevertheless, the analyzed samples show similar composition and trace element behavior to the La Placa Basalt from the close San Luis Potosí volcanic field, northeast of the study area, that show eruption ages between 29.5 ± 0.7 and 28.0 ± 0.6 Ma (Tristán-González et al., 2009 a; Aguillón-Robles et al., 2014). Like the La Placa Basalt the La Milpa andesite contain Fe-rich olivine, plagioclase (bytownite and labradorite) and pyroxene (mainly enstatite). The samples of the La Milpa Andesite show enrichment in Cr, Ni, and Ba, while Sr and La show a depletion with increasing Mg#. The high contents of Cr and Ni in the La Milpa Andesite together with the horizontal HREE patterns and the presence of olivine are preserved characteristics from mantle-derived magma (Aguillón-Robles et al., 2014). Aguillón-Robles et al. (2014) showed that high Ba, U, and minor Th values, like the La Milpa Andesite, from the nearby San Luis Potosí Volcanic

Field were derived from assimilation of calc-alkaline affine lower crustal material in the mafic magmas, this is also supported by the existence of the slightly pronounced Eu and Sr anomalies in the multielement and REE plots (Figure 47 d and h). These features, together with the strong negative anomaly in Nb and Ta (Figure 47), indicate that the parental magma was derived from partial melting (Figure 52 and Figure 53) in the upper most mantle and that it stagnated at the mantle-crust boundary. In the San Luis Potosí volcanic field, this intermediate volcanism forms together with rhyolitic ignimbrites and/or lavas typical bimodal volcanism (Tristán-González et al., 2008; Rodríguez-Ríos and Torres-Aguilera, 2009; Tristán-González et al., 2009 a; Aguillón-Robles et al., 2014) and the La Milpa Andesite might be associated to this bimodal array.

The presented results regarding the formation of the rhyolitic magmas as well as the magmatic processes that took place during the ascent of the magma are in good agreement to basic geochemical works near the study area in the states of Zacatecas, San Luis Potosí, and Aguascalientes (Verma, 1984; Orozco-Esquivel et al., 2002; Rodríguez-Ríos et al., 2007; Rodríguez-Ríos and Torres-Aguilera, 2009).

5.4.2. Implications on the eruption of the volcanic rocks of the Villa Garcia Ignimbrite complex

The concomitance of the felsic magmatic event and the extensional regime meant that fissure type volcanism occurred all over the MC and SMO and along some of the grabens and normal fault systems, the emplacement of rhyolitic ignimbrites and/or domes was associated with basaltic to andesitic lava flows forming bimodal volcanic suits (Tristán-González, 1986; Aguirre-Díaz and Labarthe-Hernández, 2003; Tristán-González et al., 2008; Rodríguez-Ríos and Torres-Aguilera, 2009; Aguillón-Robles et al., 2012). The formation of the SMO and its southeastern portion, the MC, includes three main tectono-volcanic stages and most of the volcanic rocks in the southern and central portion of the Mesa Central were emplaced during the Eocene, Oligocene and Miocene (e.g. Labarthe-Hernández et al., 1982; Aranda-Gómez and McDowell, 1998; Nieto-Samaniego et al., 2007; Aguillón-Robles et al., 2009; Tristán-González et al., 2009 a). The Eocene igneous pulse is characterized by volcanism of andesitic composition that occurred at 45 – 42 Ma and 36 – 34 Ma (Aguillón-Robles et al., 2009; Tristán-González et al., 2009 a). The second phase of volcanic activity in the Mesa Central overlaps in space and time with the main phase of volcanic activity of the Sierra Madre Occidental silicic large igneous province (Nieto-Samaniego et al., 2007; Tristán-González et al., 2009 b; Ferrari et al., 2018). As in the SMO the Oligocene to Miocene igneous

event can be distinguished in two pulses: first, an Oligocene (~32 – 28 Ma) and second, an early Miocene (~24 – 20 Ma) pulse, both consisting of mainly rhyolitic volcanic rocks, and subordinate latite and dacite (McDowell and Keizer, 1977; Labarthe-Hernández et al., 1982; Ferrari et al., 2007; Nieto-Samaniego et al., 2007; Tristán-González et al., 2009 a; Ferrari et al., 2018). The Oligocene felsic magmatism overlaps in time with an intense phase of extension of the Basin and Range extension in NNW-SSE direction that favored the ascent of the rhyolitic magmas through the brittle crust yielding in explosive (ignimbrite flare-up) as well as effusive (lava flows and domes) fissure type eruptions all over the MC (Aguirre-Díaz and Labarthe-Hernández, 2003; Aguirre-Díaz et al., 2008; Tristán-González et al., 2008; Aguillón-Robles et al., 2009; Rodríguez-Ríos and Torres-Aguilera, 2009; Aguillón-Robles et al., 2014). The third event corresponds to an extension related Miocene mafic volcanism that has been related to the evolution from a continental-arc regime to intra-plate volcanism including subalkaline andesites and alkaline basalts (Cameron et al., 1980; Cameron et al., 1989; Aguirre-Díaz and McDowell, 1993; Ferrari et al., 2005).

Regional geological and geophysical studies imply that in the southern part and central part of the Mesa Central the crust has a thickness of approximately 30 to 33 km whereas the thickness of the crust to the west is 40 to 42 km and to the east 37 km (Fix, 1975; Smith and Jones, 1979; Nieto-Samaniego et al., 1999; Nieto-Samaniego et al., 2007). The thinning of the crust in this part was apparently due to the extension of the Basin and Range during the Oligocene to Miocene. These may have favored the generation of the acidic magmas, due to decompression, and ascent of the rhyolitic and andesitic magmas from the La Herradura area through the crust (Sieck et al., 2019). The eruption ages of the La Herradura volcanic units are consistent with those of other volcanic units from the San Luis Potosí Volcanic Field (whole rock and sanidine K-Ar ages between 31.6 ± 0.9 Ma and 29.1 ± 0.7 Ma; Tristán-González et al., 2009 a; Aguillón-Robles et al., 2012) or the Rio Santa María Volcanic Field (whole rock and sanidine K-Ar ages between 32.5 ± 0.8 Ma and 31.8 ± 0.7 Ma; Labarthe-Hernández et al., 1989; Tristán-González et al., 2009 a). The volcanic domes in the southern part of the Mesa Central, in the states of Aguascalientes and Zacatecas show similar to slightly younger eruption ages (whole rock and sanidine K-Ar ages between 32.3 ± 0.5 Ma and 29.5 ±0.5 Ma; Aguillón-Robles et al., 2009).

The obtained ^{40}Ar-^{39}Ar ages of the Villa Garcia Ignimbrite are 31.59 ± 0.14 Ma and 31.15 ± 0.12 Ma and the ^{40}Ar-^{39}Ar ages for the Loreto ignimbrite are 28.97 ± 0.11 Ma and 28.66 ± 0.07 Ma.

These ages coincide with the Oligocene peak of the SMO silicic large igneous province (Ferrari et al., 2007; Tristán-González et al., 2009 b; Ferrari et al., 2018). The La Montesa Rhyolite sits stratigraphic under the ignimbrites and it could represent the first magmatic activity in the study area (exposed). The exposures are limited to the center and eastern part of the study area covering the basement and continental clastic sediments and is elongated in NNW-SSE direction. That direction is similar to the major faults associated to Basin and Range extension in this area (e.g. Tristán-González et al., 2009 b). Due to the alignment of this rhyolitic lava/dome with the main systems of normal Basin and Range faults, a structural control of the felsic magmas can be concluded. The rhyolitic domes in the southern and central portion of the Mesa Central near the study area, were generated by direct ascent of magmas from their generation zone at the base of the crust to the surface without temporary storage at intermediate depths (Aguillón-Robles et al., 2009). A similar origin is plausible for the La Montesa rhyolite regarding the geochemical results. Hildreth (1981) proposed a similar mechanism according to which magmas produced by partial melting in the lower crust ascent by diapirism during episodic extensional events.

In the SMO and in its southeastern portion, the MC, calderas are not evident for most ignimbrites. Aguirre-Díaz and Labarthe-Hernández (2003) presented a field-based model for fissure-fed ignimbrite eruptions and graben calderas mainly based on their observations of pyroclastic dykes in grabens all over the SMO and MC. In the center part of the study area an ephemeral lake volcaniclastic-lacustrine sediment, the Granadas Volcaniclastic Sequence is exposed beneath the ignimbrites. The sequence appears stratigraphically concordant on top of the La Montesa Rhyolite (Figure 54 and Figure 55). The sediments were first be interpreted as sedimentation in a caldera lake that formed after an eruption, related probably to the La Montesa Rhyolite, which can be interpreted as first volcanic activity in form of a rhyolitic lava flow or dome in the study area. Nevertheless, the presence of such sedimentation alone is a hint on a caldera but not a proof. With the lack of any other caldera evidence, the lacustrine volcaniclastic sediments from Granadas, are interpreted as the products of distal ash deposits from eruptive columns and pyroclastic flows in an ephemeral lake, probably perched against the heavily folded basement tectonic highs. More likely is that due to the eruption of the La Montesa Rhyolite yielded in the formation of a basin inside a basement high.

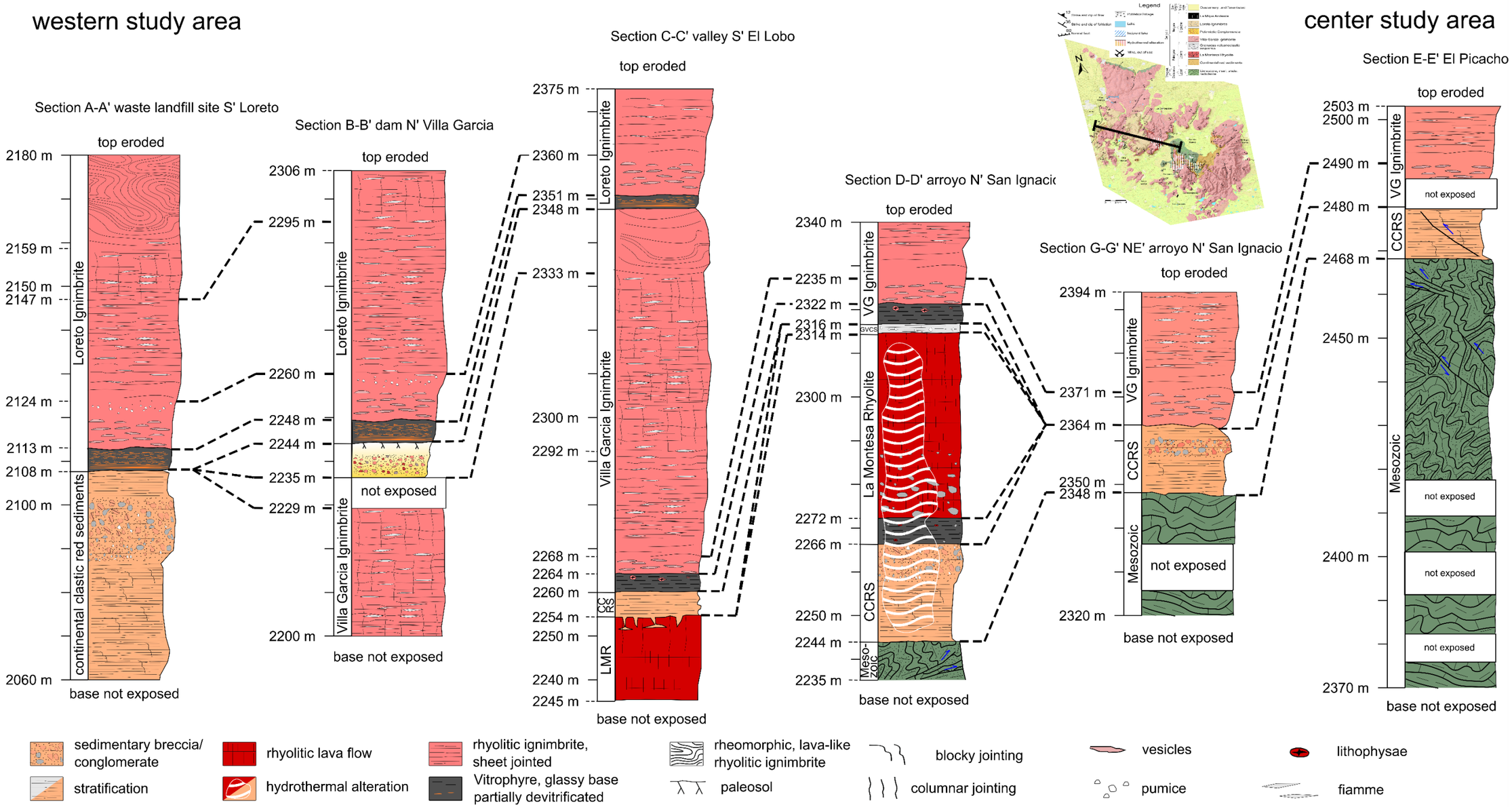

Figure 54: Measured and correlated sections of the Villa Garcia Ignimbrite complex, from the western part to the center part of the study area. The labels of the columns correspond to sections indicated in the geological map shown in Figure 30. Logged profiles are shown in Appendix J. CCRS: continental clastic red sediments, LMR: La Montesa Rhyolite, VG: Villa Garcia.

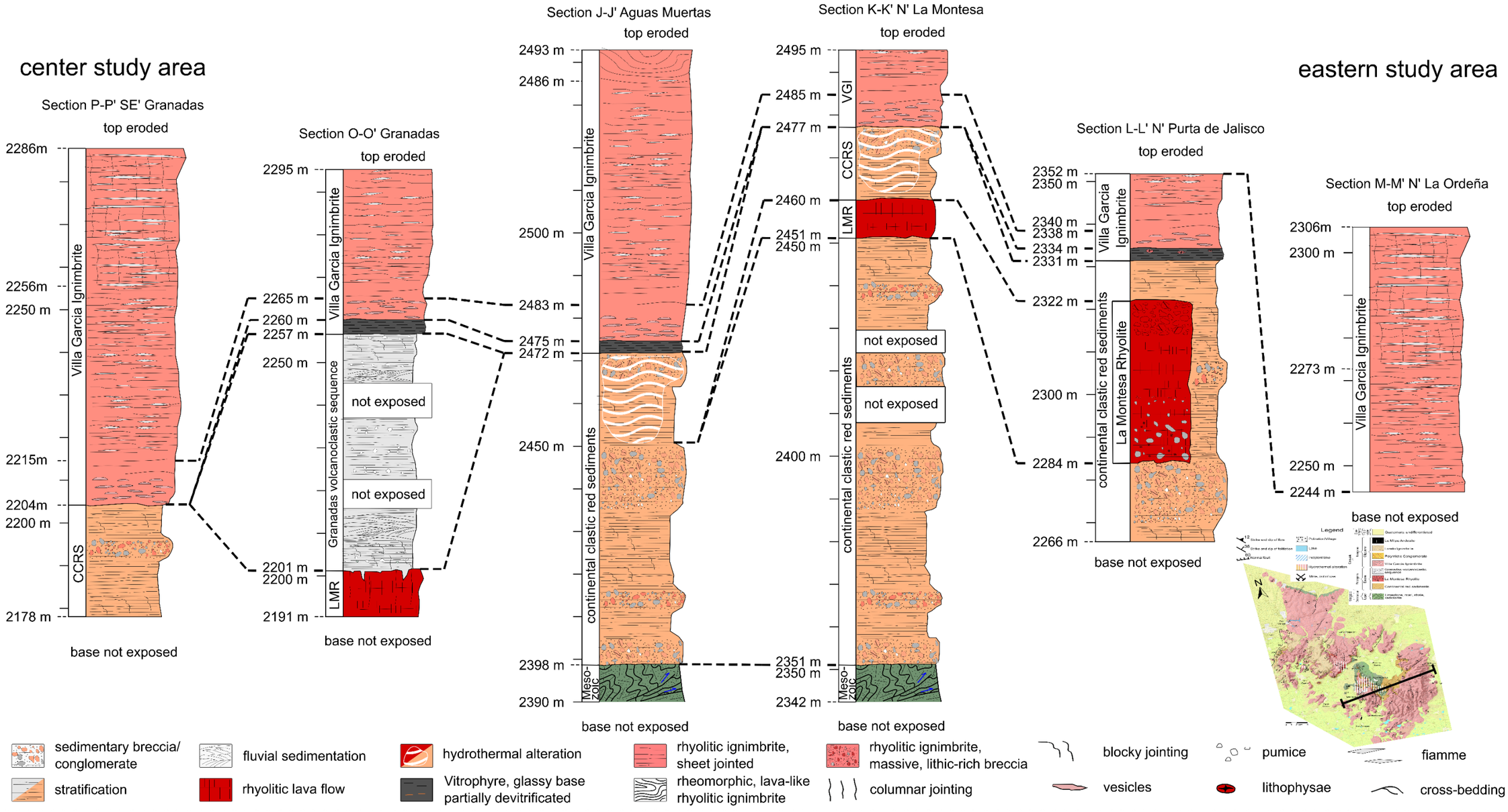

Figure 55: Measured and correlated sections of the Villa Garcia Ignimbrite complex, from the center part to the western part of the study area. The labels of the columns correspond to sections indicated in the geological map shown in Figure 30. Logged profiles are shown in Appendix J. CCRS: continental clastic red sediments, LMR: La Montesa Rhyolite, VGI: Villa Garcia Ignimbrite.

Inside that basin, a shallow waterbody with fine-grained lacustrine sedimentation was established and that the interlayered pyroclastic material is the result of a distal sequence of a pyroclastic density flows or currents, together with ash fall from high eruptive columns of rhyolitic composition. In the Pinos volcanic complex around 40 km northeast of the study appears a similar succession as in the Villa Garcia Ignimbrite complex. Aranda-Gómez et al. (2007) described a formation of red sediments, the Pinos red bed sequence, the sequence contains, like the continental clastic sediments in the study area a sediment layer containing clasts of the Peñon Blanco intrusion prior to the volcanism. In addition, these red sediments are locally interlayered with subaerial felsic volcanic rocks, including ash-fall tuffs, at least one densely welded ash-flow tuff, and water-laid or reworked pyroclastic material similar to the Granadas Volcanoclastic sequence (Aranda-Gómez et al., 2007). In summary the Granadas Volcanoclastic Sequence contains pumice-bearing layers and can be interpreted as a succession of deposits from a distal eruption, deposited in a shallow and intermittent water body.

Both ignimbrites, the Villa Garcia and the Loreto Ignimbrites are not the product of a classical caldera (Figure 56). A distal origin of the Ignimbrite can be excluded because rheomorphic and lava-like ignimbrites are the results of high-temperature eruptions and just appear close to their origin (e.g. Branney et al., 2004; Branney et al., 2008; Andrews and Branney, 2011; Robert et al., 2013; Ellis et al., 2015). The ignimbrites on this study area appear to be each a single unit that might be emplaced fast, rapidly welded, deformed and cooled. This is confirmed due to the absence of compositional changes in the mineral content and composition of each unit as well as in the whole rock geochemistry. A possible explanation is that the ignimbrites are derived from a fissure-fed eruption; the western rim of the study area neighbors the Loreto graben, as northerneastern continuation of the Aguascalientes graben (Figure 4). The eruption ages of the Villa Garcia and Loreto ignimbrites coincide with a major extension phase in the Mesa Central (Tristán-González et al., 2009 b). Nevertheless, there are no pyroclastic dykes exposed in the study area, but they might be covered by the Villa Garcia Ignimbrite and the graben fill sediments. The geochemical results show a similar process of the formation and evolution as the La Montesa Rhyolite, but in contrast, the Villa Garcia Ignimbrite as well as the Loreto Ignimbrite are the product of a major explosive eruption, following a temporary storage in a shallow magma chamber (Figure 56) in which volatiles were exsolved. Such ignimbrite-generating events occurred in many

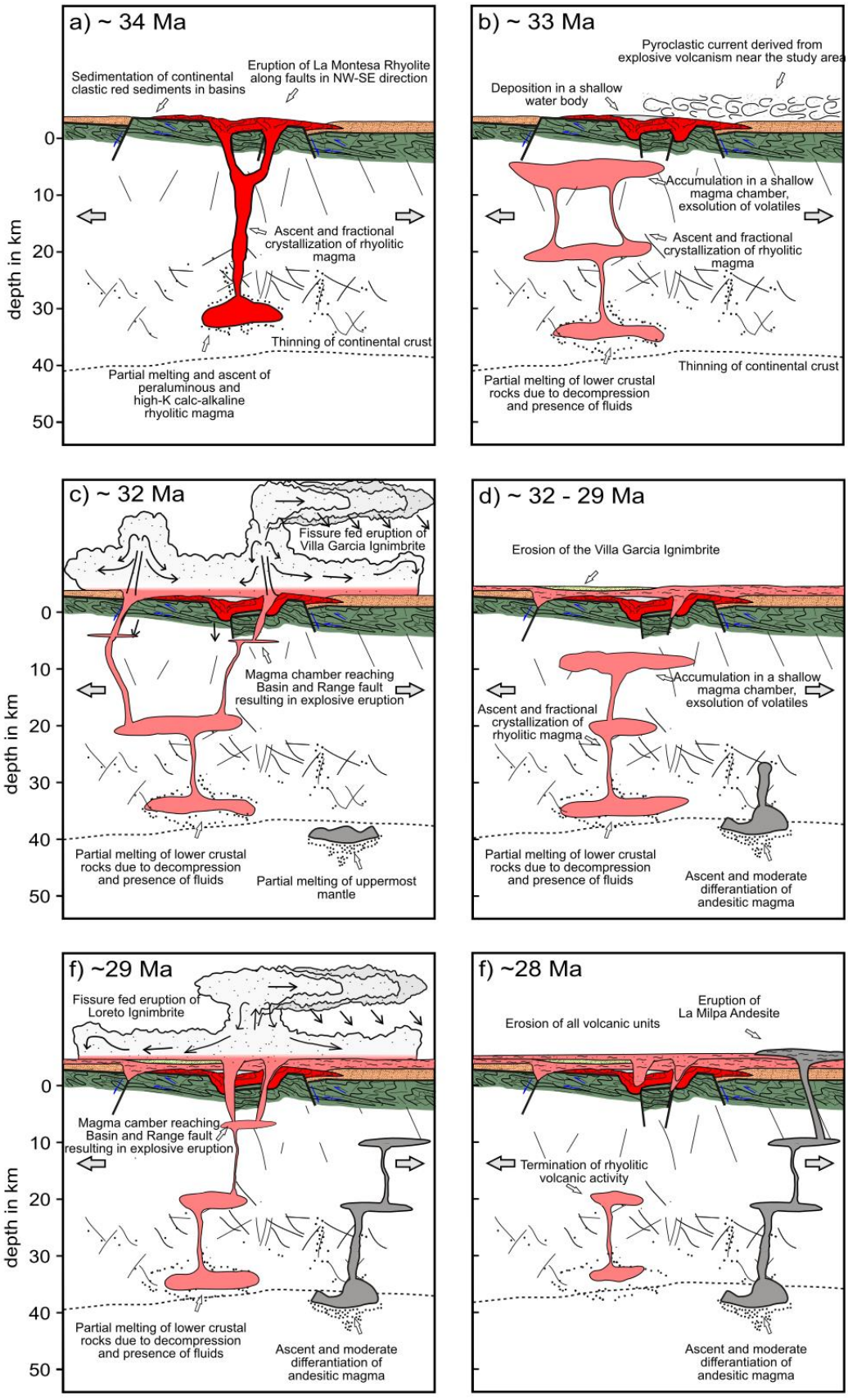
a) ~ 34 Ma
Sedimentation of continental clastic red sediments in basins
Eruption of La Montesa Rhyolite along faults in NW-SE direction
Ascent and fractional crystallization of rhyolitic magma
Thinning of continental crust
Partial melting and ascent of peraluminous and high-K calc-alkaline rhyolitic magma
b) ~ 33 Ma
Pyroclastic current derived from explosive volcanism near the study area
Deposition in a shallow water body
Accumulation in a shallow magma chamber, exsolution of volatiles
Ascent and fractional crystallization of rhyolitic magma
Thinning of continental crust
Partial melting of lower crustal rocks due to decompression and presence of fluids
c) ~ 32 Ma
Fissure fed eruption of Villa Garcia Ignimbrite
Magma chamber reaching Basin and Range fault resulting in explosive eruption
Partial melting of lower crustal rocks due to decompression and presence of fluids
Partial melting of uppermost mantle
d) ~ 32 - 29 Ma
Erosion of the Villa Garcia Ignimbrite
Accumulation in a shallow magma chamber, exsolution of volatiles
Ascent and fractional crystallization of rhyolitic magma
Partial melting of lower crustal rocks due to decompression and presence of fluids
Ascent and moderate differantiation of andesitic magma
f) ~29 Ma
Fissure fed eruption of Loreto Ignimbrite
Magma camber reaching Basin and Range fault resulting in explosive eruption
Partial melting of lower crustal rocks due to decompression and presence of fluids
Ascent and moderate differantiation of andesitic magma
f) ~28 Ma
Erosion of all volcanic units
Eruption of La Milpa Andesite
Termination of rhyolitic volcanic activity
Ascent and moderate differantiation of andesitic magma
depth in km
0
10
20
30
40
50

Figure 56. Schematic evolution of the Villa Garcia Ignimbrite complex between ca. 34 Ma and 2 Ma. a) Generation of rhyolitic magma by partial melting of the lower crust and direct ascent and eruption/emplacement of the rhyolitic magma of the La Montesa Rhyolite in an intra-plate extension-related setting. b) Ascent and accumulation of the rhyolitic magma in a shallow magma chamber, where volatiles are exsolved favoring explosive eruptions which emplaced the Villa Garcia Ignimbrite. Deposition of distal pyroclastic density flows, together with ash fall from eruptive columns of rhyolitic composition, that were deposit in a shallow and intermittent water body. c) Fissure-fed eruption of the Villa Garcia Ignimbrite and generation of andesitic magma in the upper mantle. d) Erosion and formation of paleosol on top of the Villa Garcia Ignimbrite. Partial melting, ascent and storage of rhyolitic magma continues, beginning ascent of the andesitic magma. e) Fissure-fed eruption of the of the Loreto Ignimbrite and beginning erosion of the Loreto Ignimbrite. e) Eruption of the La Milpa Andesite on top of the Villa Garcia and Loreto Ignimbrite.

areas of the Mesa Central and in the adjacent Sierra Madre Occidental (Aguirre-Díaz and Labarthe-Hernández, 2003; Aguirre-Díaz et al., 2008; Ferrari et al., 2018).

5.5. Conclusions

The Villa Garcia volcanic succession is formed by rhyolite lava, volcaniclastic sediments, welded ignimbrites and another rhyolite lava atop. They form a clear 45 km times 30 km mountain range in the southern part of the Mesa Central, between Loreto and Villa García, Zacatecas. The age of the volcanism is Oligocene and mainly calc-alkaline, probably associated in time to the Ignimbrite flare up of the Sierra Madre Occidental silicic large igneous province and were extruded during an intense phase of the Basin and Range extension. The age range of the ignimbrite volcanism is between 32 and 29 Ma (Ar/Ar ages). During the same time partial melting of the lower crust took place due to the Basin and Range associated thinning of the crust. The geochemical results confirm an intra-plate origin of the magmas by partial melting of the base of the continental crust, involving fluids enriched in HFSE and LILE and an evolution of the rhyolitic magmas due to mainly fractional crystallization.

Six major phases (Figure 56 a -f) formed the Villa Garcia volcanic succession. First, the generation of rhyolitic magma by partial melting of the lower crust in an intra-plate extension-related setting, associated to the Basin and Range extension. Second, the rhyolitic magma raised directly through the brittle crust from the lower crust, where fractional crystallization and partial assimilation took place, and erupted on top of the continental clastic red sediments, forming closed basins within the basement (Granadas volcanoclastic sequence). Third, ascent and accumulation of the rhyolitic magma in a shallow magma chamber. These large magma chambers reached shallow crustal levels mainly because of the extensional regime of the Basin and Range in which they were emplaced; reaching the high crustal level caused magmas to become volatile rich by exsolution of volatiles due to decompression. Furthermore, deposition of distal pyroclastic density currents, together with ash fall from eruptive columns of rhyolitic composition were deposited in a shallow and

intermittent water body, forming the Granadas volcanoclastic sequence. The fourth phase includes the fissure fed eruption of the Villa Garcia Ignimbrite and generation of andesitic magma in the upper mantle, forming a possible bimodal series. Followed by a phase of erosion of the Villa Garcia Ignimbrite. During the same time the partial melting, ascent and storage of rhyolitic magma continues and the andesitic magmas begin to raise. The last phase includes the contemporaneous fissure fed eruption of the Loreto Ignimbrite and the eruption of the La Milpa Andesite on top of the Villa Garcia Ignimbrite.

6. Conclusions

The present work shows the geochemical, petrological and geochronological evolution of the Oligocene rhyolitic volcanism in the central and southern Mesa Central of Mexico. Two study areas were used as case studies: the garnet-bearing rhyolitic volcanism associated to bimodal volcanism near La Herradura, in the center of the Mesa Central and the rhyolitic ignimbrite complex in the area of Villa Garcia in the southern portion of the Mesa Central. The work presents new and updated detailed stratigraphy and geological mapping of a previously poorly studied area in order to reconstruct the evolution and correlation of these rhyolitic volcanic rocks. The results show that the high-K calc-alkaline to shoshonitic and high-silica rhyolitic magmas of the study area are derived from a complex process including the partial melting of the lower crust in an intra-plate extensional setting during an intense phase of the Basin and Range extension. The geochronological analysis (zircon single grain U-Pb ages, sanidine Ar-Ar ages and whole rock K-Ar ages) show an age range between ~ 33 and 28 Ma for the rhyolitic volcanism. In case the of the rhyolitic magmas from the La Herradura area, high pressure and high temperature conditions resulted in the crystallization of almandine-rich garnet. Zircon single grain U-Pb age determinations as well geothermobarometric constraints on the garnets show contemporaneous crystallizations at lower crustal depth with zircons derived from the whole-rock samples. Simulations on the crystallization with rhyolite-MELTS show comparable results. The thin (30-33 km) and brittle crust favored a rapid ascent of the rhyolitic magmas from the lower crust, in case of the rhyolitic lavas and domes, to the surface and in case of the ignimbrites to a shallow magma chamber. Change of mineral composition of mainly K-feldspar, orthopyroxene and plagioclase in combination with the trace and REE patterns show that during the ascent and storage of the rhyolitic magmas, fractional crystallization was the main process that took place during the evolution of these magmas. Assimilation of crustal material was ales important process in the evolution of the rhyolitic magmas and might have affected them during the ascent to the surface or to the shallow magma chamber. The geochemical results confirm an intra-plate origin of the magmas by partial melting of the base of the continental crust, involving fluids enriched in HFSE and LILE.

The mafic volcanism associated to bimodal volcanism in the La Herradura area as well in the Villa Garcia area was derived from partial melting of the upper mantle, that stagnated at the mantle-

crust boundary or in the lower crust, in the case of the andesitic magmas from the La Herradura area. During the ascent of the andesitic magmas, assimilation of lower crustal rock took place. Mineralogy and simulations on the crystallization of the andesitic magmas confirm these results. In addition, the stagnated andesitic magma might have favored the partial melting of the lower crust.

The studied rhyolitic lavas and domes all are aligned along NW-SE direction, which is considered to be the orientation of the Basin and Range extension. This transtensive deformation regime generated a set of up to several km-long NW-SE trending normal faults that acted as ascent channels for the rhyolitic magmas and along which they erupted, forming aligned lava flows and domes. In contrast, the ignimbrites are the result of a major explosive eruption. Prior to the explosive eruption, the magmas were stored in a shallow magma chamber. These large magma chambers reached shallow crustal levels mainly because of the extensional regime of the Basin and Range in which they were emplaced. Reaching the high crustal level caused magmas to become volatile rich by exsolution of volatiles mainly due to decompression. Faults generated by the transtensive deformation regime have affected the roof of the magma chamber or the chamber reached Basin and Range associated normal faults, causing an opening of the closed system, and resulting in a fast decompression and the explosive eruptions of voluminous pyroclastic flows and fissure ignimbrites. The lithic load of the pyroclastic flows was deposited near the fault-related vents, forming densely welded and lava-like to rheomorphic ignimbrites.

References

Aguillón-Robles, A., Tristán-González, M., Aguirre-Díaz, G.J., Bellon, H., 2009. Syn-extensional intra-plate trachydacite-rhyolitic dome volcanism of the Mesa Central, southern Sierra Madre Occidental volcanic province, Mexico. Journal of Volcanology and Geothermal Research 187, 33–52.

Aguillón-Robles, A., Tristán-González, M., López-Doncel, R.A., García-Arreola, M.E., Almaguer-Rodríguez, J.L., Maury, R.C., 2012. Trace elements geochemistry and origin of volcanic units from the San Luis Potosí and Río Santa María volcanic fields, Mexico: the bearing of ICP-QMS data. Geofísica Internacional 51, 293–308.

Aguillón-Robles, A., Tristán-González, M., Jesús Aguirre-Díaz, G. de, López-Doncel, R.A., Bellon, H., Martínez-Esparza, G., 2014. Eocene to Quaternary mafic-intermediate volcanism in San Luis Potosí, central Mexico: The transition from Farallon plate subduction to intra-plate continental magmatism. Journal of Volcanology and Geothermal Research 276, 152–172.

Aguirre-Díaz, G.J., McDowell, F.W., 1991. The volcanic section at Nazas, Durango, Mexico, and the possibility of widespread Eocene volcanism within the Sierra Madre Occidental. Journal of Geophysical Research: Solid Earth 96, 13373–13388. https://doi.org/10.1029/91JB00245.

Aguirre-Díaz, G.J., McDowell, F.W., 1993. Nature and timing of faulting and synextensional magmatism in the southern Basin and Range, central-eastern Durango, Mexico. Geological Society of America Bulletin 105, 1435–1444.

Aguirre-Díaz, G.J., Labarthe-Hernández, G., 2003. Fissure ignimbrites: Fissure-source origin for voluminous ignimbrites of the Sierra Madre Occidental and its relationship with Basin and Range faulting. Journal of Geophysical Research 31, 773. https://doi.org/10.1130/G19665.1.

Aguirre-Díaz, G.J., Labarthe-Hernández, G., Tristán-González, M., Nieto-Obregón, J., Gutiérrez-Palomares, I., 2008. Chapter 4 The Ignimbrite Flare-Up and Graben Calderas of the Sierra Madre Occidental, Mexico, in: Gottsmann, J., Martí, J. (Eds.), Caldera Volcanism: Analysis, Modelling and Response, vol. 10. Elsevier, pp. 143–180.

Alaniz-Álvarez, S.A., Nieto-Samaniego, Á.F., 2005. El sistema de fallas Taxco-San Miguel de Allende y la Faja Volcánica Transmexicana, dos fronteras tectónicas del centro de México activas durante el Cenozoico. Boletín de la Sociedad Geológica Mexicana 57, 65–82.

Alaniz-Álvarez, S.A., Nieto-Samaniego, Á.F., Reyes-Zaragoza, M.A., Orozco-Esquivel, M.T., Ojeda-García, Á.C., Vassallo, L.F., 2001. Estratigrafía y deformación extensional en la región

San Miguel de Allende-Querétaro, México. Revista Mexicana de Ciencias Geológicas 18, 129–148.

Alaniz-Álvarez, S.A., Nieto-Samaniego, A.F., Orozco-Esquivel, M.T., Vassallo, L.F., Xu, S., 2002. El sistema de fallas Taxco-San Miguel de Allende: implicaciones en la deformación post-eocénica del centro de México. Boletín de la Sociedad Geológica Mexicana 55, 12–29

Albinson F, T., 1988. Geologic reconstruction of paleosurfaces in the Sombrerete, Colorada, and Fresnillo districts, Zacatecas State, Mexico. Economic Geology 83, 1647–1667.

Almaguer-Rodríguez, J.L., 2010. Estudio geoquímicos de elementos traza en unidades volcánicas del CVSLP: método ICP-MS (validación del método). San Luis Potosí, México: Universidad Autónoma de San Luis Potosí, Facultad de Ingeniería, Tesis Ingeniería Geológica, 89pp.

Andrews, G.D.M., Branney, M.J., 2011. Emplacement and rheomorphic deformation of a large, lava-like rhyolitic ignimbrite: Grey's Landing, southern Idaho. Geological Society of America Bulletin 123, https://doi.org/725–743. 10.1130/B30167.1.

Aranda-Gómez, J.J., McDowell, F.W., 1998. Paleogene Extension in the Southern Basin and Range Province of Mexico: Syndepositional Tilting of Eocene Red Beds and Oligocene Volcanic Rocks in the Guanajuato Mining District. International Geology Review 40, 116–134. https://doi.org/10.1080/00206819809465201.

Aranda-Gómez, J.J., Henry, C.D., Luhr, J.F., 2000. Evolución tectonomagmática post-paleocénica de la Sierra Madre Occidental y de la porción meridional de la provincia tectónica de Cuencas y Sierras, México. Boletín de la Sociedad Geológica Mexicana 53, 59–71.

Aranda-Gómez, J.J., Luhr, J.F., Housh, T.B., Valdez-Moreno, G., Chávez-Cabello, G., 2005. El volcanismo tipo intraplaca del Cenozoico tardío en el centro y norte de México: una revisión. Boletín de la Sociedad Geológica Mexicana 57, 187–225.

Aranda-Gómez, J.J., Molina-Garza, R., McDowell, F.W., Vassallo-Morales, L.F., Ortega-Rivera, M.A., Solorio-Munguía, J.G., Aguillón-Robles, A., 2007. The relationships between volcanism and extension in the Mesa Central: the case of Pinos, Zacatecas, Mexico. Revista Mexicana de Ciencias Geológicas 24, 216–233.

Armstrong, R.L., Ward, P., 1991. Evolving geographic patterns of Cenozoic magmatism in the North American Cordillera: The temporal and spatial association of magmatism and metamorphic core complexes. Journal of Geophysical Research 96, 13201–13224.

Ashley, K.T., Caddick, M.J., Steele-MacInnis, M.J., Bodnar, R.J., Dragovic, B., 2014. Geothermobarometric history of subduction recorded by quartz inclusions in garnet. Geochemistry, Geophysics, Geosystems 15, 350–360.

Ashley, K.T., Darling, R.S., Bodnar, R.J., Law, R.D., 2015. Significance of "stretched" mineral inclusions for reconstructing P–T exhumation history. Contributions to Mineralogy and Petrology 169, 55–64. https://doi.org/10.1007/s00410-015-1149-0.

Ashley, K.T., Steele-MacInnis, M., Bodnar, R.J., Darling, R.S., 2016. Quartz-in-garnet inclusion barometry under fire: Reducing uncertainty from model estimates. Geology 44, 699–702.

Ashley, K.T., Barkoff, D.W., Steele-MacInnis, M., 2017. Barometric constraints based on apatite inclusions in garnet. American Mineralogist 102, 743–749.

Asimow, P.D., Ghiorso, M.S., 1998. Algorithmic modifications extending MELTS to calculate subsolidus phase relations. American Mineralogist 83, 1127–1132.

Barboza-Gudiño, J.R., Tristán-González, M., Torres-Hernández, J.R., 1998. The Late Triassic-Early Jurassic active continental margin of western North America in northeastern Mexico. Geofísica Internacional 37, 283–292.

Barboza-Gudiño, J.R., Tristán-González, M., Torres-Hernández, J.R., Bartolini, C., 1999. Tectonic setting of pre-Oxfordian units from central and northeastern Mexico: A review, in: Bartolini, C., Wilson, J.L., Lawton, T.F. (Eds.), Mesozoic sedimentary and tectonic history of north-central Mexico. Geological Society of America, pp. 197–210.

Barboza-Gudiño, J.R., Hoppe, M., Gómez-Anguiano, M., Martínez-Macías, P.R., 2004. Aportaciones para la interpretación estratigráfica y estructural de la porción noroccidental de la Sierra de Catorce, San Luis Potosí, México. Revista mexicana de ciencias geológicas 21, 219–319.

Barboza-Gudiño, J.R., Orozco-Esquivel, M.T., Gómez-Anguiano, M., Zavala-Monsiváis, A., 2008. The Early Mesozoic volcanic arc of western North America in northeastern Mexico. Journal of South American Earth Sciences 25, 49–63. https://doi.org/10.1016/j.jsames.2007.08.003.

Barth, T.F.W., 1934. Temperatures in lavas and magmas and a new geologic thermometer. Naturen 6, 187–192.

Bartolini, C., Wilson, J.L., Lawton, T.F. (Eds.), 1999. Mesozoic sedimentary and tectonic history of north-central Mexico. Geological Society of America Special Paper 340, 380 pp.

Bartolini, C., Lang, H., Spell, T., 2003. Geochronology, geochemistry, and tectonic setting of the Mesozoic Nazas arc in north-central Mexico, and its continuation to northern South America, in: Bartolini, C., Buffler, R.T., Blickwede, J.F. (Eds.), The Circum-Gulf of Mexico and the Caribbean: Hydrocarbon Habitats, Basin Formation, and Plate Tectonics. American Association of Petroleum Geologists Memoir, pp. 427–461.

Beckhoff, B., Kanngießer, B., Langhoff, N., Wedell, R., Wolff, H., 2006. Handbook of practical X-ray fluorescence analysis. Springer Science & Business Media, 878 pp.

Benisek, A., Kroll, H., Cemic, L., 2004. New developments in two-feldspar thermometry. American Mineralogist 89, 1496–1504.

Best, M.G., Christiansen, E.H., Gromme, S., 2013. Introduction: The 36-18 Ma southern Great Basin, USA, ignimbrite province and flareup: Swarms of subduction-related supervolcanoes. Geosphere 9, 260–274. https://doi.org/10.1130/GES00870.1.

Boehnke, P., Watson, E.B., Trail, D., Harrison, T.M., Schmitt, A.K., 2013. Zircon saturation re-revisited. Chemical Geology 351, 324–334. https://doi.org/10.1016/j.chemgeo.2013.05.028.

Bradshaw, T.K., 1992. The adaptation of Pearce element ratio diagrams to complex high silica systems. Contributions to Mineralogy and Petrology 109, 450–458.

Branney, M.J., Barry, T.L., Godchaux, M., 2004. Sheathfolds in rheomorphic ignimbrites. Bulletin of Volcanology 66, 485–491. https://doi.org/10.1007/s00445-003-0332-8.

Branney, M.J., Bonnichsen, B., Andrews, G.D.M., Ellis, B., Barry, T.L., McCurry, M., 2008. ‘Snake River (SR)-type’ volcanism at the Yellowstone hotspot track: distinctive products from unusual, high-temperature silicic super-eruptions. Bulletin of Volcanology 70, 293–314. https://doi.org/10.1007/s00445-007-0140-7.

Brooks Hanson, R., Glazner, A.F., 1995. Thermal requirements for extensional emplacement of granitoids. Geology 23, 213. https://doi.org/10.1130/0091-7613(1995)023<0213:TRFEEO>2.3.CO;2.

Bryan, S.E., 2007. Silicic large igneous provinces. Episodes 30, 20–31.

Bryan, S.E., Ernst, R.E., 2008. Revised definition of Large Igneous Provinces (LIPs). Earth-Science Reviews 86, 175–202. https://doi.org/10.1016/j.earscirev.2007.08.008.

Bryan, S.E., Ferrari, L., 2013. Large igneous provinces and silicic large igneous provinces: Progress in our understanding over the last 25 years. Episodes 125, 1053–1078. https://doi.org/10.1130/B30820.1.

Bryan, S.E., Riley, T.R., Jerram, D.A., Stephens, C.J., Leat, P.T., 2002. Silicic volcanism: An undervalued component of large igneous provinces and volcanic rifted margins, in: Menzies, M.A., Klemperer, S.L., Ebinger, C.J., Baker, J. (Eds.), Volcanic Rifted Margins. Geological Society of America Special Paper 362, pp. 97–118.

Bryan, S.E., Ferrari, L., Reiners, P.W., Allen, C.M., Petrone, C.M., Ramos-Rosique, A., Campbell, I.H., 2008. New Insights into Crustal Contributions to Large-volume Rhyolite Generation in the Mid-Tertiary Sierra Madre Occidental Province, Mexico, Revealed by U–Pb Geochronology. Journal of Petrology 49, 47–77. https://doi.org/10.1093/petrology/egm070.

Bryan, S.E., Orozco-Esquivel, T., Ferrari, L., Lopez-Martinez, M., 2014. Pulling apart the mid to late Cenozoic magmatic record of the Gulf of California: Is there a Comondú arc? Geological Society, London, Special Publications 385, 389–407.

Burt, D.M., Sheridan, M.F., 1987. Types of mineralization related to fluorine-rich silicic lava flows and domes. Geological Society of America Special Paper 212, 103–109.

Cameron, K.L., Nimz, G.J., Kuentz, D., Niemeyer, S., Gunn, S., 1989. Southern Cordilleran basaltic andesite suite, southern Chihuahua, Mexico: a link between Tertiary continental arc and flood basalt magmatism in North America. Journal of Geophysical Research 94, 7817–7840.

Cameron, M., Bagby, W.C., Cameron, K.L., 1980. Petrogenesis of voluminous mid-Tertiary ignimbrites of the Sierra Madre Occidental, Chihuahua, Mexico. Contributions to Mineralogy and Petrology 74, 271–284.

Campa, M.F., Coney, P.J., 1983. Tectono-stratigraphic terranes and mineral resource distributions in Mexico. Canadian Journal of Earth Sciences 20, 1040–1051.

Carmichael, I.S.E., 1991. The redox states of basic and silicic magmas: a reflection of their source regions? Contributions to Mineralogy and Petrology 106, 129–141.

Carrillo-Bravo, J., 1982. Exploración petrolera de la Cuenca Mesozoica del Centro de México. Boletín de la Asociación Mexicana de Geólogos Petroleros 34, 21–46.

Cather, S.M., Dunbar, N.W., McDowell, F.W., McIntosh, W.C., Scholle, P.A., 2009. Climate forcing by iron fertilization from repeated ignimbrite eruptions: The icehouse–silicic large igneous province (SLIP) hypothesis. Geosphere 5, 315–324. https://doi.org/10.1130/GES00188.1.

Centeno-García, E., 2017. Mesozoic tectono-magmatic evolution of Mexico: An overview. Ore Geology Reviews 81, 1035–1052.

Centeno-García, E., Silva-Romo, G., 1997. Petrogenesis and tectonic evolution of central Mexico during Triassic-Jurassic time. Revista Mexicana de Ciencias Geológicas 14, 244-260.

Centeno-García, E., Ruíz, J., Coney, P.J., Patchett, P.J., Ortega-Gutiérrez, F., 1993. Guerrero terrane of Mexico: Its role in the Southern, Cordillera from new geochemical data. Geology 21, 419–422.

Centeno-García, E., Guerrero-Suastegui, M., Talavera-Mendoza, O., 2008. The Guerrero Composite Terrane of western Mexico: Collision and subsequent rifting in a supra-subduction zone, in: Draut, A., Clift, P.D., Scholl, D.W. (Eds.), Formation and Applications of the Sedimentary Record in Arc Collision Zones. Geological Society of America Special Paper 436, pp. 279–308.

Centeno-Garcia, E., Busby, C., Busby, M., Gehrels, G., 2011. Evolution of the Guerrero composite terrane along the Mexican margin, from extensional fringing arc to contractional continental arc. Canadian Journal of Earth Sciences 123, 1776–1797.

Chappell, B.W., White, A.J.R., 1991. Restite enclaves and the restite model, in: Didier, J., Barbarin, B. (Eds.), Developments in petrology. Elsevier, Amsterdam, pp. 375–381.

Charlier, B., Namur, O., Toplis, M.J., Schiano, P., Cluzel, N., Higgins, M.D., Auwera, J.V., 2011. Large-scale silicate liquid immiscibility during differentiation of tholeiitic basalt to granite and the origin of the Daly gap. Geology 39, 907–910.

Christiansen, E.H., Burt, D.M., Sheridan, M.F., 1986. The geology and geochemistry of Cenozoic topaz rhyolites from the western United States. Geological Society of America Special Paper 205, 88 pp.

Clemens, J.D., Wall, V.J., 1984. Origin and evolution of a peraluminous silicic ignimbrite suite: The Violet Town Volcanics. Contributions to Mineralogy and Petrology 88, 354–371.

Coney, P.J., 1978. Mesozoic-Cenozoic Cordilleran plate tectonics, in: Smith, R.B., Eaton, G.P. (Eds.), Cenozoic Tectonics and Regional Geophysics of the Western Cordillera. Geological Society of America Memoir 152, pp. 33–50.

Costa, A., Gottsmann, J., Melnik, O., Sparks, R.S.J., 2011. A stress-controlled mechanism for the intensity of very large magnitude explosive eruptions. Earth and Planetary Science Letters 310, 161–166. https://doi.org/10.1016/j.epsl.2011.07.024.

Cruz-Castillo, J.U., 2019. Análisis petrográfico y geoquímico de la Ignimbrita Guanamé en el municipio de Venado, San Luis Potosí. San Luis Potosí, México: Universidad Autónoma de San Luis Potosí, Facultad de Ingeniería, Tesis Ingeniería Geológica, 67 pp.

Cuéllar-Cárdenas, M.A., Nieto-Samaniego, Á.F., Levresse, G., Alaniz-Álvarez, S.A., Solari, L., Ortega-Obregón, C., López-Martínez, M., 2012. Límites temporales de la deformación por acortamiento Laramide en el centro de México. Revista Mexicana de Ciencias Geológicas 29, 179–203.

Dahlquist, J.A., Galindo, C., Pankhurst, R.J., Rapela, C.W., Alasino, P.H., Saavedra, J., Fanning, C.M., 2007. Magmatic evolution of the Peñón Rosado granite: petrogenesis of garnet-bearing granitoids. Lithos 95, 177–207.

Damon, P., 1981. Age trends of igneous activity in relations to metallogenesis in the southern cordillera, in: Dickinson, W.R., Payne, W.D. (Eds.), Relations of tectonics to ore deposits in the southern Cordillera. Arizona Geological Society Digest 14, pp. 137–154.

Damon, P.E., Shafiqullah, M., Clark, K.F., 1983. Geochronology of the porphyry copper deposits and related mineralization of Mexico. Canadian Journal of Earth Sciences 20, 1052–1071.

de Cserna, Z., 1976. Geology of the Fresnillo area, Zacatecas, Mexico. Geological Society of America Bulletin 87, 1191–1199.

Dickinson, W.R., Lawton, T.F., 2001. Carboniferous to Cretaceous assembly and fragmentation of Mexico. Geological Society of America Bulletin 113, 1142–1160.

Duque-Trujillo, J., Ferrari, L., Orozco-Esquivel, T., López-Martínez, M., Lonsdale, P., Bryan, S.E., Kluesner, J., Piñero-Lajas, D., Solari, L., 2015. Timing of rifting in the southern Gulf of California and its conjugate margins: Insights from the plutonic record. Geological Society of America Bulletin 127, 702–736. https://doi.org/10.1130/B31008.1.

Eguiluz De Antuñano, S., Aranda-García, M., Marrett, R., 2000. Tectónica de la Sierra Madre Oriental, México. Boletín de la Sociedad Geológica Mexicana 53, 1–26.

Elkins, L.T., Grove, T.L., 1990. Ternary feldspar experiments and thermodynamic models. American Mineralogist 75, 544–559.

Ellis, B.S., Cordonnier, B., Rowe, M.C., Szymanowski, D., Bachmann, O., Andrews, G.D.M., 2015. Groundmass crystallisation and cooling rates of lava-like ignimbrites: the Grey's Landing ignimbrite, southern Idaho, USA. Bulletin of Volcanology 77, 87-102. https://doi.org/10.1007/s00445-015-0972-5.

Enami, M., Nishiyama, T., Mouri, T., 2007. Laser Raman microspectrometry of metamorphic quartz: A simple method for comparison of metamorphic pressures. American Mineralogist 92, 1303–1315.

Espinoza, F., Morata, D., Polvé, M., Lagabrielle, Y., Maury, R.C., Guivel, C., Cotten, J., Bellon, H., Suárez, M., 2008. Bimodal back-arc alkaline magmatism after ridge subduction: Pliocene felsic rocks from Central Patagonia (47° S). Lithos 101, 191–217.

Faure, Gunter; Mensing, Teresa M. (2005): Isotopes: principles and applications: John Wiley & Sons, Hoboken, New Jersey. 897 pp.

Ferrari, L., López-Martínez, M., Rosas-Elguera, J., 2002. Ignimbrite flare-up and deformation in the southern Sierra Madre Occidental, western Mexico: Implications for the late subduction history of the Farallon plate. Tectonics 21, 1-23.

Ferrari, L., Valencia-Moreno, M., Bryan, S., 2005. Magmatismo y tectónica en la Sierra Madre Occidental y su relación con la evolución de la margen occidental de Norteamérica. Boletín de la Sociedad Geológica Mexicana 57, 343–378.

Ferrari, L., Valencia-Moreno, M., Bryan, S., 2007. Magmatism and tectonics of the Sierra Madre Occidental and its relation with the evolution of the western margin of North America, in: Alanis-Álvarez, S.A., Nieto-Samaniego, Á.F. (Eds.), Geology of México: Celebrating the Centenary of the Geological Society of México, vol. 422. Geological Society of America Special Paper, pp. 1–39.

Ferrari, L., López-Martínez, M., Orozco-Esquivel, T., Bryan, S.E., Duque-Trujillo, J., Lonsdale, P., Solari, L., 2013. Late Oligocene to Middle Miocene rifting and synextensional magmatism in the southwestern Sierra Madre Occidental, Mexico: The beginning of the Gulf of California rift. Geosphere 9, 1161–1200.

Ferrari, L., Orozco-Esquivel, T., Bryan, S.E., Lopez-Martinez, M., Silva-Fragoso, A., 2018. Cenozoic magmatism and extension in western Mexico: Linking the Sierra Madre Occidental silicic large igneous province and the Comondú Group with the Gulf of California rift. Earth-Science Reviews 183, 115–152.

Fitton, J.G., 1972. The genetic significance of almandine-pyrope phenocrysts in the calc-alkaline Borrowdale Volcanic Group, northern England. Contributions to Mineralogy and Petrology 36, 231–248.

Fitz-Diaz, E., Hudleston, P., Tolson, G., 2011. Comparison of tectonic styles in the Mexican and Canadian Rocky Mountain fold-thrust belt. Geological Society, London, Special Publications 349, 149–167.

Fix, J.E., 1975. The crust and upper mantle of central Mexico. Geophysical Journal of the Royal Astronomical Society 43, 453–499.

Freydier, C., Martinez, J.R., Lapierre, H., Tardy, M., Coulon, C., 1996. The Early Cretaceous Arperos oceanic basin (western Mexico). Geochemical evidence for an aseismic ridge formed near a spreading center. Tectonophysics 259, 343–367.

Frost, B.R., Frost, C.D., 2008. A Geochemical Classification for Feldspathic Igneous Rocks. Journal of Petrology 49, 1955–1969. https://doi.org/10.1093/petrology/egn054.

Fuhrman, M.L., Lindsley, D.H., 1988. Ternary-feldspar modeling and thermometry. American Mineralogist 73, 201–215.

Fuhrmann, U., Lippolt, H.J., Hess, J.C., 1987. Examination of some proposed K-Ar standards: 40Ar39Ar analyses and conventional K-Ar data. Chemical Geology (Isotope Geoscience section) 66, 41–51.

Gaetani, G.A., Ghiorso, M.S., Sack, R.O., Hirschmann, M., Asimov, P.D., 1998. Melts. Science 282, 1834–1835.

Ghiorso, M.S., 1997. Thermodynamic models of igneous processes. Annual Review of Earth and Planetary Sciences 25, 221–241.

Ghiorso, M.S., Evans, B.W., 2008. Thermodynamics of rhombohedral oxide solid solutions and a revision of the Fe-Ti two-oxide geothermometer and oxygen-barometer. American Journal of Science 308, 957–1039.

Ghiorso, M.S., Gualda, G.A.R., 2015. An H 2 O–CO 2 mixed fluid saturation model compatible with rhyolite-MELTS. Contributions to Mineralogy and Petrology 169, 53.

Ganguly, J., Cheng, W., Tirone, M., 1996 a. Thermodynamics of aluminosilicate garnet solid solution: new experimental data, an optimized model, and thermometric applications. Contributions to Mineralogy and Petrology 126, 137–151.

Ganguly, J., Chakraborty, S., Sharp, T.G., Rumble, D., 1996 b. Constraint on the time scale of biotite-grade metamorphism during Acadian Orogeny from a natural garnet-garnet diffusion couple. American Mineralogist 81, 1208–1216.

Gilbert, J.S., Rogers, N.W., 1989. The significance of garnet in the Permo-Carboniferous volcanic rocks of the Pyrenees. Journal of the Geological Society 146, 477–490.

Gill, J.B., 1981. Orogenic Andesites and Plate Tectonics. Springer Science & Business Media. 390 pp.

Green, T.H., 1976. Experimental generation of cordierite-or garnet-bearing granitic liquids from a pelitic composition. Geology 4, 85–88.

Green, T.H., 1977. Garnet in silicic liquids and its possible use as a PT indicator. Contributions to Mineralogy and Petrology 65, 59–67.

Green, T.H., 1992. Experimental phase equilibrium studies of garnet-bearing I-type volcanics and high-level intrusives from Northland, New Zealand. Earth and Environmental Science Transactions of The Royal Society of Edinburgh 83, 429–438.

Green, T.H., Ringwood, A.E., 1968. Origin of garnet phenocrysts in calc-alkaline rocks. Contributions to Mineralogy and Petrology 18, 163–174.

Green, T.H., Ringwood, A.E., 1972. Crystallization of garnet-bearing rhyodacite under high-pressure hydrous conditions. Journal of the Geological Society of Australia 19, 203–212.

Gualda, G.A.R., Ghiorso, M.S., Lemons, R.V., Carley, T.L., 2012. Rhyolite-MELTS: a modified calibration of MELTS optimized for silica-rich, fluid-bearing magmatic systems. Journal of Petrology 53, 875–890.

Gunderson, R., Cameron, K., Cameron, M., 1986. Mid-Cenozoic high-K calc-alkalic and alkalic volcanism in eastern Chihuahua, Mexico: Geology and geochemistry of the Benavides-Pozos area. Geological Society of America Bulletin 97, 737–753.

Guo, P., Xu, W.-L., Yu, J.-J., Wang, F., Tang, J., Li, Y., 2016. Geochronology and geochemistry of Late Triassic bimodal igneous rocks at the eastern margin of the Songnen–Zhangguangcai Range Massif, Northeast China: petrogenesis and tectonic implications. International Geology Review 58, 196–215.

Guzman, E.J., de Cserna, Z., 1963. Tectonic history of Mexico, in: Childs, O.E., Beebe, B.W. (Eds.), Backbone of the Americas: Tectonic History from Pole to Pole: A Symposium. American Association of Petroleum Geologists, pp. 113–129.

Harangi, S.Z., Downes, H., Kósa, L., Szabó, C.S., Thirwall, M.F., Mason, P.R.D., Mattey, D., 2001. Almandine garnet in calc-alkaline volcanic rocks of the Northern Pannonian Basin (Eastern–

Central Europe): Geochemistry, petrogenesis and geodynamic implications. Journal of Petrology 42, 1813–1843.

Harker, A., 1909. The natural history of igneous rocks. Methuen, London, 258 pp.

Heinrichs, H., Herrmann, A.G., 2013. Praktikum der analytischen Geochemie. Springer-Verlag.

Henry, C.D., Aranda-Gómez, J.J., 1992. The real southern Basin and Range: Mid-to late Cenozoic extension in Mexico. Geology 20, 701–704.

Hensen, B.J., Green, D.H., 1973. Experimental study of the stability of cordierite and garnet in pelitic compositions at high pressures and temperatures. Contributions to Mineralogy and Petrology 38, 151–166.

Hildreth, W., 1981. Gradients in silicic magma chambers: Implications for lithospheric magmatism. Journal of Geophysical Research 86, 10153–10192. https://doi.org/10.1029/JB086iB11p10153.

Hochstaedter, A.G., Gill, J.B., Kusakabe, M., Newman, S., Pringle, M., Taylor, B., Fryer, P., 1990. Volcanism in the Sumisu Rift, I. Major element, volatile, and stable isotope geochemistry. Earth and Planetary Science Letters 100, 179–194.

Hodges, K.V., McKenna, L.W., 1987. Realistic propagation of uncertainties in geologic thermobarometry. American Mineralogist 72, 671–680.

Hoppe, M., Barboza-Gudiño, J.R., Schulz, H.M., 2002. Late Triassic submarine fan deposits in northwestern San Luis Potosi, Mexico-lithology, facies and diagenesis. Neues Jahrbuch fur Geologie und Palaontologie-Monatshefte, 705–724.

Hora, J.M., Kronz, A., Möller-McNett, S., Wörner, G., 2013. An Excel-based tool for evaluating and visualizing geothermobarometry data. Computers & geosciences 56, 178–185.

Idier, C., 2003. Caractéristiques des evènements magmatiques Eocènes-Oligocènes et Plio-Quaternaires du champ volcanique de San Luis Potosi (Mexique). Ecole Doctorale des Sciences de la Mer Université de Bretagne Occidentale, France. Mèmoire de Licence, 55pp.

Janoušek, V., Farrow, C.M., Erban, V., 2006. Interpretation of whole-rock geochemical data in igneous geochemistry: introducing Geochemical Data Toolkit (GCDkit). Journal of Petrology 47, 1255–1259.

Janoušek, V., Moyen, J.-F., Martin, H., Erban, V., Farrow, C., 2015. Geochemical Modelling of Igneous Processes: Principles and Recipes in R Language. Springer.

Jicha, B.R., Scholl, D.W., Rea, D.K., 2009. Circum-Pacific arc flare-ups and global cooling near the Eocene-Oligocene boundary. Geology 37, 303–306. https://doi.org/10.1130/G25392A.1.

Kelley, K.A., Cottrell, E., 2009. Water and the oxidation state of subduction zone magmas. Science 325 (5940), 605–607. https://doi.org/10.1126/science.1174156.

Keppie, J.D., 2004. Terranes of Mexico revisited: A 1.3 billion year odyssey. International Geology Review 46, 765–794.

Kohn, M.J., 2014. "Thermoba-Raman-try": Calibration of spectroscopic barometers and thermometers for mineral inclusions. Earth and Planetary Science Letters 388, 187–196.

Kohn, M.J., Spear, F.S., 1991. Error propagation for barometers: 2. Application to rocks. American Mineralogist 76, 138–147.

Kuiper, K.F., Deino, A., Hilgen, F.J., Krijgsman, W., Renne, P.R., Wijbrans, a., JR, 2008. Synchronizing rock clocks of Earth history. Science 320 (5875), 500–504.

Labarthe-Hernández, G., Tristán-González, M., 1980. Cartografía geológica hoja Santa María del Río. San Luis Potosí: Universidad Autónoma de San Luis Potosí, Instituto de Geología y Metalurgia, Folleto Técnico 67, 32 p.

Labarthe-Hernández, G., Jiménez-López, L.S., 1991. Cartografía geológica 1: 50000 de las hojas Cerritos de Bernal, Santo Domingo, El Estribo y La Herradura, estado de San Luis Potosí 113, 69 pp.

Labarthe-Hernández, G., Jiménez-López, L.S., 1992. Características físicas y estructura de lavas e ignimbritas riolíticas en la Sierra de San Miguelito, S.L.P. San Luis Potosí: Universidad Autónoma de San Luis Potosí, Instituto de Geología y Metalurgia, Folleto Técnico 114, 31 p.

Labarthe-Hernández, G., Jiménez-López, L.S., 1993. Geologia del domo Cerro Grande, Sierra de San Miguelito, SLP. San Luis Potosí: Universidad Autónoma de San Luis Potosí, Instituto de Geología y Metalurgia, Folleto Técnico 117, 22 p.

Labarthe-Hernández, G., Jiménez-López, L.S., 1994. Geología de la porción sureste de la Sierra de San Miguelito. San Luis Potosí: Universidad Autónoma de San Luis Potosí, Instituto de Geología y Metalurgia, Folleto Técnico 120, 34 p.

Labarthe-Hernández, G., Tristán-González, M., Aranda-Gómez, J.J., 1982. Revisión estratigráfica del Cenozoico de la parte central del estado de San Luis Potosí. Universidad Autónoma de San Luis Potosí, Instituto de Geología, Folleto Técnico 85, 208 pp.

Labarthe-Hernández, G., Tristán-González, M., Aguillón-Robles, A., Jiménez-López, L.S., Romero, A., 1989. Cartografía geológica 1: 50,000 de las hojas El Refugio y Mineral El Realito, Estados de San Luis Potosí y Guanajuato: Universidad Autónoma de San Luis Potosí. Universidad Autónoma de San Luis Potosí, Instituto de Geología, Folleto Técnico 112, 85 pp.

Lantai, C., 1991. Genesis of garnets from andesite of Karanca Mountains. Acta Geologica Hungarica 34, 133–154.

Le Bas, M.J., Le Maitre, R.W., Streckeisen, A., Zanettin, B., 1986. A Chemical Classification of Volcanic Rocks Based on the Total Alkali-Silica Diagram. Journal of Petrology 27, 745–750.

Lee, J.K.W., Williams, I.S., Ellis, D.J., 1997. Pb, U and Th diffusion in natural zircon. Nature 390, 159-162.

Leroy, J.L., Rodriguez-Rios, R., Dewonck, S., 2002. The topaz-bearing rhyolites from the San Luis Potosi area (Mexico): characteristics of the lava and growth conditions of topaz. Bulletin de la Societe Geologique de France 173, 579–588. https://doi.org/10.2113/173.6.579.

Lipman, P.W., 2007. Incremental assembly and prolonged consolidation of Cordilleran magma chambers: Evidence from the Southern Rocky Mountain volcanic field. Geosphere 3, 42–70. https://doi.org/10.1130/GES00061.1.

López-Doncel, R.A., 2003. La Formación Tamabra del Cretácico medio en la porción central del margen occidental de la Plataforma Valles-San Luis Potosí, centro-noreste de México. Revista mexicana de ciencias geológicas 20, 1–19.

López-Infanzón, M., 1986. Estudio petrogenético de las rocas ígneas en las Formaciones Huizachal y Nazas. Boletín de la Sociedad Geológica Mexicana 47, 1–41.

Ludwig, K.R., 2003. Isoplot 3.00: A geochronological toolkit for Microsoft Excel. Berkeley Geochronology Center Special Publication 4, 1-75.

Luhr, J.F., Aranda-Gomez, J.J., Pier, J.G., 1989. Spinel-lherzolite-bearing quaternary volcanic centers in San Luis Potosí, Mexico: 1. Geology, mineralology, and petrology. Journal of Geophysical Research 94, 7916–7940. https://doi.org/10.1029/JB094iB06p07916.

Magonthier, M.C., 1988. Distinctive rhyolite suites in the mid-Tertiary ignimbritic complex of the Sierra Madre Occidental, western Mexico. Bulletin de la Société Géologique de France 4, 57–68.

Martin, A.J., Ganguly, J., DeCelles, P.G., 2010. Metamorphism of Greater and Lesser Himalayan rocks exposed in the Modi Khola valley, central Nepal. Contributions to Mineralogy and Petrology 159, 203.

Martini, M., Pedraglio, L.F., Martínez, M.L., Valencia, V.A., 2010. Stratigraphic redefinition of the Zihuatanejo area, southwestern Mexico. Revista Mexicana de Ciencias Geológicas 27, 412–430.

Mascuñano, E., Levresse, G., Cardellach, E., Tritlla, J., Corona-Esquivel, R., Meyzen, C., 2013. Post-Laramide, Eocene magmatic activity in Sierra de Catorce, San Luis Potosí, México. Revista Mexicana de Ciencias Geológicas 30, 299–311.

McDonough, W.F., Sun, S.-S., 1995. The composition of the Earth. Chemical Geology 120, 223–253. https://doi.org/10.1016/0009-2541(94)00140-4.

McDowell, F.W., 2007. Geologic transect across the northern Sierra Madre Occidental volcanic field, Chihuahua and Sonora, Mexico. Geological Society of America Digital Map and Chart Series, 6, 1-70.

McDowell, F.W., McIntosh, W.C., 2012. Timing of intense magmatic episodes in the northern and central Sierra Madre Occidental, western Mexico. Geosphere 8, 1505-1526. https://doi.org/10.1130/GES00792.1.

McDowell, F.W., Keizer, R.P., 1977. Timing of mid-Tertiary volcanism in the Sierra Madre Occidental between Durango city and Mazatlán, Mexico. Geological Society of America Bulletin 88, 1479–1487.

McDowell, F.W., Clabaugh, S.E., 1979. Ignimbrites of the Sierra Madre Occidental and their relation to the tectonic history of western Mexico, in: Chapin, C.E., Elston, W.E. (Eds.), Ash-flow tuffs, vol. 180. Geological Society of America, pp. 113–124.

McDowell, F.W., Mauger, R.L., 1994. K-Ar and U-Pb zircon chronology of Late Cretaceous and Tertiary magmatism in central Chihuahua State, Mexico. Geological Society of America Bulletin 106, 118–132.

McDowell, F.W., Roldán-Quintana, J., Amaya-Martínez, R., 1997. Interrelationship of sedimentary and volcanic deposits associated with Tertiary extension in Sonora, Mexico. GSA Bulletin 109 (10), 1349–1360. https://doi.org/10.1130/0016-7606(1997)109<1349:IOSAVD>2.3.CO;2.

Mezger, K., Krogstad, E.J., 1997. Interpretation of discordant U-Pb zircon ages: An evaluation. Journal of Metamorphic Geology 15, 127–140.

Mirnejad, H., Blourian, G.H., Kheirkhah, M., Akrami, M.A., Tutti, F., 2008. Garnet-bearing rhyolite from Deh-Salm area, Lut block, Eastern Iran: anatexis of deep crustal rocks. Mineralogy and Petrology 94, 259–269.

Miyashiro, A., 1978. Nature of alkalic volcanic rock series. Contributions to Mineralogy and Petrology 66, 91–104.

Morimoto, N., 1988. Nomenclature of Pyroxenes. Mineralogy and Petrology 39, 55–76. https://doi.org/10.1007/BF01226262.

Mortensen, J.K., Hall, B.V., Bissig, T., Friedman, R.M., Danielson, T., Oliver, J., Rhys, D.A., Ross, K.V., Gabites, J.E., 2008. Age and Paleotectonic Setting of Volcanogenic Massive Sulfide Deposits in the Guerrero Terrane of Central Mexico: Constraints from U-Pb Age and Pb Isotope Studies. Economic Geology 103, 117–140.

Murray, B.P., Busby, C.J., Ferrari, L., Solari, L.A., 2013. Synvolcanic crustal extension during the mid-Cenozoic ignimbrite flare-up in the northern Sierra Madre Occidental, Mexico: Evidence from the Guazapares Mining District region, western Chihuahua. Geosphere 9, 1201–1235.

Nieto-Samaniego, A.F., Macías-Romo, C., Alaniz-Álvarez, S.A., 1996. Nuevas edades isotópicas de la cubierta volcánica cenozoica de la parte meridional de la Mesa Central, México. Revista Mexicana de Ciencias Geológicas 13, 117–122.

Nieto-Samaniego, Á.F., Alaniz-Álvarez, S.A., Labarthe-Hernández, G., 1997. La deformación cenozoica poslaramídica en la parte meridional de la Mesa Central, México. Revista Mexicana de Ciencias Geológicas 14, 13–25.

Nieto-Samaniego, Á.F., Ferrari, L., Alaniz-Alvarez, S.A., Labarthe-Hernández, G., Rosas-Elguera, J., 1999. Variation of Cenozoic extension and volcanism across the southern Sierra Madre Occidental volcanic province, Mexico. Geological Society of America Bulletin 111, 347–363.

Nieto-Samaniego, Á.F., Alaniz-Álvarez, S.A., Camprubí, A., 2007. Mesa Central of México: Stratigraphy, structure, and Cenozoic tectonic evolution, in: Alaniz-Álvarez, S.A., Nieto-Samaniego, Á.F. (Eds.), Geology of México: Celebrating the Centenary of the Geological Society of México. Geological Society of America Special Paper 422, pp. 41–70.

Orozco-Esquivel, M.T., Nieto-Samaniego, A.F., Alaniz-Álvarez, S.A., 2002. Origin of rhyolitic lavas in the Mesa Central, Mexico, by crustal melting related to extension. Journal of

Volcanology and Geothermal Research 118, 37–56. https://doi.org/10.1016/S0377-0273(02)00249-4.

Ortega-Obregón, C., Solari, L., Gómez-Tuena, A., Elías-Herrera, M., Ortega-Gutiérrez, F., Macías-Romo, C., 2014. Permian–Carboniferous arc magmatism in southern Mexico: U–Pb dating, trace element and Hf isotopic evidence on zircons of earliest subduction beneath the western margin of Gondwana. International Journal of Earth Sciences 103, 1287–1300. https://doi.org/10.1007/s00531-013-0933-1.

Padilla, R.J., Sánchez, R.J., 1985. Las estructuras de la Curvatura de Monterrey, Estados de Coahuila, Nuevo León, Zacatecas y San Luis Potosí. Revista Mexicana de Ciencias Geológicas 6, 1–20.

Pantoja-Alor, J., 1972. La Formación Nazas del Levantamiento de Villa Juárez, Estado de Durango. Segunda Convención Nacional de la Sociedad Geológica Mexicana, Memorias, 25–31.

Paton, C., Woodhead, J.D., Hellstrom, J.C., Hergt, J.M., Greig, A., Maas, R., 2010. Improved laser ablation U-Pb zircon geochronology through robust downhole fractionation correction. Geochemistry, Geophysics, Geosystems 11, 1-36. https://doi.org/10.1029/2009GC002618.

Pearce, T.H., 1968. A contribution to the theory of variation diagrams. Contributions to Mineralogy and Petrology 19, 142–157.

Pearce, J.A., Cann, J.R., 1973. Tectonic setting of basic volcanic rocks determined using trace element analyses. Earth and Planetary Science Letters 19, 290–300.

Peccerillo, A., Taylor, S.R., 1976. Geochemistry of Eocene calc-alkaline volcanic rocks from the Kastamonu area, northern Turkey. Contributions to Mineralogy and Petrology 58, 63–81.

Petrus, J.A., Kamber, B.S., 2012. VizualAge: A Novel Approach to Laser Ablation ICP-MS U-Pb Geochronology Data Reduction. Geostandards and Geoanalytical Research 36, 247–270. https://doi.org/10.1111/j.1751-908X.2012.00158.x.

Pinto-Linares, P.J., Levresse, G., Tritlla, J., Valencia, V.A., Torres-Aguilera, J.M., González, M., Estrada, D., 2008. Transitional adakite-like to calc-alkaline magmas in a continental extensional setting at La Paz Au-Cu skarn deposits, Mesa Central, Mexico: metallogenic implications. Revista Mexicana de Ciencias Geológicas 25, 39–58.

Ponce S, B.F., Clark, K.F., 1988. The Zacatecas mining district; a Tertiary caldera complex associated with precious and base metal mineralization. and the Bulletin of the Society of Economic Geologists 83, 1668–1682.

Powell, M., Powell, R., 1977. Plagioclase-alkali-feldspar geothermometry revisited. Mineralogical Magazine 41, 253–256.

Pownceby, M.I., Wall, V.J., O'Neill, H.S.C., 1987. Fe-Mn partitioning between garnet and ilmenite: experimental calibration and applications. Contributions to Mineralogy and Petrology 97, 116–126.

Pownceby, M.I., Wall, V.J., O'Neill, H.S.C., 1991. An experimental study of the effect of Ca upon garnet-ilmenite Fe-Mn exchange equilibria. American Mineralogist 76, 1580–1588.

Purdy, J.W., Jäger, E., 1976. K-Ar ages on rock-forming minerals from the Central Alps. Memorie degli Istituti di Geologia e Mineralogia dell' Università di Padova 30, 1–31.

Putirka, K.D., 2008. Thermometers and barometers for volcanic systems. Reviews in Mineralogy and Geochemistry 69, 61–120.

Quintero-Legorreta, O., 1992. Geología de la región de Comanja, estados de Guanajuato y Jalisco. Revista Mexicana de Ciencias Geológicas 10, 6–25.

Ranson, W.A., Fernández, L.A., Simmons Jr, W.B., de la Vega, Salvador Enciso, 1982. Petrology of the metamorphic rocks of Zacatecas, Zac., Mexico. Boletín de la Sociedad Geológica Mexicana 43, 37–59.

Reed, S.J.B., 2005. Electron microprobe analysis and scanning electron microscopy in geology. Cambridge University Press, 189 pp.

René, M., Stelling, J., 2007. Garnet-bearing granite from the Třebíč pluton, Bohemian massif (Czech Republic). Mineralogy and Petrology 91, 55–69.

Rivera, J., Ponce, L., 1986. Estructura de la corteza al oriente de la Sierra Madre Occidental, México, basada en la velocidad del grupo de las ondas de Rayleigh. Geofísica Internacional 25, 383-402.

Robert, G., Andrews, G.D.M., Ye, J., Whittington, A.G., 2013. Rheological controls on the emplacement of extremely high-grade ignimbrites. Geology 41, 1031–1034. https://doi.org/10.1130/G34519.1.

Rocha-Echavarría, N.A., Aguillón-Robles, A., Rodríguez-Ríos, R., Bellon, H., Torres-Hernández, J.R., 2006. Petrología y geoquímica de los centros volcánicos de la Sierra de Pinos Zac y su

relación con el Campo Volcánico de San Luis Potosí (resumen). Reunión Anual, Unión Geofísica Mexicana, Puerto Vallarta, Jal., GEOS 26, 106.

Rodríguez-Ríos, R., Aguillón-Robles, A., Leroy, J.L., 2007. Evolución petrológica y geoquímica de un complejo de domos topacíferos en el Campo Volcánico de San Luis Potosí (México). Revista Mexicana de Ciencias Geológicas 24, 328–343.

Rodríguez-Ríos, R., Torres-Aguilera, J.M., 2009. Evolución petrológica y geoquímica del vulcanismo bimodal oligocénico en el campo volcánico de San Luis Potosí (México). Revista Mexicana de Ciencias Geológicas 26, 658–673.

Rosenfeld, J.L., Chase, A.B., 1961. Pressure and temperature of crystallization from elastic effects around solid inclusions in minerals? American Journal of Science 259, 519–541.

Ruiz, J., Patchett, P.J., Arculus, R.J., 1988. Nd-Sr isotope composition of lower crustal xenoliths—Evidence for the origin of mid-Tertiary felsic volcanics in Mexico. Contributions to Mineralogy and Petrology 99 (1), 36–43.

Salinas-Prieto, J.C., Monod, O., Faure, M., 2000. Ductile deformations of opposite vergence in the eastern part of the Guerrero Terrane (SW Mexico). Journal of South American Earth Sciences 13, 389–402.

Schaaf, P., Heinrich, W., Besch, T., 1994. Composition and Sm-Nd isotopic data of the lower crust beneath San Luis Potosí, central Mexico: Evidence from a granulite-facies xenolith suite. Chemical Geology 118, 63–84.

Schumacher, E., 1975. Herstellung von 99, 9997% 38Ar für die 40K/40Ar Geochronologie. Geochronologia Chimica 24, 441–442.

Serna-Bafún, J.H., 2018. Control estructural para explicar el emplazamiento del volcanismo final en el norte del Complejo Volcánico de la Sierra de San Miguelito. San Luis Potosí, México: Universidad Autónoma de San Luis Potosí, Facultad de Ingeniería, Tesis de Licienciatura, 185 pp.

Shand, S.J., 1943. Eruptive rocks: Their genesis, Composition, Classification, and Their Relation to Ore-Deposits, with a Chapter on Meteorite. John Wiley & Sons, New York, 444 pp.

Sheibi, M., Esmaeily, D., Nédélec, A., Bouchez, J.L., Kananian, A., 2010. Geochemistry and petrology of garnet-bearing S-type Shir-Kuh Granite, southwest Yazd, Central Iran. Island Arc 19, 292–312.

Shukuno, H., Tamura, Y., Tani, K., Chang, Q., Suzuki, T., Fiske, R.S., 2006. Origin of silicic magmas and the compositional gap at Sumisu submarine caldera, Izu–Bonin arc, Japan. Journal of Volcanology and Geothermal Research 156, 187–216.

Sieck, P., López-Doncel, R., Dávila-Harris, P., Aguillón-Robles, A., Wemmer, K., Maury, R.C., 2019. Almandine garnet-bearing rhyolites associated to bimodal volcanism in the Mesa Central of Mexico: Geochemical, petrological and geochronological evolution. Journal of South American Earth Sciences 92, 310-328. https://doi.org/10.1016/j.jsames.2019.03.018.

Sláma, J., Košler, J., Condon, D.J., Crowley, J.L., Gerdes, A., Hanchar, J.M., Horstwood, M.S.A., Morris, G.A., Nasdala, L., Norberg, N., 2008. Plešovice zircon—a new natural reference material for U–Pb and Hf isotopic microanalysis. Chemical Geology 249, 1–35.

Smith, D.L., Jones, R.L., 1979. Thermal anomaly in northern Mexico: An extension of the Rio Grande rift?, in: Rieker, R.E. (Ed.), The Rio Grande rift—Tectonics and magmatism. American Geophysical Union, Washington, D.C., pp. 269–278.

Solari, L.A., Gómez-Tuena, A., Bernal, J.P., Pérez-Arvizu, O., Tanner, M., 2010. U-Pb Zircon Geochronology with an Integrated LA-ICP-MS Microanalytical Workstation: Achievements in Precision and Accuracy. Geostandards and Geoanalytical Research 34, 5–18. https://doi.org/10.1111/j.1751-908X.2009.00027.x.

Solari, L.A., Ortega-Obregón, C., Bernal, J.P., 2015. U–Pb zircon geochronology by LAICPMS combined with thermal annealing: Achievements in precision and accuracy on dating standard and unknown samples. Chemical Geology 414, 109–123. https://doi.org/10.1016/j.chemgeo.2015.09.008.

Steiger, R.H., Jäger, E., 1977. Subcommission on geochronology: Convention on the use of decay constants in geo- and cosmochronology. Earth and Planetary Science Letters 36, 359–362. https://doi.org/10.1016/0012-821X(77)90060-7.

Stevens, G., Villaros, A., Moyen, J.-F., 2007. Selective peritectic garnet entrainment as the origin of geochemical diversity in S-type granites. Geology 35, 9–12.

Stewart, J.H., 1978. Basin-range structure in western North America: A review, in: Smith, R.B., Eaton, G.P. (Eds.), Cenozoic tectonics and regional geophysics of the western Cordillera. Geological Society of America Memoirs 152, pp. 1–31.

Stewart, J.H., 1998. Regional characteristics, tilt domains, and extensional history of the late Cenozoic Basin and Range province, western North America, in: Faulds, J.E., Stewart, J.H.

(Eds.), Accommodation zones and transfer zones; The regional segmentation of the Basin and Range Province. Geological Society of America Special Paper 323, pp. 47–74.

Stormer, J.C., 1975. A practical two-feldspar geothermometer. American Mineralogist 60, 667–674.

Swanson, E.R., 1989. A new type of maar volcano from the State of Durango-the El Jagüey-La Breña complex reinterpreted. Revista Mexicana de Ciencias Geológicas 8, 243–247.

Swanson, E.R., McDowell, F.W., 1984. Calderas of the Sierra Madre Occidental Volcanic Field western Mexico. Journal of Geophysical Research 89, 8787-8799. https://doi.org/10.1029/JB089iB10p08787.

Swanson, E.R., Kempter, K.A., McDowell, F.W., McIntosh, W.C., 2006. Major ignimbrites and volcanic centers of the Copper Canyon area: A view into the core of Mexico's Sierra Madre Occidental. Geosphere 2, 125-141. https://doi.org/10.1130/GES00042.1.

Talavera-Mendoza, O., Ruiz, J., Gehrels, G.E., Valencia, V.A., Centeno-García, E., 2007. Detrital zircon U/Pb geochronology of southern Guerrero and western Mixteca arc successions (southern Mexico): New insights for the tectonic evolution of southwestern North America during the late Mesozoic. Geological Society of America Bulletin 119, 1052–1065.

Tardy, M., Longoria, J.F., Martínez-Reyes, J., Mitre, L.M., Patillo, M., Sánchez, R.J., 1975. Observaciones generales sobre la estructura la estructura de la Sierra Madre Oriental: La aloctonía del conjunto Cadena Alta-Altiplano Central, entre Torreón, Coahuila y San Luis Potosí, S.L.P. México. Revista del Instituto de Geología, Universidad Nacional Autónoma de México, 75, 1-11.

Torres-Hernández, J.R., Labarthe-Hernández, G., Aguillón-Robles, A., Gómez-Anguiano, M., Mata-Segura, J.L., 2006. The pyroclastic dikes of the Tertiary San Luis Potosí volcanic field: Implications on the emplacement of Panalillo ignimbrite. Geofísica Internacional 45, 243–253.

Tristán-González, M., 1986. Estratigrafía y tectónica del graben de Villa de Reyes en los estados de San Luis Potosí y Guanajuato, México. Universidad Autónoma de San Luis Potosí, Instituto de Geología, Folleto Técnico 107, 91 pp.

Tristán-González, M., Torres-Hernández, J.R., Mata-Segura, J.L., 1994. Una deformación Pre-Laramídica, en la secuencia Vulcano-sedimentaria, de la parte oriental del Terreno Guerrero. GEOS 14, 82.

Tristán-González, M., Labarthe-Hernández, G., Aguirre-Díaz, G.J., Aguillón-Robles, A., 2008. Tectono-volcanic control of fissure type vents for the 28 Ma Panalillo ignimbrite in the Villa de Reyes Graben, San Luis Potosí, México. IOP Conference Series: Earth and Environmental Science 3. https://doi.org/10.1088/1755-1307/3/1/012026.

Tristán-González, M., 2008. Evolución tectono-magmática durante el Paleógeno en la porción sur-oriental de la Mesa Central. Juriquilla, Querétaro, México: Centro de Geociencias, Universidad Nacional Autónoma de México. tesis doctoral, 207pp.

Tristán-González, M., Aguillón-Robles, A., Barboza-Gudiño, J.R., Torres-Hernández, J.R., Bellon, H., López-Doncel, R.A., Rodríguez-Ríos, R., Labarthe-Hernández, G., 2009 a. Geocronología y distribución espacial del vulcanismo en el Campo Volcánico de San Luis Potosí. Boletín de la Sociedad Geológica Mexicana 61, 287–303.

Tristán-González, M., Aguirre-Díaz, G.J., Labarthe-Hernández, G., Torres-Hernández, J.R., Bellon, H., 2009 b. Post-Laramide and pre-Basin and Range deformation and implications for Paleogene (55–25 Ma) volcanism in central Mexico: A geological basis for a volcano-tectonic stress model. Tectonophysics 471, 136–152.

Trujillo-Candelaria, J.A., 1985. Origen del fallamiento, in: Flores-Núñez, J. (Ed.), Fallamiento de terrenos en Celaya. Sociedad Mexicana de Mecánica de Suelos, pp. 3–9.

Umhoefer, P.J., Dorsey, R.J., Willsey, S., Mayer, L., Renne, P., 2001. Stratigraphy and geochronology of the Comondú Group near Loreto, Baja California Sur, Mexico. Sedimentary Geology 144, 125–147.

Verma, S.P., 1984. Sr and Nd isotopic evidence for petrogenesis of mid-Tertiary felsic volcanism in the mineral district of Zacatecas, Zac.(Sierra Madre Occidental), Mexico. Chemical Geology 46, 37–53.

Verma, S.P., 2001. Geochemical evidence for a rift-related origin of bimodal volcanism at Meseta Río San Juan, North-Central Mexican Volcanic Belt. International Geology Review 43, 475–493.

Vidal-Solano, J.R., Paz-Moreno, F.A., Demant, A., López-Martínez, M., 2007. Ignimbritas hiperalcalinas del Mioceno medio en Sonora Central: revaluación de la estratigrafía y significado del volcanismo terciario. Revista Mexicana de Ciencias Geológicas 24, 47–67.

Villegas-Grimaldo, A., 2015. Evolución geoquímica del vulcanismo efusivo del Graben de Villa de Reyes en la porción meridional del Campo Volcánico de San Luis Potosi. San Luis Potosí,

México: Universidad Autónoma de San Luis Potosí, Facultad de Ingeniería, Tesis de Licenciatura, 56pp.

Ward, P.L., 1995. Subduction cycles under western North America during the Mesozoic and Cenozoic eras, in: Miller, D.M., Busby, C. (Eds.), Jurassic magmatism and tectonics of the North American Cordillera. Geological Society of America Special Paper 299, pp. 1-45.

Wark, D.A., 1991. Oligocene ash flow volcanism, northern Sierra Madre Occidental: Role of mafic and intermediate-composition magmas in rhyolite genesis. Journal of Geophysical Research 96, 13389–13411. https://doi.org/10.1029/90JB02666.

Waters, L.E., Lange, R.A., 2016. No effect of H2O degassing on the oxidation state of magmatic liquids. Earth and Planetary Science Letters 447, 48–59. https://doi.org/10.1016/j.epsl.2016.04.030.

Wemmer, K., 1991. K/Ar-Altersdatierungsmöglichkeiten für retrograde Deformationsprozesse im spröden und duktilen Bereich--Beispiele aus der KTB-Vorbohrung (Oberpfalz) und dem Bereich der Insubrischen Linie (N-Italien). Göttinger Arbeiten Geologie und Paläontologie 51, 1-61.

Wetherill, G.W., 1956. Discordant uranium-lead ages, I. Eos, Transactions American Geophysical Union 37, 320–326.

Whitney, J.A., Stormer, J.C., 1977. The distribution of NaAlSi3O8 between coexisting microcline and plagioclase and its effect on geothermometric calculations. American Mineralogist 62, 687–691.

Wilson, B.M., 1989. Igneous petrogenesis. Klumer Academic Publishers. 466 pp.

Wood, C.P., 1974. Petrogenesis of garnet-bearing rhyolites from Canterbury, New Zealand. New Zealand Journal of Geology and Geophysics 17, 759–787.

Xu, S.S., Nieto-Samaniego, Á.F., Alaniz-Álvarez, S.A., 2004. Vertical shear mechanism of faulting and estimation of strain in the Sierra de San Miguelito. Mesa Central, Mexico: Geological Acta 2, 189–201.

York, D., Evensen, N.M., Martınez, M.L., Basabe Delgado, J. de, 2004. Unified equations for the slope, intercept, and standard errors of the best straight line. American Journal of Physics 72, 367–375.

Young, E., Myers, A., Munson, E., Conklin, N., 1969. Mineralogy and geochemistry of fluorapatite from Cerro de Mercado, Durango, Mexico. U.S. Geological Survey Professional Paper, p. D84 D93, 84–93.

Appendix

Appendix A: Reference of published article

Almandine garnet-bearing rhyolites associated to bimodal volcanism in the Mesa Central of Mexico: Geochemical, petrological and geochronological evolution by Pascal Sieck, Rubén López-Doncel, Pablo Dávila-Harris, Alfredo Aguillón-Robles, Klaus Wemmer, René C. Maury published in Journal of South American Earth Science, Volume 92, June 2019, pages 310 – 318. The publication is available under: https://doi.org/10.1016/j.jsames.2019.03.018.

Journal of South American Earth Sciences 92 (2019) 310–328
Available online 22 March 2019

Contents lists available at ScienceDirect

Journal of South American Earth Sciences

journal homepage: www.elsevier.com/locate/jsames

Almandine garnet-bearing rhyolites associated to bimodal volcanism in the Mesa Central of Mexico: Geochemical, petrological and geochronological evolution

Pascal Sieck[a,*], Rubén López-Doncel[b], Pablo Dávila-Harris[a], Alfredo Aguillón-Robles[b], Klaus Wemmer[c], René C. Maury[d]

[a] División de Geociencias Aplicadas, Instituto Potosino de Investigación Científica y Tecnológica (IPICyT), Camino a la Presa San José 2055, C.P. 78216, San Luis Potosí, Mexico
[b] Instituto de Geología, Universidad Autónoma de San Luis Potosí, Av. Manuel Nava 5, 78240, San Luis Potosí, Mexico
[c] Geoscience Centre, Georg-August-Universität Göttingen, Goldschmidtstraße 3, 37077, Göttingen, Germany
[d] Université de Bretagne Occidentale, UMR 6538 Domaines Océaniques, Place N. Copernic, 29280, Plouzané, France

ARTICLE INFO

Keywords:
Garnet-bearing rhyolite
Bimodal volcanism
Mesa central
Oligocene
Mexico

ABSTRACT

Garnet-bearing rhyolitic flows and ignimbrites occur together with an andesitic lava flow in the central part of the Mesa Central in the western part of the Mexican state of San Luis Potosí, forming a typical K-rich sub-alkaline intra-plate tectonic setting bimodal series. Electron microprobe analysis indicates that the garnet is homogeneous and primarily almandine with subordinately pyrope, grossular, spessartine, and andradite. The chemistry of the garnets as well as the chemistry of the host rhyolite implies the crystallization of garnet as a primary phase from a lower crustal peraluminous magma. Rhyolite-MELTS simulations on the crystallization conf rms this information. Trace element analyses on the rhyolitic ignimbrite and the garnet-bearing rhyolite suggest that the petrogenesis of these acidic rocks involved partial melting of the lower crust and fractional crystallization. The andesitic lava flow is metaluminous and its trace element patterns suggest that the parental magma was derived from upper mantle partial melting and that it was stored at the mantle-crust boundary. We propose that the southern Basin and Range extension event favored the direct ascent of these magmas from the source through the brittle and thin crust (30–33 km), where slight interaction with the country rock took place, to the surface. Ue Pb dating on zircons from the rhyolites yielded ages ranging from 32.26 ± 0.92 Ma to 31.52 ± 0.48 Ma, consistent with the 31.25 ± 0.70 Ma whole rock Ke Ar age of the garnet-bearing rhyolite. This information supports the interpretation that the garnets are not xenocrysts but they are crystallized from a rhyolitic magma at lower crustal depths and ascended fast through the brittle crust, so the garnets could be preserved.

Appendix B: Representative chemical compositions of feldspars from the La Herradura area.

Appendix B 1: Representative chemical compositions of feldspars from the El Sombrero Ignimbrite.

Unit	El Sombrero Ignimbrite														
Sample	ZATT Pl01	ZATT Pl02	ZATT Pl03	ZATT Pl04	ZATT Kfs01	ZATT Kfs02	ZATT Kfs03	ZATT Kfs04	LH3TR Pl01	LH3TR Pl02	LH3TR Pl03	LH3TR Pl04	LH3TR Pl05	LH3TR Kfs01	LH3TR Kfs02
SiO_2	61.72	61.09	63.2	63.18	65.41	64.64	65.01	65.054	57.758	59.193	59.369	61.868	60.537	64.905	65.045
Al_2O_3	24.43	24.11	23.07	23.12	19.31	19.61	19.51	19.231	26.791	25.451	24.951	23.446	24.875	19.298	19.167
FeO	0.18	0.21	0.17	0.18	0.19	0.14	0.2	0.15	0.25	0.18	0.16	0.19	0.19	0.21	0.17
CaO	5.48	6.03	4.18	4.1	0.73	0.73	0.55	0.497	8.445	6.898	7.397	5.687	6.412	0.259	0.294
Na_2O	7.35	6.96	7.71	7.97	4.12	3.97	4.1	4.2	6.144	6.997	6.609	7.482	7.389	3.527	3.318
K_2O	1.73	1.68	2.11	2.01	10.15	10.5	10.48	10.116	0.642	0.858	1.067	1.47	0.946	11.406	11.461
Total	100.9	100.08	100.43	100.55	99.91	99.58	99.85	99.25	100.03	99.58	99.55	100.14	100.35	99.61	99.46
Cations based on 8 oxygens															
Si	2.731	2.733	2.805	2.796	2.972	2.945	2.953	2.973	2.594	2.657	2.674	2.759	2.693	2.964	2.98
Al	1.274	1.271	1.207	1.206	1.034	1.053	1.044	1.036	1.418	1.346	1.325	1.232	1.304	1.039	1.035
Fe	0.007	0.008	0.006	0.007	0.007	0.005	0.008	0.006	0.009	0.007	0.006	0.007	0.007	0.008	0.007
Ca	0.26	0.289	0.199	0.194	0.035	0.035	0.027	0.024	0.406	0.332	0.357	0.272	0.306	0.013	0.014
Na	0.631	0.604	0.664	0.684	0.363	0.351	0.361	0.372	0.535	0.609	0.577	0.647	0.637	0.312	0.295
K	0.098	0.096	0.119	0.114	0.588	0.61	0.607	0.59	0.037	0.049	0.061	0.084	0.054	0.664	0.67
Mole fraction end-members															
An	26.29	29.26	20.23	19.59	3.6	3.56	2.7	2.47	41.54	33.52	35.86	27.11	30.67	1.28	1.47
Ab	63.81	61.06	67.6	68.97	36.75	35.21	36.3	37.73	54.7	61.52	57.98	64.55	63.95	31.56	30.1
Or	9.9	9.69	12.17	11.45	59.65	61.24	60.99	59.8	3.76	4.96	6.16	8.34	5.39	67.16	68.42

Appendix B 2: Representative chemical compositions of feldspars from the La Herradura Rhyolite.

Unit	La Herradura Rhyolite																					
Sample	LH2VR Pl01	LH2VR Pl02	LH2VR Pl03	LH2VR Pl04	LH2VR Pl05	LH2VR Kfs01	LH2VR Kfs02	LH2VR Kfs03	LH2VR Kfs04	ZAVO Pl01	ZAVO Pl02	ZAVO Pl03	ZAVO Kfs01	ZAVO Kfs02	LHVT Pl01	LHVT Pl02	LHVT Pl03	LHVT Pl04	LHVT Kfs01	LHVT Kfs02	LHVT Kfs03	LHVT Kfs04
SiO_2	59.41	56.25	56.83	58.87	56.87	64.11	63.35	63.51	63.86	57.87	58.33	56.74	63.97	64.06	59.66	64.46	57.67	56.52	64.58	63.98	64	63.83
Al_2O_3	25.61	28.46	27.61	26.11	27.67	19.5	19.88	19.48	19.99	26.97	26.89	27.61	19.59	19.21	25.29	19.32	26.3	27.98	19.27	19.91	19.74	19.79
FeO	0.13	0	0.22	0.13	0.15	0.23	0.16	0.19	0.2	0.14	0.19	0.13	0.15	0.2	0.19	0.21	0.17	0.15	0.14	0.18	0.17	0.17
CaO	7.03	9.94	9.11	7.25	9.18	0.4	0.13	0.43	0.42	8.07	7.87	9.89	0.38	0.25	7.04	0.42	7.93	9.2	0.3	0.37	0.3	0.49
Na_2O	6.64	5.51	5.89	6.8	5.68	2.98	2.1	2.94	3.02	6.37	6.39	5.63	2.94	2.77	6.78	3.48	6.19	5.74	3.55	3.19	3.13	3.29
K_2O	1.11	0.59	0.7	0.99	0.68	12.08	13.5	11.72	12.09	0.82	0.96	0.61	12	11.99	1.01	10.89	0.92	0.65	11.11	11.82	11.89	11.47
Total	99.93	100.75	100.36	100.14	100.23	99.31	99.12	98.27	99.59	100.24	100.64	100.62	99.03	98.47	99.96	98.77	99.18	100.24	98.94	99.45	99.24	99.04
Cations based on 8 oxygens																						
Si	2.664	2.514	2.546	2.629	2.554	2.944	2.923	2.947	2.921	2.587	2.599	2.54	2.945	2.971	2.673	2.971	2.61	2.536	2.969	2.928	2.936	2.933
Al	1.353	1.499	1.458	1.374	1.465	1.055	1.081	1.065	1.078	1.421	1.412	1.457	1.063	1.05	1.335	1.049	1.403	1.479	1.044	1.074	1.068	1.071
Fe	0.005	0	0.008	0.005	0.006	0.009	0.006	0.007	0.008	0.005	0.007	0.005	0.006	0.008	0.007	0.008	0.006	0.006	0.005	0.007	0.007	0.007
Ca	0.338	0.476	0.437	0.347	0.442	0.02	0.006	0.022	0.021	0.386	0.376	0.474	0.018	0.012	0.338	0.021	0.384	0.442	0.015	0.018	0.015	0.024
Na	0.577	0.477	0.511	0.588	0.495	0.265	0.187	0.265	0.268	0.553	0.552	0.489	0.263	0.249	0.589	0.311	0.543	0.499	0.316	0.283	0.278	0.293
K	0.064	0.034	0.04	0.056	0.039	0.708	0.795	0.694	0.706	0.047	0.055	0.035	0.705	0.709	0.057	0.64	0.053	0.037	0.651	0.69	0.696	0.672
Mole fraction end-members																						
An	34.51	48.23	44.24	34.98	45.29	1.99	0.65	2.2	2.08	39.19	38.24	47.53	1.88	1.27	34.34	2.14	39.21	45.17	1.48	1.84	1.51	2.45
Ab	59	48.36	51.73	59.34	50.73	26.72	18.96	27.02	26.95	56.05	56.21	48.98	26.63	25.66	59.82	31.97	55.37	51.01	32.2	28.56	28.14	29.59
Or	6.49	3.41	4.04	5.68	3.97	71.29	80.39	70.79	70.97	4.77	5.55	3.49	71.49	73.07	5.84	65.88	5.42	3.81	66.32	69.6	70.35	67.96

Appendix B 3: Representative chemical compositions of feldspars from the Zaragoza Andesite.

Unit	Zaragoza Andesite							
Sample	LH3A Pl01	LH3A Pl02	LH3A Pl03	LH3A Pl04	LH3A Pl05	LH3A Pl06	LH3A Pl07	LH3A Pl08
SiO_2	57.37	55.99	55.54	55.72	57.62	57.25	57.75	56.52
Al_2O_3	25.6	27.59	27.82	27.74	26.43	26.46	26.62	27.15
FeO	0.26	0.24	0.28	0.21	0.23	0.23	0.19	0.2
CaO	9.49	9.36	9.88	9.83	7.89	8.83	8.48	9.19
Na_2O	5.42	5.15	4.86	5.07	6.07	5.54	6.07	5.61
K_2O	1.32	1.52	1.44	1.14	1.44	1.35	1.11	1.02
Total	99.45	99.86	99.81	99.71	99.68	99.66	100.23	99.69
Cations based on 8 oxygens								
Si	2.605	2.53	2.515	2.524	2.595	2.589	2.588	2.556
Al	1.37	1.469	1.485	1.481	1.403	1.411	1.406	1.448
Fe	0.01	0.009	0.011	0.008	0.009	0.009	0.007	
Ca	0.462	0.453	0.479	0.477	0.381	0.428	0.407	0.445
Na	0.477	0.451	0.427	0.445	0.53	0.486	0.527	0.492
K	0.076	0.088	0.083	0.066	0.083	0.078	0.064	0.059
Mole fraction end-members								
An	45.5	45.68	48.44	48.28	38.3	43.17	40.81	44.7
Ab	46.99	45.47	43.17	45.05	53.36	48.97	52.82	49.4
Or	7.51	8.85	8.39	6.68	8.34	7.86	6.37	5.9

Appendix C: Representative chemical compositions of pyroxenes from the La Herradura area

Appendix C 1: Representative chemical compositions of pyroxenes from El Sombrero Ignimbrite.

Unit	EL Sombrero Ignimbrite				
Sample	LH3TR Px01	LH3TR Px01	ZATT Px01	ZATT Px02	ZATT Px03
SiO_2	47.71	48.99	47.93	48.13	48.37
TiO2	0.16	0.24	0.35	0.33	0.3
Al_2O_3	0.34	0.67	0.67	0.69	0.67
FeO	39.94	27.97	28.09	27.5	27.48
MnO	0.96	0.68	0.75	0.75	0.69
MgO	6.32	5.58	4.27	4.23	4.35
CaO	3.75	15.48	16.84	16.83	17.09
Na_2O	0.09	0.14	0.2	0.17	0.19
Total	99.27	99.74	99.1	98.64	99.14
Cations based on 8 oxygens					
Si	1.987	1.978	1.958	1.975	1.972
Ti	0.005	0.007	0.011	0.01	0.009
Al	0.017	0.032	0.032	0.033	0.032
Fe	1.391	0.944	0.96	0.943	0.937
Mn	0.034	0.023	0.026	0.026	0.024
Mg	0.392	0.336	0.26	0.259	0.264
Ca	0.167	0.669	0.737	0.74	0.746
Na	0.007	0.011	0.016	0.014	0.015
Mole fraction end-members					
Wo	8.58	34.34	37.66	38.08	38.32
En	20.11	17.22	13.3	13.33	13.58
Fs	71.31	48.43	49.04	48.58	48.1
Mg#	0.22	0.26	0.22	0.22	0.22

Appendix C 2: Representative chemical compositions of pyroxenes from La Herradura Rhyolite.

Unit	La Herradura Rhyolite																				
Sample	LHVT Px01	LHVT Px02	LHVT Px03	LHVT Px04	LHVT Px05	LHVT Px06	LHVT Px07	LHVT Px08	ZAVO Px01	ZAVO Px02	ZAVO Px03	ZAVO Px04	ZAVO Px05	LH2VR Px01	LH2VR Px02	LH2VR Px03	LH2VR Px04	LH2VR Px05	LH2VR Px06	LH2VR Px07	LH2VR Px08
SiO_2	46.61	46.78	46.69	46.9	46.63	46.84	46.69	46.97	46.17	47.01	47.41	47.16	47.15	46.35	46.73	46.87	46.6	46.17	46.3	46.3	46.93
TiO2	0.19	0.22	0.25	0.2	0.15	0.22	0.28	0.28	0.33	0.19	0.18	0.18	0.27	0.25	0.28	0.28	0.23	0.31	0.23	0.26	0.21
Al_2O_3	1.83	1.46	1.95	2.15	1.61	1.47	1.99	1.93	2.46	1.48	1.48	1.6	1.65	2.17	2.12	1.45	2.06	2.01	1.99	2.1	1.61
FeO	40.9	40.68	40.1	40.46	40.97	40.9	39.97	40.43	41.95	41.57	41.82	40.79	40.15	41.12	40.86	41.23	41.33	42.56	42.54	41.64	41.38
MnO	0.71	0.61	0.64	0.47	0.46	0.52	0.61	0.56	0.57	0.44	0.43	0.53	0.56	0.48	0.53	0.53	0.53	0.64	0.58	0.6	0.61
MgO	8.26	8.87	8.66	8.76	8.56	8.66	8.74	8.48	8.05	8.34	8.72	8.43	8.78	8.28	8.1	8.28	7.86	7.8	7.43	8.67	8.14
CaO	0.37	0.38	0.36	0.32	0.44	0.29	0.41	0.46	0.36	0.25	0.2	0.23	0.41	0.24	0.4	0.49	0.31	0.33	0.32	0.36	0.3
Na_2O			0.02	0.02	0.04	0.02	0.05	0.01				0.07				0.04	0.01	0.04		0.04	
Total	98.87	99	98.65	99.26	98.86	98.92	98.73	99.13	99.9	99.28	100.25	98.98	98.98	98.88	99.02	99.18	98.94	99.85	99.39	99.97	99.18
Cations based on 8 oxygens																					
Si	1.934	1.932	1.934	1.929	1.931	1.939	1.93	1.939	1.899	1.944	1.938	1.951	1.947	1.922	1.936	1.939	1.936	1.905	1.923	1.896	1.944
Ti	0.006	0.007	0.008	0.006	0.005	0.007	0.009	0.009	0.01	0.006	0.006	0.006	0.009	0.008	0.009	0.009	0.007	0.01	0.007	0.008	0.007
Al	0.089	0.071	0.095	0.104	0.079	0.072	0.097	0.094	0.119	0.072	0.071	0.078	0.08	0.106	0.104	0.071	0.101	0.098	0.098	0.101	0.079
Fe	1.419	1.405	1.389	1.392	1.419	1.416	1.382	1.396	1.443	1.437	1.43	1.411	1.386	1.426	1.416	1.427	1.436	1.468	1.478	1.426	1.433
Mn	0.025	0.021	0.022	0.016	0.016	0.018	0.021	0.02	0.02	0.016	0.015	0.019	0.02	0.017	0.019	0.019	0.019	0.022	0.02	0.021	0.021
Mg	0.511	0.546	0.535	0.537	0.528	0.534	0.539	0.522	0.494	0.514	0.531	0.52	0.541	0.511	0.5	0.511	0.487	0.48	0.46	0.529	0.503
Ca	0.017	0.017	0.016	0.014	0.02	0.013	0.018	0.02	0.016	0.011	0.009	0.01	0.018	0.011	0.018	0.022	0.014	0.015	0.014	0.016	0.013
Na			0.001	0.002	0.003	0.001	0.004	0.001				0.005				0.003	0.001	0.003		0.003	0
Mole fraction end-members																					
Wo	0.8496	0.8499	0.82	0.72	0.99	0.65	0.94	1.05	0.81	0.56	0.45	0.52	0.93	0.56	0.91	1.11	0.72	0.75	0.73	0.8	0.68
En	26.244	27.754	27.57	27.64	26.87	27.21	27.78	26.92	25.29	26.2	26.97	26.78	27.79	26.25	25.88	26.07	25.14	24.44	23.58	26.85	25.8
Fs	72.907	71.4	71.62	71.64	72.14	72.14	71.28	72.03	73.9	73.24	72.59	72.71	71.28	73.19	73.21	72.82	74.14	74.81	75.7	72.35	73.53
Mg#	0.27	0.29	0.28	0.28	0.28	0.28	0.28	0.27	0.26	0.27	0.28	0.27	0.28	0.27	0.26	0.27	0.26	0.26	0.24	0.28	0.26

Appendix C 3: Representative chemical compositions of pyroxenes from Zaragoza Andesite.

Unit	Zaragoza Andesite													
Sample	LH3A Px01	LH3A Px02	LH3A Px03	LH3A Px04	LH3A Px05	LH3A Px06	LH3A Px07	LH3A Px08	LH3A Px09	LH3A Px10	LH3A Px11	LH3A Px12	LH3A Px13	LH3A Px14
SiO_2	52.22	52.51	52.43	51.66	50.88	53.18	52.42	51.16	52.36	52.47	51.71	51.62	51.15	51.22
TiO2	0.77	0.76	0.67	0.76	1.1	0.65	0.61	1.12	0.7	0.77	0.79	0.65	1.25	1.16
Al_2O_3	2.24	2.3	2.08	2.51	2.83	1.9	2.7	2.4	1.74	1.98	2.3	2.13	3.16	2.97
FeO	4.82	4.95	4.96	5.1	7.94	4.84	4.82	9.23	4.98	4.83	5.1	7.44	7.11	7.03
MnO	0.12	0.16	0.13	0.11	0.19	0.17	0.12	0.2	0.16	0.04	0.14	0.27	0.23	0.17
MgO	17.02	16.75	17.03	16.89	15.46	16.79	17.53	14.69	17.18	16.52	16.6	17	16	16.32
CaO	21.04	21.24	21.23	21.27	19.87	21.7	20.28	20.07	21.41	21.82	21.97	19.65	19.61	19.81
Na_2O	0.35	0.38	0.34	0.31	0.33	0.35	0.52	0.19	0.28	0.31	0.33	0.25	0.32	0.32
Total	98.58	99.04	98.86	98.6	98.59	99.57	98.99	99.05	98.81	98.75	98.95	98.99	98.83	98.99
Cations based on 8 oxygens														
Si	1.931	1.935	1.934	1.911	1.906	1.951	1.923	1.922	1.933	1.942	1.909	1.913	1.905	1.901
Ti	0.021	0.021	0.019	0.021	0.031	0.018	0.017	0.032	0.019	0.022	0.022	0.018	0.035	0.032
Al	0.098	0.1	0.09	0.11	0.125	0.082	0.117	0.106	0.076	0.086	0.1	0.093	0.139	0.13
Fe	0.149	0.152	0.153	0.158	0.249	0.148	0.148	0.29	0.154	0.149	0.157	0.231	0.221	0.218
Mn	0.004	0.005	0.004	0.003	0.006	0.005	0.004	0.006	0.005	0.001	0.004	0.009	0.007	0.005
Mg	0.939	0.92	0.937	0.932	0.863	0.918	0.958	0.823	0.946	0.912	0.914	0.939	0.888	0.903
Ca	0.834	0.839	0.839	0.843	0.797	0.853	0.797	0.808	0.847	0.865	0.869	0.78	0.782	0.788
Na	0.025	0.027	0.024	0.022	0.024	0.025	0.037	0.014	0.02	0.022	0.024	0.018	0.023	0.023
Mole fraction end-members														
Wo	43.4	43.88	43.51	43.63	41.76	44.44	41.88	42.06	43.51	44.92	44.8	40.02	41.36	41.27
En	48.85	48.14	48.56	48.21	45.22	47.83	50.35	42.84	48.58	47.32	47.09	48.16	46.94	47.31
Fs	7.75	7.98	7.93	8.16	13.02	7.74	7.77	15.09	7.91	7.76	8.11	11.82	11.7	11.43
Mg#	0.88	0.87	0.88	0.89	0.79	0.87	0.9	0.74	0.89	0.87	0.9	0.85	0.8	0.83

Appendix D: Representative chemical compositions of amphiboles from the La Herradura area

Appendix D 1: Representative chemical compositions of amphiboles from the Zaragoza Andesite.

Unit	Zaragoza Andesite											
Sample	LH3A Hbl01	LH3A Hbl02	LH3A Hbl03	LH3A Hbl04	LH3A Hbl05	LH3A Hbl06	LH3A Hbl07	LH3A Hbl08	LH3A Hbl09	LH3A Hbl10	LH3A Hbl11	LH3A Hbl12
SiO_2	36.21	34.28	36.26	35.63	36.66	38.03	36.09	36.81	37.49	36.39	36.43	38.24
TiO_2	7.72	8.04	7.84	7.92	5.54	5.7	8.57	7.66	7.74	7.81	7.51	5.24
Al2O3	15.52	15.04	15.62	15.37	15.06	15.23	15.66	15.32	15.55	15.42	15.45	15.61
FeO	9.89	14.51	11.03	13.51	11.77	7.98	10.46	9.5	9.57	9.28	11.78	6.29
MnO	0.05	0.04	0	0.07	0.04	0.04	0.02	0	0.02	0.05	0.07	0.01
MgO	16.54	16.25	15.84	15.58	18.67	19.02	16.03	17.7	17.74	17.12	16.79	20.58
CaO	0.02	0.09	0.08	0.05	0.09	0.03	0.03	0.05	0.04	0.1	0.04	0.05
Na_2O	0.44	0.34	0.23	0.2	0.11	0.13	0.45	0.55	0.48	0.38	0.21	0.27
K2O	8.85	8.55	8.68	9.16	9.64	9.45	8.59	8.74	8.8	8.78	9.35	9.48
Formula (Cations based on 23 oxygenes)												
Si	5.533	5.273	5.538	5.426	5.535	5.724	5.484	5.545	5.574	5.536	5.491	5.701
Al^{iv}	2.467	2.727	2.462	2.574	2.465	2.276	2.516	2.455	2.426	2.464	2.509	2.299
Al^{vi}	0.327	0	0.35	0.186	0.216	0.425	0.288	0.265	0.299	0.301	0.235	0.445
Ti	0.887	0.93	0.901	0.907	0.629	0.645	0.98	0.868	0.865	0.893	0.851	0.587
Fe^{2+}	1.264	1.867	1.408	1.721	1.486	1.005	1.33	1.196	1.19	1.181	1.484	0.784
Mg	3.768	3.727	3.607	3.537	4.203	4.268	3.631	3.974	3.932	3.882	3.771	4.574
Mn	0.006	0.005	0	0.009	0.005	0.006	0.002	0	0.002	0.007	0.008	0.002
Ca	0.003	0.015	0.013	0.008	0.014	0.005	0.005	0.007	0.007	0.015	0.007	0.008
Na	0.131	0.101	0.067	0.059	0.031	0.039	0.132	0.159	0.138	0.113	0.06	0.077
K	1.725	1.677	1.69	1.779	1.856	1.815	1.665	1.679	1.669	1.704	1.797	1.803
OH*	2	2	2	2	2	2	2	2	2	2	2	2
Mg#	0.75	0.67	0.72	0.67	0.74	0.81	0.73	0.77	0.77	0.77	0.72	0.85

Appendix E: Results of rhyolite-MELTS crystallization models from the La Herradura area

See e-Appendix.

Appendix E 1: Results of the crystallization models of the La Herradura Rhyolite with 2 wt.% H_2O.

Appendix E 2: Results of the crystallization models of the La Herradura Rhyolite with 3 wt.% H_2O.

Appendix E 3: Results of the crystallization models of the La Herradura Rhyolite with 5 wt.% H_2O

Appendix E 4: Results of the crystallization models of the La Herradura Rhyolite with 7 wt.% H_2O.

Appendix E 5: Results of the crystallization models of the Zaragoza Andesite with 0.25 wt.% H_2O.

Appendix E 6: Results of the crystallization models of the Zaragoza Andesite with 0.50 wt.% H_2O.

Appendix E 7: Results of the crystallization models of the Zaragoza Andesite with 0.75 wt.% H_2O.

Appendix E 8: Results of the crystallization models of the Zaragoza Andesite with 1.00 wt.% H_2O.

Appendix E 9: Results of the crystallization models of the El Sombrero Ignimbrite with 2 wt.% H_2O.

Appendix E 10: Results of the crystallization models of the El Sombrero Ignimbrite with 3 wt.% H_2O.

Appendix E 11: Results of the crystallization models of the El Sombrero Ignimbrite with 5 wt.% H_2O.

Appendix E 12: Results of the crystallization models of the El Sombrero Ignimbrite with 7 wt.% H_2O.

Appendix F: Results of the two feldspar thermometer calculations from the La Herradura rhyolitic volcanic rocks

Appendix F 1: Alkali feldspar – plagioclase EPMA results from the El Sombrero Ignimbrite, sample ZATT.

Analysis	1	2	3	4	5	6	7	8
	ZATT	ZATT	ZATT	ZATT	ZATT	ZATT	ZATT	ZATT
Sample	Line01	Line01	Line01	Line01	Line01	Line01	Line01	Line01
Name	PL01	PL02	PL03	PL04	Kfs01	Kfs02	Kfs03	Kfs04
SiO_2	61.72	61.09	63.20	63.18	65.41	64.64	65.01	65.05
Al_2O_3	24.43	24.11	23.07	23.12	19.31	19.61	19.51	19.23
FeO	0.18	0.21	0.17	0.18	0.19	0.14	0.20	0.15
CaO	5.48	6.03	4.18	4.10	0.73	0.73	0.55	0.50
Na_2O	7.35	6.96	7.71	7.97	4.12	3.97	4.10	4.20
K_2O	1.73	1.68	2.11	2.01	10.15	10.50	10.48	10.12
Sum	100.90	100.08	100.43	100.55	99.91	99.58	99.85	99.25
Cations based on 8 oxygens								
Si	2.7298	2.7263	2.7991	2.7958	2.9670	2.9484	2.9560	2.9690
Al	1.2732	1.2682	1.2045	1.2058	1.0325	1.0541	1.0457	1.0344
Fe	0.0067	0.0078	0.0063	0.0067	0.0072	0.0053	0.0076	0.0057
Ca	0.2598	0.2885	0.1981	0.1943	0.0354	0.0355	0.0269	0.0243
Na	0.6305	0.6022	0.6621	0.6840	0.3619	0.3514	0.3617	0.3717
K	0.0978	0.0955	0.1192	0.1135	0.5875	0.6112	0.6078	0.5890

Appendix F 2: Results of the formation temperature calculation for the sample ZATT with the two-feldspar thermometer after Putirka (2008).

Two-fledspar thermometer				Plagioclase			
			Analysis	1	2	3	4
P (kbar)	7		X_{An}	0.2629	0.2926	0.2023	0.1959
			X_{Ab}	0.6381	0.6106	0.6760	0.6897
	Analysis	X_{An}	X_{Ab}	T (°C) ± 2σ			
Alkali feldspar				897.61	915.27	861.44	856.92
	5	0.0360	0.3675	± 59.3	± 51.2	± 46.3	± 47.2
				890.68	908.07	855.05	850.60
	6	0.0356	0.3521	± 57.8	± 50.2	± 48.4	± 44.3
				897.64	915.31	861.47	856.94
	7	0.0270	0.3630	± 52.6	± 50.6	± 47.6	± 44.9
				902.19	920.04	865.66	861.09
	8	0.0247	0.3773	±55.7	± 53.2	± 46.1	±45.8

Appendix: F 3 Alkali feldspar – plagioclase EPMA results from the El Sombrero Ignimbrite, sample LH3TR.

Analysis	9	10	11	12	13	14	15
	LH3TR	LH3TR	LH3TR	LH3TR	LH3TR	LH3TR	LH3TR
Sample	Line02	Line02	Line02	Line02	Line02	Line02	Line02
Name	Pl01	Pl02	Pl03	Pl04	Pl05	Kfs01	Kfs02
SiO_2	57.76	59.19	59.37	61.87	60.54	64.91	65.05
Al_2O_3	26.79	25.45	24.95	23.45	24.88	19.30	19.17
FeO	0.25	0.18	0.16	0.19	0.19	0.21	0.17
CaO	8.45	6.90	7.40	5.69	6.41	0.26	0.29
Na_2O	6.14	7.00	6.61	7.48	7.39	3.53	3.32
K_2O	0.64	0.86	1.07	1.47	0.95	11.41	11.46
Sum	100.03	99.58	99.55	100.14	100.35	99.61	99.46
Cations based on 8 oxygens							
Si	2.589	2.657	2.668	2.755	2.693	2.966	2.974
Al	1.415	1.346	1.322	1.231	1.304	1.039	1.033
Fe	0.009	0.007	0.006	0.007	0.007	0.008	0.007
Ca	0.406	0.332	0.356	0.271	0.306	0.013	0.014
Na	0.534	0.609	0.576	0.646	0.637	0.312	0.294
K	0.037	0.049	0.061	0.084	0.054	0.665	0.669

Appendix F 4: Results of the formation temperature calculation for the sample LH3TR with the two-feldspar thermometer after Putirka (2008).

Two-feldspar thermometer				Plagioclase				
			Analysis	9	10	11	12	13
P (kbar)	7		X_{An}	0.4155	0.3352	0.3586	0.2711	0.3067
			X_{Ab}	0.5469	0.6152	0.5798	0.6454	0.6395
Alkali feldspar								
Analysis	X_{An}	X_{Ab}	T (°C) ± 2σ					
				907.48	869.22	880.38	836.56	854.75
14	0.0128	0.3156		± 53.1	± 46.4	± 47.4	± 44.3	± 43.6
				912.30	873.65	884.93	840.66	859.03
15	0.0147	0.3010		± 52.7	± 48.1	± 48.2	± 44.5	±45.0

Appendix F 5: Alkali feldspar – plagioclase EPMA results from the garnet-bearing La Herradura Rhyolite, sample LH2VR.

Analysis	1	2	3	4	5	6	7	8	9
	LH2VR	LH2VR	LH2VR	LH2VR	LH2VR	LH2VR	LH2VR	LH2VR	LH2VR
Sample	Line01	Line01	Line01	Line01	Line01	Line01	Line01	Line01	Line01
Name	Pl01	Pl02	Pl03	Pl04	Pl05	Kfs01	Kfs02	Kfs03	Kfs04
SiO_2	59.41	56.25	56.83	58.87	56.87	64.11	63.35	63.51	63.86
Al_2O_3	25.61	28.46	27.61	26.11	27.67	19.50	19.88	19.48	19.99
FeO	0.13	0.00	0.22	0.13	0.15	0.23	0.16	0.19	0.20
CaO	7.03	9.94	9.11	7.25	9.18	0.73	0.73	0.75	0.50
Na_2O	6.64	5.51	5.89	6.80	5.68	4.12	4.07	4.10	4.20
K_2O	1.11	0.59	0.70	0.99	0.68	10.15	10.50	10.48	10.12
Sum	99.93	100.75	100.36	100.14	100.23	98.84	98.69	98.51	98.86
Cations based on 8 oxygens									
Si	2.657	2.511	2.546	2.631	2.548	2.946	2.923	2.936	2.931
Al	1.350	1.498	1.458	1.375	1.461	1.056	1.081	1.061	1.082
Fe	0.005	0.000	0.008	0.005	0.006	0.009	0.006	0.007	0.008
Ca	0.337	0.476	0.437	0.347	0.441	0.036	0.036	0.037	0.024
Na	0.576	0.477	0.511	0.589	0.493	0.367	0.364	0.368	0.374
K	0.063	0.034	0.040	0.056	0.039	0.595	0.618	0.618	0.592

Appendix F 6: Results of the formation temperature calculation for the sample LH2VR with the two-feldspar thermometer after Putirka (2008).

	Two-feldspar thermometer			Plagioclase				
			Analysis	1	2	3	4	5
	P (kbar)	7	X_{An}	0.3451	0.4823	0.4424	0.3498	0.4529
			X_{Ab}	0.5900	0.4836	0.5173	0.5934	0.5073
	Analysis	X_{An} X_{Ab}	T (°C) ± 2σ					
Alkali feldspar				945.62	1018.23	998.63	948.48	1003.87
	6	0.0360 0.3675		± 49.3	± 53.9	± 48.1	± 48.3	± 52.1
				941.25	1013.16	993.76	944.08	998.94
	7	0.0352 0.3578		± 49.0	± 52.5	± 47.3	± 47.9	± 52.3
				940.93	1012.79	993.40	943.76	998.58
	8	0.0365 0.3595		± 48.5	± 52.1	± 47.2	± 47.9	± 51.7
				950.70	1024.12	1004.30	953.60	1009.60
	9	0.0247 0.3773		± 48.7	± 52.4	± 47.9	± 47.6	± 51.8

Appendix F 7: Alkali feldspar – plagioclase EPMA results from the garnet-bearing La Herradura Rhyolite, sample ZAVO.

Analysis	10	11	12	13	14
Sample Name	ZAVO Line02 Pl01	ZAVO Line02 Pl02	ZAVO Line02 Pl03	ZAVO Line02 Kfs01	ZAVO Line02 Kfs02
SiO_2	57.87	58.33	56.74	63.97	64.06
Al_2O_3	26.97	26.89	27.61	19.59	19.21
FeO	0.14	0.19	0.13	0.15	0.20
CaO	8.07	7.87	9.89	0.26	0.29
Na_2O	6.37	6.39	5.63	3.53	3.32
K_2O	0.82	0.96	0.61	11.41	11.46
Sum	100.24	100.64	100.62	98.90	98.53
Cations based on 8 oxygens					
Si	2.588	2.598	2.538	2.947	2.961
Al	1.422	1.412	1.456	1.063	1.046
Fe	0.005	0.007	0.005	0.006	0.008
Ca	0.386	0.376	0.474	0.013	0.015
Na	0.553	0.552	0.489	0.315	0.297
K	0.047	0.054	0.035	0.670	0.676

Appendix F 8: Results of the formation temperature calculation for the sample ZAVO with the two-feldspar thermometer after Putirka (2008).

Two-feldspar thermometer					Plagioclase		
				Analysis	10	11	12
	P (kbar)		7	X_{An}	0.3919	0.3824	0.4753
				X_{Ab}	0.5604	0.5621	0.4898
Alkali feldspar	Analysis	X_{An}	X_{Ab}	T (°C) ± 2σ			
					896.37	891.73	932.66
	13	0.0128	0.3156		± 45.6	± 43.8	± 44.6
					901.08	896.39	937.76
	14	0.0147	0.301		± 45.4	± 44.0	± 44.7

Appendix F 9: Alkali feldspar – plagioclase EPMA results from the garnet-bearing La Herradura Rhyolite, sample LHVT.

Analysis	15	16	17	18	19	20	21	22
	LHVT	LHVT	LHVT	LHVT	LHVT	LHVT	LHVT	LHVT
Sample	Line03	Line03	Line03	Line03	Line03	Line03	Line03	Line03
Name	Pl01	Pl02	Pl03	Pl04	Kfs01	Kfs02	Kfs03	Kfs04
SiO_2	59.66	64.46	57.67	56.52	64.58	63.98	64.00	63.83
Al_2O_3	25.29	19.32	26.30	27.98	19.27	19.91	19.74	19.79
FeO	0.19	0.21	0.17	0.15	0.14	0.18	0.17	0.17
CaO	7.04	0.42	7.93	9.20	0.30	0.37	0.30	0.49
Na_2O	6.78	3.48	6.19	5.74	3.55	3.19	3.13	3.29
K_2O	1.01	10.89	0.92	0.65	11.11	11.82	11.89	11.47
Sum	99.96	98.77	99.18	100.24	98.94	99.45	99.24	99.04
Cations based on 8 oxygens								
Si	2.667	2.963	2.606	2.534	2.966	2.936	2.943	2.938
Al	1.332	1.047	1.401	1.478	1.043	1.077	1.070	1.073
Fe	0.007	0.008	0.006	0.006	0.005	0.007	0.007	0.007
Ca	0.337	0.021	0.384	0.442	0.015	0.018	0.015	0.024
Na	0.588	0.310	0.542	0.499	0.316	0.284	0.279	0.293
K	0.057	0.639	0.053	0.037	0.651	0.692	0.698	0.674

Appendix F 10: Results of the formation temperature calculation for the sample LHVT with the two-feldspar thermometer after Putirka (2008).

Two-feldspar thermometer				Plagioclase			
			Analysis	15	16	17	18
	P (kbar)	7	X_{An}	0.3434	0.0214	0.3921	0.4517
			X_{Ab}	0.5982	0.3197	0.5537	0.5101
	Analysis	X_{An} X_{Ab}	T (°C) ± 2σ				
Alkali feldspar				889.13	825.43	913.06	940.83
	19	0.0148 0.3220		± 48.3	± 50.1	± 52.3	± 50.0
				885.21	822.05	908.92	936.43
	20	0.0184 0.2856		± 48.6	± 49.3	± 52.7	± 50.5
				868.32	807.47	891.13	917.56
	21	0.0151 0.2814		± 48.2	± 49.8	± 52.4	± 50.4
				905.00	839.09	929.79	958.61
	22	0.0245 0.2959		± 48.3	± 50.6	± 52.0	± 50.3

Appendix G: Results of the garnet ilmenite cation exchange thermometer calculations from the garnet-bearing La Herradura Rhyolite.

Appendix G 1: EPMA results of the garnet-ilmenite transects of the sample LH5R, garnet-ilmenite Line01. Increasing No. refers to the measured direction (Ilmenite to Garnet).

No.	1	2	3	4	5	6	7	8		9	10	11	12	13
Com.	LH5R Grt-Ilm Line01 Ilm01	LH5R Grt-Ilm Line01 Ilm02	LH5R Grt-Ilm Line01 Ilm03	LH5R Grt-Ilm Line01 Ilm04	LH5R Grt-Ilm Line01 Ilm05	LH5R Grt-Ilm Line01 Ilm06	LH5R Grt-Ilm Line01 Ilm07	LH5R Grt-Ilm Line01 Ilm08		LH5R Grt-Ilm Line01 Grt01	LH5R Grt-Ilm Line01 Grt02	LH5R Grt-Ilm Line01 Grt03	LH5R Grt-Ilm Line01 Grt04	LH5R Grt-Ilm Line01 Grt05
SiO_2	0.00	0.03	0.04	0.00	0.04	0.00	0.02	0.37		35.78	36.01	36.28	35.97	36.38
TiO_2	51.98	52.26	52.11	52.06	51.96	51.63	51.61	50.60		0.57	0.38	0.23	0.21	0.17
Al_2O_3	0.19	0.20	0.15	0.20	0.16	0.18	0.18	0.28		20.72	20.66	20.98	20.87	20.78
FeO	47.86	48.52	48.02	47.29	47.03	47.47	47.64	47.97		36.46	36.75	36.11	37.27	36.16
MnO	0.44	0.37	0.40	0.46	0.43	0.44	0.42	0.45		1.46	1.36	1.48	1.47	1.41
MgO	0.69	0.70	0.71	0.69	0.63	0.66	0.67	0.70		3.10	2.96	3.14	3.13	3.08
CaO	0.01	0.08	0.02	0.03	0.00	0.01	0.00	0.00		1.54	1.55	1.62	1.53	1.60
Cr_2O_3	0.06	0.04	0.05	0.03	0.01	0.04	0.06	0.04		0.00	0.01	0.03	0.02	0.03
Total	101.23	102.19	101.49	100.74	100.22	100.42	100.55	100.37		99.62	99.68	99.87	100.45	99.61
Composition														
Ilm	1	2	3	4	5	6	7	8	Grt	1	2	3	4	5
Si	0	0.001	0.001	0	0.001	0	0.000	0.009	Si	2.90	2.92	2.93	2.89	2.95
Al	0.005	0.006	0.005	0.006	0.005	0.005	0.005	0.008	Ti	0.03	0.02	0.01	0.01	0.01
Ti	0.977	0.974	0.977	0.981	0.984	0.978	0.976	0.960	Al	1.98	1.98	2.00	1.98	1.98
Fe	1.001	1.005	1.001	0.991	0.990	1.000	1.002	1.012	Cr	0.00	0.00	0.00	0.00	0.00
Mn	0.009	0.008	0.008	0.010	0.009	0.009	0.009	0.010	Fe^{3+}	0.15	0.14	0.11	0.21	0.10
Mg	0.026	0.026	0.026	0.026	0.024	0.025	0.025	0.026	Fe^{2+}	2.33	2.36	2.32	2.30	2.35
Ca	0.000	0.002	0.000	0.001	0.000	0.000	0.000	0.000	Mn	0.10	0.09	0.10	0.10	0.10
Cr	0.001	0.001	0.001	0.001	0.000	0.001	0.001	0.001	Mg	0.37	0.36	0.38	0.38	0.37
Fe^{3+}	0.058	0.066	0.058	0.046	0.038	0.056	0.059	0.078	Ca	0.13	0.13	0.14	0.13	0.14
Fe^{2+}	0.942	0.940	0.943	0.946	0.952	0.944	0.943	0.934						
									X_{Mn}^{Grt}	0.03425	0.03176	0.03444	0.03440	0.03260
									X_{Fe}^{Grt}	0.79256	0.80076	0.78966	0.79118	0.79470
X_{Mn}^{Ilm}	0.00955	0.00798	0.00855	0.00999	0.00920	0.00962	0.00924	0.00989	X_{Mg}^{Grt}	0.12758	0.12165	0.12831	0.12913	0.12572

Appendix G 2: Results of temperature calculations with the garnet-ilmenite cation exchange thermometer for the sample LH5R, Line01. Temperature calculation were carried out for the 3 closet points to the contact of ilmenite and garnet. For position of the measurement points see Appendix G 1.

Sample	Mineral pair	KD ± 2σ	T(K) ± 2σ	T(°C) ± 2σ
LH5R Grt-Ilm Line01	Ilm06-Grt01	4.34 ± 0.42	1033.04 ± 52.44	759.89 ± 52.44
LH5R Grt-Ilm Line01	Ilm06-Grt02	3.90 ± 0.35	1075.62 ± 51.94	802.47 ± 51.94
LH5R Grt-Ilm Line01	Ilm06-Grt03	4.38 ± 0.37	1028.85 ± 45.48	755.70 ± 45.48
LH5R Grt-Ilm Line01	Ilm07-Grt01	4.51 ± 0.33	1013.90 ± 37.49	740.75 ± 37.49
LH5R Grt-Ilm Line01	Ilm07-Grt02	4.14 ± 0.40	1054.80 ± 55.34	781.65 ± 55.34
LH5R Grt-Ilm Line01	Ilm07-Grt03	4.55 ± 0.38	1009.87 ± 42.89	736.72 ± 42.89*
LH5R Grt-Ilm Line01	Ilm08-Grt01	4.21 ± 0.34	1047.97 ± 44.67	774.82 ± 44.67
LH5R Grt-Ilm Line01	Ilm08-Grt02	3.86 ± 0.37	1091.90 ± 58.85	818.75 ± 58.85
LH5R Grt-Ilm Line01	Ilm08-Grt03	4.25 ± 0.41	1043.65 ± 53.82	770.50 ± 53.82

Appendix G 3: EPMA results of the garnet-ilmenite transects of the sample LH5R, garnet-ilmenite line02. Increasing No. refers to the measured direction (Ilmenite to Garnet).

No.	1	2	3	4	5	6	7	8	9	10	11	12	13	14	15	16
Com.	LH5R Grt-Ilm Line02 Ilm01	LH5R Grt-Ilm Line02 Ilm012	LH5R Grt-Ilm Line02 Ilm03	LH5R Grt-Ilm Line02 Ilm04	LH5R Grt-Ilm Line02 Ilm05	LH5R Grt-Ilm Line02 Ilm06	LH5R Grt-Ilm Line02 Ilm07	LH5R Grt-Ilm Line02 Ilm08	LH5R Grt-Ilm Line02 Ilm09	LH5R Grt-Ilm Line02 Ilm10	LH5R Grt-Ilm Line02 Ilm11	LH5R Grt-Ilm Line02 Ilm12	LH5R Grt-Ilm Line02 Ilm13	LH5R Grt-Ilm Line02 Ilm14	LH5R Grt-Ilm Line02 Ilm15	LH5R Grt-Ilm Line02 Ilm16
SiO_2	0	0.06	0.03	0	0.00	0	0.01	0.01	0.01	0	0	0.02	0.02	0.06	0.00	0.02
TiO_2	51.93	51.77	51.66	51.36	51.27	51.41	51.68	51.63	51.31	51.45	51.22	51.34	50.73	51.21	50.85	50.38
Al_2O_3	0.11	0.12	0.15	0.11	0.12	0.12	0.12	0.14	0.13	0.16	0.15	0.16	0.13	0.12	0.15	0.13
FeO	47.08	45.24	46.95	45.83	47.62	46.51	47.03	46.79	45.61	46.44	46.07	44.68	46.46	45.34	45.92	46.48
MnO	0.31	0.47	0.35	0.33	0.38	0.32	0.36	0.36	0.36	0.36	0.33	0.34	0.33	0.40	0.27	0.47
MgO	0.64	0.69	0.62	0.66	0.63	0.61	0.63	0.60	0.62	0.58	0.63	0.61	0.63	0.66	0.57	0.60
CaO	0	0	0	0	0	0	0	0	0	0	0	0	0	0	0	0.02
Cr_2O_3	0.05	0	0.04	0	0.02	0	0.04	0.03	0	0.07	0.03	0	0.02	0	0	0.05
Total	100.1	98.3	99.7	98.2	100.0	98.9	99.8	99.5	98.0	99.0	98.4	97.1	98.3	97.8	97.7	98.1
Composition																
Ilm	1	2	3	4	5	6	7	8	9	10	11	12	13	14	15	16
Si	0	0.001	0.001	0	0	0	0.000	0.000	0.000	0	0	0.000	0.000	0.001	0.000	0.000
Al	0.003	0.004	0.004	0.003	0.003	0.004	0.004	0.004	0.004	0.005	0.004	0.005	0.004	0.004	0.005	0.004
Ti	0.985	0.994	0.983	0.990	0.977	0.986	0.983	0.985	0.991	0.986	0.987	0.998	0.981	0.991	0.987	0.978
Fe	0.993	0.966	0.993	0.983	1.009	0.992	0.995	0.992	0.980	0.989	0.987	0.965	0.999	0.976	0.991	1.003
Mn	0.007	0.010	0.008	0.007	0.008	0.007	0.008	0.008	0.008	0.008	0.007	0.007	0.007	0.009	0.006	0.010
Mg	0.024	0.026	0.023	0.025	0.024	0.023	0.024	0.023	0.024	0.022	0.024	0.024	0.024	0.025	0.022	0.023
Ca	0	0	0	0	0	0	0	0	0.000	0.000	0.000	0.000	0.000	0.000	0.000	0.000
Cr	0.001	0	0.001	0	0.000	0	0.001	0.001	0	0	0	0	0	0	0	0.001
Fe^{3+}	0.038	0.007	0.040	0.025	0.064	0.036	0.043	0.038	0	0.033	0.031	0	0.049	0.017	0	0.058
Fe^{2+}	0.955	0.960	0.953	0.958	0.945	0.957	0.952	0.955	0.960	0.956	0.956	0.965	0.950	0.958	0.959	0.945
X_{Mn}^{Ilm}	0.0067	0.0101	0.0076	0.0072	0.0084	0.0069	0.0079	0.0078	0.0079	0.0078	0.0071	0.0074	0.0073	0.0088	0.0060	0.0104

Appendix G 3: (continued):

No.	17	18	19	20	21	22
Com.	LH5R Grt-Ilm Line02 Grt01	LH5R Grt-Ilm Line02 Grt02	LH5R Grt-Ilm Line02 Grt03	LH5R Grt-Ilm Line02 Grt04	LH5R Grt-Ilm Line02 Grt05	LH5R Grt-Ilm Line02 Grt06
SiO_2	33.172	35.222	34.929	34.535	34.679	34.605
TiO_2	3.085	0.341	0.202	0.191	0.131	0.091
Al_2O_3	19.037	20.558	20.577	20.618	20.592	20.663
FeO	35.116	34.795	35.816	36.326	35.896	35.055
MnO	1.326	1.307	1.135	1.314	1.254	1.161
MgO	2.828	2.931	3.086	3.078	3.056	3.087
CaO	1.302	1.451	1.492	1.45	1.437	1.428
Cr_2O_3	0.026	0	0.028	0.038	0.034	0.031
Total	95.892	96.59	97.265	97.55	97.079	96.121
Composition						
Grt	1	2	3	4	5	6
Si	2.822	2.940	2.897	2.859	2.882	2.899
Ti	0.197	0.021	0.013	0.012	0.008	0.006
Al	1.908	2.023	2.011	2.012	2.017	2.040
Cr	0.002	0	0.002	0.002	0.002	0.002
Fe^{3+}	0.052	0.054	0.169	0.245	0.199	0.147
Fe^{2+}	2.446	2.375	2.315	2.270	2.296	2.309
Mn	0.096	0.092	0.080	0.092	0.088	0.082
Mg	0.359	0.365	0.382	0.380	0.379	0.386
Ca	0.119	0.130	0.133	0.129	0.128	0.128
X_{Mn}^{Grt}	0.0316	0.0312	0.0274	0.0321	0.0305	0.0284
X_{Fe}^{Grt}	0.8103	0.8018	0.7959	0.7908	0.7942	0.7948
X_{Mg}^{Grt}	0.1188	0.1232	0.1311	0.1323	0.1310	0.1327

Appendix G 4: Results of temperature calculations with the garnet-ilmenite cation exchange thermometer for the sample LH5R, Line02. Temperature calculation were carried out for the 3 closet points to the contact of ilmenite and garnet. For position of the measurement points see Appendix G 3.

Sample	Mineral pair	KD ± 2σ	T(K) ± 2σ	T(°C) ± 2σ
LH5R Grt-Ilm Line02	Ilm14-Grt01	4.29 ± 0.37	1035.43 ± 39.73	762.28 ± 39.73
LH5R Grt-Ilm Line02	Ilm14-Grt02	4.28 ± 0.40	1038.52 ± 51.64	765.37 ± 51.64
LH5R Grt-Ilm Line02	Ilm14-Grt03	3.78 ± 0.34	1105.55 ± 55.85	832.40 ± 55.85
LH5R Grt-Ilm Line02	Ilm15-Grt01	6.32 ±0.81	872.68 ± 51.52	599.53 ± 51.52
LH5R Grt-Ilm Line02	Ilm15-Grt02	6.30 ± 0.74	875.31 ± 46.84	602.16 ± 46.84
LH5R Grt-Ilm Line02	Ilm15-Grt03	5.57 ± 0.56	923.27 ± 43.66	650.12 ± 43.66
LH5R Grt-Ilm Line02	Ilm16-Grt01	3.62 ± 0.28	1127.44 ± 49.76	854.29 ± 49.76
LH5R Grt-Ilm Line02	Ilm16-Grt02	3.61 ± 0.34	1130.78 ± 61.98	857.63 ± 61.98
LH5R Grt-Ilm Line02	Ilm16-Grt03	3.19 ± 0.29	1210.10 ± 68.03	936.95 ± 68.03

Appendix G 5: EPMA results of the garnet-ilmenite transects of the sample LH5R, garnet-ilmenite line03. Increasing No. refers to the measured direction (Garnet to Ilmenite).

No.	1	2	3	4	5	6	7	8	9	10	11
Com.	LH5R Grt-Ilm Line03 Ilm01	LH5R Grt-Ilm Line03 Ilm02	LH5R Grt-Ilm Line03 Ilm03	LH5R Grt-Ilm Line03 Ilm04	LH5R Grt-Ilm Line03 Ilm05	LH5R Grt-Ilm Line03 Ilm06	LH5R Grt-Ilm Line03 Ilm07	LH5R Grt-Ilm Line03 Ilm08	LH5R Grt-Ilm Line03 Ilm09	LH5R Grt-Ilm Line03 Ilm10	LH5R Grt-Ilm Line03 Ilm11
SiO_2	0.03	0.03	0	0.05	0	0	0	0	0	0.04	0.06
TiO_2	51.93	52.16	51.88	52.20	51.99	52.27	52.1	52.04	51.76	51.73	51.46
Al_2O_3	0.21	0.14	0.23	0.13	0.18	0.16	0.2	0.18	0.20	0.16	0.17
FeO	47.41	48.07	47.61	47.39	47.31	46.46	48.0	46.98	47.22	47.30	47.10
MnO	0.36	0.42	0.32	0.38	0.38	0.40	0.4	0.49	0.43	0.33	0.43
MgO	0.65	0.66	0.73	0.64	0.73	0.72	0.8	0.70	0.66	0.67	0.66
CaO	0	0	0	0	0	0	0	0	0	0	0
Cr_2O_3	0	0	0.03	0.03	0.05	0	0.04	0	0.03	0.04	0
Total	100.52	101.45	100.75	100.77	100.59	99.95	101.37	100.31	100.26	100.25	99.86
Composition											
Ilm	1	2	3	4	5	6	7	8	9	10	11
Si	0.001	0.001	0	0.001	0	0	0	0	0	0.001	0.002
Al	0.006	0.004	0.007	0.004	0.005	0.005	0.004	0.005	0.006	0.005	0.005
Ti	0.981	0.978	0.978	0.983	0.981	0.989	0.977	0.984	0.981	0.980	0.979
Fe	0.996	1.002	0.998	0.993	0.993	0.978	1.001	0.988	0.995	0.997	0.997
Mn	0.008	0.009	0.007	0.008	0.008	0.008	0.009	0.010	0.009	0.007	0.009
Mg	0.024	0.025	0.027	0.024	0.027	0.027	0.028	0.026	0.025	0.025	0.025
Ca	0	0	0	0	0	0	0	0	0	0	0
Cr	0	0	0.001	0.001	0.001	0	0.001	0	0.001	0.001	0
Fe^{3+}	0.046	0.057	0.054	0.040	0.047	0.023	0.061	0.040	0.048	0.048	0.050
Fe^{2+}	0.950	0.946	0.945	0.953	0.946	0.955	0.941	0.947	0.947	0.949	0.947
X_{Mn}^{Ilm}	0.0078	0.0091	0.0069	0.0082	0.0082	0.0085	0.0087	0.0105	0.0093	0.0072	0.0095

Appendix G 5: (continued)

No.	12	13	14	15	16	17	18	19
Com.	LH5R Grt-Ilm Line03 Grt01	LH5R Grt-Ilm Line03 Grt02	LH5R Grt-Ilm Line03 Grt03	LH5R Grt-Ilm Line03 Grt04	LH5R Grt-Ilm Line03 Grt05	LH5R Grt-Ilm Line03 Grt06	LH5R Grt-Ilm Line03 Grt07	LH5R Grt-Ilm Line03 Grt08
SiO_2	36.30	35.96	35.75	36.50	36.13	36.29	36.00	35.94
TiO_2	0.73	0.40	0.29	0.19	0.17	0.12	0.13	0.10
Al_2O_3	21.13	21.07	20.94	20.75	20.72	20.77	20.76	20.81
FeO	36.21	36.04	36.93	36.80	37.31	36.93	36.01	35.86
MnO	1.43	1.30	1.53	1.22	1.31	1.30	1.52	1.29
MgO	3.02	3.08	3.23	3.18	3.22	3.16	3.02	2.98
CaO	1.54	1.52	1.45	1.49	1.49	1.37	1.37	1.46
Cr_2O_3	0	0.03	0.02	0	0.007	0.01	0	0.02
Total	100.35	99.39	100.15	100.12	100.36	99.95	98.79	98.46
Composition								
Grt	1	2	3	4	5	6	7	8
Si	2.9216	2.9183	2.8824	2.9430	2.9083	2.9313	2.9411	2.9443
Ti	0.0439	0.0246	0.0173	0.0113	0.0100	0.0073	0.0077	0.0062
Al	2.0048	2.0155	1.9897	1.9713	1.9659	1.9774	1.9984	2.0091
Cr	0	0.0016	0.0014	0	0.0004	0.0006	0	0.0012
Fe^{3+}	0.0641	0.0972	0.2093	0.1202	0.1970	0.1448	0.1041	0.0888
Fe^{2+}	2.3731	2.3493	2.2810	2.3611	2.3144	2.3498	2.3560	2.3681
Mn	0.0975	0.0895	0.1046	0.0831	0.0890	0.0890	0.1051	0.0894
Mg	0.3625	0.3722	0.3887	0.3816	0.3868	0.3809	0.3678	0.3644
Ca	0.1325	0.1319	0.1255	0.1284	0.1281	0.1188	0.1198	0.1285
X_{Mn}^{Grt}	0.0329	0.0304	0.0361	0.0281	0.0305	0.0303	0.0356	0.0303
X_{Fe}^{Grt}	0.8002	0.7983	0.7866	0.7992	0.7930	0.7996	0.7990	0.8026
X_{Mg}^{Grt}	0.1222	0.1265	0.1341	0.1292	0.1326	0.1296	0.1247	0.1235

Appendix G 6: Results of temperature calculations with the garnet-ilmenite cation exchange thermometer for the sample LH5R, Line03. Temperature calculation were carried out for the 3 closet points to the contact of ilmenite and garnet. For position of the measurement points see Appendix G 5.

Sample	Mineral pair	KD ± 2σ	T(K) ± 2σ	T(°C) ± 2σ
LH5R Grt-Ilm Line03	Ilm09-Grt01	4.25 ± 0.38	1041.66 ± 49.5	768.51 ± 49.5
LH5R Grt-Ilm Line03	Ilm09-Grt02	3.94 ± 0.35	1082.06 ± 52.95	808.91 ± 52.95
LH5R Grt-Ilm Line03	Ilm09-Grt03	4.74 ± 0.46	992.60 ± 48.63	719.45 ± 48.63
LH5R Grt-Ilm Line03	Ilm10-Grt01	5.49 ± 0.55	927.20 ± 29.59	654.05 ± 29.59
LH5R Grt-Ilm Line03	Ilm10-Grt02	5.09 ± 0.46	959.37 ± 34.30	686.22 ± 34.30
LH5R Grt-Ilm Line03	Ilm10-Grt03	6.12 ± 0.62	888.93 ± 33.96	615.78 ± 33.96
LH5R Grt-Ilm Line03	Ilm11-Grt01	4.19 ± 0.36	1048.50 ± 42.55	775.35 ± 42.55
LH5R Grt-Ilm Line03	Ilm11-Grt02	3.89 ± 0.35	1089.42 ± 56.69	816.27 ± 56.69
LH5R Grt-Ilm Line03	Ilm11-Grt03	4.68 ± 0.42	998.76 ± 40.54	725.61 ± 40.54

Appendix G 7: EPMA results of the garnet-ilmenite transects of the sample ZA4R, garnet-ilmenite line01. Increasing No. refers to the measured direction (Garnet to Ilmenite to Garnet).

No.	1	2	3		4	5		6	7
Com.	ZA4R Grt-Ilm Line01 Grt01	ZA4R Grt-Ilm Line01 Grt02	ZA4R Grt-Ilm Line01 Grt03		ZA4R Grt-Ilm Line01 Ilm01	ZA4R Grt-Ilm Line01 Ilm02		ZA4R Grt-Ilm Line01 Grt04	ZA4R Grt-Ilm Line01 Grt05
SiO_2	36.12	35.84	36.15		0.03	0.01		36.26	36.29
TiO_2	0.10	0.24	0.47		52.15	52.07		0.76	0.24
Al_2O_3	21.18	20.56	20.82		0.05	0.10		21.07	20.74
FeO	35.80	36.78	37.05		47.73	47.17		36.52	36.63
MnO	1.27	1.33	1.12		0.37	0.33		1.27	1.30
MgO	3.28	3.37	3.12		0.74	0.72		3.18	3.24
CaO	1.33	1.42	1.46		0.00	0		1.57	1.44
Cr_2O_3	0	0.02	0.01		0.02	0		0.04	0
Total	99.08	99.55	100.21		101.09	100.36		100.66	99.88
Composition									
Grt	1	2	3	Ilm	1	2	Grt	4	5
Si	2.9337	2.9072	2.9153	Si	0.0007	0.0004	Si	2.9083	2.9314
Ti	0.0063	0.0145	0.0287	Al	0.0015	0.0030	Ti	0.0457	0.0143
Al	2.0280	1.9651	1.9789	Ti	0.9810	0.9845	Al	1.9916	1.9750
Cr	0	0.0015	0.0007	Fe	0.9984	0.9918	Cr	0.0027	0
Fe^{3+}	0.0920	0.1901	0.1325	Mn	0.0078	0.0071	Fe^{3+}	0.0977	0.1336
Fe^{2+}	2.3399	2.3044	2.3661	Mg	0.0274	0.0271	Fe^{2+}	2.3521	2.3413
Mn	0.0870	0.0869	0.0766	Ca	0.0001	0	Mn	0.0862	0.0891
Mg	0.3973	0.4069	0.3747	Cr	0.0005	0	Mg	0.3806	0.3907
Ca	0.1158	0.1235	0.1265	Fe^{3+}	0.0516	0.0409	Ca	0.1351	0.1246
				Fe^{2+}	0.9469	0.9509			
X_{Mn}^{Grt}	0.0296	0.0297	0.0260				X_{Mn}^{Grt}	0.0292	0.0302
X_{Fe}^{Grt}	0.7959	0.7887	0.8037				X_{Fe}^{Grt}	0.7962	0.7948
X_{Mg}^{Grt}	0.1351	0.1393	0.1273	X_{Mn}^{Ilm}	0.0079	0.0072	X_{Mg}^{Grt}	0.1289	0.1326

Appendix G 8: Results of temperature calculations with the garnet-ilmenite cation exchange thermometer for the sample ZA4R, Line01. Temperature calculation were carried out for the 2 closet points to the contact in ilmenite and for the 3 closet points in the garnet. For position of the measurement points see Appendix G 7.

Sample	Mineral pair	KD ± 2σ	T(K) ± 2σ	T(°C) ± 2σ
ZA4R Grt-Ilm Line01	Ilm01-Grt01	4.54 ± 0.43	1012.48 ± 49.26	739.33 ± 49.26
ZA4R Grt-Ilm Line01	Ilm01-Grt02	4.61 ± 0.41	1007.22 ± 45.41	734.07 ± 45.41
ZA4R Grt-Ilm Line01	Ilm01-Grt03	3.96 ± 0.34	1080.15 ± 45.41	807.00 ± 45.41
ZA4R Grt-Ilm Line01	Ilm01-Grt04	4.47 ± 0.43	1018.24 ± 50.92	745.09 ± 50.92
ZA4R Grt-Ilm Line01	Ilm01-Grt05	4.65 ± 0.46	1001.27 ± 50.68	728.12 ± 50.68
ZA4R Grt-Ilm Line01	Ilm02-Grt01	4.99 ± 0.47	970.19 ± 44.91	697.04 ± 44.91
ZA4R Grt-Ilm Line01	Ilm02-Grt02	5.06 ± 0.48	965.48 ± 44.68	692.33 ± 44.68
ZA4R Grt-Ilm Line01	Ilm02-Grt03	4.34 ± 0.39	1031.90 ± 48.6	758.75 ± 48.6
ZA4R Grt-Ilm Line01	Ilm02-Grt04	4.91 ± 0.44	975.30 ± 43.14	702.15 ± 43.14
ZA4R Grt-Ilm Line01	Ilm02-Grt05	5.10 ± 0.48	959.84 ± 43.92	686.69 ± 43.92

Appendix G 9: EPMA results of the garnet-ilmenite transects of the sample ZA4R, garnet-ilmenite line02. Increasing No. refers to the measured direction (Ilmenite to Garnet).

No.	1	2	3	4		5	6	7	8	9
Com.	ZA4R Grt-Ilm Line02 Ilm01	ZA4R Grt-Ilm Line02 Ilm02	ZA4R Grt-Ilm Line02 Ilm03	ZA4R Grt-Ilm Line02 Ilm04		ZA4R Grt-Ilm Line02 Grt01	ZA4R Grt-Ilm Line02 Grt02	ZA4R Grt-Ilm Line02 Grt03	ZA4R Grt-Ilm Line02 Grt04	ZA4R Grt-Ilm Line02 Grt05
SiO_2	0.05	0.03	0.05	0.04	SiO_2	36.39	36.35	35.99	36.68	36.26
TiO_2	51.78	51.31	51.55	50.61	TiO_2	0.37	0.23	0.14	0.09	0.05
Al_2O_3	0.07	0.09	0.08	0.08	Al_2O_3	20.83	21.20	20.92	20.97	20.87
FeO	47.84	47.99	47.51	47.33	FeO	37.28	36.97	36.24	36.30	37.24
MnO	0.41	0.35	0.44	0.47	MnO	1.28	1.19	1.34	1.22	1.34
MgO	0.66	0.71	0.75	0.72	MgO	3.19	3.30	3.14	3.20	3.24
CaO	0	0	0	0	CaO	1.52	1.46	1.50	1.49	1.56
Cr_2O_3	0.01	0.04	0.01	0	Cr_2O_3	0.02	0.03	0.03	0.05	0
Total	100.79	100.45	100.36	99.24		100.88	100.73	99.27	99.99	100.6
Composition										
Ilm	1	2	3	4	Grt	1	2	3	4	5
Si	0.0012	0.0007	0.0013	0.0010	Si	2.9147	2.9096	2.9233	2.9564	2.9105
Al	0.0022	0.0026	0.0023	0.0025	Ti	0.0222	0.0135	0.0086	0.0052	0.0030
Ti	0.9779	0.9735	0.9774	0.9727	Al	1.9659	2.0001	2.0025	1.9923	1.9737
Fe	1.0047	1.0125	1.0016	1.0114	Cr	0.0013	0.0018	0.0017	0.0029	0
Mn	0.0088	0.0075	0.0093	0.0101	Fe^{3+}	0.1590	0.1517	0.1319	0.0816	0.1994
Mg	0.0248	0.0268	0.0281	0.0272	Fe^{2+}	2.3382	2.3232	2.3298	2.3653	2.3005
Ca	0	0	0	0	Mn	0.0869	0.0807	0.0919	0.0831	0.0911
Cr	0.0002	0.0008	0.0001	0	Mg	0.3814	0.3943	0.3801	0.3844	0.3874
Fe^{3+}	0.0587	0.0718	0.0598	0.0741	Ca	0.1304	0.1250	0.1301	0.1288	0.1345
Fe^{2+}	0.9460	0.9407	0.9418	0.9374						
					X_{Mn}^{Grt}	0.0296	0.0276	0.0314	0.0281	0.0313
					X_{Fe}^{Grt}	0.7962	0.7948	0.7946	0.7987	0.7896
X_{Mn}^{Ilm}	0.0089	0.0077	0.0095	0.0103	X_{Mg}^{Grt}	0.1299	0.1349	0.1297	0.1298	0.1330

Appendix G 10: Results of temperature calculations with the garnet-ilmenite cation exchange thermometer for the sample ZA4R, Line02. Temperature calculation were carried out for the 3 closet points to the contact of ilmenite and garnet. For position of the measurement points see Appendix G 9.

Sample	Mineral pair	KD ± 2σ	T(K) ± 2σ	T(°C) ± 2σ
ZA4R Grt-Ilm Line02	Ilm02-Grt01	4.67 ± 0.42	997.77 ± 45.3	724.62 ± 45.3
ZA4R Grt-Ilm Line02	Ilm02-Grt02	4.37 ± 0.43	1030.79 ± 53.32	757.64 ± 53.32
ZA4R Grt-Ilm Line02	Ilm02-Grt03	4.96 ± 0.51	971.03 ± 50.86	697.88 ± 50.86
ZA4R Grt-Ilm Line02	Ilm03-Grt01	3.75 ± 0.35	1110.27 ± 58.8	837.12 ± 58.8
ZA4R Grt-Ilm Line02	Ilm03-Grt02	3.51 ± 0.34	1150.87 ± 65.8	877.72 ± 65.8
ZA4R Grt-Ilm Line02	Ilm03-Grt03	3.98 ± 0.40	1077.26 ± 59.98	804.11 ± 59.98
ZA4R Grt-Ilm Line02	Ilm04-Grt01	3.45 ± 0.28	1159.32 ± 55.05	886.17 ± 55.05
ZA4R Grt-Ilm Line02	Ilm04-Grt02	3.23 ± 0.31	1203.47 ± 71.37	930.32 ± 71.37
ZA4R Grt-Ilm Line02	Ilm04-Grt02	3.67 ± 0.34	1123.37 ± 59.83	850.22 ± 59.83

Appendix G 11: EPMA results of the garnet-ilmenite transects of the sample ZA4R, garnet-ilmenite line03. Increasing No. refers to the measured direction (Garnet to Ilmenite)

No.	1		2	3	4	5	6	7	8	9	10
Com.	ZA4R Grt-Ilm Line04 Grt01		ZA4R Grt-Ilm Line04 Ilm01	ZA4R Grt-Ilm Line04 Ilm02	ZA4R Grt-Ilm Line04 Ilm03	ZA4R Grt-Ilm Line04 Ilm04	ZA4R Grt-Ilm Line04 Ilm05	ZA4R Grt-Ilm Line04 Ilm06	ZA4R Grt-Ilm Line04 Ilm07	ZA4R Grt-Ilm Line04 Ilm08	ZA4R Grt-Ilm Line04 Ilm09
SiO_2	36.10		0	0.04	0	0	0.02	0.02	0.02	0.05	0.03
TiO_2	0.81		51.84	51.97	51.91	54.82	53.23	52.48	53.13	52.61	52.28
Al_2O_3	20.81		0.06	0.01	0.05	0.46	0.05	0.07	0.09	0.11	0.06
FeO	36.74		48.83	47.92	47.86	43.11	46.35	47.25	46.50	46.94	48.49
MnO	1.29		0.35	0.37	0.35	0.19	0.34	0.31	0.36	0.35	0.35
MgO	3.03		0.54	0.65	0.62	0.41	0.56	0.50	0.56	0.43	0.69
CaO	1.47		0	0	0	0	0	0	0	0	0
Cr_2O_3	0.05		0	0.0	0	0.036	0.005	0.005	0.023	0	0
Total	100.29		101.57	100.92	100.73	98.97	100.55	100.60	100.63	100.47	101.83
Composition											
Grt	1	Ilm	1	2	3	4	5	6	7	8	9
Si	2.9116	Si	0	0.0010	0	0	0.0005	0.0005	0.0005	0.0014	0.0007
Ti	0.0491	Al	0.0016	0.0003	0.0014	0.0136	0.0016	0.0022	0.0026	0.0031	0.0016
Al	1.9784	Ti	0.9746	0.9802	0.9809	1.0295	1.0001	0.9897	0.9976	0.9922	0.9776
Cr	0.0031	Fe	1.0209	1.0049	1.0055	0.9004	0.9684	0.9909	0.9709	0.9845	1.0083
Fe^{3+}	0.0970	Mn	0.0073	0.0079	0.0073	0.0040	0.0072	0.0065	0.0076	0.0075	0.0073
Fe^{2+}	2.3815	Mg	0.0202	0.0243	0.0233	0.0151	0.0207	0.0186	0.0208	0.0162	0.0254
Mn	0.0879	Ca	0	0	0	0	0	0	0	0	0
Mg	0.3645	Cr	0	0.00	0	0.0007	0.0001	0.00	0.0005	0	0
Ca	0.1270	Fe^{3+}	0.0729	0.0554	0.0548	0	0	0.0257	0.0012	0.0145	0.0620
		Fe^{2+}	0.9480	0.9495	0.9507	0.9004	0.9684	0.9652	0.9697	0.9700	0.9463
XMn Grt	0.0297										
XFe Grt	0.8043										
XMg Grt	0.1231	XMn Ilm	0.0075	0.0080	0.0075	0.0043	0.0073	0.0066	0.0076	0.0076	0.0074

Appendix G 12: Results of temperature calculations with the garnet-ilmenite cation exchange thermometer for the sample ZA4R, Line03. Temperature calculation were carried out for the closet points to the contact of ilmenite and garnet. For position of the measurement points see Appendix G 11.

Sample	Mineral pair	KD ± 2σ	T(K) ± 2σ	T(°C) ± 2σ
ZA4R Grt-Ilm Line04	Ilm01-Grt01	4.79 ± 0.43	984.99 ± 44.33	711.84 ± 44.33
ZA4R Grt-Ilm Line04	Ilm02-Grt01	4.45 ± 0.40	1019.57 ± 47.68	746.42 ± 47.68
ZA4R Grt-Ilm Line04	Ilm03-Grt01	4.78 ± 0.42	985.94 ± 43.38	712.79 ± 43.38

Appendix H: Results of Raman analysis

Sample	Counts	Peak position ν_{964} (cm^{-1})	T (°C)	Comment
DurangoApatite1-0	288000	964.432	20	Standard
DurangoApatite1-1	334000	964.453	20	Standard
DurangoApatite1-2	368000	964.459	20	Standard
DurangoApatite1-3	366000	964.448	20	Standard
DurangoApatite1-4	334000	964.433	20	Standard
DurangoApatite1-5	352000	964.469	21	Standard
DurangoApatite1-6	368000	964.481	21	Standard
DurangoApatite1-7	324000	964.465	21	Standard
DurangoApatite1-8	280000	964.427	21	Standard
DurangoApatite1-9	289000	964.434	20	Standard
DurangoApatite1-10	305000	964.481	20	Standard
DurangoApatite1-11	321000	964.504	20	Standard
DurangoApatite1-12	366000	964.529	20	Standard
DurangoApatite1-13	343000	964.511	20	Standard
DurangoApatite1-14	362000	964.514	21	Standard
DurangoApatite1-15	329000	964.504	21	Standard
ZA4R_Matrix Apatite_1-0	12000	964.345	21	Matrix Apatite
ZA4R_Matrix Apatite_1-1	9000	964.461	21	Matrix Apatite
ZA4R_Matrix Apatite_1-2	11000	964.278	21	Matrix Apatite
ZA4R_Matrix Apatite_1-3	10000	964.222	21	Matrix Apatite
ZA4R_Matrix Apatite_1-4	11000	964.136	21	Matrix Apatite
ZA4R_Apatite_1-0	39000	965.064	21	Sample
ZA4R_Apatite_1-1	41000	965.098	21	Sample
ZA4R_Apatite_1-2	41000	965.059	21	Sample
ZA4R_Apatite_1-3	36600	965.069	21	Sample
ZA4R_Apatite_1-4	30000	965.063	21	Sample
ZA4R_Apatite_1-5	16000	965.084	21	Sample
ZA4R_Apatite_1-6	5000	964.953	21	Sample

Appendix H: continued

Sample	Counts	Peak position ν_{964} (cm^{-1})	T (°C)	Comment
ZA4R_Apatite_2-0	35000	965.083	21	Sample
ZA4R_Apatite_2-1	38000	965.117	21	Sample
ZA4R_Apatite_2-2	41000	965.136	21	Sample
ZA4R_Apatite_2-3	35000	965.104	21	Sample
ZA4R_Apatite_2-4	31000	965.062	21	Sample
ZA4R_Apatite_2-5	25000	965.043	21	Sample
ZA4R_Apatite_2-6	23000	965.006	21	Sample
ZA4R_Apatite_2-7	18000	964.974	21	Sample
ZA4R_Matrix Apatite_2-0	1400	963.942	20	Matrix Apatite
ZA4R_Matrix Apatite_2-1	1800	963.952	20	Matrix Apatite
ZA4R_Matrix Apatite_2-2	2100	964.381	20	Matrix Apatite
ZA4R_Matrix Apatite_2-3	1400	964.253	20	Matrix Apatite
ZA4R_Matrix Apatite_2-4	1500	964.248	20	Matrix Apatite
DurangoApatite1-16	326000	964.195	20	Standard
DurangoApatite1-17	325000	964.189	20	Standard
DurangoApatite1-18	324000	964.2	20	Standard
DurangoApatite1-19	314000	964.204	20	Standard
DurangoApatite1-20	316000	964.193	20	Standard
DurangoApatite1-21	316702	964.156	20	Standard
DurangoApatite1-22	318000	964.152	20	Standard
DurangoApatite1-23	319000	964.149	20	Standard
DurangoApatite1-24	300000	964.151	20	Standard
DurangoApatite1-25	298000	964.147	20	Standard
ZA4R_Apatite_3-0	36000	965.174	21	Sample
ZA4R_Apatite_3-1	48000	965.21	21	Sample
ZA4R_Apatite_3-2	57000	965.2	21	Sample
ZA4R_Apatite_3-3	57000	965.34	21	Sample
ZA4R_Apatite_3-4	41000	965.245	21	Sample

Appendix H: continued

Sample	Counts	Peak position ν_{964} (cm^{-1})	T (°C)	Comment
ZA4R_Apatite_4-0	15000	965.078	21	Sample
ZA4R_Apatite_4-1	19000	965.193	21	Sample
ZA4R_Apatite_4-2	26000	965.217	21	Sample
ZA4R_Apatite_4-3	21000	965.186	21	Sample
ZA4R_Apatite_4-4	14000	965.175	21	Sample
ZA4R_Apatite_4-5	9000	965.156	21	Sample
ZA4R_Matrix Apatite_3-0	1400	963.964	22	Matrix Apatite
ZA4R_Matrix Apatite_3-1	1300	964.131	22	Matrix Apatite
ZA4R_Matrix Apatite_3-2	1900	964.229	22	Matrix Apatite
ZA4R_Matrix Apatite_3-3	1600	964.361	22	Matrix Apatite
ZA4R_Matrix Apatite_3-4	1500	964.265	22	Matrix Apatite
DurangoApatite1-26	293000	964.213	22	Standard
DurangoApatite1-27	287000	964.215	22	Standard
DurangoApatite1-28	294000	964.208	22	Standard
DurangoApatite1-29	303000	964.204	22	Standard
DurangoApatite1-30	312000	964.196	22	Standard
DurangoApatite1-31	314000	964.175	21	Standard
DurangoApatite1-32	308000	964.153	21	Standard
DurangoApatite1-33	306000	964.167	21	Standard
DurangoApatite1-34	299000	964.159	21	Standard
DurangoApatite1-35	294000	964.144	21	Standard
LH5R_Apatite_1-0	25000	965.063	21	Sample
LH5R_Apatite_1-1	29000	965.121	21	Sample
LH5R_Apatite_1-2	33000	965.167	21	Sample
LH5R_Apatite_1-3	30000	965.186	21	Sample
LH5R_Apatite_1-4	26000	965.153	21	Sample
LH5R_Apatite_1-5	24000	965.142	21	Sample
LH5R_Apatite_2-0	12000	965.162	21	Sample
LH5R_Apatite_2-1	14000	965.195	21	Sample
LH5R_Apatite_2-2	18000	965.207	21	Sample
LH5R_Apatite_2-3	17000	965.198	21	Sample
LH5R_Apatite_2-4	15000	965.173	21	Sample

Appendix H: continued

Sample	Counts	Peak position ν_{964} (cm^{-1})	T (°C)	Comment
LH5R_Matrix Apatite_1-0	3600	963.964	22	Matrix Apatite
LH5R_Matrix Apatite_1-1	3800	964.221	22	Matrix Apatite
LH5R_Matrix Apatite_1-2	4100	964.299	22	Matrix Apatite
LH5R_Matrix Apatite_1-3	4000	964.241	22	Matrix Apatite
LH5R_Matrix Apatite_1-4	4100	964.185	22	Matrix Apatite
LH5R_Matrix Apatite_1-5	3700	963.986	22	Matrix Apatite
LH5R_Matrix Apatite_2-0	2600	964.132	22	Matrix Apatite
LH5R_Matrix Apatite_2-1	2900	964.188	22	Matrix Apatite
LH5R_Matrix Apatite_2-2	3100	964.245	22	Matrix Apatite
LH5R_Matrix Apatite_2-3	2400	964.233	22	Matrix Apatite
LH5R_Matrix Apatite_2-4	1900	964.176	22	Matrix Apatite
DurangoApatite1-36	362000	964.395	21	Standard
DurangoApatite1-37	366000	964.389	21	Standard
DurangoApatite1-38	372000	964.412	21	Standard
DurangoApatite1-39	375000	964.419	21	Standard
DurangoApatite1-40	374000	964.432	21	Standard
DurangoApatite1-41	370000	964.386	21	Standard
DurangoApatite1-42	363000	964.352	21	Standard
DurangoApatite1-43	365000	964.341	21	Standard
DurangoApatite1-44	362000	964.333	21	Standard
DurangoApatite1-45	357000	964.327	21	Standard
LH5R_Apatite_3-0	15000	965.172	21	Sample
LH5R_Apatite_3-1	18000	965.191	21	Sample
LH5R_Apatite_3-2	22000	965.213	21	Sample
LH5R_Apatite_3-3	26000	965.248	21	Sample
LH5R_Apatite_3-4	21000	965.204	21	Sample
LH5R_Apatite_3-5	1900	965.185	21	Sample
LH5R_Apatite_4-0	13000	965.133	21	Sample
LH5R_Apatite_4-1	15000	965.165	21	Sample
LH5R_Apatite_4-2	18000	965.187	21	Sample
LH5R_Apatite_4-3	16000	965.193	21	Sample
LH5R_Apatite_4-4	12000	965.15	21	Sample

Appendix H: continued

Sample	Counts	Peak position of ν_{964} (cm^{-1})	T (°C)	Comment
LH5R_Matrix Apatite_3-0	7500	964.246	22	Matrix Apatite
LH5R_Matrix Apatite_3-1	8700	964.288	22	Matrix Apatite
LH5R_Matrix Apatite_3-2	9200	964.313	22	Matrix Apatite
LH5R_Matrix Apatite_3-3	9600	964.333	22	Matrix Apatite
LH5R_Matrix Apatite_3-4	9100	964.306	22	Matrix Apatite
LH5R_Matrix Apatite_3-5	7200	964.264	22	Matrix Apatite
DurangoApatite1-46	365000	964.605	22	Standard
DurangoApatite1-47	371000	964.591	22	Standard
DurangoApatite1-48	373000	964.61	22	Standard
DurangoApatite1-49	372000	964.594	22	Standard
DurangoApatite1-50	370000	964.584	22	Standard
DurangoApatite1-51	368000	964.563	22	Standard
DurangoApatite1-52	368000	964.563	22	Standard
DurangoApatite1-53	371000	964.569	22	Standard
DurangoApatite1-54	372000	964.548	22	Standard
DurangoApatite1-55	370000	964.558	22	Standard
DurangoApatite1-56	365000	964.592	22	Standard
DurangoApatite1-57	367000	964.602	22	Standard
DurangoApatite1-58	366000	964.588	22	Standard
DurangoApatite1-59	361000	964.594	22	Standard
DurangoApatite1-60	359000	964.601	22	Standard

Appendix I: Results of the U-Pb zircon age determinations

Appendix I 1: Results of the U-Pb LA-ICP-MS age determinations and U-Pb zircon ages of single grain analysis of the sample LHVT. [1] U and Th concentrations are calculated employing an external standard zircon as in Paton et al. (2010) [2] 2 σ uncertainties propagated according to Paton et al. (2010); $^{207}Pb/^{206}Pb$ ratios, ages and errors are calculated according to Petrus and Kamber (2012).

					CORRECTED RATIOS[2]							CORRECTED AGES [Ma]								DISC.
Sample	Analysis	U[1] [ppm]	Pb[1] [ppm]	Th/ U	$^{207}Pb/^{235}U$	2 σ	$^{206}Pb/^{238}U$	2 σ	rho	$^{207}Pb/^{206}Pb$	2 σ	$^{207}Pb/^{235}U$	2 σ	$^{206}Pb/^{238}U$	2 σ	$^{207}Pb/^{206}Pb$	2 σ	Best age	2 σ	%
LHVT	LHVT_01	123.7	77.9	0.6	0.05	0.0088	0.005	0.00028	-0.04	0.071	0.015	47.3	8.6	32.5	1.8	1120	160	32.5	1.8	31.3
LHVT	LHVT_02	201	91	0.5	0.1	0.013	0.006	0.00022	0.04	0.135	0.019	95	12	35.5	1.4	2110	190	35.5	1.4	62.6
LHVT	LHVT_03	195.8	133.7	0.7	0.13	0.026	0.006	0.00042	0.25	0.172	0.043	120	23	37.1	2.7	2570	220	37.1	2.7	69.1
LHVT	LHVT_04	89	59	0.7	0.04	0.012	0.005	0.00045	-0.18	0.059	0.02	38	12	31.7	2.9	1070	230	31.7	2.9	16.6
LHVT	LHVT_05	508	156.5	0.3	0.03	0.0039	0.005	0.00012	0.01	0.052	0.0062	34.5	3.9	32.7	0.8	530	110	32.7	0.8	5.1
LHVT	LHVT_06	454.1	117	0.3	0.03	0.0042	0.005	0.00014	-0.08	0.054	0.0069	34	4.1	31.3	0.9	610	110	31.3	0.9	8
LHVT	LHVT_07	144.8	42.3	0.3	0.07	0.008	0.005	0.00042	0.15	0.1	0.013	71.3	7.6	34.6	2.7	1660	140	34.6	2.7	51.5
LHVT	LHVT_08	492	107.4	0.2	0.03	0.0041	0.005	0.0002	0.14	0.049	0.0066	31.7	4	32.1	1.3	480	170	32.1	1.3	-1.3
LHVT	LHVT_09	337	60.7	0.2	0.15	0.012	0.006	0.00024	-0.01	0.184	0.016	143	10	38.2	1.5	2712	91	38.2	1.5	73.3
LHVT	LHVT_10	1256	1245	1	0.03	0.0024	0.005	0.000099	0.25	0.048	0.0037	31.1	2.4	30.3	0.6	308	73	30.3	0.6	2.6
LHVT	LHVT_11	126.2	67.3	0.5	0.08	0.013	0.005	0.00033	-0.01	0.115	0.018	81	13	33.6	2.1	2020	210	33.6	2.1	58.5
LHVT	LHVT_12	311.6	137.3	0.4	0.08	0.0097	0.005	0.00028	0.34	0.117	0.013	80.1	9	33.5	1.8	1910	140	33.5	1.8	58.2
LHVT	LHVT_13	669	125	0.2	0.11	0.01	0.005	0.00019	-0.11	0.155	0.018	103	9.6	33.1	1.2	2400	190	33.1	1.2	67.9
LHVT	LHVT_14	576	146.4	0.3	0.07	0.0061	0.005	0.00016	0.09	0.106	0.0099	71.1	5.8	32.6	1	1765	85	32.6	1	54.1
LHVT	LHVT_15	484.2	63.9	0.1	0.06	0.005	0.005	0.00015	0.03	0.099	0.0085	64.2	5.1	30.8	1	1650	110	30.8	1	52.1

Appendix I 2: Results of the U-Pb LA-ICP-MS age determinations and U-Pb zircon ages of single grain analysis of the sample ZARTO. [1] U and Th concentrations are calculated employing an external standard zircon as in Paton et al. (2010) [2] 2 σ uncertainties propagated according to Paton et al. (2010); $^{207}Pb/^{206}Pb$ ratios, ages and errors are calculated according to Petrus and Kamber (2012).

					CORRECTED RATIOS[2]							CORRECTED AGES [Ma]								DISC.
Sample	Analysis	U[1] [ppm]	Pb[1] [ppm]	Th/ U	$^{207}Pb/^{235}U$	2 σ	$^{206}Pb/^{238}U$	2 σ	rho	$^{207}Pb/^{206}Pb$	2 σ	$^{207}Pb/^{235}U$	2 σ	$^{206}Pb/^{238}U$	2 σ	$^{207}Pb/^{206}Pb$	2 σ	Best age	2 σ	%
ZARTO	ZARTO_01	168.9	132.8	0.8	0.06	0.011	0.005	0.0003	-0.04	0.095	0.018	61	10	31.3	1.8	1440	230	31.3	1.8	48.7
ZARTO	ZARTO_02	157.8	77.3	0.5	0.04	0.0087	0.005	0.0003	-0.11	0.061	0.013	42	8.5	34.6	1.9	1000	170	34.6	1.9	17.6
ZARTO	ZARTO_03	165.6	65.9	0.4	0.04	0.0088	0.005	0.0002	0.14	0.054	0.013	38.5	8.9	32.2	1.5	810	160	32.2	1.5	16.4
ZARTO	ZARTO_04	120.9	50.4	0.4	0.11	0.014	0.005	0.0003	0.36	0.147	0.018	102	12	34.6	2.1	2390	170	34.6	2.1	66.1
ZARTO	ZARTO_05	129	55.1	0.4	0.14	0.019	0.006	0.0004	0.1	0.179	0.026	129	17	36.4	2.3	2620	160	36.4	2.3	71.8
ZARTO	ZARTO_06	600	76.9	0.1	0.03	0.0033	0.005	0.0001	-0.02	0.049	0.005	33.2	3.4	31.6	0.6	437	92	31.6	0.6	4.8
ZARTO	ZARTO_07	1018	137.8	0.1	0.05	0.0046	0.005	0.0002	0.37	0.078	0.0068	50.1	4.4	30.9	1.2	1235	100	30.9	1.2	38.3
ZARTO	ZARTO_08	234	31.3	0.1	0.1	0.019	0.004	0.0003	0.54	0.175	0.033	97	17	28.4	2.2	2690	190	28.4	2.2	70.7
ZARTO	ZARTO_09	698	279	0.4	0.06	0.0063	0.005	0.0002	0.34	0.084	0.0097	54.6	6	31.2	1.1	1300	170	31.2	1.1	42.9
ZARTO	ZARTO_10	204.9	91.6	0.5	0.16	0.024	0.006	0.0005	-0.02	0.192	0.031	153	21	39.4	3.4	2760	200	39.4	3.4	74.2
ZARTO	ZARTO_11	310	98.8	0.3	0.06	0.0085	0.005	0.0002	-0.12	0.087	0.014	56.6	8.2	31.2	1.4	1460	160	31.2	1.4	44.9

Appendix I 3: Results of the U-Pb LA-ICP-MS age determinations and U-Pb zircon ages of single grain analysis of the sample ZATT. [1] U and Th concentrations are calculated employing an external standard zircon as in Paton et al. (2010) [2] 2 σ uncertainties propagated according to Paton et al. (2010); $^{207}Pb/^{206}Pb$ ratios, ages and errors are calculated according to Petrus and Kamber (2012).

					CORRECTED RATIOS[2]							CORRECTED AGES [Ma]								DISC.
Sample	Analysis	U[1] [ppm]	Pb[1] [ppm]	Th/ U	$^{207}Pb/^{235}U$	2 σ	$^{206}Pb/^{238}U$	2 σ	rho	$^{207}Pb/^{206}Pb$	2 σ	$^{207}Pb/^{235}U$	2 σ	$^{206}Pb/^{238}U$	2 σ	$^{207}Pb/^{206}Pb$	2 σ	Best age	2 σ	%
ZATT	ZATT_01	81.2	32	0.4	0.1	0.014	0.005	0.0005	0.19	0.138	0.021	94	13	33	3.1	2290	150	33	3.1	64.9
ZATT	ZATT_02	120.5	81.5	0.7	0.12	0.026	0.006	0.0005	0.06	0.166	0.043	119	22	36.1	2.9	2470	260	36.1	2.9	69.7
ZATT	ZATT_03	68.3	30.8	0.5	0.12	0.018	0.006	0.0004	0.25	0.158	0.023	119	17	37.1	2.7	2470	150	37.1	2.7	68.8
ZATT	ZATT_04	230	127.7	0.6	0.08	0.0094	0.005	0.0002	0.29	0.118	0.012	81.6	8.8	34.4	1.1	1880	140	34.4	1.1	57.8
ZATT	ZATT_05	137.3	74.8	0.5	0.07	0.012	0.005	0.0003	0.01	0.097	0.018	65	11	33.6	1.7	1810	210	33.6	1.7	48.3
ZATT	ZATT_06	158.7	96.4	0.6	0.12	0.017	0.005	0.0004	0.15	0.173	0.032	110	16	34.3	2.5	2520	240	34.3	2.5	68.8
ZATT	ZATT_07	172.1	80.3	0.5	0.05	0.01	0.005	0.0003	0.02	0.073	0.018	47	10	28.7	1.9	1050	230	28.7	1.9	38.9
ZATT	ZATT_08	240.7	163.4	0.7	0.09	0.014	0.005	0.0004	0.36	0.126	0.018	88	13	34.6	2.4	2110	180	34.6	2.4	60.7
ZATT	ZATT_09	114.9	74.5	0.7	0.15	0.018	0.006	0.0003	0.24	0.192	0.024	138	16	35.8	1.9	2660	140	35.8	1.9	74.1
ZATT	ZATT_10	73.7	35.3	0.5	0.09	0.013	0.005	0.0004	0.13	0.12	0.022	83	12	32.7	2.5	2120	190	32.7	2.5	60.6
ZATT	ZATT_11	82.1	45.8	0.6	0.12	0.017	0.006	0.0004	-0.01	0.159	0.022	115	15	35.6	2.5	2630	160	35.6	2.5	69
ZATT	ZATT_12	572	351	0.6	0.15	0.022	0.006	0.0004	0.57	0.184	0.027	139	19	39.6	2.4	2660	190	39.6	2.4	71.5
ZATT	ZATT_13	233	114	0.5	0.05	0.0066	0.005	0.0002	-0.24	0.067	0.01	46.6	6.4	33.6	1.3	1070	220	33.6	1.3	27.9
ZATT	ZATT_14	150.2	95.1	0.6	0.06	0.011	0.005	0.0003	0.08	0.099	0.02	63	10	30	1.9	1550	250	30	1.9	52.4
ZATT	ZATT_15	184.2	117.5	0.6	0.07	0.011	0.005	0.0002	-0.11	0.104	0.017	70	11	34.7	1.5	1620	230	34.7	1.5	50.4
ZATT	ZATT_16	183.6	76.6	0.4	0.08	0.01	0.005	0.0002	0.11	0.107	0.014	76.3	9.5	33.8	1.5	1800	110	33.8	1.5	55.7
ZATT	ZATT_17	177.2	76.9	0.4	0.03	0.0052	0.005	0.0002	0.1	0.052	0.0081	34	5.1	31.7	1.5	750	150	31.7	1.5	6.8
ZATT	ZATT_18	329.5	224.5	0.7	0.03	0.0056	0.005	0.0003	-0.03	0.051	0.0084	34.7	5.5	32.2	1.6	540	170	32.2	1.6	7.2
ZATT	ZATT_19	357	178.1	0.5	0.04	0.0051	0.005	0.0002	0.08	0.062	0.0083	41	5	32.2	1.4	720	110	32.2	1.4	21.5
ZATT	ZATT_20	267.1	141.5	0.5	0.04	0.007	0.005	0.0003	-0.09	0.056	0.011	37.8	6.8	31.6	1.6	570	180	31.6	1.6	16.4
ZATT	ZATT_21	93	58.2	0.6	0.03	0.01	0.005	0.0003	0.18	0.042	0.014	32.5	9.9	31.2	2.1	1100	330	31.2	2.1	4
ZATT	ZATT_22	35.2	23	0.7	0.07	0.021	0.005	0.0006	-0.17	0.104	0.037	70	19	35	3.7	1890	320	35	3.7	50
ZATT	ZATT_23	194	76.5	0.4	0.06	0.0073	0.005	0.0003	0.03	0.094	0.014	60.7	7	32	2	1740	130	32	2	47.3
ZATT	ZATT_24	243	128	0.5	0.07	0.011	0.005	0.0002	0.16	0.092	0.016	64	10	34.4	1.4	1570	240	34.4	1.4	46.3
ZATT	ZATT_25	281	158.7	0.6	0.05	0.011	0.005	0.0003	-0.06	0.082	0.017	53	11	29.6	1.7	1420	200	29.6	1.7	44.2

Appendix I 4: Results of the U-Pb LA-ICP-MS age determinations and U-Pb zircon ages of single grain analysis of the sample LH3TR. [1] U and Th concentrations are calculated employing an external standard zircon as in Paton et al. (2010) [2] 2 σ uncertainties propagated according to Paton et al. (2010); $^{207}Pb/^{206}Pb$ ratios, ages and errors are calculated according to Petrus and Kamber (2012).

					CORRECTED RATIOS[2]							CORRECTED AGES [Ma]								DISC.
Sample	Analysis	U^{1} [ppm]	Pb^{1} [ppm]	Th/U	$^{207}Pb/^{235}U$	2 σ	$^{206}Pb/^{238}U$	2 σ	rho	$^{207}Pb/^{206}Pb$	2 σ	$^{207}Pb/^{235}U$	2 σ	$^{206}Pb/^{238}U$	2 σ	$^{207}Pb/^{206}Pb$	2 σ	Best age	2 σ	%
LH3TR	LH3TR_01	232	108.4	0.5	0.04	0.0041	0.005	0.0002	0.39	0.066	0.0072	39.9	4	29.7	1.6	810	170	29.7	1.6	25.6
LH3TR	LH3TR_02	114.7	50.4	0.4	0.04	0.0083	0.005	0.0003	0.08	0.055	0.014	38.2	8.1	33.7	2.1	830	190	33.7	2.1	11.8
LH3TR	LH3TR_03	299.2	135.9	0.5	0.04	0.0039	0.005	0.0002	0	0.057	0.0066	36.3	3.8	29.9	1.2	670	110	29.9	1.2	17.6
LH3TR	LH3TR_04	73.5	38.2	0.5	0.15	0.016	0.006	0.0005	0.1	0.171	0.024	143	14	38.9	3.3	2630	150	38.9	3.3	72.8
LH3TR	LH3TR_05	478	453	1	0.03	0.0034	0.005	0.0001	0.04	0.051	0.0054	33.1	3.3	30.9	0.8	528	87	30.9	0.8	6.6
LH3TR	LH3TR_06	245.2	187	0.8	0.04	0.006	0.005	0.0003	0.21	0.065	0.0098	42.2	5.8	32.3	1.7	1010	160	32.3	1.7	23.5
LH3TR	LH3TR_07	184	121	0.7	0.04	0.0088	0.005	0.0002	-0.02	0.058	0.013	40.8	8.6	33.3	1.3	750	200	33.3	1.3	18.4
LH3TR	LH3TR_08	483	252.7	0.5	0.12	0.011	0.006	0.0003	0.32	0.17	0.021	112	10	35.5	1.8	2490	130	35.5	1.8	68.3
LH3TR	LH3TR_09	134	67	0.5	0.03	0.0069	0.005	0.0003	-0.02	0.055	0.012	34.8	7	29.7	1.6	960	240	29.7	1.6	14.7
LH3TR	LH3TR_10	128.3	64.3	0.5	0.05	0.0081	0.005	0.0002	-0.08	0.069	0.012	46.5	7.9	31.5	1.5	1430	150	31.5	1.5	32.3
LH3TR	LH3TR_11	82.1	59.1	0.7	0.05	0.0096	0.005	0.0003	-0.1	0.072	0.016	45.7	9.3	31	1.7	1280	190	31	1.7	32.2
LH3TR	LH3TR_12	69.7	31.3	0.5	0.12	0.017	0.006	0.0004	0.21	0.145	0.022	114	16	39.2	2.4	2460	140	39.2	2.4	65.6
LH3TR	LH3TR_13	72.5	43	0.6	0.04	0.011	0.005	0.0003	-0.08	0.057	0.019	35	11	31.1	2	1130	250	31.1	2	11.1
LH3TR	LH3TR_14	311	194	0.6	0.03	0.0038	0.005	0.0002	0.09	0.048	0.006	31.4	3.7	30.9	1.1	540	130	30.9	1.1	1.6
LH3TR	LH3TR_15	284	119.4	0.4	0.12	0.0074	0.005	0.0002	0.04	0.161	0.011	111	6.8	33.8	1	2490	79	33.8	1	69.5
LH3TR	LH3TR_16	223.9	132.6	0.6	0.09	0.0084	0.005	0.0002	0.09	0.127	0.011	87.1	7.9	33.9	1.4	2032	100	33.9	1.4	61.1
LH3TR	LH3TR_17	300	211.1	0.7	0.03	0.0039	0.005	0.0002	-0.26	0.05	0.0069	33.6	3.8	33.7	1.1	610	160	33.7	1.1	-0.3
LH3TR	LH3TR_18	749	438	0.6	0.04	0.004	0.005	0.0002	-0.32	0.057	0.007	40.9	3.9	33.8	1.2	440	160	33.8	1.2	17.4
LH3TR	LH3TR_19	102.1	51.7	0.5	0.06	0.0085	0.005	0.0003	0.06	0.099	0.014	63.3	8	31.6	1.7	1730	140	31.6	1.7	50.1
LH3TR	LH3TR_20	110	48	0.4	0.07	0.0096	0.005	0.0003	-0.03	0.105	0.015	67.8	9.1	31.5	2	1830	160	31.5	2	53.5
LH3TR	LH3TR_21	131.5	95.9	0.7	0.04	0.0079	0.005	0.0003	0.27	0.064	0.011	42.3	7.8	33.1	1.9	890	160	33.1	1.9	21.7

Appendix I 5: Results of the U-Pb LA-ICP-MS age determinations and U-Pb zircon ages of single grain analysis of the sample LH5R. [1] U and Th concentrations are calculated employing an external standard zircon as in Paton et al. (2010) [2] 2 σ uncertainties propagated according to Paton et al. (2010); $^{207}Pb/^{206}Pb$ ratios, ages and errors are calculated according to Petrus and Kamber (2012).

				CORRECTED RATIOS[2]									CORRECTED AGES (Ma)								DISC.
Analysis	U[1] [ppm]	Th[1] [ppm]	Th/U	$^{207}Pb/^{206}Pb$	±2σ abs	$^{207}Pb/^{235}U$	±2σ abs	$^{206}Pb/^{238}U$	±2σ abs	$^{208}Pb/^{232}Th$	±2σ abs	Rho	$^{206}Pb/^{238}U$	±2σ	$^{207}Pb/^{235}U$	±2σ	$^{207}Pb/^{206}Pb$	±2σ	Best age	±2σ	%
LH5R_Zrn_01	328	64.7	0.20	0.051	0.011	0.036	0.008	0.005	0.000	0.002	0.000	-0.09	32.4	1.2	36	7.4	250	390	32.4	1.2	10.00
LH5R_Zrn_02	135	65.3	0.48	0.065	0.026	0.045	0.014	0.005	0.000	0.002	0.000	-0.23	32	2.1	43	14	230	710	32	2.1	25.58
LH5R_Zrn_03	146.7	62.9	0.43	0.124	0.022	0.089	0.014	0.005	0.001	0.004	0.001	-0.08	34.3	3.5	86	13	1960	330	34.3	3.5	60.12
LH5R_Zrn_04	424	93.5	0.22	0.046	0.010	0.032	0.006	0.005	0.000	0.001	0.000	-0.05	30.7	1.8	31.6	5.9	130	400	30.7	1.8	2.85
LH5R_Zrn_05	1310	119.3	0.09	0.044	0.006	0.032	0.004	0.005	0.000	0.002	0.000	-0.28	31.64	1	31.5	3.9	40	260	31.64	1	-0.44
LH5R_Zrn_06	465	102.6	0.22	0.047	0.011	0.034	0.007	0.005	0.000	0.001	0.000	-0.29	33.3	1.6	33.8	7.2	20	430	33.3	1.6	1.48
LH5R_Zrn_07	244.8	167.7	0.69	0.052	0.018	0.034	0.012	0.005	0.000	0.002	0.000	0.37	30	2.1	34	12	340	760	30	2.1	11.76
LH5R_Zrn_08	661	268	0.41	0.055	0.012	0.034	0.008	0.004	0.000	0.001	0.000	-0.13	27.8	1.2	35.5	7.2	380	430	27.8	1.2	21.69
LH5R_Zrn_09	597	177.6	0.30	0.051	0.009	0.032	0.006	0.005	0.000	0.002	0.000	0.08	31.8	1.1	33.4	5.7	160	370	31.8	1.1	4.79
LH5R_Zrn_10	434	90.5	0.21	0.048	0.015	0.031	0.010	0.005	0.000	0.002	0.001	0.14	33.6	1.7	31.1	9.5	-70	550	33.6	1.7	-8.04
LH5R_Zrn_11	367	117.4	0.32	0.064	0.010	0.043	0.007	0.005	0.000	0.002	0.000	-0.10	32	1.6	42.9	6.4	570	330	32	1.6	25.41
LH5R_Zrn_12	672	150.5	0.22	0.052	0.008	0.034	0.005	0.005	0.000	0.002	0.000	-0.07	30.4	1.2	34.2	5.2	240	330	30.4	1.2	11.11
LH5R_Zrn_13	527	187.9	0.36	0.052	0.011	0.036	0.007	0.005	0.000	0.002	0.000	0.29	31.7	1.3	35.3	6.9	110	380	31.7	1.3	10.20
LH5R_Zrn_14	322	120.2	0.37	0.054	0.017	0.035	0.010	0.005	0.000	0.002	0.000	-0.17	30.3	1.4	34.5	10	100	580	30.3	1.4	12.17
LH5R_Zrn_15	164	80.7	0.49	0.642	0.052	1.920	0.160	0.021	0.001	0.076	0.008	0.10	135.8	6.9	1090	52	4592	130	135.8	6.9	87.54
LH5R_Zrn_16	1450	137	0.09	0.045	0.007	0.033	0.005	0.005	0.000	0.001	0.000	-0.15	32.48	0.87	32.6	4.9	30	300	32.48	0.87	0.37
LH5R_Zrn_17	363.5	51.7	0.14	0.055	0.012	0.035	0.007	0.005	0.000	0.003	0.001	0.06	31.4	1.6	35.1	6.9	240	410	31.4	1.6	10.54
LH5R_Zrn_18	428	190.4	0.44	0.045	0.013	0.029	0.008	0.005	0.000	0.002	0.000	0.01	30.3	1.8	28.7	7.4	-80	500	30.3	1.8	-5.57
LH5R_Zrn_19	348.6	194.7	0.56	0.055	0.013	0.035	0.008	0.005	0.000	0.002	0.000	0.15	32.9	1.5	34.6	8	230	460	32.9	1.5	4.91
LH5R_Zrn_20	160.2	90.8	0.57	0.055	0.020	0.034	0.012	0.005	0.000	0.002	0.000	-0.16	32.8	2.3	34	12	0	630	32.8	2.3	3.53

Appendix I 5: continued

				CORRECTED RATIOS[2]									CORRECTED AGES (Ma)								DISC.
Analysis	U[1] [ppm]	Th[1] [ppm]	Th/U	$^{207}Pb/^{206}Pb$	±2σ abs	$^{207}Pb/^{235}U$	±2σ abs	$^{206}Pb/^{238}U$	±2σ abs	$^{208}Pb/^{232}Th$	±2σ abs	Rho	$^{206}Pb/^{238}U$	±2σ	$^{207}Pb/^{235}U$	±2σ	$^{207}Pb/^{206}Pb$	±2σ	Best age	±2σ	%
LH5R_Zrn_21	190	93.6	0.49	0.078	0.023	0.046	0.013	0.005	0.000	0.002	0.001	0.19	31.6	2.2	45	13	670	620	31.6	2.2	29.78
LH5R_Zrn_22	93.3	49	0.53	0.057	0.024	0.045	0.018	0.005	0.000	0.003	0.001	0.28	33.1	2.7	44	17	300	700	33.1	2.7	24.77
LH5R_Zrn_23	334	52	0.16	0.058	0.011	0.039	0.007	0.005	0.000	0.003	0.001	-0.22	33.3	1.5	40	7.2	290	380	33.3	1.5	16.75
LH5R_Zrn_24	261	58.1	0.22	0.050	0.014	0.030	0.008	0.005	0.000	0.002	0.000	-0.07	29.2	1.6	29.4	8.2	220	440	29.2	1.6	0.68
LH5R_Zrn_25	423.5	73.9	0.17	0.058	0.014	0.036	0.008	0.005	0.000	0.003	0.001	0.02	29.8	1.3	35.5	8.1	260	450	29.8	1.3	16.06
LH5R_Zrn_26	247	30.2	0.12	0.078	0.024	0.052	0.014	0.005	0.000	0.006	0.002	-0.09	33.5	2.5	51	14	890	590	33.5	2.5	34.31
LH5R_Zrn_27	190.8	36.8	0.19	0.084	0.016	0.058	0.011	0.005	0.000	0.004	0.001	0.03	32.1	2.1	57	11	1060	470	32.1	2.1	43.68
LH5R_Zrn_28	191	70.5	0.37	0.058	0.015	0.036	0.009	0.005	0.000	0.002	0.000	0.04	30	1.7	37.3	8.7	280	470	30	1.7	19.57
LH5R_Zrn_29	226	83.1	0.37	0.057	0.018	0.044	0.013	0.006	0.000	0.003	0.001	-0.16	35.4	1.9	43	13	160	590	35.4	1.9	17.67
LH5R_Zrn_30	197	41.6	0.21	0.066	0.025	0.041	0.015	0.005	0.000	0.003	0.001	0.08	31.4	2.2	40	15	460	620	31.4	2.2	21.50
LH5R_Zrn_31	333.1	105.4	0.32	0.047	0.015	0.029	0.009	0.005	0.000	0.002	0.001	-0.08	29.9	1.7	29.1	8.6	50	560	29.9	1.7	-2.75
LH5R_Zrn_32	432	140.3	0.32	0.051	0.010	0.033	0.006	0.005	0.000	0.002	0.000	-0.32	31.7	1.1	32.3	5.7	80	360	31.7	1.1	1.86
LH5R_Zrn_33	146.9	68.2	0.46	0.099	0.032	0.064	0.020	0.005	0.000	0.002	0.001	-0.01	33	2.8	62	19	970	750	33	2.8	46.77
LH5R_Zrn_34	438	67.5	0.15	0.045	0.011	0.033	0.007	0.005	0.000	0.002	0.001	-0.09	32.1	1.3	32.9	7.3	150	380	32.1	1.3	2.43
LH5R_Zrn_35	159.2	65.5	0.41	0.062	0.019	0.043	0.014	0.005	0.000	0.002	0.001	0.01	34.8	2.3	42	13	210	570	34.8	2.3	17.14
LH5R_Zrn_36	531	107.7	0.20	0.055	0.014	0.037	0.010	0.005	0.000	0.002	0.000	-0.17	33	1.7	37	9.6	420	470	33	1.7	10.81
LH5R_Zrn_37	149.3	37.7	0.25	0.043	0.018	0.034	0.013	0.005	0.000	0.003	0.001	0.33	32.5	2.8	33	13	-240	620	32.5	2.8	1.52
LH5R_Zrn_38	231.6	48	0.21	0.064	0.019	0.043	0.012	0.005	0.000	0.003	0.001	0.04	33.3	2.5	43	12	360	600	33.3	2.5	22.56
LH5R_Zrn_39	298	84.8	0.28	0.050	0.013	0.035	0.010	0.005	0.000	0.002	0.000	0.17	30.8	1.9	34.9	9.3	290	460	30.8	1.9	11.75
LH5R_Zrn_40	595	127.7	0.21	0.054	0.011	0.034	0.007	0.005	0.000	0.002	0.000	-0.29	30.7	1.4	35.2	6.7	250	350	30.7	1.4	12.78
LH5R_Zrn_41	161	51.6	0.32	0.053	0.018	0.033	0.012	0.005	0.000	0.002	0.001	-0.19	33.2	2.4	33	11	110	640	33.2	2.4	-0.61
LH5R_Zrn_42	312	76.4	0.24	0.052	0.010	0.036	0.008	0.005	0.000	0.002	0.000	0.33	33.3	1.5	35.8	8	90	390	33.3	1.5	6.98

Appendix I 5: continued

				CORRECTED RATIOS[2]									CORRECTED AGES (Ma)								DISC.
Analysis	U[1] [ppm]	Th[1] [ppm]	Th/U	$^{207}Pb/^{206}Pb$	±2σ abs	$^{207}Pb/^{235}U$	±2σ abs	$^{206}Pb/^{238}U$	±2σ abs	$^{208}Pb/^{232}Th$	±2σ abs	Rho	$^{206}Pb/^{238}U$	±2σ	$^{207}Pb/^{235}U$	±2σ	$^{207}Pb/^{206}Pb$	±2σ	Best age	±2σ	%
LH5R_Zrn_43	519	71	0.14	0.053	0.012	0.034	0.007	0.005	0.000	0.002	0.001	-0.14	31.2	1.3	33.4	6.9	140	420	31.2	1.3	6.59
LH5R_Zrn_44	378	187	0.49	0.048	0.009	0.033	0.006	0.005	0.000	0.002	0.000	0.08	31.4	1.3	32.8	6	100	370	31.4	1.3	4.27
LH5R_Zrn_45	122	53.4	0.44	0.059	0.023	0.045	0.018	0.005	0.000	0.002	0.001	0.21	33.8	2.8	43	17	40	640	33.8	2.8	21.40
LH5R_Zrn_46	302	54.1	0.18	0.047	0.013	0.036	0.009	0.005	0.000	0.002	0.001	-0.10	32.6	1.5	35.2	9.2	240	440	32.6	1.5	7.39
LH5R_Zrn_47	182	58.2	0.32	0.060	0.016	0.037	0.010	0.005	0.000	0.002	0.001	0.22	32	2.2	35.9	9.8	140	510	32	2.2	10.86
LH5R_Zrn_48	892	75.3	0.08	0.047	0.007	0.030	0.004	0.005	0.000	0.002	0.000	-0.04	30.8	0.88	30.3	4.1	40	270	30.8	0.88	-1.65
LH5R_Zrn_49	181.8	55.5	0.31	0.052	0.007	0.307	0.041	0.043	0.002	0.024	0.003	0.36	273.1	10.0	275.0	34.0	220	270	273.1	10.0	0.69
LH5R_Zrn_50	176.6	108.4	0.61	0.083	0.008	1.193	0.110	0.107	0.003	0.043	0.003	-0.06	656.0	15.0	809.0	48.0	1240	180	656.0	15.0	18.91

Appendix I 6: Results of the U-Pb LA-ICP-MS age determinations and U-Pb zircon ages of single grain analysis of the sample ZA4R. [1] U and Th concentrations are calculated employing an external standard zircon as in Paton et al. (2010) [2] 2 σ uncertainties propagated according to Paton et al. (2010); $^{207}Pb/^{206}Pb$ ratios, ages and errors are calculated according to Petrus and Kamber (2012).

				CORRECTED RATIOS[2]									CORRECTED AGES (Ma)								DISC.
Analysis	U[1] [ppm]	Th[1] [ppm]	Th/U	$^{207}Pb/^{206}Pb$	±2σ abs	$^{207}Pb/^{235}U$	±2σ abs	$^{206}Pb/^{238}U$	±2σ abs	$^{208}Pb/^{232}Th$	±2σ abs	Rho	$^{206}Pb/^{238}U$	±2 σ	$^{207}Pb/^{235}U$	±2σ	$^{207}Pb/^{206}Pb$	±2σ	Best age	±2σ	%
ZA4R_Zrn-01	348	78.2	0.22	0.066	0.016	0.039	0.010	0.005	0.000	0.002	0.001	0.45	30.7	2.1	38.7	9.3	950	390	30.7	2.1	20.67
ZA4R_Zrn-02	926	41.4	0.04	0.053	0.009	0.046	0.008	0.006	0.000	0.004	0.001	-0.33	41.6	1.3	45.8	7.3	290	370	41.6	1.3	9.17
ZA4R_Zrn-03	470	210	0.45	0.052	0.012	0.037	0.008	0.005	0.000	0.002	0.000	0.20	31.6	1.6	36.9	8	290	410	31.6	1.6	14.36
ZA4R_Zrn-04	276	207	0.75	0.085	0.018	0.055	0.011	0.005	0.000	0.002	0.000	0.00	30.8	1.7	54	11	1090	450	30.8	1.7	42.96
ZA4R_Zrn-05	170.7	98.2	0.58	0.072	0.021	0.057	0.016	0.005	0.000	0.003	0.000	0.05	32.9	2.8	55	15	940	550	32.9	2.8	40.18
ZA4R_Zrn-06	139	25.39	0.18	0.126	0.049	0.063	0.022	0.004	0.000	0.008	0.002	-0.32	23.3	2.6	61	20	1430	640	23.3	2.6	61.80
ZA4R_Zrn-07	108.8	43.78	0.40	0.069	0.024	0.045	0.017	0.005	0.000	0.003	0.001	-0.11	32.4	2.4	44	16	250	690	32.4	2.4	26.36
ZA4R_Zrn-08	103	43.2	0.42	0.055	0.027	0.040	0.017	0.005	0.000	0.002	0.001	0.27	32.1	2.9	41	17	-280	800	32.1	2.9	21.71
ZA4R_Zrn-09	99	44	0.44	0.082	0.036	0.048	0.019	0.005	0.000	0.003	0.001	-0.24	32.5	2.4	46	18	110	760	32.5	2.4	29.35
ZA4R_Zrn-10	159.4	60	0.38	0.062	0.025	0.039	0.015	0.005	0.001	0.002	0.001	-0.03	32.6	3.2	38	15	-20	790	32.6	3.2	14.21
ZA4R_Zrn-11	168	41.7	0.25	0.098	0.028	0.058	0.016	0.005	0.000	0.005	0.002	-0.17	31.2	2.2	57	15	1240	580	31.2	2.2	45.26
ZA4R_Zrn-12	349	79	0.23	0.061	0.015	0.042	0.009	0.005	0.000	0.002	0.001	-0.29	30.6	2.5	43.7	9.3	700.0	490.0	30.6	2.5	30.00

Appendix J: Stratigraphic sections of the Villa Garcia Ignimbrite complex

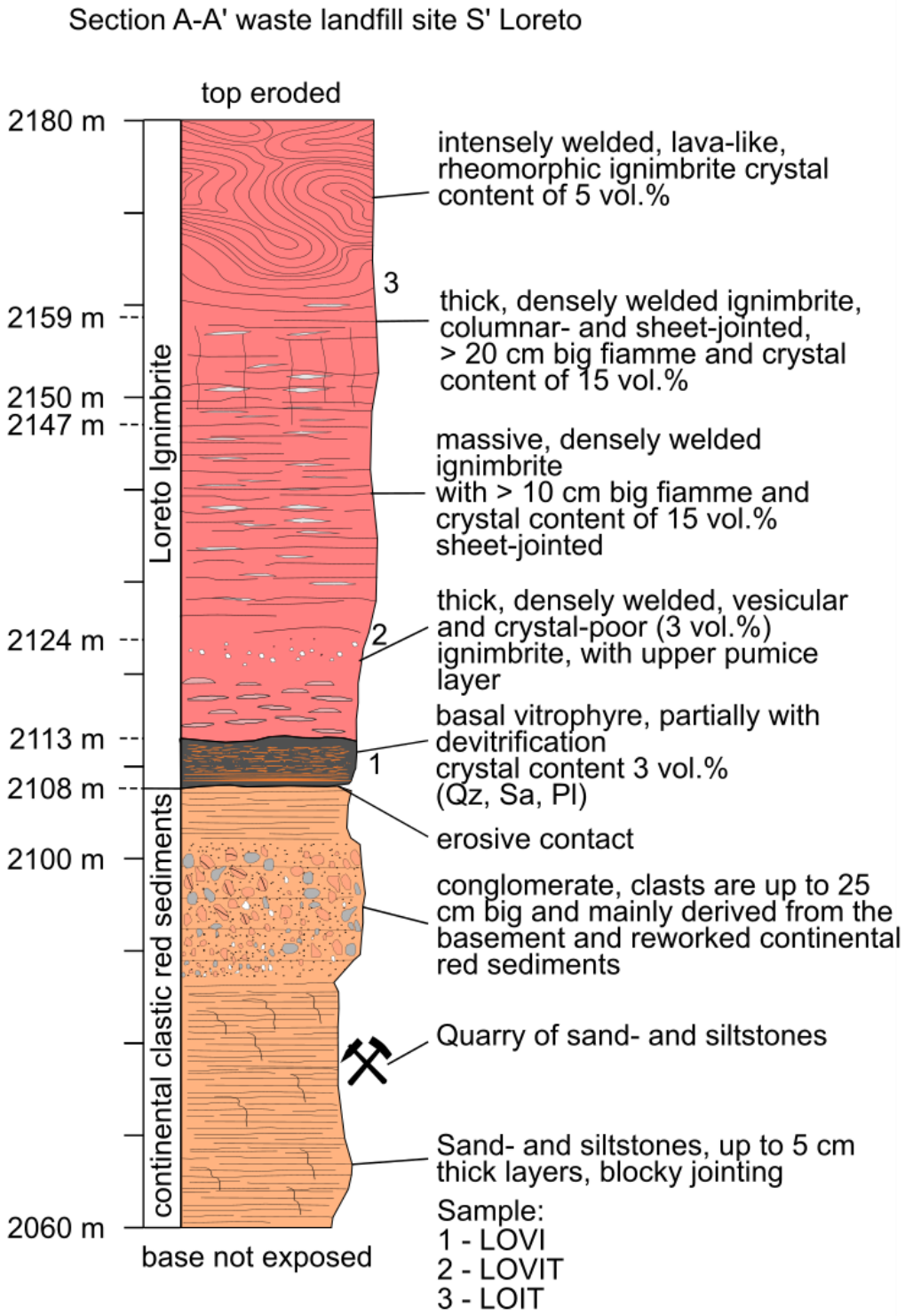

Appendix J 1: Logged section A-A' near the waste landfill of Loreto (Zacatecas). The labels correspond to the sections indicated in the geological map shown in Figure 30. Symbols and stratigraphy are explained in Figure 32. Qz: quartz, Pl: plagioclase, Sa: sanidine.

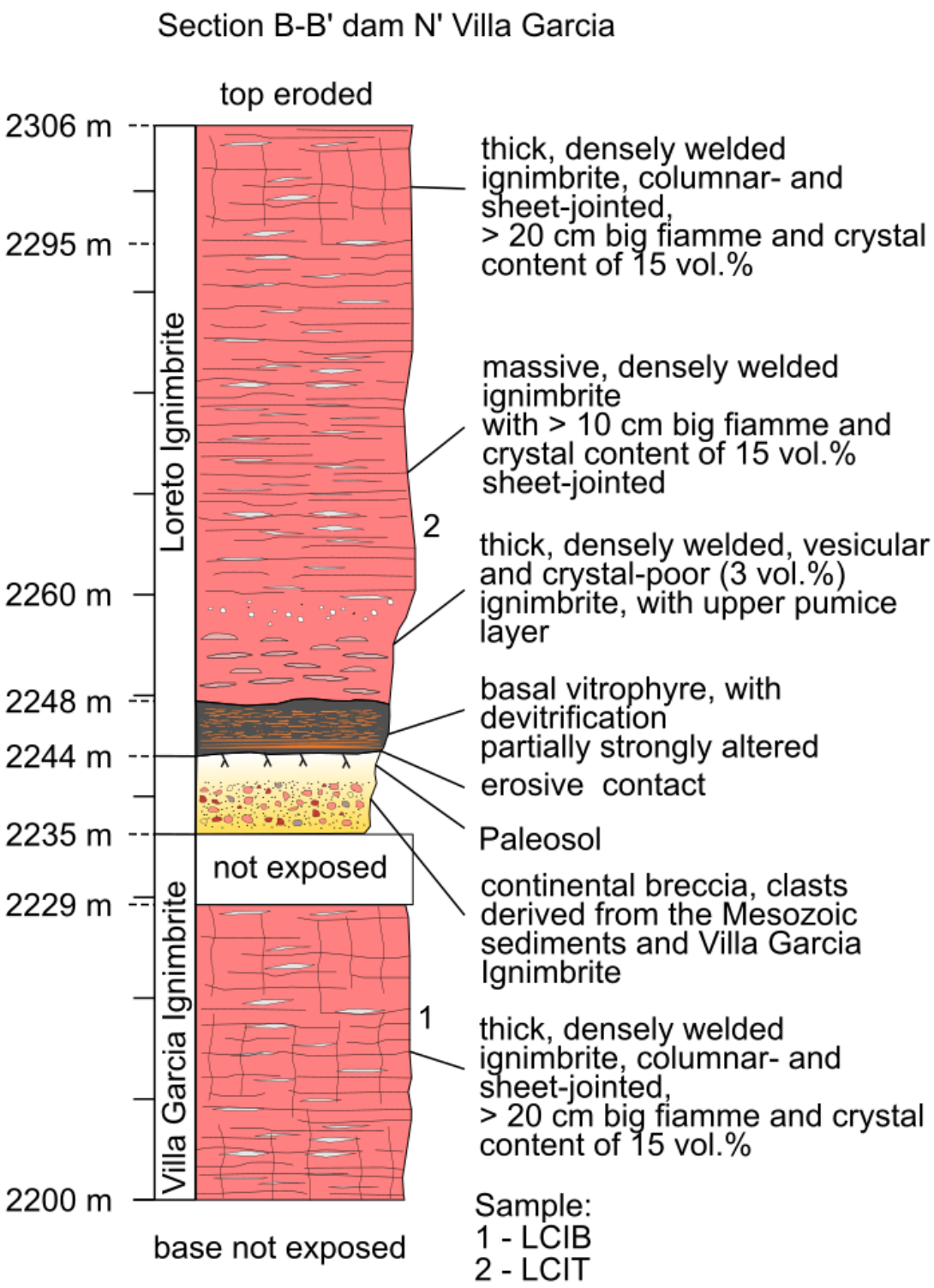

Appendix J 2: Logged section B-B' near the dam north of Villa Garcia (Zacatecas). The labels correspond to the sections indicated in the geological map shown in Figure 30. Symbols and stratigraphy are explained in Figure 32.

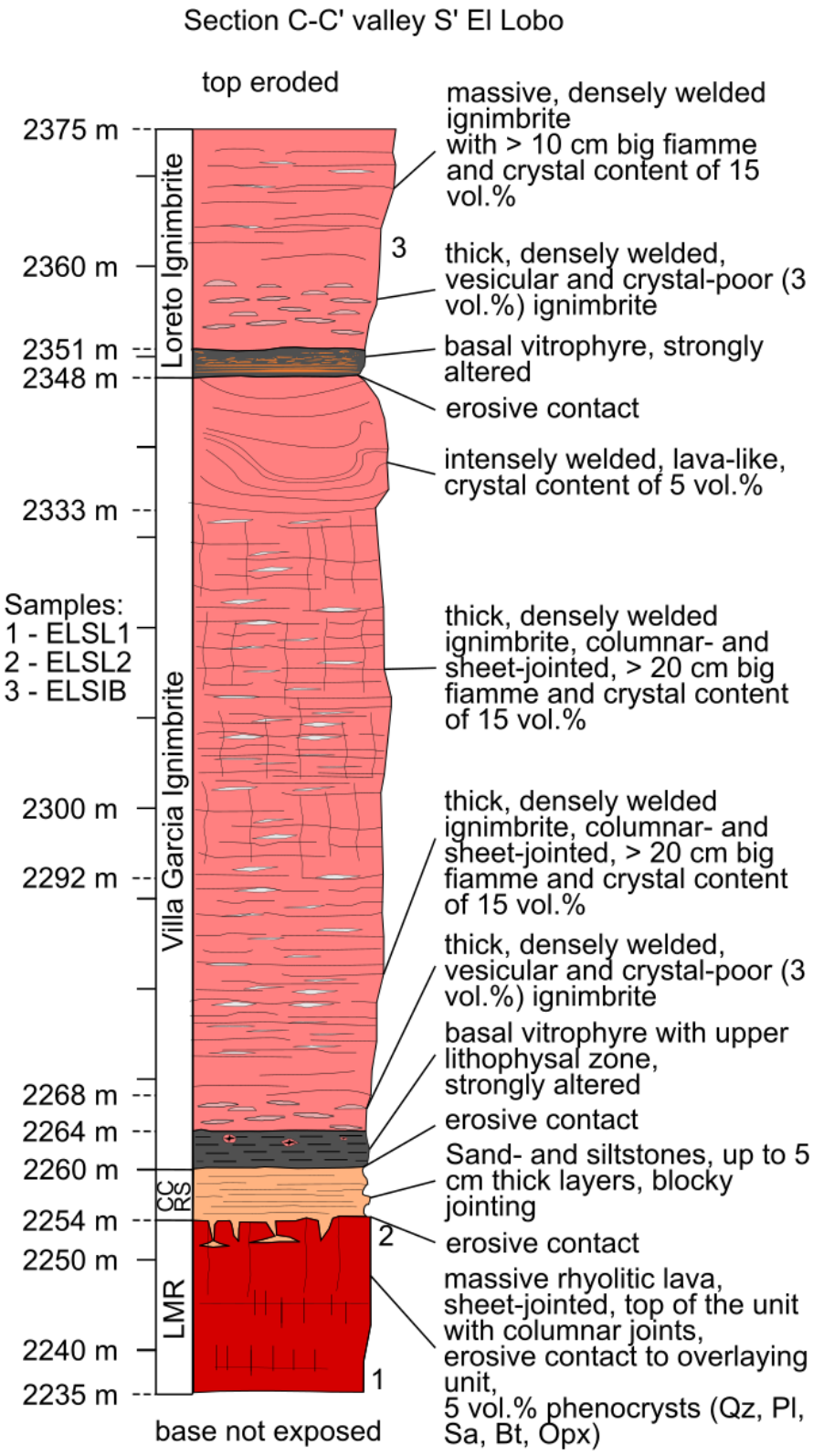

Appendix J 3: Logged section C-C' in the valley south of El Lobo (Zacatecas). The labels correspond to the sections indicated in the geological map shown in Figure 30. Symbols and stratigraphy are explained in Figure 32. Bt: biotite, opx: orthopyroxene, Pl: plagioclase, Qz: quartz, Sa: sanidine.

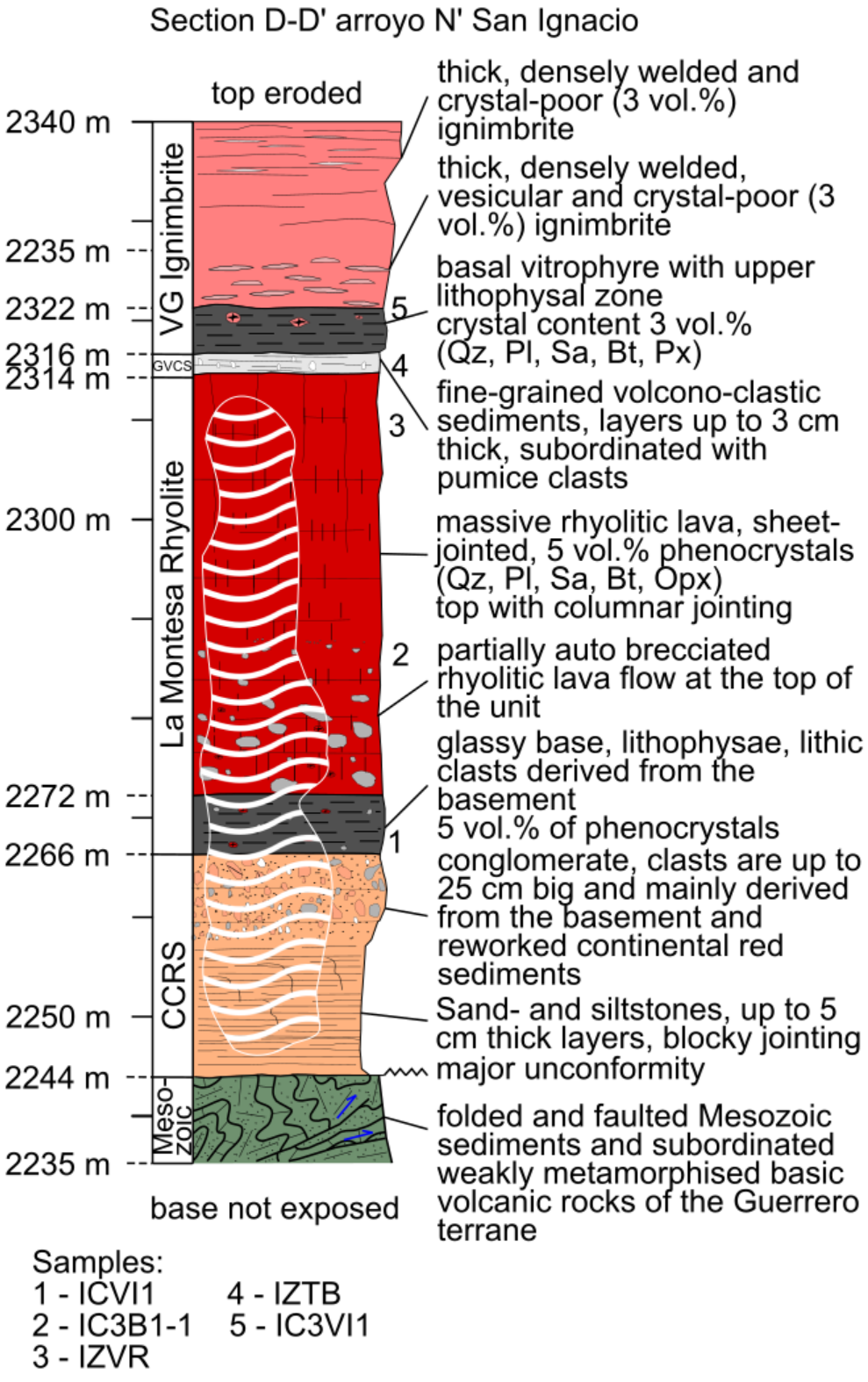

Appendix J 4: Logged section D-D' in the river bed north of San Ignacio (Zacatecas). The labels correspond to the sections indicated in the geological map shown in Figure 30. Symbols and stratigraphy are explained in Figure 32. CCRS: continental clastic red sediments, GVCS: Granadas volcanoclastic sequence, Bt: Biotite, Opx: orthopyroxene, Pl: plagioclase, Qz: quartz, Sa: sanidine.

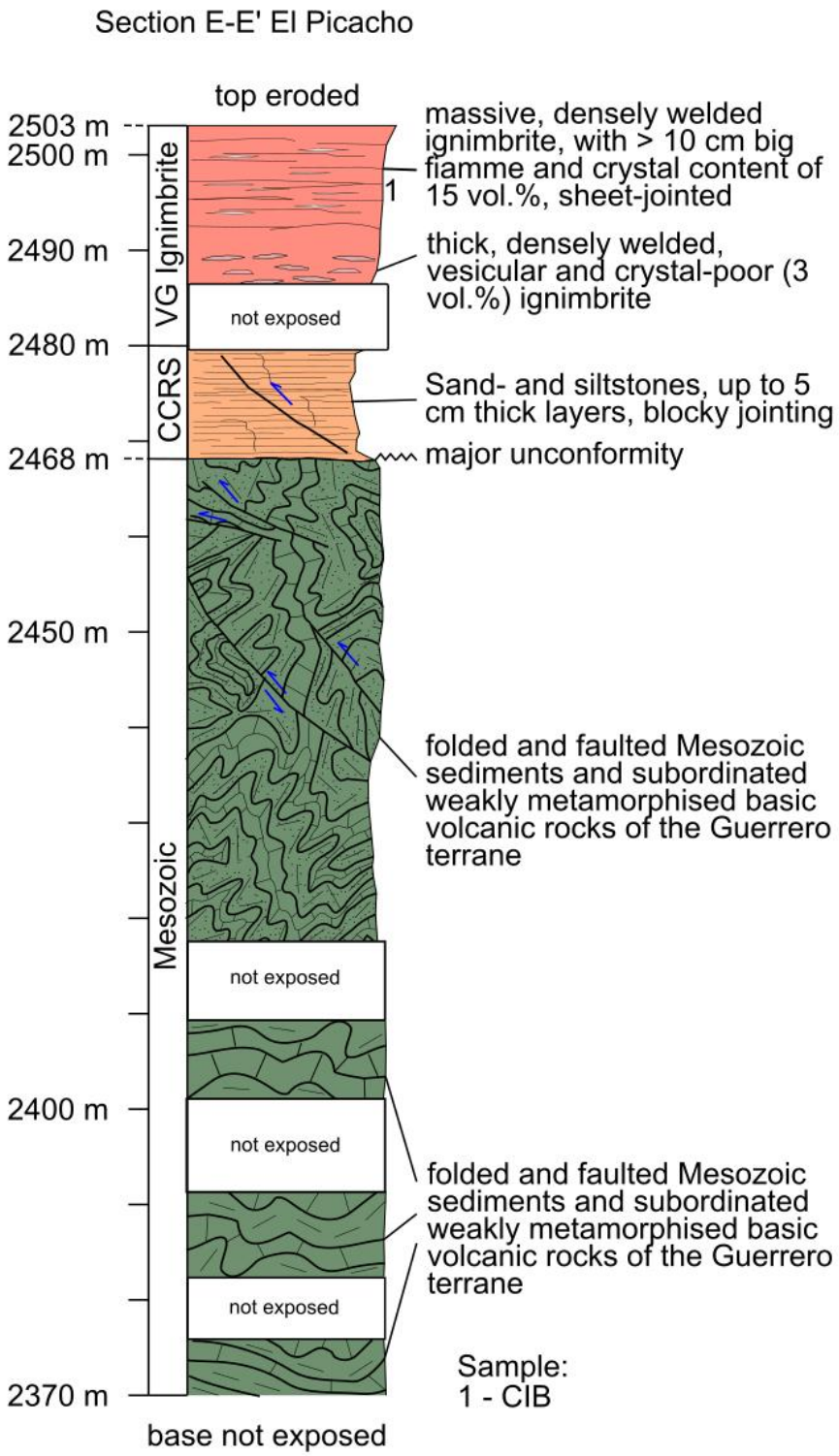

Appendix J 5: Logged section E-E' at the Cerro El Picacho in the center of the study area. The labels correspond to the sections indicated in the geological map shown in Figure 30. Symbols and stratigraphy are explained in Figure 32. CCRS: continental clastic red sediments, VG: Villa Garcia.

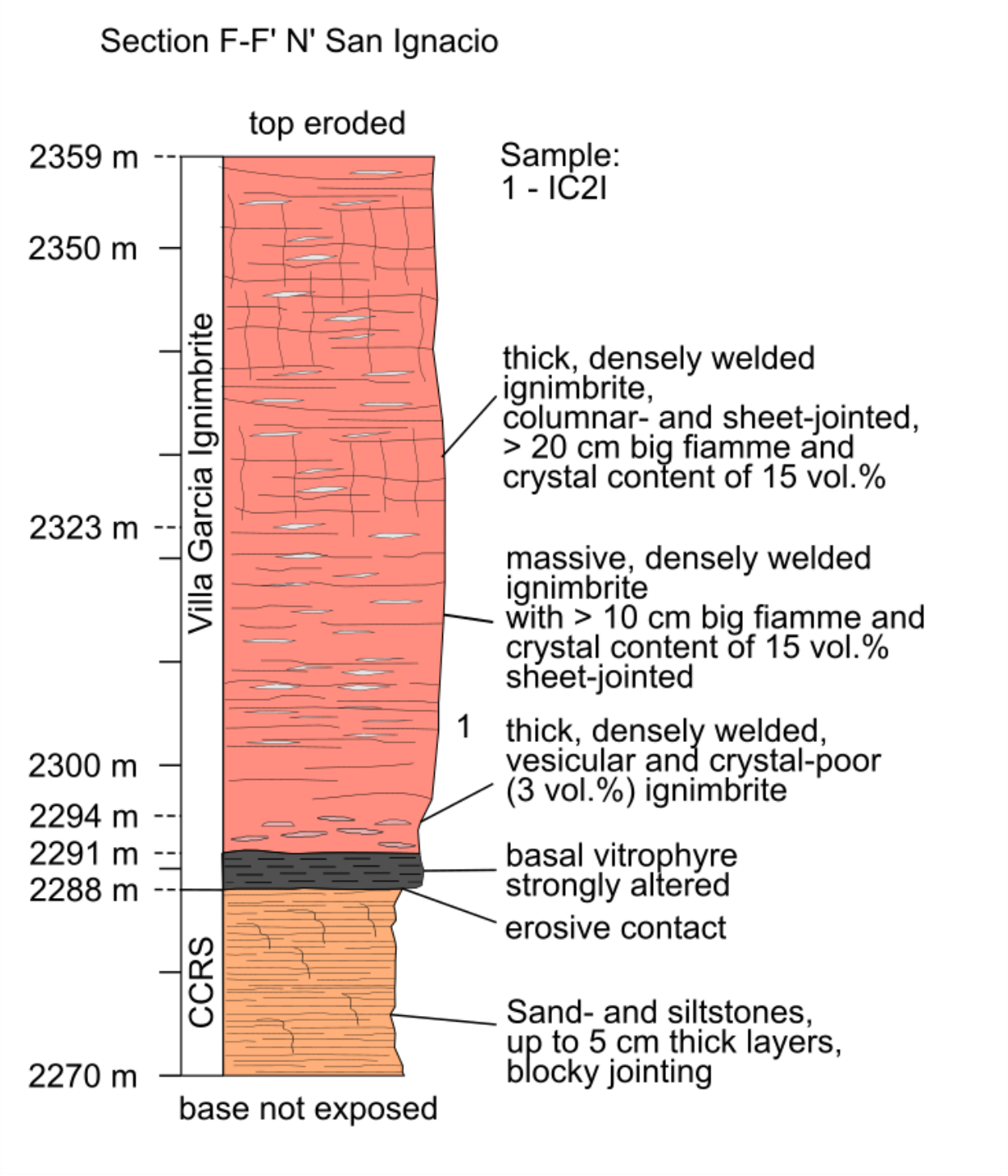

Appendix J 6: Logged section F-F' north of San Ignacio (Zacatecas). The labels correspond to the sections indicated in the geological map shown in Figure 30. Symbols and stratigraphy are explained in Figure 32. CCRS: continental clastic red sediments.

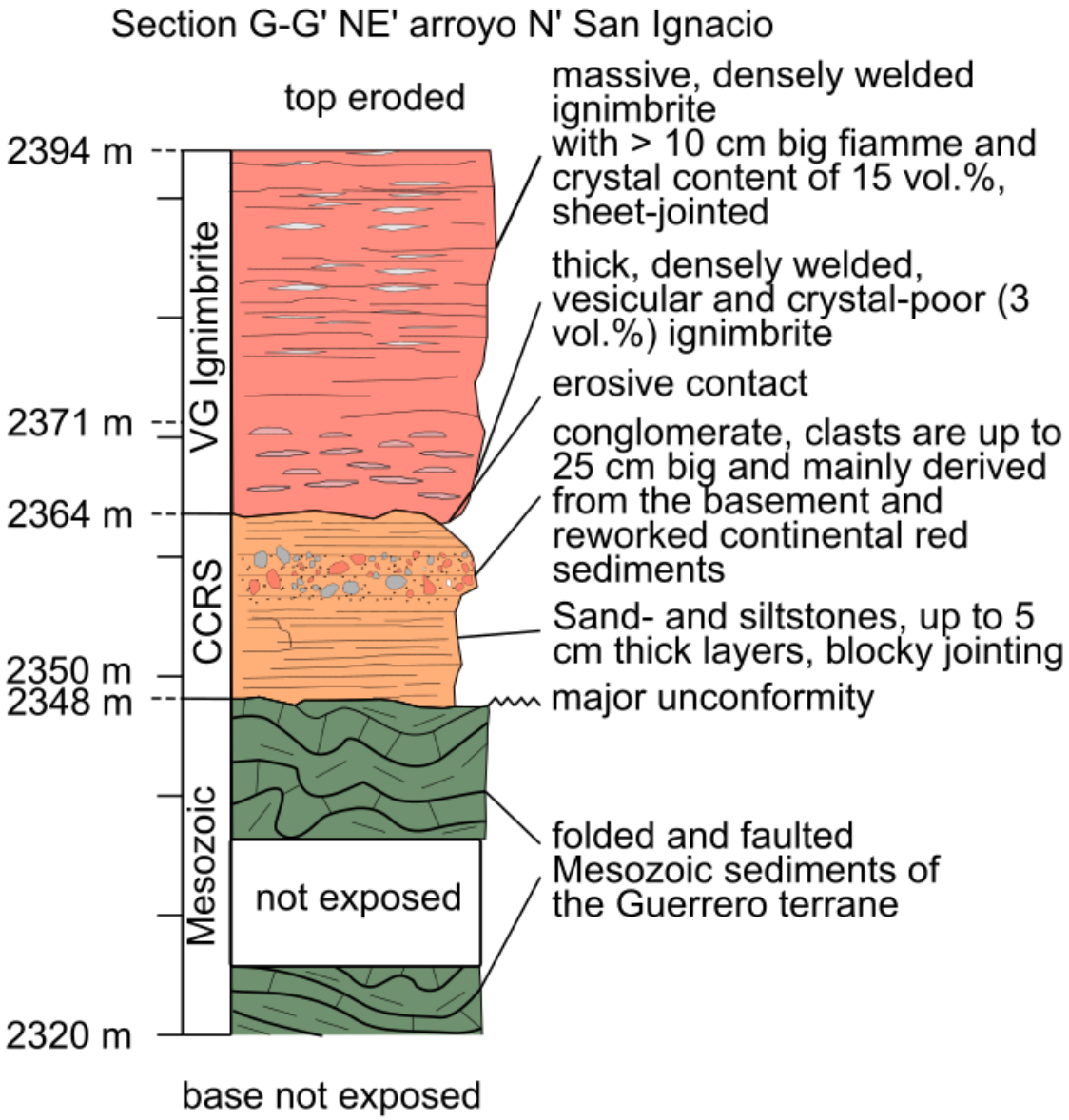

Appendix J 7: Logged section G-G' Northeast of the arroyo north of San Ignacio (Zacatecas). The labels correspond to the sections indicated in the geological map shown in Figure 30. Symbols and stratigraphy are explained in Figure 32. CCRS: continental clastic red sediments, VG: Villa Garcia.

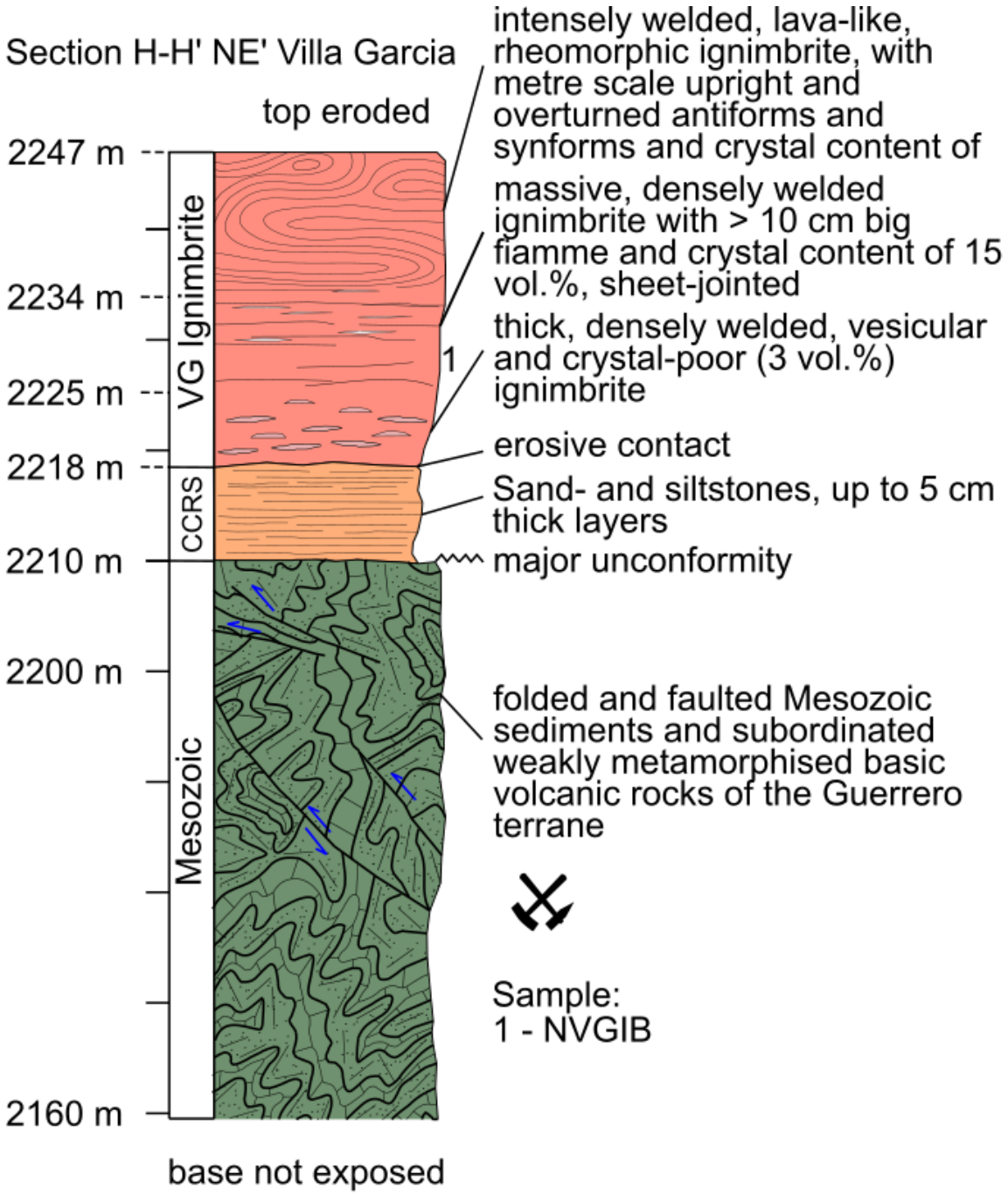

Appendix J 8: Logged section H-H' northeast of Villa Garcia (Zacatecas). The labels correspond to the sections indicated in the geological map shown in Figure 30. Symbols and stratigraphy are explained in Figure 32. CCRS: continental clastic red sediments, VG: Villa Garcia.

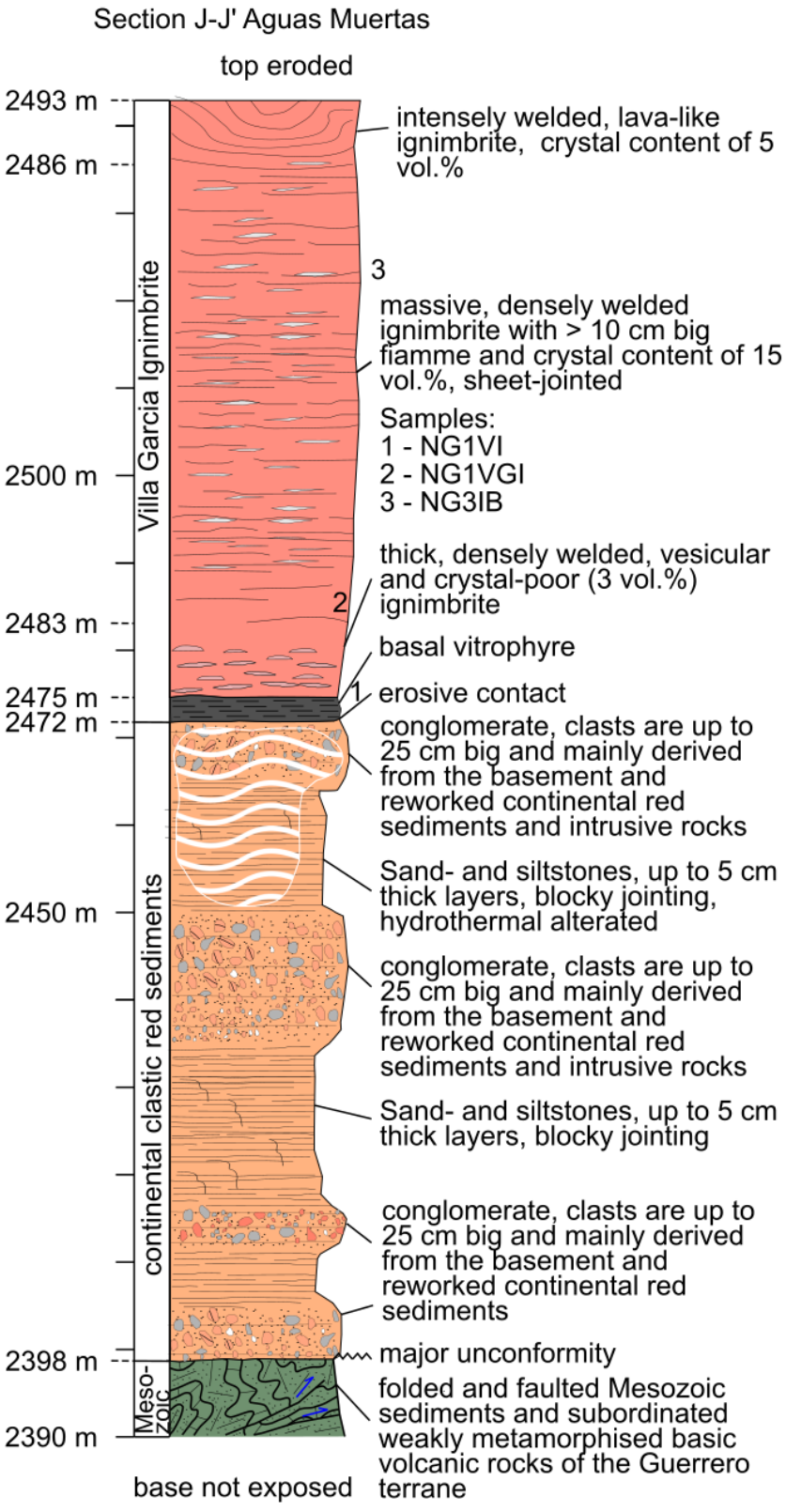

Appendix J 9: Logged section J-J' near Aguas Muertas (Zacatecas). The labels correspond to the sections indicated in the geological map shown in Figure 30. Symbols and stratigraphy are explained in Figure 32.

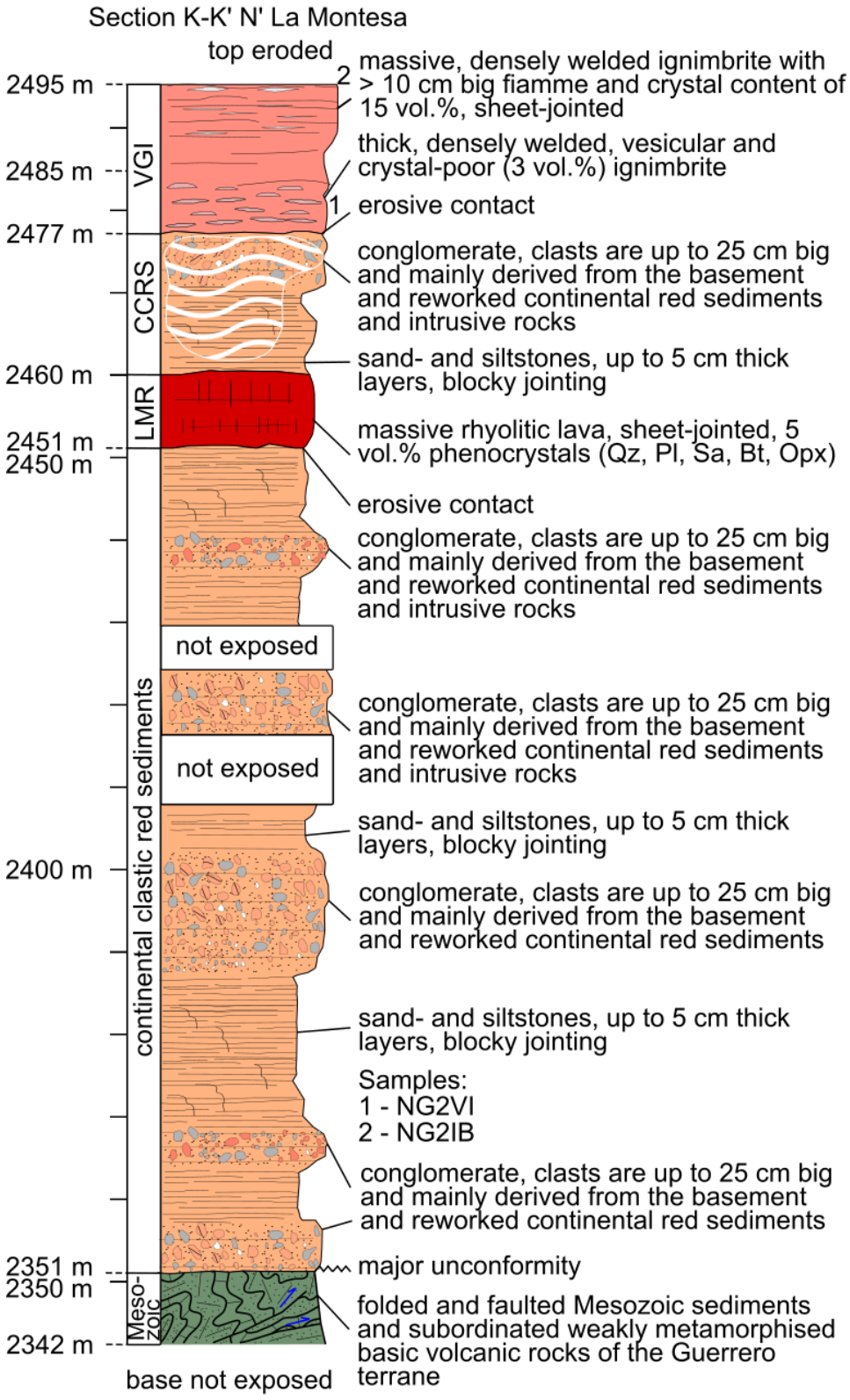

Appendix J 10: Logged section K-K' north of La Montesa (Zacatecas). The labels correspond to the sections indicated in the geological map shown in Figure 30. Symbols and stratigraphy are explained in Figure 32. CCRS: continental clastic red sediments, LMR: La Montesa Rhyolite, VGI: Villa Garcia Ignimbrite Bt: Biotite, Opx: orthopyroxene, Pl: plagioclase, Qz: quartz, Sa: sanidine.

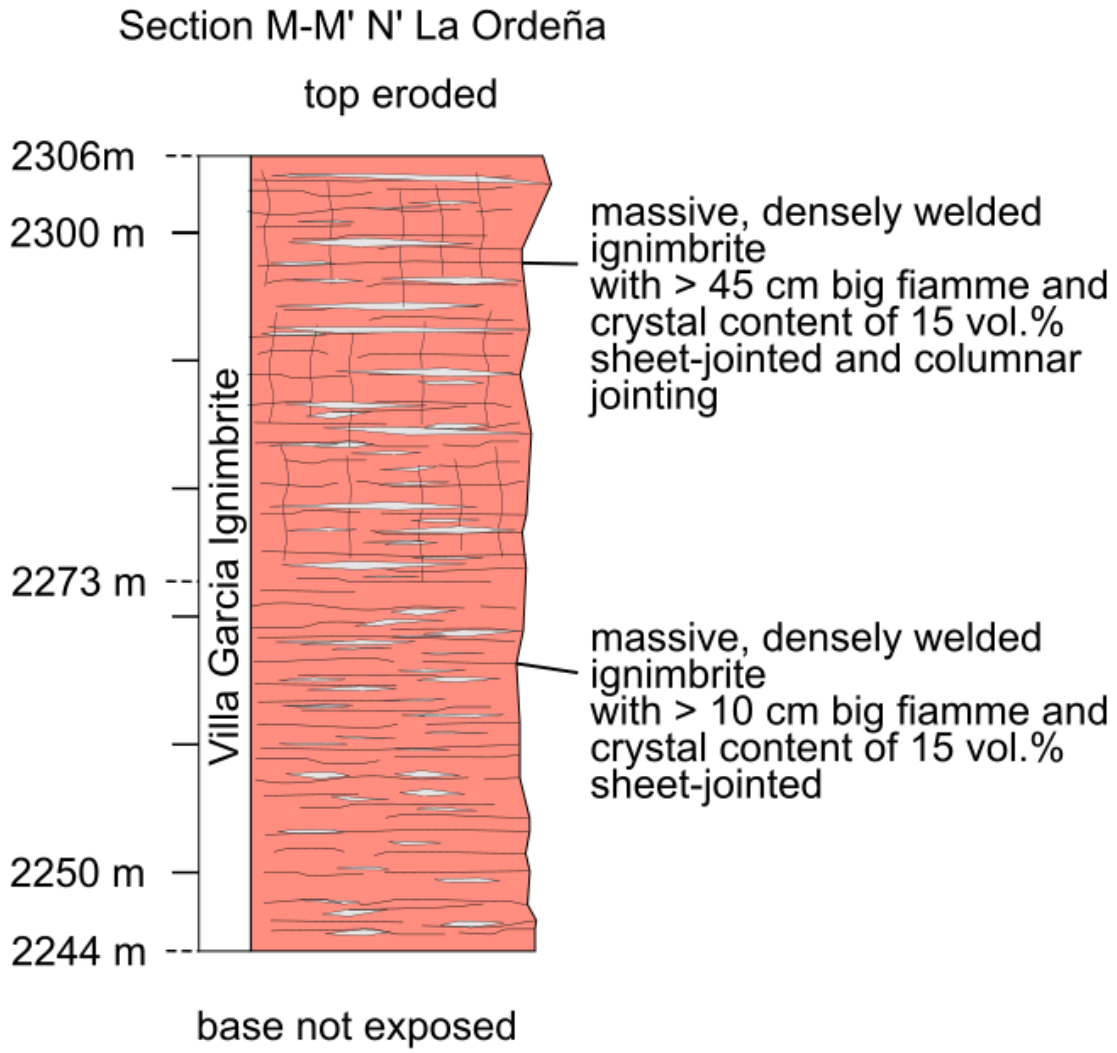

Appendix J 11: Logged section N-N' north La Ordeña (Zacatecas). The labels correspond to the sections indicated in the geological map shown in Figure 30. Symbols and stratigraphy are explained in Figure 32.

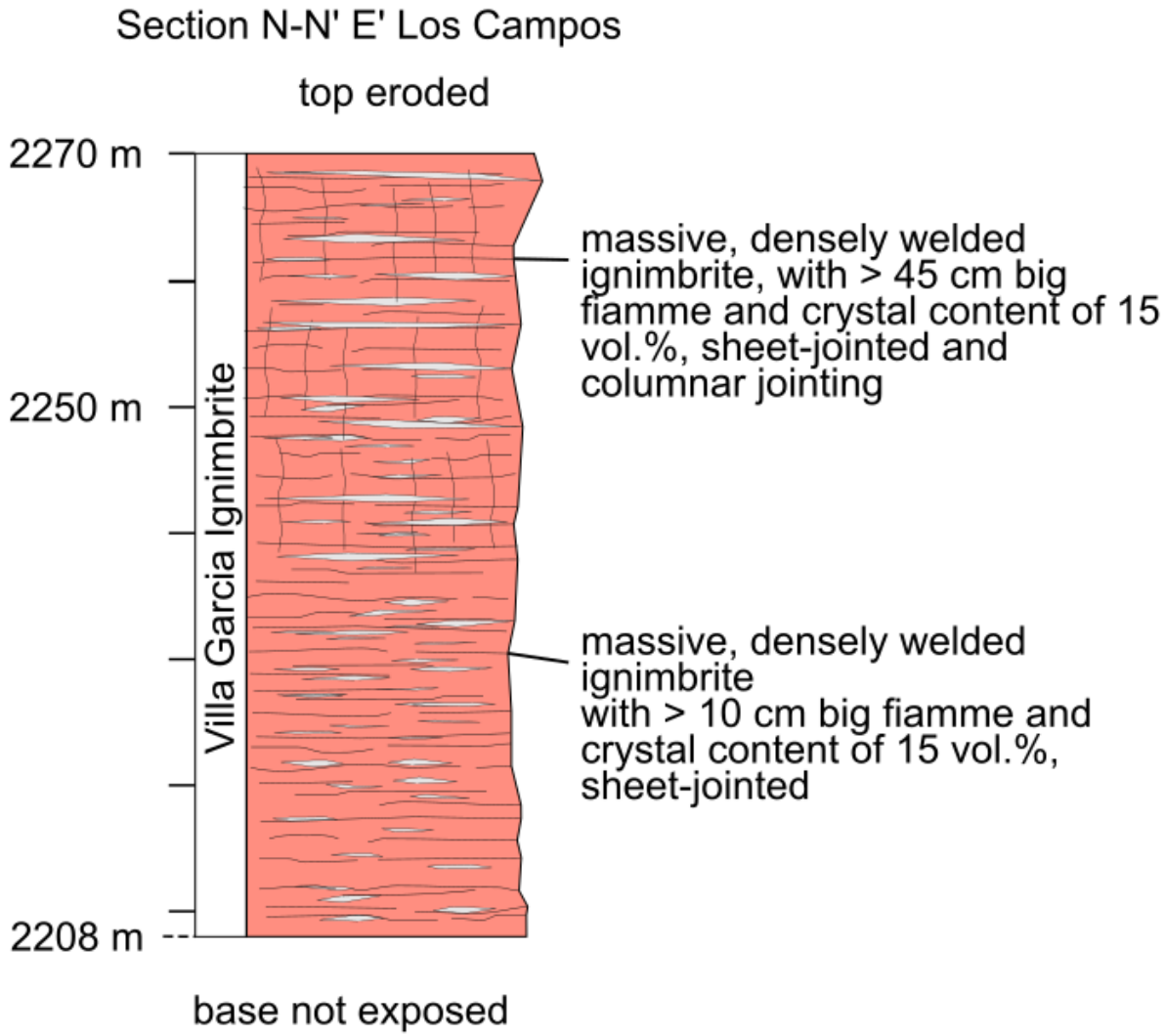

Appendix J 12: Logged section N-N' east of Los Campos (Jalisco). The labels correspond to the sections indicated in the geological map shown in Figure 30. Symbols and stratigraphy are explained in Figure 32.

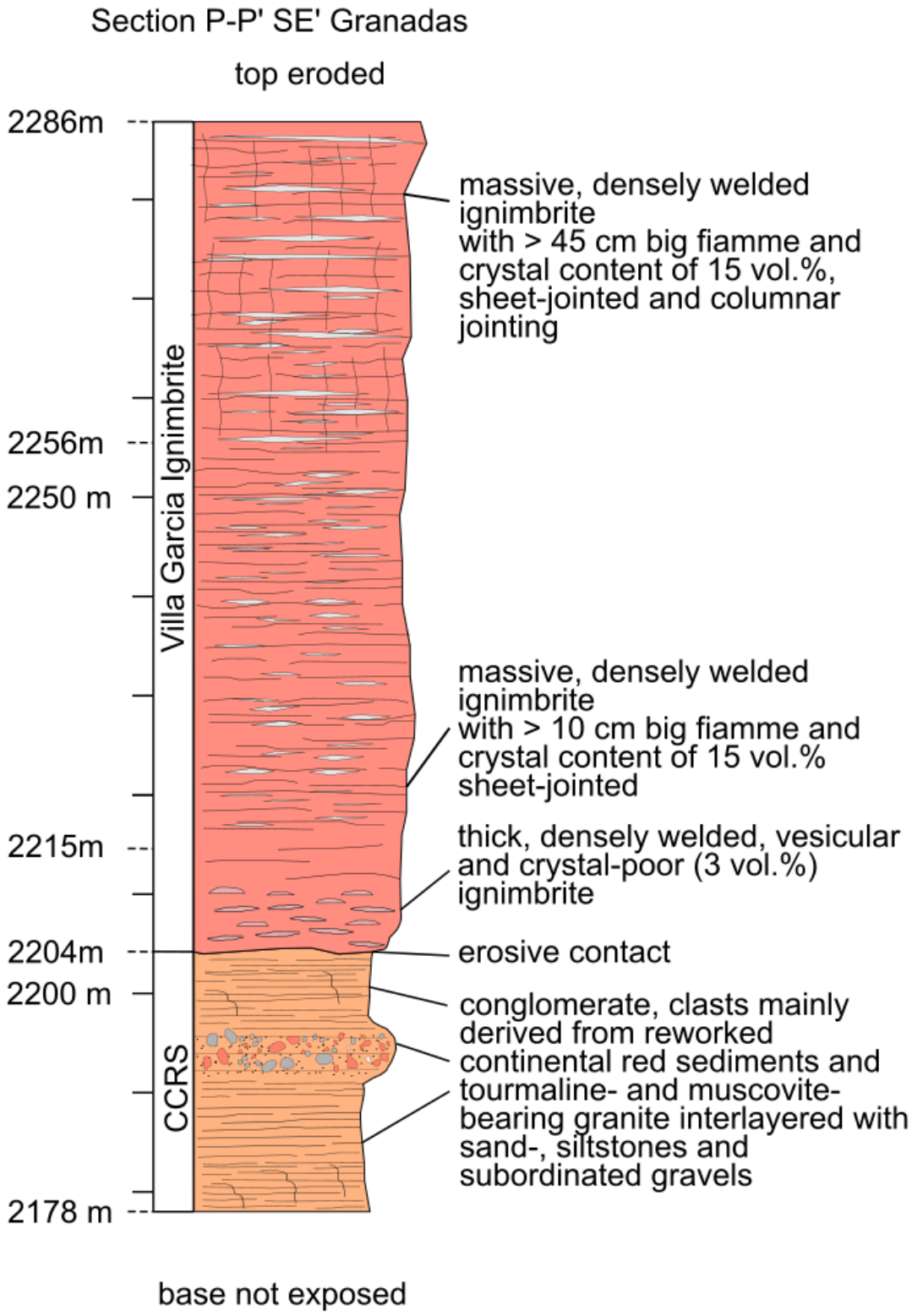

Appendix J 13: Logged section P-P' southeast of Granadas (Zacatecas). The labels correspond to the sections indicated in the geological map shown in Figure 30. Symbols and stratigraphy are explained in Figure 32. CCRS: continental clastic red sediments.

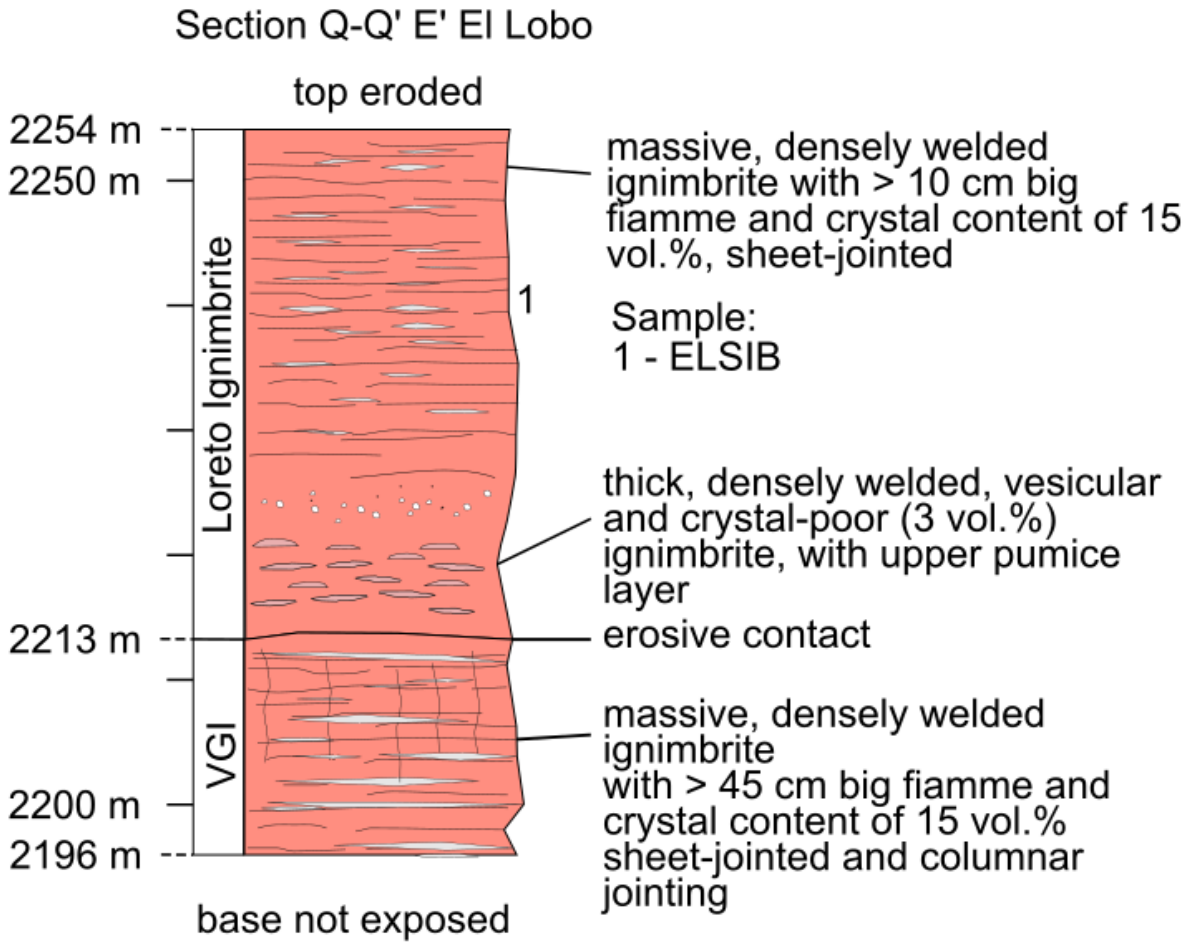

Appendix J 14: Logged section Q-Q' east of El Lobo (Zacatecas). The labels correspond to the sections indicated in the geological map shown in Figure 30. Symbols and stratigraphy are explained in Figure 32.

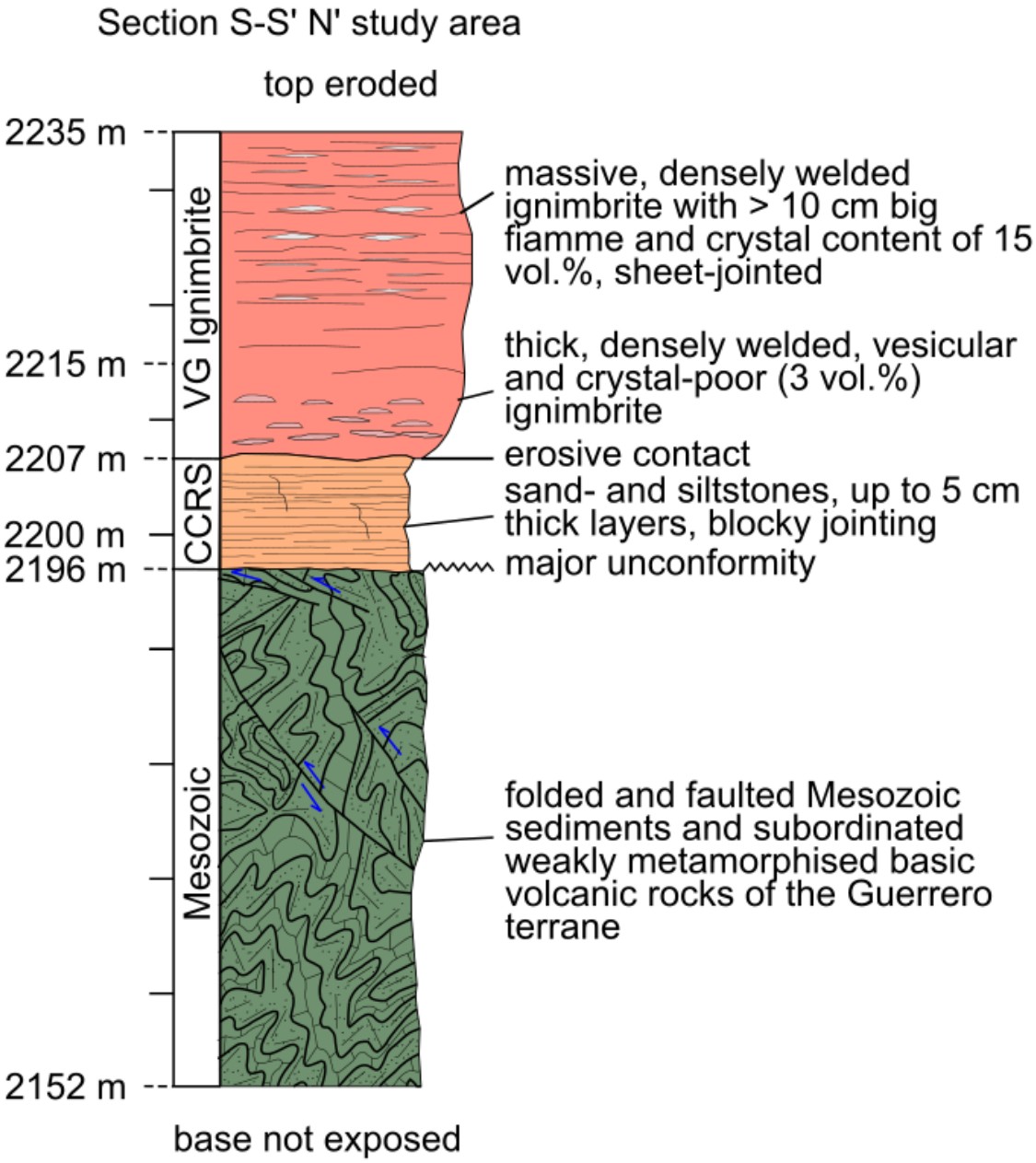

Appendix J 15: Logged section S-S' northern study area. The labels correspond to the sections indicated in the geological map shown in Figure 30. Symbols and stratigraphy are explained in Figure 32. CCRS: continental clastic red sediments, VG: Villa Garcia.

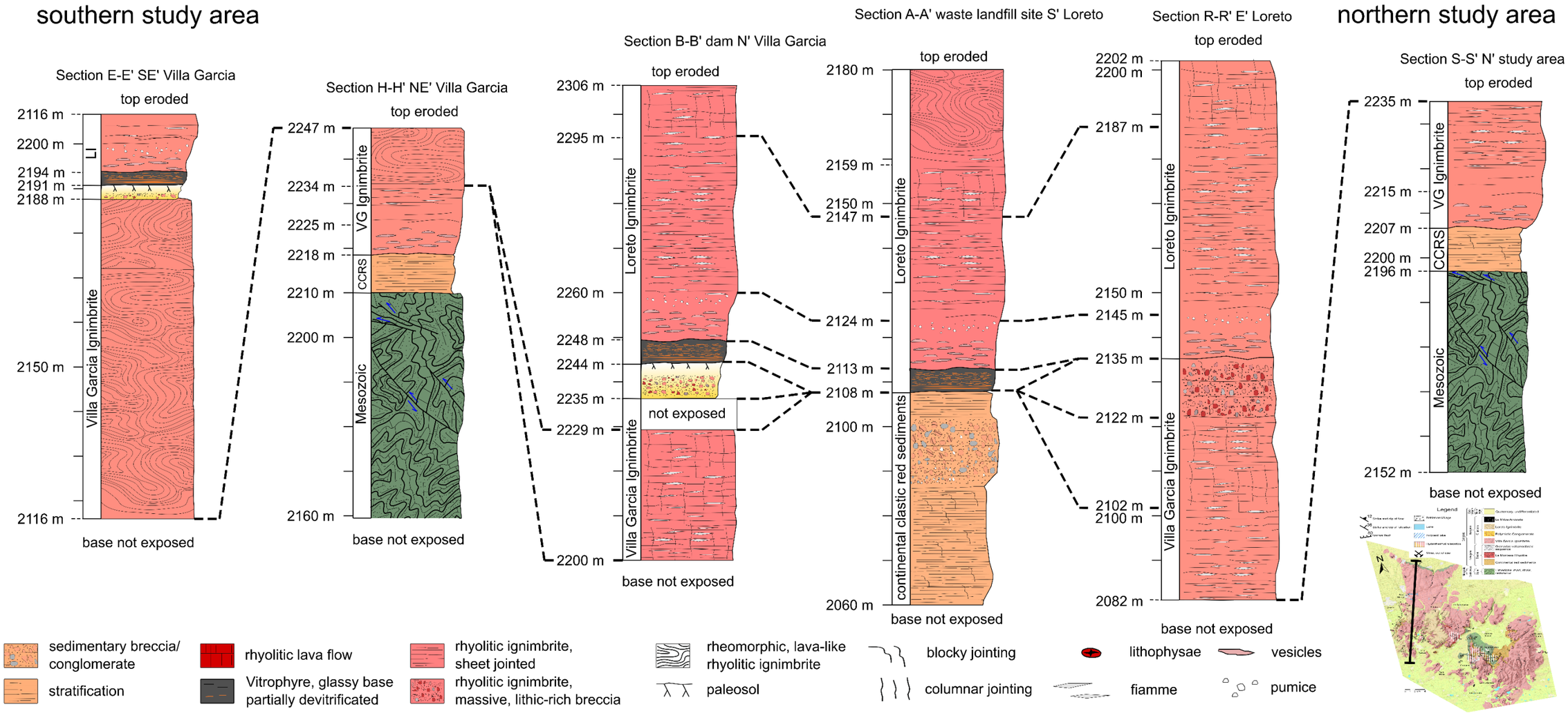

Appendix J 16: Measured and correlation sections in the Villa Garcia Ignimbrite complex, from the center part to the western part of the study area. The labels of the columns correspond to sections indicated in the geological map shown in Figure 30. Logged profiles are shown in Appendix J. CCRS: continental clastic red sediments, VG: Villa Garcia, LI: Loreto Ignimbrite

Appendix K: Representative chemical compositions of feldspars, olivine, and pyroxenes from the Villa Garcia area

See e-Appendix.

Appendix K1: Representative chemical compositions of feldspars from the La Montesa Rhyolite.
Appendix K2: Representative chemical compositions of feldspars from the Villa Garcia Ignimbrite.
Appendix K3: Representative chemical compositions of feldspars from the Loreto Ignimbrite.
Appendix K4: Representative chemical compositions of feldspars from the La Milpa Andesite.
Appendix K5: Representative chemical compositions of pyroxenes from the Villa Garcia volcanic succession.
Appendix K5: Representative chemical compositions of olivines from the La Milpa Andesite.